AB-INITIO INVESTIGATION OF 2D MATERIALS FOR GAS SENSING, ENERGY STORAGE AND SPINTRONIC APPLICATIONS

Saba Khan

April 2023

United Arab Emirates University
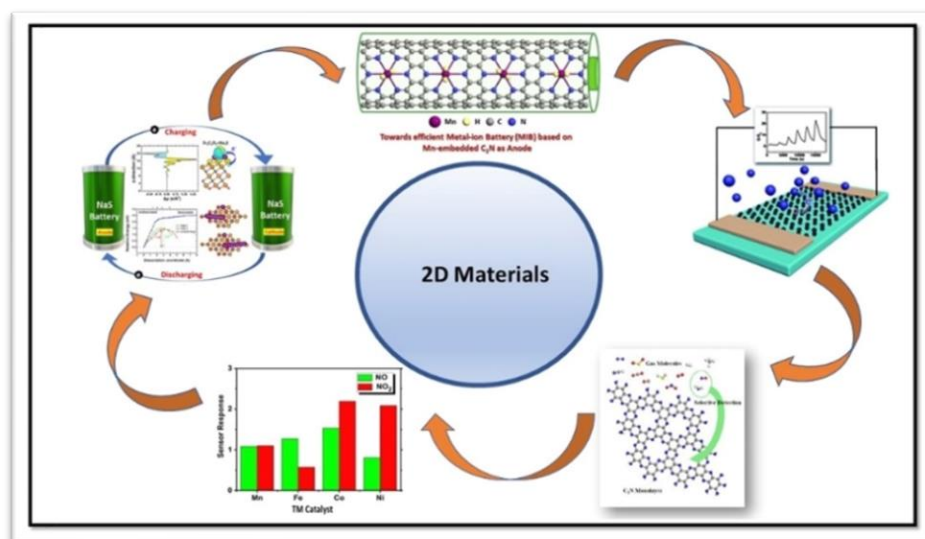
College of Science

AB-INITIO INVESTIGATION OF 2D MATERIALS FOR GAS SENSING, ENERGY STORAGE AND SPINTRONIC APPLICATIONS

Saba Khan

This dissertation is submitted in partial fulfilment of the requirements for the degree of Doctor of Philosophy in Physics

April 2023

**United Arab Emirates University Doctorate Dissertation
2023: 37**

Cover: Image related to use of 2D materials in selective gas sensing and energy storage applications developed in research.

(Photo: By Saba Khan)

Declaration of Original Work

I, Saba Khan, the undersigned, a graduate student at the United Arab Emirates University (UAEU), and the author of this dissertation entitled "*Ab-initio investigation of 2D Materials for Gas sensing, Energy Storage and Spintronic Applications*", hereby, solemnly declare that this is the original research work done by me under the supervision of Prof. Nacir Tit, in the College of Science at UAEU. This work has not previously formed the basis for the award of any academic degree, diploma or a similar title at this or any other university. Any materials borrowed from other sources (whether published or unpublished) and relied upon or included in my dissertation have been properly cited and acknowledged in accordance with appropriate academic conventions. I further declare that there is no potential conflict of interest with respect to the research, data collection, authorship, presentation and/or publication of this dissertation.

Student's Signature:_____

Date: 25/04/2023

Advisory Committee

1) Advisor: Prof. Nacir Tit

Title: Professor

Department of Physics

College of Science

2) Co-advisor: Prof. Noureddine Amrane

Title: Professor

Department of Physics

College of Science

3) Member: Prof. Saleh Thaker

Title: Professor

Department of Physics

College of Science

Approval of the Doctorate Dissertation

This Doctorate Dissertation is approved by the following Examining Committee Members:

1) Advisor (Committee Chair): Prof. Nacir Tit.
   Title: Professor
   Department of Physics
   College of Science, UAE University

   Signature _____   Date ___17/4/2023___

2) Member: Dr. Adel Najar
   Title: Associate Professor
   Department of Physics
   College of Science, UAE University

   Signature _____   Date ___17/4/2023___

3) Member: Dr. Fathy Hassan
   Title: Assistant Professor
   Department of Chemistry
   College of Science, UAE University

   Signature _____   Date ___17/4/2023___

4) Member (External Examiner): Prof. Baker Mohammad
   Title: Professor
   Department of Electrical Engineering and Computer Science.
   Institution: Khalifa University, Abu-Dhabi, UAE

   Signature _____   Date _17/4/2023___

This Doctorate Dissertation is accepted by:

Dean of the College of Science: Professor Maamar Benkraouda

Signature _____

Date _____11/9/2023_____

Dean of the College of Graduate Studies: Professor Ali Al-Marzouqi

Signature Ali Hassan _____

 Date _____11/09/2023_____

Abstract

The field of Two Dimensional (2D) materials has been extensively studied since their discovery in 2004, owing to their remarkable combination of properties. My thesis focuses on exploring novel 2D materials such as Graphene Nanoribbon (GNR), holey carbon nitride C_2N, and MXenes for energy storage, gas sensing, and spintronic applications, utilizing state-of-the-art techniques that combine Density Functional Theory (DFT) and Non-Equilibrium Greens Functions (NEGF) formalism; namely Vienna Ab-initio Simulation Package (VASP) and Atomistic Toolkit (ATK) package. Firstly, on the side of gas sensing, the burning of fossil fuels raises the level of toxic gas and contributes to global warming, necessitating the development of highly sensitive gas sensors. To start with, the adsorption and gas-sensing properties of bilaterally edge doped (B/N) GNRs were investigated. The transport properties revealed that the bilateral B/N edge-doping of GNR yielded Negative Differential Resistance (NDR) IV-characteristics, due to the electron back-scattering which was beneficial for selective gas sensing applications. Therefore, both GNR: B/N were found to be good sensors for NO_2 and SO_3 respectively. After that, the catalytic activity of four magnetic transition metal "TM" elements (e.g., Mn, Fe, Co and Ni) embedded in C_2N pores, as Single-Atom Catalysts (SAC), was tested towards detecting toxic oxidizing gases. The results of spin-polarized transport properties revealed that Ni- and Fe-embedded C_2N are the most efficient in detecting NO/ NO_2 and NO_2 molecules.

Secondly, on the side of energy storage, since the fossil fuels reserves are depleting at an alarming rate, there is an urgent need for alternative forms of energy to meet the ever-growing demand for energy. Hydrogen is a popular form of clean energy. However, its storage and handling are challenging because of its explosive nature. The effect of magnetic moment on the hydrogen adsorption and gas-sensing properties in Mn-embedded in C_2N were investigated. Two distinct configurations of embedment were considered: (i) SAC: $1Mn@C_2N$; and (ii) DAC: $Mn_2@C_2N$. Based on the huge changes in electronic and magnetic properties and the low recovery time (i.e., $\tau \ll 1$ s, $\tau = 92$ µs and 1.8 ms, respectively), we concluded that C_2N:Mn is an excellent candidate for (reusable) hydrogen magnetic gas sensor with high sensitivity and selectivity and rapid recovery time. Then, a comparative study of hydrogen storage capabilities on Metal-

catalyst embedded (Ca versus Mn) C_2N is presented which demonstrated the stability of these metal structures embedded on the C_2N substrate. We proposed $Ca@C_2N$ and $Mn@C_2N$ for dual applications- hydrogen storage and a novel electrode for prospective metal-ion battery applications owing to its high irreversible uptake capacity 200 $mAhg^{-1}$. Thirdly, on the side of data storage, spintronics is an emerging field for the next generation nanoelectronics devices to reduce their power consumption and to increase their memory and processing capabilities. Designing 2D-materials that exhibit half-metallic properties is important in spintronic devices that are used in low-power high-density logic circuits. We tested samples comprising of SAC and DAC of Mn embedded in a C_2N sample size 2×2 primitive cells as well as their combinations in neighboring large pores. Many other TM catalysts were screened, and the results show the existence of half metallicity in just five cases: (a) C_2N:Mn (DAC, SAC-SAC, and SAC-DAC); (b) C_2N:Fe (DAC); and (c) C_2N:Ni (SAC-DAC). Our results further showed the origins of half-metallicity to be attributed to both FMC and synergetic interactions between the catalysts with the six mirror images, formed by the periodic-boundary conditions. Lastly, on the side of batteries, sodium-sulfur batteries show great potential for storing large amounts of energy due to their ability to undergo a double electron- redox process, as well as the plentiful abundance of sodium and sulfur resources. However, the shuttle effect caused by intermediate sodium polysulfides (Na_2S_n) limits their performance and lifespan. To address this issue, we proposed two functionalized MXenes $Hf_3C_2T_2$ and $Zr_3C_2T_2$ (T= F, O), as cathode additives to suppress the shuttle effect. We found that both $Hf_3C_2T_2$ and $Zr_3C_2T_2$ systems inhibit the shuttle effect by binding to Na_2S_n with a binding energy higher than the electrolyte solvents. The decomposition barrier for Na_2S_n on the O functionalized MXenes gets reduced which enhances the electrochemical process. Overall, our findings show that the tuning of 2D materials can lead to promising applications in various fields, including energy storage, gas sensing, and spintronics.

Keywords: 2D materials, gas-sensing, metal-ion batteries, spintronics, hydrogen storage, metal-sulfur batteries.

Title and Abstract (in Arabic)

دراسة نظرية لمواد ثنائية الأبعاد و تطبيقاتها في مجالات استشعار الغازات، و تخزين الطاقة، و تخزين المعلومات

الملخص

منذ زمن اكتشاف الغرافين عام 2004 تركزت العديد من الأبحاث على دراسة المواد ثنائية الأبعاد. منذ ذلك العهد، تم تصنيع العديد من الأنواع من السبائك ثنائية الأبعاد و ظهرت العديد من التطبيقات في مجالات متنوعة مثل البيئة، توليد الطاقة، تخزين الطاقة، و تخزين المعلومات. في هذه الأطروحة ركزنا على شرائح الجرافين (GNR) و شرائح و سبائك C_2N، و أخيرا شرائح المكسين (MXenes). اعتمدنا في جميع بحوثنا النظرية على برامج محاكاة ذات سمعة عالمية أهمها مثل VASP و ATK في حساب الخصائص الكهربائية و المغناطيسية و الناقلية الكهربائية. في نطاق استشعار الغازات السامة، هناك بابين. في الباب 1، قمنا باستخدام شرائح الجرافين المنضبة بعنصرين النتروجين و البورون على حافتيهما (B/N-edge doped GNR). لقد تم الحصول على المقاومة التفاضلية السلبية (NDR) نتيجة لتراجع التيار الكهربائي جراء وجود الشوائب على الطريق. لقد تم استخدام الظاهرة "NDR" في تحسين استشعار الغازات السامة على سبيل المثال (NO_2, SO_3). في حين أن الباب 5 ركز على دراسة سبائك C_2N المنضبة بعناصر المعادن الممغنطة (Mn, Fe, Co, Ni). لقد أظهرت هذه المنضبات حساسية عالية لاستشعار الغازات المؤكسدة السامة نظرا لوجود سر و يكمن في التغير للعزم المغناطيسي الهائل بعد التصاق الغازات بالمعدن.في نطاق تخزين الطاقة، و خصوصا تخزين غاز الهيدروجين، قمنا باستخدام سبائك C_2N المنضبة بذرات معدن ممغنط مثل المغنيزيوم "Mn" و الغير ممغنط مثل الكالسيوم "Ca"، حيث تم رفق ذرة واحدة (SAC) أو ذرتين (DAC) داخل جوف الثغرة الكبرى لمادة C_2N. كانت النتائج مثيرة حيث تم ربط جزيئات الهيدروجين بذرات المعدن Mn أوCa و سببت زيادات بنسب ملحوظة في سعة استقطاب غاز الهيدروجين. في نطاق تخزين المعلومات عن طريق الخصائص العزم المغزلي للالكترونات (Spintronics)، لقد قمنا بدراسة سبائك C_2N المنضبة بذرة واحدة أو ذرتين من معدن ممغنط "Mn". لقد أظهرت النتائج أن التأثيرات المغناطيسية بين كل من: SAC-SAC أوSAC-DAC أوDAC-DAC قد تؤدي ليس فحسب لتشكيل عزم مغناطيسي بل لتشكيل مواد ذات خاصية نصف ناقلة (Half metal). لقد كانت لهذه الدراسة فائدة كبيرة في فهم ميكانيكية تكوين الخصائص النصف ناقلة من أجل تحقيق تطبيقها في تصنيع أجهزة تخزين المعلومات المعاصرة. في نطاق البطاريات و تخزين الطاقة، خاصة تلك ذات الكفاءة العالية و التي تشتغل في درجات حرارة عادية مثل بطاريات كبريتات الصوديوم، لقد قمنا بدراسة بعض العوائق المعروفة في سبيل تذليلها و التقليل من اثارها السلبية مستقبلا و بالتالي تمديد عمر البطارية. من ضمن هذه المعوقات نذكر تاكل قطب البطارية المكونة من الكبريت نتيجة تفاعله الكيميائي مع أيونات الصوديوم. لقد قمنا خلال هذه الدراسة باقتراح شرائح المكسين (MXenes) لرفقها بالقطب السالب للبطارية حتى تقوم بحماية القطب من الاضمحلال والتلاشي السريع. هذا الحل يؤدي الى زيادة عمر البطارية و كفاءة عملها. في النهاية كملخص، لقد قمنا باستخدام برامج محاكاة عالية الجودة و الكفاءة في دراسة استشعار

الغازات السامة، و تخزين الطاقة و تخزين المعلومات. كانت الدراسة مفيدة جدا في توضيح أهم العوامل التي تتحكم في تفادي العوائق لفائدة تحسين الأداء و الكفاءة في تشغيل الأجهزة الخاصة بكل تطبيق.

كلمات البحث الرئيسية: المواد ثنائية الأبعاد، استشعار الغازات، تخزين غاز الهيدروجين، معادن-البطاريات الكبريتية، Spintronics، ATKو VASP.

Author's Contribution

The contribution of Saba Khan to the dissertation was as follows:

I. Participated in construction of the research problem, conducted literature review in order to understand the underlying principles/phenomenon involved and identification of the research gap.

II. Carried out the DFT calculations, such as atomic relaxations, band structure and Density of states calculations, in order to benchmark the simulations with the available existing experimental/theoretical data.

III. Responsible for assimilation and analysis of data, which resulted in dissemination of results in the form of journal publications.

IV. Contributed to writing the manuscripts resulting in publishing papers in high quality (top) journals.

Acknowledgements

Dedication

Dedicated to my mother, who instilled in me the value of education and encouraged me to pursue my dreams, and to my husband, whose unwavering support and love have been my constant source of strength throughout my PhD journey!

Table of Contents

List of Tables

List of Figures

List of Abbreviations

A-GNR   Armchair-edged Graphene Nanoribbon

AFMC   Antiferromagnetic Coupling

ATK   Atomistic Took Kit

APS   Aminopropysilane

BZ   Brillouin Zone

CB   Conduction Band

C_{60} Fullerene

CDD   Charge Density Difference

CIB   Calcium Ion Batteries

CI-NEB   Climbing Image-Nudged Elastic Band

C_2N Carbon Nitride

C_2N-NR   Carbon Nitride-Nanoribbon

C_2N-ML   Carbon Nitride-Monolayer

CPMD   Car-Parrinello Molecular Dynamics

CNT   Carbon Nanotube

2D   Two-Dimensional

DAC   Dimer Atom Catalyst

DC   Direct Current

DFT   Density Functional Theory

DSSC	Dye Sensitized Solar Cell
DOL	1, 3 Dioxolane
DOS	Density of States
DME	1, 2 Dimethoxyethane
DNA	Deoxyribonucleic Acid
E_g	Band Gap
FET	Field Effect Transistors
FMC	Ferromagnetic Coupling
FNN	First Nearest Neighbors
G-FET	Graphene-based Field Effect Transistor
GGA	Generalized Gradient Approximation
GNR	Graphene Nanoribbon
HOMO	Highest Occupied Molecular Orbital
h-2D	Holey 2-Dimensional
IAEA	International Atomic Energy Agency
IV	Current-Voltage
LDH	Layered Double Hydroxide
LIB	Lithium-ion Batteries
LUMO	Lowest Unoccupied Molecular Orbital
MA	Metal Atom
MC	Metal Catalyst

MD	Molecular Dynamics
MIB	Metal-ion Batteries
MOF	Metal Organic Frameworks
MOX	Metal Oxides
MWCNT	Multi Walled Carbon Nanotube
Na-SP	Sodium Polysulfide
NaSB	Sodium Sulfur Battery
NDR	Negative Differential Resistance
NEGF	Non-Equilibrium Greens Function
ODOS	Orbital Density of States
ORR	Oxidation Reduction Reaction
PAW	Projected-Augmented Plane Waves
PC	Primitive Cell
PBE	Perdew-Burke Ernzerhof
PDOS	Partial Density of States
PPB	Parts per Billion
PPM	Parts per Million
RT	Room Temperature
SAC	Single Atom Catalyst
SIB	Sodium-ion Battery

SIESTA	Spanish Initiative for Electronic Simulation with Thousands of Atoms
SWCNT	Single Walled Carbon Nanotube
T_c	Curie Temperature
TDOS	Total Density of States
TM	Transition Metal
TVCR	Top to Valley Current Ratio
USEPA	United States Environmental Protection Agency
VASP	Vienna Ab-initio Simulation Package
VB	Valence Band
VdW	Van der Waal
ZZ-GNR	Zigzag Edged Graphene Nanoribbon

Chapter 1: Introduction

1.1 Background of 2D Materials

Two-dimensional (2D) materials have attracted a lot of attention from researchers and engineers due to their unique properties and potential applications in various fields. Since the discovery of graphene in 2004 by Novoselov and Geim [1] which fetched them a Nobel Prize in 2010, tremendous efforts have been taken to study 2D systems and to employ their fascinating combination of properties in real life applications. Graphene is a thermodynamically stable monolayer of sp^2 hybridized carbon atoms. The electronic structure of graphene displays an almost linear crossing between the valence and conduction band at the K-corner of the Brillouin zone, forming the so called 'Dirac' cones. Due to this almost linear dispersion relation, the electrons possess exceptionally high mobility ($\mu \sim 2x10^5$ cm^2/Vs) which far exceeds that of GaAs. Therefore, graphene is being explored heavily for novel electronic devices with exceptional ultra-fast response. In terms of gas sensing, graphene has been demonstrated to possess the sensitivity to detect even a single gas molecule [2], however this can be further enhanced, and selectivity can be generally induced upon chemically functionalization [3-6].

Here are some of the key significances of 2D materials:

1. Novel electronic and optical properties: 2D materials exhibit properties that are not present in their bulk counterparts due to their reduced dimensionality [7]. For example, graphene is a single layer of carbon atoms with exceptional electronic and mechanical properties that can be utilized in electronic and optoelectronic devices.

2. High surface area: 2D materials have high surface area to volume ratios, which makes them ideal for catalysis, sensing, and energy storage applications.

3. Lightweight and flexibility: 2D materials are thin and flexible, which makes them useful for designing wearable devices and flexible electronics.

4. Ecofriendly: 2D materials are often more environmentally friendly than conventional materials due to their low carbon footprint and potential for recyclability.

5. Versatility: There is a wide range of 2D materials available with different properties, which makes them useful for a broad range of applications, including electronics, photonics, energy, catalysis, sensing, and biomedical engineering.

Overall, the unique properties of 2D materials make them promising candidates for a range of technological applications, and research in this area is expected to continue to grow in the coming years. In the present work, several novel 2D systems have been explored. These 2D materials have been explained below subsequently followed by an introduction of the specific applications they were tailored for and employed in. The research problems addressed have been briefly introduced in this Chapter and explained in detail in the subsequent Chapters. Thereafter in this Chapter, a detailed review of the methodology used in all our calculations (Ab initio DFT based simulations) has been presented and described.

1.1.1 Graphene Nanoribbons (GNR)

Strips of graphene that have a narrow width (less than 100 nm) are called Graphene Nanoribbons (GNR). They were initially studied as a theoretical model to examine the effect of the edges on the electronic properties of the material. It was observed that a zigzag edged GNR are metallic whereas the armchair edged nanoribbon can be metallic or semiconducting (depending on GNR width) with an intrinsic magnetic moment. The opening up of a band gap in armchair GNR can be attributed to an antiferromagnetic coupling between the magnetic moments of the carbon atoms occupying the opposite sites. This gap is inversely proportional to the width of the nanoribbon, as predicted by DFT simulations [9].
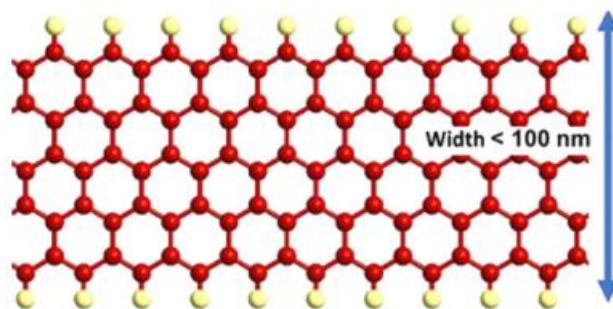
Figure 1.1: Structure of Zigzag-edged Graphene Nanoribbon.

Even though they were proposed as a theoretical concept, width controlled GNRs as shown in Figure 1.1 have been synthesized through graphite nanotomy wherein, a sharp diamond knife slices graphite nano blocks, which are further exfoliated to produce GNRs [10]. They can also be synthesized via unzipping multi walled CNTs by a solution of potassium permanganate and sulfuric acid [11]. GNRs show great potential in terms of applicability and are extensively employed as electrode materials for energy storage purposes. In our case we found pristine GNR unsuitable for toxic gas sensing, however upon suitable functionalization, the transport characteristics showed negative differential resistance NDR behavior. Such NDR regions in the I-V curves, have immense potential towards the selective detection of toxic gases as explained in Chapter 2.

1.1.2 Carbon Nitrides

In 2015, C_2N which belongs to the category of holey 2D materials, was synthesized by Mahmood and co-workers through a bottom-up wet chemical reaction [12]. The reaction scheme and morphology are depicted in Figure 1.2. C_2N has been shown to be thermodynamically stable. The periodic distribution of holes as well the presence of the more electronegative Nitrogen species, opens-up finite direct band gap ($E_g \approx 1.90$ eV) which makes this material suitable for electronics industry that require semiconductors [12-14]. Moreover, the presence of periodically placed pores provides the opportunity for embedding atoms of different elements which can make it suitable for applications such as gas sensing, energy storage and spintronics [15,16].
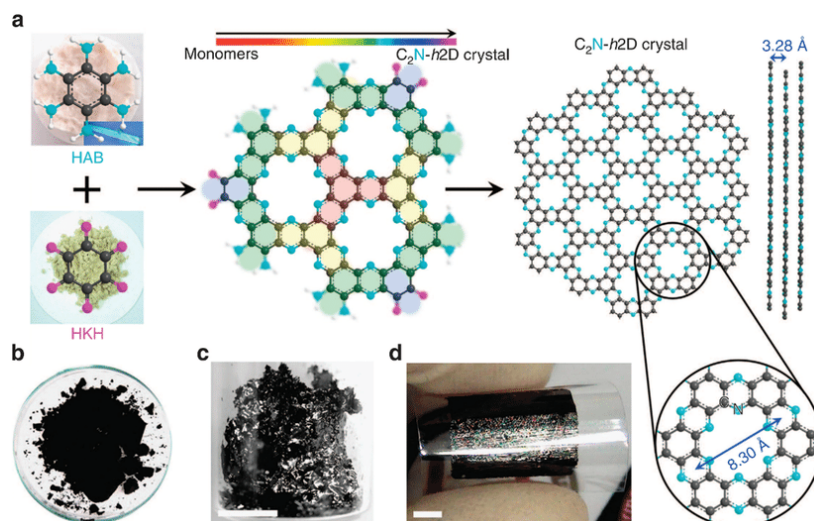
Figure 1.2: Reaction Scheme of Synthesis of C_2N.

C_2N belongs to the family of holey-2D Materials (h-2D), and sometimes more specifically called "holey graphene" since the chemical composition is two-thirds carbon with regular pores. Holey graphene has been extensively functionalized to make it suitable for several applications such as energy storage (batteries and super capacitors), fuel cells, gas sensors, energy conversion reactions, Dye Sensitized Solar Cells (DSSCs) and hydrogen storage [13]. In the field of gas sensing, the selectivity of the sensing substrate can be changed depending on the type of metal atoms that have been embedded into the pores. It has also been observed that the number of metal atoms imbedded into the system can affect the selectivity and efficiency of the sensor. Several standardized synthesis techniques for functionalization of 2D holey graphene and 3D porous graphene have been developed [14].

C_2N has periodically placed large pores having a diameter of 8.3 Å. Because of these pores, it has the advantage that it can easily be functionalized with different atoms to tailor its properties to suit different applications. Through DFT calculations, we found pristine C_2N to be unsuitable for our applications of interest, namely gas sensing and hydrogen storage. Also, it does not exhibit intrinsic half metallicity thereby making pristine C_2N unsuitable for spintronics applications. However, we explored its attractive morphology and functionalized it with suitable configurations of metal atoms and thereby achieved positive results for all the above-mentioned applications. Functionalized-C_2N has been

explored for hydrogen storage and sensing in Chapters 3 and 4, for toxic gas sensing in Chapter 5 and for spintronics applications in Chapter 6.

1.1.3 MXenes

MXenes are a new class of 2D materials that are essentially TM carbides, nitrides or carbonitrides. They have an interesting combination of properties such as large and tunable interlayer spaces, excellent hydrophilicity, extraordinary conductivity, compositional diversity, and abundant surface chemistries, which makes them an attractive class of materials for battery applications. Successful syntheses of these MXenes were recently reported. The structure for one of the MXenes employed in the present work is shown in Figure 1.3. Namely, Zhou and coworkers [17] reported the successful growth of $Hf_3C_2T_x$ MXenes and showed them to be conductive and relevant for lithium and sodium ion batteries with reversible volumetric capacities of 1567 and 504 mAh/cm^{-3}, respectively. The same researchers (Zhou's group) [18] also reported the successful synthesis of $Zr_3C_2T_x$ MXenes and they compared the obtained 2D structures to $Ti_3C_2T_x$ MXenes and proved them to be more stable at high-temperature conditions.
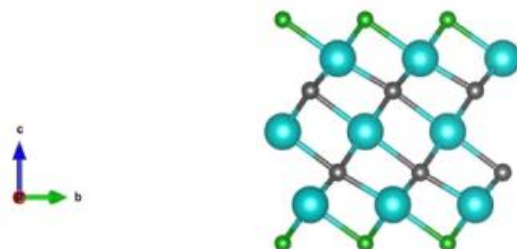
Figure 1.3: Structure of recently synthesized MXene-$Hf_3C_2F_2$.

Many efforts have been triggered in the direction of exploring MXenes for Na-S batteries as promising anchoring materials. In a recent theoretical effort, Jayan et al examined the interactions between a VS_2 monolayer and the Na-polysulfides. It was observed that all the polysulfides bind to the VS_2 layer with a binding energy stronger than that between them and the electrolyte such as 1,3-dioxolane (DOL) and 1,2-dimethoxyethane (DME) [19]. In another effort, Nahian et al were able to immobilize the Sodium Polysulfide (NaPS) by using Mo_2TiC_2 monolayer as the Anchoring Material (AM) in a Na-S battery [20]. It has been found that the passivation of the MXenes, play a

great role in influencing the MXene-NaPS interaction. Therefore, with optimum functionalization the interaction can be mediated, and MXenes can be suitably proposed as a promising AM for Na-S batteries for overcoming the shuttle effect. In Chapter 7, on the same lines we have studied the two novel MXenes ($Hf_3C_2T_2$, $Zr_3C_2T_2$ where $T = F$, O) for suppression of shuttle effect in NaSBs.

1.2 Statement of Problems and Hypothesis

1.2.1 Sensing Toxic Gases (NO, NO$_2$, SO$_3$)

The burning of fossil fuels, and other human activities have strengthened the greenhouse effect in recent years. The cumulative greenhouse gas emissions contribute to global warming, which can lead to catastrophic repercussions for humans in the long run. Human activities have dangerously tipped the atmospheric levels of these toxic gases above the safety limits in several cities. As a consequence of which, about 6.7 million people lose their lives because of degraded air quality. It becomes imperative to develop sustainable technologies that can detect the presence and concentration of these noxious gases. These proposed sensors should fulfill the criteria of being selective, sensitive, exhibit fast response and should have minimal environmental impact.

Concerning the imminent threat that toxic gases pose to human health and environment, it is an established fact that the major contributors to global acidification are nitrogen oxides (NO_x) and sulfur oxides (SO_x). These gases are mostly emitted by burning hydrocarbons and fossil fuels and they harm both human health and the environment. The United States Environmental Protection Agency (US-EPA) have set the safety levels for NO_2 at 100 ppb (Parts Per Billion) per hour on an average [21]. An exposure beyond these levels of safety could be hazardous to human beings resulting in even death. NO_x interacts with atmospheric oxygen and is also a major cause of acid rain. On the other hand, sulfur generally combines with oxygen to form two categories of oxides- sulfur dioxide (SO_2) and sulfur trioxide (SO_3) which have very different properties. Sulfur trioxide is highly toxic for humans and corrodes metals in the environment. In the third European Union ministerial conference, which was attended by environment ministers of 49 countries, it was decided that the issue of "air pollution affecting human health" must be dealt with somewhat high priority [22, 23].

Therefore, to increase human and environmental safety, developing sensors with high selectivity and sensitivity at order of 1 ppb for these hazardous gases is the need of the day.

Gas sensing applications can benefit greatly from the use of 2D materials due to their unique characteristics. These materials possess a high surface-to-volume ratio, allowing for increased sensitivity to trace amounts of gas through greater interaction between gas molecules and the material's surface area. Additionally, the electronic properties of 2D materials can be altered by adjusting their composition, thickness, and structure, enabling the creation of gas sensors tailored to detect specific gases with increased selectivity and sensitivity. 2D materials also exhibit a fast response time due to their thinness and high surface-to-volume ratio, making them ideal for real-time monitoring applications. Moreover, 2D materials are stable under various environmental conditions, such as high temperatures and humidity levels, making them more robust than other gas sensing materials that may degrade over time. Finally, 2D materials can be integrated with low-power electronics, resulting in energy-efficient gas sensors that can operate for extended periods without requiring frequent battery replacements. These advantages make 2D materials a promising option for gas sensing applications, particularly in fields such as environmental monitoring, healthcare, and industrial safety. The gas sensing efficiency of edge doped GNR has been extensively studied in Chapter 2 for detecting toxic gases of environmental concern. Especially the NDR behavior in the I-V curves for edge modified GNR, is responsible for the enhancement of the sensor's efficiency towards these toxic gases.

On the other hand, C_2N has the morphology and surface characteristics that are suitable for the gas sensing applications at room temperature (RT). After its successful synthesis, many efforts have been triggered to tune its properties by embedding relevant atoms in its pores. In Chapter 5, we studied the effect of 4 transition metal (TM) atoms (Mn, Fe, Co, Ni) embedded as Single atom catalysts (SAC) in the C_2N pores towards tuning the selectivity of C_2N to detect toxic oxidizing gases (NO/NO$_2$).

1.2.2 Hydrogen Storage and Sensing

The excessive consumption of energy sources, whether non-renewable or renewable, has been triggered by perpetual growing demand for energy. Hydrogen storage is a crucial

component in the advancement and implementation of hydrogen fuel cells as a sustainable energy source. The following are some reasons why hydrogen storage is significant:

- Efficient energy storage: Hydrogen has the highest energy content per unit of mass compared to other fuels, which makes it a promising fuel for energy storage. Fuel cells convert hydrogen and oxygen into electricity, with water being the only by-product.

- Transportation: Hydrogen is a clean fuel that can be used for transportation, such as in fuel cell vehicles. However, hydrogen is a gas at ambient conditions, making it challenging to store and transport effectively. Hence, the development of efficient hydrogen storage technologies is necessary to enable the widespread use of hydrogen in transportation.

- Renewable energy: Hydrogen can be generated from renewable sources like solar and wind power, making it a potential solution to reduce greenhouse gas emissions. Nevertheless, the efficient storage of hydrogen is critical to guarantee the reliable delivery of clean energy to users.

- Power grid: Hydrogen energy storage systems can be incorporated into power grids to balance the supply and demand of electricity, which is especially critical for intermittent renewable energy sources like solar and wind power.

Along with efficient storage solutions it is also imperative to develop reliable sensors for detecting the presence of hydrogen. There are several reasons for this. Firstly, as hydrogen is a highly flammable gas, it can pose a significant safety risk if not detected in time. In industrial settings, hydrogen sensors can identify leaks in places like fuel cells, refineries, and chemical plants, preventing explosions and fires. Secondly, hydrogen is a significant component of the Earth's atmosphere, and monitoring its concentration can help detect environmental changes like air pollution, climate change, and volcanic activity. Thirdly, as a clean energy carrier that can be produced from renewable sources such as solar and wind power, hydrogen sensors can aid in monitoring the production and storage of hydrogen in fuel cells that are used in various applications, including transportation, power generation, and heating. Lastly, hydrogen breath tests are used to

detect gastrointestinal disorders, and hydrogen sensors can accurately measure the concentration of hydrogen in exhaled breath, enabling the diagnosis of conditions such as lactose intolerance and bacterial overgrowth in the small intestine. In summary, hydrogen sensing plays a crucial role in ensuring safety, monitoring environmental changes, promoting the use of clean energy, and aiding in medical diagnostics. Consequently, it is a key area of research and development with numerous applications in various fields.

From the perspective of hydrogen storage, light metal atoms (eg., Na, K, Ca, Mg) can be embedded in the pores of C_2N in order to increase the affinity between the substrate and the gas. These light metal atoms offer two key advantages in comparison to other conventional transition metals namely:

1. Their binding energies to the substrate C_2N are higher than the cohesive energies which minimizes the clustering effect, and thereby leading to uniform distribution of metal atoms over the holes of the layer.

2. The binding energy between the adsorbed hydrogen and the metal atoms lies in the range between strong physisorption to weak chemisorption (i.e., between -0.2 eV to -0.6 eV) which is recommended by the International Atomic Energy Agency 'IAEA' for hydrogen storage applications.

In recent years, several carbon-nitride monolayers have been studied. Some of them have been experimentally synthesized while others have been proposed theoretically, but all of them have been found to be thermodynamically stable [24, 25].

The metal embedded C_2N structures have been experimentally shown to be thermodynamically stable, while being catalytically active for Oxygen Reduction Reactions (ORR). If one can achieve stability of single metal atoms embedded in the pores of C_2N, the catalytic activity of metal sites would get enhanced exponentially on account of an increase in the surface area of individual metal atoms [26, 27]. Stable SAC and DAC structures have been achieved in C_2N have been achieved experimentally [28]. These metal atoms embedded in C_2N sheets have been tested for an improvement in the lifetime and performance of metal ion batteries and for sensing toxic gases [29].

Such trends have been explored in Chapters 3 and 4, wherein C_2N with SAC/DAC configurations of light metal atoms (Calcium) vs transition metals (Manganese) has been explored for the purpose of hydrogen sensing as well as storage. Upon embedment of even a single metal atom, the electronic structure C_2N changes drastically by closure of the bandgap. Also, these metal atoms strengthen the interactions between the exposed hydrogen and the substrate, thereby enhancing the sensing and storing capabilities of C_2N.

1.2.3 Half Metallic Structures for Spintronics Applications

Spintronics has been proposed as the future technology to meet the demands of heavy data storage while shrinking the size of the devices to keep them compact and portable. It utilizes the fundamental spin of an electron in addition to its charge for data transfer and storage applications. Half metals are materials that act as a conductor to electrons of one spin while as an insulator to electrons of another spin. Thus, half metals are capable of completely spin-polarizing electrical current. This asymmetry in electronic states for charge carriers with different spins was observed in Heusler compounds [31] such as manganese perovskite. Efforts have been taken to look for half metallicity in 2D materials [32, 33].

From the perspective of spintronic applications of 2D materials, half metallicity was first theoretically reported in ZZ-GNR in 2007 [8]. By applying electric field in the transversal direction, the electronic bang gap opened up for one spin of electrons whereas it remained metallic for the other spin. In C_2N, the behavior has been shown to change, from semi conducting to half metallic, on account of hole doping with a quite low critical concentration of 5×10^{13} cm^{-2} has been reported [8, 9]. Efforts must be directed towards, understanding the origins of this half metallic behavior. If provided half metallicity, C_2N would be beneficial in the flexible spintronics industry since it has been found to be light weight, flexible and thermodynamically stable.

In spintronics, the goal is to employ the degree of freedom of spin of electrons in logic and memory devices. Transition metals have been shown to be beneficial for spin splitting for magnetic electronic devices. Fe atoms adsorbed on graphene have been shown to tune its properties ranging from hydrogen storage to catalyst for formaldehyde decomposition, and to CO oxidation at room temperature [25]. If adsorbed onto C_2N it

10

has also shown to induce half metallicity at a critical concentration [34]. Exploring the same direction, in Chapter 5 we have studied various combinations of TMs, embedded in the pores of C_2N that lead to half metallicity. The entire 3d block of the periodic table (Sc-Zn) was scanned, and half metallicity was found to exist in 5 cases.

1.2.4 Enhancing the Stability and Lifetime of Batteries

Efficient batteries are required to match demand and supply of energy. The most common form, metal-ion batteries involve a conversion of chemical energy into electrical energy via shuttling of metal ions back and forth between the electrodes in charge/discharge phases. Therefore, it is also popularly referred to as the 'rocking-chair' battery. These batteries have gained tremendous popularity in recent years, due to which they are being extensively applied and used. However, they suffer from their own shortcomings such as dendritic formations which could lead to an internal short circuit thereby raising concerns of safety and lifetime. Tremendous research efforts have been directed towards proposing robust rechargeable Metal-ion Batteries (MIB) as an alternate battery for upcoming electronic devices owning to their high reversible capacity, high energy density and superior life cycles [35]. Their applications range from portable consumer electronics such as laptops, mobile phones and to large scale energy storage applications such as electric vehicles [36].

Conventional metal-ion batteries that employ alkali metal ions, which intercalate the cathode and anode materials, are the most widely used batteries. Their applications range from portable electronic devices to larger electric vehicles. Conventional lithium-ion batteries that employ graphite as the anode material have been known to suffer from dendrite formation at low discharge potential (i.e., < 0.1 V) and the existence of large hysteresis voltammetry [37].

The different carbon nitride monolayers have distinct properties (C_3N_4 is intrinsically half metallic whereas C_2N is semi-conducting) they offer great potential to be tested as possible anode materials for metal-ion batteries [38]. They could offer an efficient solution that overcomes the existing problems of dendrite formation and life cycle.

C_2N has been proposed as a suitable candidate as an anode-material in both Sodium-ion Batteries (SIBs) and Calcium-ion Batteries (CIBs), because it overcomes existing problem of dendrite formation in Lithium-ion Batteries (LIBs). It also would be

beneficial for the fabrication of portable electronic devices which utilize low-dimensional batteries [39-42]. Experimentalists have been able to successfully embed Transition Metal (TM) atoms in C_2N pores while overcoming the issue of clustering (i.e., M@C_2N using M = Pd and Co atoms) [44]. Due to their striking structural characteristics (e.g., periodically placed pores of optimum diameters, high aspect ratios and enhanced spacing between C_2N monolayers) the M@C_2N electrodes have outshined the conventional graphite-based electrodes in terms of performance. Experimentalists have been able to overcome the issue of clustering, thereby leading to homogenous embedment of metal atoms in the C_2N pores [44]. In Chapter 4, exploring on the same lines, the stability of Calcium SAC/DAC in C_2N has been tested, thereby proposing it as a novel electrode for Ca-ion batteries. The uptake capacity of the electrode has been studied and the results are reported in the same Chapter.

However, metal-ion batteries face a challenge in terms of their energy density, which fails to meet the upcoming demand for large scale stationary energy storage applications [45]. Metal-sulfur batteries have been proposed as an alternative to conventional technology, due to their superior performance [46], non-toxic nature, and cost effectiveness [47]. In terms of properties, Sodium (Na) is analogous to Lithium (Li), therefore the interaction with the sulfur electrode would be the same. However, it has higher natural abundance [48] making it a more attractive metal for batteries. Conventional Sodium-Sulfur (Na-S) batteries that operate at elevated temperatures (~300°C) have been scaled up to be used in commercial applications in 2002. They work on the basis of the following reaction:

$$2Na + nS \leftrightarrow Na_2S_n \ (n \geq 3) \tag{1.1}$$

These batteries are rechargeable and outdo their metal-ion counterparts on account of their higher theoretical energy density (760 Wh/kg, calculated by using the total mass of Na and S), life cycles and efficiency. Also, these batteries employ electrodes which are cheaper, which brings down the cost of the overall unit, thereby making them highly attractive for stationary energy-storage applications [49]. Sodium sulfur batteries have a calendar life of 15 years and a full charge/discharge durability of 4500 cycles. Since the active materials of the Na-S battery are in molten states, there is no transition between solid and liquid due to charge and discharge, and there is no side reaction, so long life

12

can be expected. Because of their high energy density and robustness, the NaS battery has the potential to be used for space applications [50, 51].

Conventional Na-S batteries, operate at 300-350°C inside a thermal enclosure to ensure that the conductivity of the solid electrolyte (sodium alumina) is sufficiently high and to also ensure that the polysulfides are in the molten state since it exceeds the melting point of S (115°C) and Na (98°C). However, such elevated temperatures raise serious safety concerns and increase the cost of operation and maintenance [52].

Room temperature (RT) Na-S were first reported in 2006, and they have been reported to have higher energy densities (1274 Wh/kg) in comparison to the batteries working at elevated temperatures. A possible reason for that is, in room temperature Na-S batteries, Na_2S is the final discharge product instead of sodium polysulfides as per the reaction below:

$$2Na + nS \leftrightarrow Na_2S_n \ (n \geq 1) \tag{1.2}$$

However, these batteries also suffer from some shortcomings. In RT Na-S batteries, Na-polysulfides are formed as intermediates during the charge/discharge cycles. These can easily reach the Na anodes and undergo redox reactions resulting in lower order polysulfides, which leads to a loss in active material and an interfacial deterioration. Secondly, the polysulfide shuttle effect, which is caused by the dissolution of intermediate Na polysulfide species in the electrolyte leads to irreversible loss of sulfur, resulting in rapid capacity fading and poor Coulombic efficiency of the cells. Effective immobilization of these polysulfides can overcome the challenges posed by the "shuttle effect" thereby increasing the overall durability of the battery. Therefore, several efforts have been directed towards the search for suitable anchoring materials (AM) which can attract sodium polysulfides with sufficiently high binding energy. In Chapter 7, we have explored the two members of the novel MXene family ($Hf_3C_2T_2$ and $Zr_3C_2T_2$ where T = F/O) as suitable anchoring materials to be employed in NaSB. The interaction of the 6 Na_2S_n with the anchoring layers were studied and they were found to be stronger than the interactions with the commonly employed electrolytes (DOL/DME). Thus, they can be proposed as suitable anchoring layers in NaSBs, which would enhance their lifetime and stability.

1.3 Research Methodology

All the calculations presented in this work, were carried out within in the framework of Density Functional Theory (DFT) as incorporated in Vienna Ab-initio Simulation Package (VASP) [53] and a combination of DFT with Non-Equilibrium Greens Functions (NEGF) formalism in the Atomistic Tool Kit (ATK) [54, 55] package.

Different morphologies of four different materials were studied, namely Graphene Nanoribbon, C_2N, Hf_3C_2 and Zr_3C_2. The sample details were as follows:

1. Each graphene nanoribbon doped with boron (or nitrogen) consists of 102 Carbon and 2 Boron (or 2 Nitrogen) atoms, while the dangling bonds at both edges of nanoribbon were passivated with 26 Hydrogen atoms.

2. The primitive cell of C_2N consists of 18 atoms (i.e., 12 Carbon + 6 Nitrogen atoms), so most of the calculations will be performed on a supercell composed of 2x2 primitive cells (PCs) having 72 atoms (excluding metal catalyst atom(s)); in case of periodic sample, per monolayer.

3. In the case of C_2N nanoribbons, we used about 150 atoms including the hydrogen atoms to saturate the two edges.

4. $M_3X_2T_2$ MXenes (M = transition metal (Hf/Zr), X = C/N, T = passivating atom mostly from group 13 and/or 14) are layered hexagonal (belonging to the space group P63/mmc), with two formula units per primitive cell. So, as a model, we considered a computational supercell of size 3×3 primitive cells (i.e., containing 63 atoms).

In the framework of DFT (e.g., VASP), within the Generalized Gradient Approximation (GGA) of Perdew-Burke-Ernzerhof (PBE) exchange-correlation functional, all atoms were allowed to relax until the Hellmann-Feynman forces on all atoms and the total energy became less than 0.01 eV/ Å and 10^{-6} eV, respectively. Monkhorst-Pack [56] technique was used for the Brillouin-zone sampling. The DFT-D3 [57] method of Grimme was employed to take account of the Van-der-Waals (VdW) interactions between gas molecules and the 2D substrate layer. The plane wave basis set with a cutoff kinetic energy of 500 eV was used to expand the valence electron wave-functions for all the three samples (functionalized GNR, C_2N and MXenes). Gaussian smearing with a

width of 0.05 eV was chosen for the broadening of the electronic energy levels. A vacuum space of about 15-20 Å is added in the direction perpendicular to 2D-materials plane to avoid interactions with images.

The binding energy of the metal catalyst embedded in 2D substrate is evaluated as follows:

$$E_{Binding} = E_{SUB+MC} - E_{SUB} - E_{MC} \qquad (1.3)$$

where E_{SUB+MC}, E_{SUB} and E_{MC} stand for the total energy of the system of metal catalyst embedded in pristine substrate, pristine 2D substrate monolayer and free metal catalyst (MC) respectively.

Furthermore, one also can define the recursive binding energy, E_{rec} for the metal catalyst atom as to be the binding energy of the last metal atom to be added on the already doped substrate. It is defined as:

$$E_{rec} = E_{MAn@Mater} - E_{MAn-1@Mater} - E_{MA} \qquad (1.4)$$

where $E_{MAn@Mater}$, $E_{MAn-1@Mater}$ and $E_{(MA)}$ stand for total energies of metal atoms in the material after and before adding the n-th metal atom and single-free metal atom respectively.

In case $|E_{rec}| > |E_{coh}|$, with E_{coh} being the cohesive energy, then the metal atom is more stable by its attachment to the substrate; otherwise, if $|E_{rec}| \leq |E_{coh}|$, then the new metal atom has more tendency to cluster with its peers.

Using total energy calculations, the adsorption energy of the gas molecule/NaPS on the 2D substrate is defined as:

$$E_{Ads} = \frac{E_{SUB+MOL} - E_{SUB} - E_{MOL}}{N} \qquad (1.5)$$

where $E_{SUB+MOL}$, E_{SUB} and E_{MOL} are total energies of molecule(s) adsorbed on the substrate, the 2D substrate and free single molecule, respectively; whereas N is the number of molecules adsorbed onto the substrate. The more negative adsorption energy (E_{ads}) would indicate the stronger interaction between adsorbate and absorbent.

The charge exchange between substrate and molecule are calculated using the Mulliken population charge analysis in SIESTA and the Bader analysis [58] in VASP.

The magnetization can be calculated using the spin-polarized total DOS as follows:

$$M = \mu_B \int_{-\infty}^{E_F} [G_{tot}^{up}(E) + G_{tot}^{down}(E)] dE \qquad (1.6)$$

where μ_B is the Bohr magneton, E_F is Fermi energy, $G_{tot}^{up}(E)$ and $G_{tot}^{down}(E)$ are the total densities of states of the system with spin-up and spin-down polarizations respectively. It should be emphasized that $G_{tot}^{down}(E)$ is presented to be negative and the total density of states $G_{tot}(E) = G_{tot}^{up}(E) - G_{tot}^{down}(E)$ is normalized to yield the total number of valence electrons in the system (N):

$$N = \int_{-\infty}^{E_F} [G_{tot}^{up}(E) - G_{tot}^{down}(E)] dE \qquad (1.7)$$

Concerning the transport and gas-sensing properties, the IV-curves are calculated by ATK package using the device configuration, where the TM-catalyst-embedded into the pore of C_2N-NR, which consists of the central region. The calculation of the current versus bias is performed using the two-terminal Landauer-Buttiker formula [59] given by:

$$I(V_b) = \frac{2e}{h} \int_{-\infty}^{+\infty} T(E, V_b)[f_L(E - \mu_L) - f_R(E - \mu_R)] dE \qquad (1.8)$$

where V_b, $T(E, V_b)$, $\mu_{L/R}$ and $f_{L/R}$ are the applied forward bias, bias-dependent transmission coefficient, electro-chemical and Fermi-Dirac distribution function of the left/right electrode, respectively. Based on the IV results, the differential resistance versus bias is evaluated ($R = \Delta V / \Delta I$), using the finite-difference method. The sensor response [60, 61] of the device is defined as:

$$S = \frac{|G_g - G_o|}{G_o} = \frac{|R_g - R_o|}{R_g} \qquad (1.9)$$

where G is the conductance (i.e., G=1/R), G_g (G_o) and R_g (R_o) are the conductance and resistance in presence (absence) of gas molecule on the functionalized 2D (substrate) device, respectively. In order to decide about whether the sensor should be reusable or disposable, one may estimate the recovery time given by:

$$\tau = \upsilon_o^{-1} \exp\left[-\frac{E_{ads}}{k_B T}\right] \qquad (1.10)$$

where υ_0 is the attempt frequency, E_{ads} is the adsorption energy, k_B and T are the Boltzmann constant and the absolute temperature, respectively.

Moreover, the charge density difference($CDD = \Delta\rho$), between the adsorbent and adsorbate was calculated based on the following equation.

$$\Delta\rho = \rho_{SUB+MOL} - (\rho_{SUB} + \rho_{MOL}) \qquad (1.11)$$

Where $\rho_{SUB+MOL}$, ρ_{SUB} and ρ_{MOL} refer to the charge density of the substrate and molecule (together), charge density of the substrate and the charge density of the free molecule.

The calculation of the catalytic decomposition of the NaPS on the surface of the functionalized MXenes was done using the climbing-image nudged elastic band (CI-NEB) method (Chapter 7).

1.4 Research Outcomes and Applications

The overarching aim of my thesis was to tune the properties of novel 2D materials to cater to specifically three applications namely, gas sensing, energy storage and spintronics. In the pristine form, all the chosen materials have been found to be stable, however unsuitable for the above-mentioned applications in their pristine forms. Therefore, the real challenge was how to tailor the properties of these materials suitably to cater to the application intended through functionalization. From the research conducted, and what has been presented in this thesis many practical applications can be drawn which have been enlisted below:

(a) Sensing oxidizing toxic gases: Gases such as $CO_x/NO_x/SO_x$ etc. cause harm to the environment and contribute to global acidification thereby leading to global warming. These gases, when present in higher concentrations, are detrimental towards human health. Therefore, it becomes imperative that they are sensed with resistivity below the threshold to reach the toxic limit. In Chapter 2, we have presented how by double edge B/N doping GNR tune the detection selectivity towards NO_2/O_2 and SO_3 respectively.

Also in Chapter 5, we have tested the efficacy of 4 TM atoms (Mn, Fe, Co and Ni) as SACs embedded in C_2N towards developing an efficient sensor towards oxidizing gases (NO/NO$_2$)

(b) Sensing and storage of Hydrogen gas**: Hydrogen plays a key role in meeting the energy requirements while causing no pollution to the environment. The only by-products formed in the process are water and heat. However, hydrogen gas when present in a higher concentration becomes explosive and the repercussions can be catastrophic. Therefore, hydrogen sensors need to be employed in places where hydrogen gas is used and handled to ensure safety of the workers. The criterion to use is that the binding energy of the gas on the substrate should range from -0.2 eV to -0.6 eV, to suit hydrogen storage. In Chapter 3 and 4, we have explored the applicability of metal doped C_2N towards this goal. Initially we had tested a single atom catalyst (SAC) of Mn, because of its strategic position in the periodic table. Upon showing favorable results for H_2 storage, its efficacy was compared to other light metals such as Calcium with results presented in Chapter 4.

(c) Achievement of better alternatives to the conventional graphite electrodes used in lithium-ion batteries: Due to dendritic formations in these electrodes, the batteries suffer from an internal short circuit leading to the failure of batteries and lifetime limited. C_2N offers the possibility of homogenous dispersion of metal ions thereby strengthening its candidature for overcoming dendritic failures. In Chapter 4, we have discussed which metals atoms can be suitably embedded in C_2N to achieve this goal and their numerous configurations. Their efficacy in terms of uptake capacity has been discussed.

(d) Spintronics applications: C_2N pores offer the ideal platform for transition metals to get embedded leading to a change in its electronic and magnetic properties. By testing various configurations of these embedded transition metals, half metallicity can be obtained in the originally semiconducting C_2N which renders it suitable as a possible spin filter in spintronic applications. In Chapter 6, we have various combinations of TM atoms (the entire 3d block was scanned) that can be stably embedded in the host C_2N, which can induce half metallic characteristics

18

on account of a combined effects of synergetic and long-range ferromagnetic coupling interactions.

(e) Increasing the stability of sodium-sulfur batteries. Due to the occurrence of the shuttle effect, the stability and reusability of RT-Na-S batteries suffer greatly thereby reducing its employability. However, by using a suitable additive on the anode, which binds to the Na-S intermediates, with sufficient adhesive strength this shuttle effect can be avoided. In Chapter 7, we have proposed two novel, recently synthesized MXenes-$Hf_3C_2T_2$, $Zr_3C_2T_2$ (where T=F, O) as a possible additive electrode on the cathode to inhibit shuttle effect.

Our research findings have been presented and organized in the following Chapters in the chronology in which they were conducted.

Chapter 2: Selective Gas Sensing using Bilaterally Edge Doped Graphene Nano Ribbon

2.1 Summary

The adsorption and gas-sensing properties of B/N edge-doped Graphene Nanoribbons (GNRs) are investigated using state-of-the-art computational technique, which is based on a combination of Density-Functional Theory (DFT) and Non-Equilibrium Green's Functions (NEGF) formalism. First, the assessment of the effects dopants' positions, with respect to edges of GNR, on the transport properties revealed that the bilaterally B/N edge doping of GNR would yield Negative-Differential Resistance (NDR) IV-characteristics, due to the electronic back-scattering events. Then, the double-edge-doped GNR:B and GNR:N were used to study the gas-sensing properties. The results of adsorption tests show that chemisorption processes can be attained for NO_2 and O_2 molecules on GNR:B and SO_3 molecule on GNR:N. Furthermore, the results of calculations of transport properties show that the chemisorption processes of these molecules can yield enormous rectifications to the IV-characteristics to sweep the NDR behaviors and should consequently yield large sensors responses in GNR-based devices. Comparison to many other gases is performed and it is concluded that double edge-doping in both GNR:B and GNR:N would yield exceptionally high selectivity towards detecting toxic NO_2 and SO_3 gases, respectively. The combined GNR:B- and GNR:N-based sensors are suggested to be used as gas-sensor and alarm-sensor for NO_2 gas, respectively. Our theoretical findings are corroborated with available experimental data.

Redrafted from

2.2 Introduction

The breakthrough discovery of graphene by Geim and Novoselov [1] had not only earned them Nobel Prize in physics in 2010 but also paved the way for cornucopia of new fundamental low-dimensional physics and immense field of advanced technological applications [1, 2, 6, 62]. Graphene possesses a unique combination of mechanical strength (stability) and electronic properties, which make it attractive for materials engineering [1, 2, 6, 62]. From the mechanical perspective, carbon atom has the flexibility to make suitable hybridization to adapt to its environment and yield 0-3 dimensional novel nanomaterials with multi-functional applications. More specifically, carbon in graphene has the sp^2 hybridization to produce honeycomb atomic structure [6]. From the electronic-structure perspective, graphene has zero bandgap with two linear bands crossing each other at Fermi level (i.e., Dirac cones at K-points of the Brillouin zone). As a result, graphene has a massless Dirac (relativistic) fermion with rather high mobility (at order of 105 cm^2/Vs) [1]. These properties are fundamental recipes in making graphene the material of the 21-st century for the development of highspeed next generation devices with characteristics exceeding those of silicon and conventional semiconductors [1]. Technological applications of graphene are quite diverse and encompass many fields: (1) Nano-electronics (e.g., synthesis of small transistor [63]); (2) Photonics (e.g., band-gap engineering using quantum-confinement effects in nanoribbons [64-67], and BN-doping to create a band-gap [67]); (3) Spintronics (e.g., induction of ferromagnetism by the adsorbed hydrogen atoms in nanoribbons [68]; (4) Biomedical (e.g., graphene nano-ribbons are utilized as strain sensors [69]); (5) Energy storage (e.g., multi-layered derived-graphene like C_2N and C_3N have been used in electrodes of Lithium-ion batteries for Hydrogen storage [15]); and (6) Gas sensing (e.g., ability to detect several gases like CO, CO_2, NO, NO_2 and NH_3 [2, 6, 70, 71]). In this latter application, graphene can be functionalized to compete with the metal oxides (such as SnO_2, TiO_2 and ZnO) to reach better selectivity towards certain gases. In gas-sensing applications, the simple fabrication procedure and cost effectiveness of chemiresistive gas sensor have attracted a lot of attention worldwide [72, 73]. Experimental efforts have shown that the functionalized Graphene Nanoribbons (GNRs) do have the ability to sense gases with a resolution down to ppm (Part Per Million) with fast response and

recovery times [74, 75]. In addition to these advantages, the operating temperature of GNR-based gas-sensor can be optimized to Room Temperature (RT) much easier than the case of oxide-based sensors [69, 76]. Recently, further improvement was experimentally achieved by Cho and coworkers [77]. They reported great enhancement in sensor response in case of edge-functionalized GNR chemical sensor much better than doped Carbon Nanotube (CNT)-based and doped reduced-Graphene Oxide (rGO)-based sensors. They demonstrated for the first time that chemically functionalizing the edge sites with aminopropylsilane (APS) molecules would significantly enhance the performance of GNR-based sensor. The sensor's response was 30% to detect NO_2 gas of dose 0.125 ppm with a response time of about 6s [77]. They claimed that this GNR-APS sensor to be the fastest and most sensitive one so far been ever reported. They also compared the latter's sensor response to the ones of CNT-APS- and rGO-APS-based sensors and they found that GNR-based one to exhibit better than them by 30-fold and 93-fold, respectively [77]. On the computational side, Density Functional Theory (DFT) has been the most reliable technique, if not the lonely one, appropriate and reliable to study the ground state properties such as the problems of molecular adsorption on surfaces and gas-sensing properties [78, 79]. Regarding GNR, Son, Cohen and Louie used DFT to study the scaling rules for the bandgaps of GNR as function of width [66]. They studied both zigzag-edged and armchair-edged GNRs (i.e., hereafter, denoted as ZGNR, AGNR, respectively), where the edge carbon atoms are saturated with hydrogen atoms. They showed that Na-AGNR is metallic if $Na = 3p + 2$, where p is any positive integer and Na is the number of dimer lines radically to GNR (i.e., along the width). Otherwise, AGNR is semiconducting with decreasing bandgap with the increasing width. They also reported that ZGNR to be always metallic but with possibility of opening small-induced gap, that may rise as an effect of magnetism due to the polarization of edges (i.e., kind of spintronics' effects). Concerning the DFT studies of the adsorption of gas molecules on GNRs, Huang and coworkers [78] studied the adsorption of gas molecules (CO, NO, NO_2, O_2, N_2, CO_2 and NH_3) on armchair edged GNRs. They reported high sensitivity towards detecting NH_3. These results were corroborated with the theoretical ones obtained by Saffarzadeh [79]. Dopants and defects can play important roles in enhancing the adsorption of gas molecules on graphene [80-

22

83]. Zhang and coworkers used DFT method to study the interactions between 4 different graphenes (including pristine, B- and N-doped and defective graphenes) and small molecules (CO, NO, NO_2 and NH_3) [80]. They demonstrated that all the four gas molecules showed much stronger adsorption on doped/defected graphenes than that on pristine graphene. The binding energies of molecules on defected graphene are also larger than those on B/N dopants [81]. Here, it is worth to emphasize that in case of energy storage applications, the Adsorption Energies (E_{ad}) should be moderate (i.e., not too strong nor too weak); for instance, in case of hydrogen storage in multi-layered graphene or C_2N or C_3N, E_{ad} should be at the order of 0.1-0.3 eV. So, defects should be avoided as not to be helpful in energy storage applications and catalyst or dopants should be picked/ selected in rather wise way (e.g., good candidates could be: Li, K, Na, Ca) [84-90].

On the other hand, for sake of gas-sensing applications, stronger binding energies should be sought. Besides defects, catalytic effects, such as those due to transition metal atoms decorating graphene and CNT are shown to enhance the gas-sensing properties [91-92]. For instance, Zhang and coworkers studied the adsorption of toxic gases on Ti-doped graphene [94]. Other transition metals (e.g., Fe, Co, Ni and Cu) are also known to enhance the sensitivity and selectivity of graphene-based sensors for gas detection [93-97]. Concerning the threats to health and environment, it is an established fact that the major contributors to global acidification are nitrogen oxides (NO_x) and sulfur oxides (SO_x). These gases are mostly emitted by burning hydrocarbons and fossil fuels and they harm both human health and the environment. The United States Environmental Protection Agency (US-EPA) have set the safety levels for NO_2 at 100 ppb (parts per billion) per hour on an average [21]. An exposure beyond these levels of safety could be hazardous to human beings resulting in even death. NO_x interacts with atmospheric oxygen and is also a major cause of acid rain. On the other hand, sulfur generally combines with oxygen to form two categories of oxides- Sulfur Dioxide (SO_2) and Sulfur Trioxide (SO_3) which have very different properties. Sulfur trioxide is highly toxic for humans and corrodes metals in the environment. In the third European Union ministerial conference, which was attended by environment ministers of 49 countries, it

was decided that the issue of "air pollution affecting human health" must be dealt with somewhat high priority [22-23].

Therefore, to increase human and environmental safety, developing sensors with high selectivity and sensitivity at order of 1 ppb for these hazardous gases is the need of the day. The reliable calculation of transport properties requires a combination of the DFT and Non-Equilibrium Greens Function (NEGF) formalism [83]. In a related work [98], we have used this combination to study the origins of negative-differential resistance in ZnO nanoribbons under the effect of nitrogen doping. Then, we explored such N doped ZnO-NR in investigating the gas-sensing properties [99].

The results showed that H_2 gas would play the role of reducing gas on the absorbent (i.e., ZnO-NR: N), thus, enhancing the electric current; whereas both O_2 and CO_2 gases would oxidize the absorbent and, consequently, hamper the electric current. As far as deviations in IV characteristics are concerned, it is concluded that huge sensor responses are obtained on ZnO-NR: N-based devices and achievement of high selectivity towards the gases (H_2, O_2, and CO_2) was obtained. Such selectivity is mainly caused by the existence of the Negative Differential Resistance (NDR) in the adsorbent sample. So, in the present work, we aim to explore the possibility of NDR existence in B/N edge-doped GNR to assess which molecules can be chemisorbed and able to rectify the IV-characteristics. So, these molecules should become our target in the gas-sensing study. To address such a problem, we planned the present investigation. The Chapter is organized as follows: Section 2.3 presents details of the used computational methods. The results and their discussions are shown in Section 2.4. The last section summarizes our main findings.

2.3 Computational Method

In this study, all calculations were carried out in the framework of DFT and NEGF using Vienna Ab-initio Simulation Package (VASP) [53] and Atomistic Tool Kit (ATK) [54-55] codes, respectively. Each graphene nanoribbon doped with boron (nitrogen) consists of 102 C and 2 B (2 N) atoms, while the dangling bonds at both edges of nanoribbon were passivated with 26 H atoms. In the framework of DFT within the Generalized Gradient Approximations (GGA) of Perdew-Burke-Ernzerhof (PBE) exchange–correlation functional, all atoms in doped GNRs were allowed to relax until the

Hellmann-Feynman forces on all atoms and the total energy became less than 0.01 eV/Å and 10^{-5} eV, respectively. Monkhorst-Pack (MP) technique was followed for the Brillouin zone sampling [56]. Note that DFT-D3 method of Grimme was also employed to take account of the Van-der Waals (VdW) interactions between gas molecules and graphene nanoribbons [57]. The plane wave basis set with a cutoff kinetic energy of 400 eV was used to expand the valence electron wave functions. Gaussian smearing with a width of 0.05 eV was chosen for the occupation of electronic energy levels. A vacuum space of 15 Å was added in the direction perpendicular to graphene nanoribbon to avoid interactions with images. The charge redistribution between gas molecules and graphene nanoribbons was estimated by means of Bader charge calculations [58]. The bonding strength between adsorbate and adsorbent can be estimated in terms of adsorption energy. In this study, the adsorption energy between gas molecules and doped GNRs was calculated by:

$$E_{ads} = \frac{E_{gas-GNR} - E_{GNR} - NE_{gas}}{N} \qquad (2.1)$$

where $E_{gas-GNR}$, E_{GNR} and E_{gas} are total energies of gas molecules adsorbed on doped GNR, doped GNR and gas molecule, respectively; whereas N is the number of gas molecules adsorbed on doped GNR. The more negative the adsorption energy indicates the stronger interaction between adsorbate and adsorbent. The transport properties of all devices were calculated by two terminal Landauer-Büttiker formula [59] given by

$$I(V_b) = \frac{2e}{h} \int_{-\infty}^{+\infty} T(E, V_b)[f_L(E - \mu_L) - f_R(E - \mu_R)] dE \qquad (2.2)$$

where V_b, $T(E, V_b)$, $\mu_{L/R}$, and $f_{L/R}$ are the applied forward bias, bias-dependent transmission coefficient, electrochemical potential, and Fermi- Dirac distribution function of the left/right electrode, respectively. Based on transport properties of GNR devices (i.e., IV-curves), the differential resistance (R) can be estimated by

$$R = \frac{dV}{dI} = \frac{1}{G} \qquad (2.3)$$

where G is the conductance. The sensor response of the device [60, 61] is defined as

$$S = \frac{|G_g - G_o|}{G_g} = \frac{|R_g - R_o|}{R_g} \qquad (2.4)$$

where G_g (G_o) and R_g (R_o) are the conductance and resistance in the presence (absence) of gas molecule on GNR device, respectively.

2.4 Results and Discussion

2.4.1 Atomic Relaxations

Two kinds of samples were used in the calculations of adsorption and transport properties, consecutively. First, we used GNR sample with periodic boundary conditions, as applied along the longitudinal direction of the nanoribbon, to study the adsorption properties (i.e., such calculations would include atomic relaxations, band structures, density of states and charge-density contour plots). A second type of sample should comprise of two electrodes on both sides of GNR to probe the transport properties (i.e., such calculations would be useful to produce: IV curves, resistance and sensor response versus applied bias). Figure 2.1 shows the relaxed atomic structures of periodic samples of pristine and doped GNRs, before and after the occurrence of chemisorption with the gas molecules, which are ordered as follows:

a) Pristine GNR, shown in Figure 2.1(a) and consisting of GNR of zigzag edges saturated with hydrogen atoms, is composed of a total of 110 atoms (i.e., 88 C atoms and 22 H atoms). After altering a relaxation using DFT method, the pristine GNR has a width W = 9.1 Å and a length L = 27.05 Å; and the average values of bond lengths of C-C to be about 1.41 Å and C-H to be about 1.07 Å. Table 2.1 summarizes the structural parameters of all the 6 structures shown in Figure 2.1.

b) B-doped GNR is shown in Figure 2.1(b) with two boron atoms occupying substitutional doping positions at the two edges. It should be noticed that the atomic radius of free boron atom to be a bit larger than that of carbon (i.e., $R_B = 0.87$ Å $> R_C = 0.67$ Å). Due to this fact, the atomic relaxation yields B-C bond-length larger than that of C-C (Table 2.1). There is also an angular distortion of the value $Ang_{(C\text{-}B\text{-}C)} = 128°$ at the edge due to atomic size consideration in addition to the existence of unpaired electron in boron to amend the hybridization state.

c) N-doped GNR is shown in Figure 2.1(c) with two nitrogen atoms as substitutional dopants at the two edges. We quote that the radius of free carbon atom is bigger than the one of free nitrogen atom (i.e., $R_C = 0.67$ Å $> R_N = 0.56$ Å). So, indeed, the atomic relaxation yields bond-length N-C smaller than that of C-C (Table 2.1). The angular distortion of $Ang_{(C\text{-}N\text{-}C)} = 122°$ is smaller than the previous case due

to atomic size considerations. Using the relaxed B- and N-doped GNR structures of Figure 2.1(b) and Figure 2.1(c), respectively, molecular chemisorption was achieved, and results are shown in Figure 2.1(d-f).
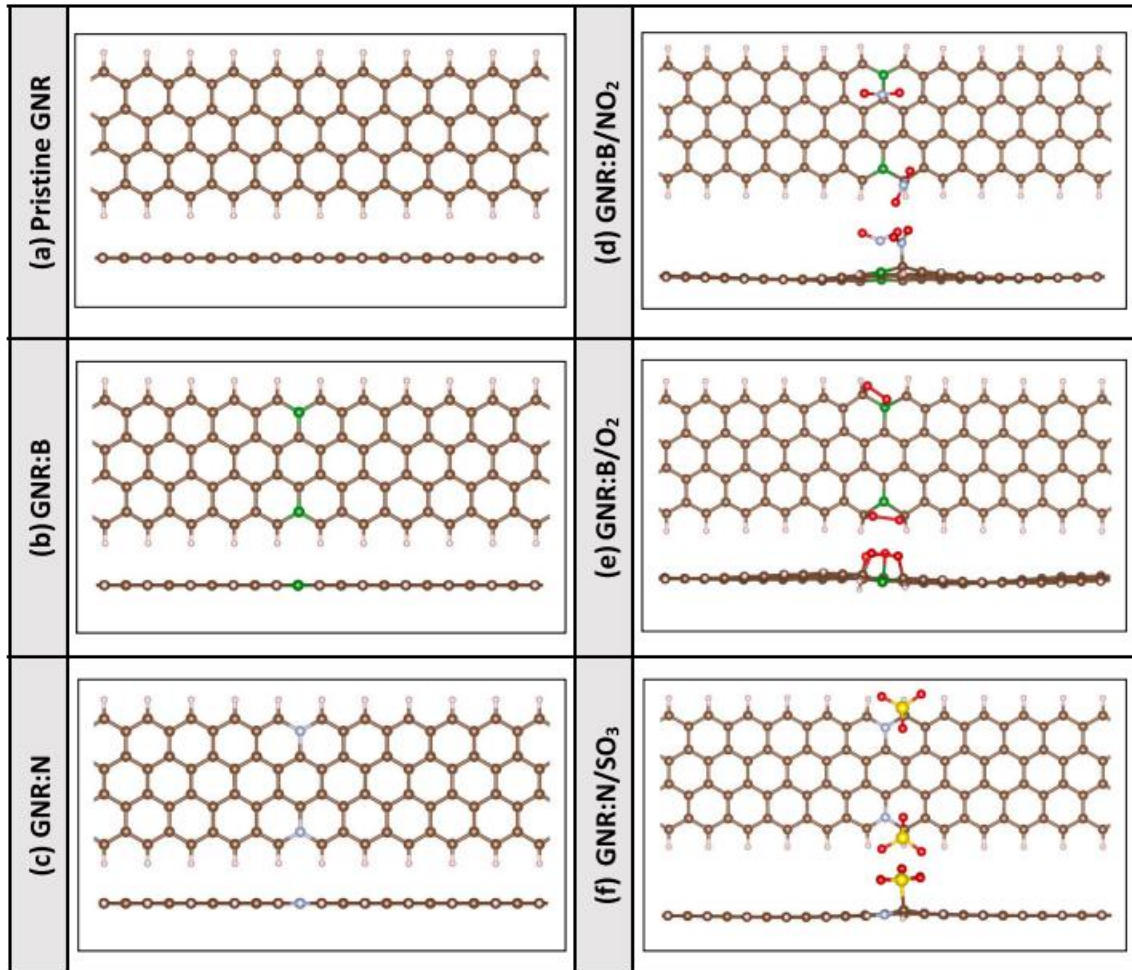
Figure 2.1: Relaxed atomic structure of pristine and B-/N-doped GNR before and after the chemisorption of gases.

** Color: C = brown, B = green, N = grey, H = pink, O = red, S = yellow.

Table 2.1: Structural/Geometrical parameters of pristine and B-/N- doped GNR samples before and after the chemisorption of NO_2, O_2 and SO_3 gas molecules are shown.

(a) Pristine GNR	(b) GNR:B
d(C-C) = 1.40–1.41 Å	d(B-C) = 1.47–1.50 Å
d(C-H) = 1.07 Å	d(C-C) = 1.39–1.42 Å
	d(C-H) = 1.06–1.07 Å
	Ang(C-B-C) = 116°, 116°, 128°
(c) GNR:N	**(d) GNR:B/NO_2**
d(N-C) = 1.36–1.39 Å	d(B-C) = 1.48–1.49 Å
d(C-C) = 1.40–1.42 Å	d(C-C) = 1.40–1.43 Å
d(C-H) = 1.07 Å	d(C-H) = 1.09–1.10 Å
Ang(C-N-C) = 119°, 119°, 122°	d(C-N) = 1.54 Å
	d(N-O) = 1.24 Å
	Ang(O-N-O) = 125°
(e) GNR:B/O_2	**(f) GNR:N/SO_3**
d(B-C) = 1.55–1.58 Å	d(N-C) = 1.34–1.46 Å
d(C-C) = 1.40–1.44 Å	d(C-C) = 1.40–1.43 Å
d(C-H) = 1.10 Å	d(C-H) = 1.09–1.10 Å
d(C-O) = 1.43, 1.44, 1.50 Å	d(C-S) = 1.97 Å
d(B-O) = 1.60 Å	d(S-O) = 1.45–1.47 Å
d(O-O) = 1.47, 1.67 Å	Ang(O-S-O) = 115°–117°
Ang(C-B-C) = 108°, 122°	

d) Figures 2.1(d) and (e) show the chemisorption of NO_2 and O_2 molecules on B-doped GNR (GNR:B), respectively.

e) The free NO_2 molecule has a bond length $b_{(N-O)} = 1.197$ Å and an angle Ang $_{(O-N-O)} = 134°$. After a trial to relax 2 NO_2 molecules on the respective two boron atoms located at the GNR-edges, the chemisorption processes of these 2 NO_2 molecules occur without molecular dissociations and likely through the breaking of resonant N-O π-bonds. The new bond length is elongated to become $d_{(N-O)} = 1.24$ Å with reduced angular distortion to an angle Ang$_{(O-N-O)} = 125°$. It is interesting to see NO_2 molecules bind to carbon atom not to boron, as the former atom is more electronegative and more ready to alter covalent bonding with nitrogen, as far as they stand in the lattice.

f) Such binding of NO_2 molecule to carbon is associated with charge transfer. NO_2 molecule plays a role of oxidizing the graphene, with charge transferred to each molecule of amount $\Delta q = 0.36e$, per molecule as is displayed in Table 2.2.

g) Concerning the molecule O_2, when it is free, it has a double bond of bond-length $b_{(O=O)} = 1.12$ Å. A trial to relax these two O_2 molecules on 2 respective boron

atoms located at the GNR-edges yielded two distinct scenarios: One O_2 molecule exhibited a molecular dissociation to pave the way for the two oxygen atoms to bind to the two carbon atoms neighboring boron.

h) The distance between these two split oxygen atoms is $d_{(O\text{-}O)} = 1.67$ Å. The second O_2 molecule alters a chemisorption process without dissociation, in which one O atom binds to boron and the other O atom binds to the carbon neighboring the same boron. The O-O bond length is elongated to $d_{(O\text{-}O)} = 1.47$ Å due to the breaking of π-bond. Both O_2 molecules play roles of oxidizing the graphene with a drained charge of value $\Delta q = 1.015e$, taken by each molecule, as indicated in Table 2.2.

i) Concerning SO_3 molecule, when it is free, it is planar with bond length $b_{(S\text{-}O)} = 1.42$ Å and angle $Ang_{(O\text{-}SO)} = 120°$. The trial of relaxing these 2 SO_3 molecules on respective two N dopants located at GNR-edge led them bind to the neighboring C atoms. Both molecules exhibit identical chemisorption processes without molecular dissociation. The relaxed bond length is elongated to become $d_{(S\text{-}O)} = 1.46$ Å and molecular angle is reduced to $Ang_{(O\text{-}SO)} = 116°$, due to the breaking of both the π-binding resonance of three S-O bonds and the sp2 hybridization.

j) Such binding processes must have been accompanied with charge transfers, in which the SO_3 molecules acted in roles of oxidizing the graphene, with a drained charge of value $\Delta q = 0.615$ e per molecule, as is illustrated in Table 2.2.

Table 2.2: DFT results of adsorption energies of NO_2 and O_2 molecules on GNR:B and SO_3 molecule on GNR:N and their associated charge transfers (Δq) calculated by Bader charge analysis method.

Molecule/adsorbent	E_{bind} (eV)	$\Delta q/e$
NO_2/GNR:B	−1.235	0.360
O_2/GNR:B	−1.965	1.015
SO_3/GNR:N	−1.865	0.615

2.4.2 Effect of Doping Positions on Transport Properties

In general, the electrical conductivity in metals is controlled by the states near Fermi level. Furthermore, Zigzag-edged GNR (ZZ-GNR) is naturally metallic as its 1D-Brillouin zone comprises the graphene's special reciprocal K-point. Concerning the electric conductivity in nano-devices (e.g., GNR-based devices), it is a well-known fact that impurities and defects are the main reason for the existence of universal conductance fluctuations. Such fluctuations would make the IV-characteristics sensitive to the positions of the impurities. In this part, the effect of position(s) of dopant(s) on the transport properties is put under focus. We considered devices containing z-GNR samples doped with either boron or nitrogen atoms. Starting with the case of boron doping, we considered the calculations of IV-curves corresponding to three different realizations:

- 1B dopant at one edge of GNR.
- 1B dopant at the center of GNR.
- 2B dopants simultaneously put at the two edges of the GNR.
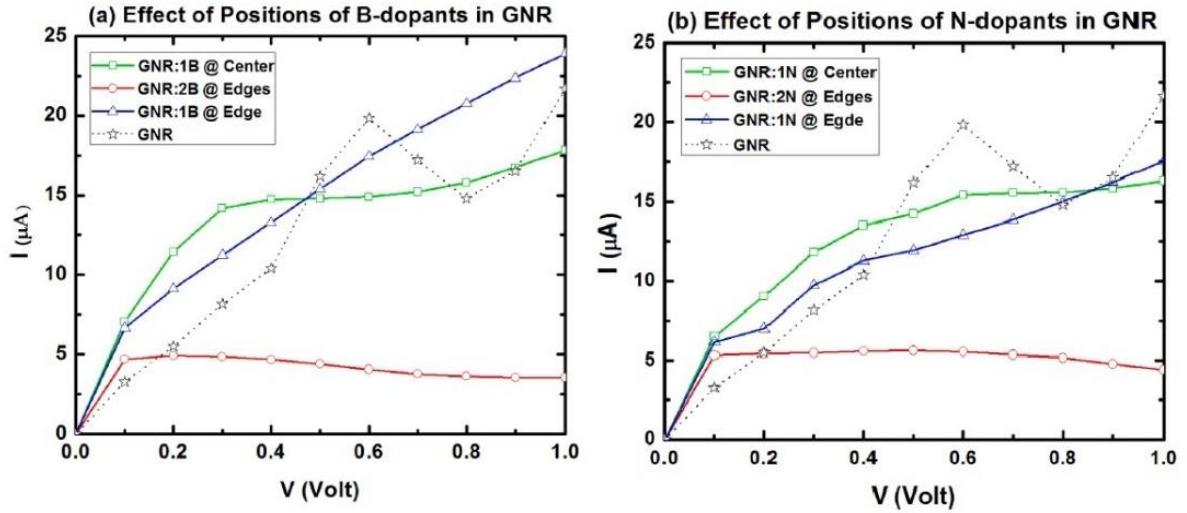
Figure 2.2: IV characteristics to test the effect of dopants' position with respect to edges of GNR-based devices: (a) B-doping, (b) N-doping.

Figure 2.2(a) shows the IV characteristics due to the three preceding realizations and compares them to the case of pristine GNR. The dotted curve corresponds to pristine GNR and the others, correspondences are as follows: green curve to GNR:1B @ center; blue curve to GNR:1B @ edge; and red curve to GNR:2B atoms @ edges. It seems that

in pristine GNR, the majority of current density flows through the two edges because of the fact that the hydrogen bonds are weak and do contribute to the population of states at the Fermi level. If one B atom is placed at one edge, when the current flows, it gets negatively charged (because it is originally missing 1 electron with respect to the standard average of 4 electrons per atom). So that that negatively charged boron starts exhibiting some back-scattering. But the electric current can always find its way through by going through the other edge. A similar scenario may take place when B atom is placed at center, the current persists to flow at order of magnitude of pristine because the current density can be supported by channels at the 2 edges. One would clarify that the observed NDR in the case of pristine graphene might originate from quantum coherence as far as nanoribbon is ultra-narrow (i.e., consisting of just four conductive channels). Furthermore, in the case of placing 2B atoms at the two edges simultaneously, the current drops drastically, as shown in Figure 2.2(a). One can clearly notice the appearance of NDR due to the back-scattering events [101]. Such NDR characteristics can be explored in gas-sensing applications. Namely, when the device is exposed to gas molecules, if chemisorption is attained, the IV-characteristics gets drastically rectified, and the sensor response would be well pronounced [99].

In the case of N-doping, the results of testing of effect of dopants positions are shown in Figure 2.2(b). The trends are basically the same. Notice that in case of 2 N atoms placed at the two edges, the obtained IV characteristics looks like the case of 2 B atoms at the two edges. So, in the rest of paper, we decided to carry on with two samples in which we have either 2 B dopants or 2 N dopants at GNR-edges to explore to study the gas-sensing properties.

2.4.3 Electronic Band Structures

Figures 2.3 and 2.4 show the band structures and density of states (DOS) corresponding to the structures described in Figure 1. These two figures should be discussed in parallel as they strongly correlate to each other. Figure 2.3 displays the bands structure along the ΓX-high symmetry line of 1-dimensional Brillouin Zone (BZ) within an energy range of 1 eV around Fermi level, which is taken as the energy reference (i.e., $E_F = 0$). Whereas Figure 2.4 displays all the electronic states within the energy range -2 eV $\leq$ E $\leq +2$ eV.
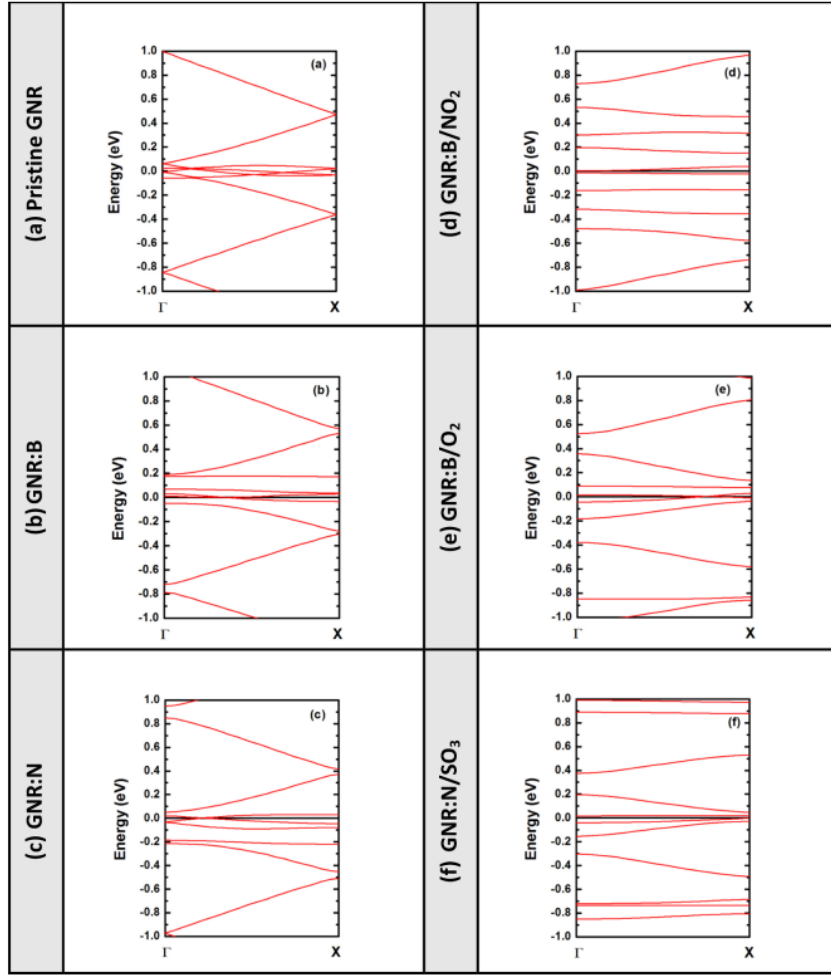
Figure 2.3: Band structures of pristine and B/N-doped GNR before and after the chemisorption of gas molecules.

The first common remark about panels of Figure 2.3 is the fact that all the samples have at least two bands crossing at Fermi level. So, all samples are expected to have metallic behavior. As a second remark, by focusing on Figure 2.3(a), which corresponds to pristine GNR, one can notice two trends:

a) Some bands are varying linearly and do correspond to bulk graphene states (C-C bonds)

b)   Some bands are slowly varying and grouped or rather almost localized near Fermi level and they should be attributed to C-H bonds. These bands could be the supporters of the electric current density when a bias is applied.

These bands are projected into a peak at Fermi level, as shown in DOS in Figure 2.4(a). One can notice that DOS is constant within the interval [−1 eV, +1 eV] away from Fermi level due to the linear dispersion of bands of the former trend. In Figure 2.3(b), the

32

introduction of 2 boron atoms at the GNR-edge causes some splitting in the bands of C-H bonds and some bands becoming strongly localized likely due to the unpaired electron in boron atoms in addition to the electrons of C-H bonds.

Figure 2.4(b) displays a stronger peak at Fermi level attributed to such flat bands. The flat band, at energy of about 0.2 eV above E_F, might be attributed to boron atoms and reveals the electro-positivity aspect of boron (i.e., being cations, B atoms have tendency to contribute with states to the conduction band).

In Figure 2.3(c), as compared to pristine GNR, the introduction of 2 nitrogen atoms causes similar splitting effects in the states near Fermi level like what was caused by boron atoms in Figure 2.3(b). However, there is a contrast that the flat band at energy of −0.2 eV below E_F might be attributed to nitrogen atoms and might reveal the electronegativity of nitrogen (i.e., being anions, N atoms have tendency to contribute with its states to the valence band). Figure 2.3(d) corresponds to the band structure of GNR: B after the occurrence of chemisorption with 2 NO_2 molecules.

Comparing Figures 2.3(d) to 2.3(b), it seems that the 2 NO_2 molecules bind strongly to the lattice through carbon atoms. So that their overlaps cause strong splitting of states near Fermi level to become almost all fragmented as also shown in Figure 2.4(d).

Figure 2.3(e) corresponds to the band structure of GNR: B after the chemisorption processes of 2 O_2 molecules. By comparing Figure 2.3(e) and 2.3(b), one can notice the band-splitting as well as the flipping of bands' symmetry. This latter reversal symmetry in k-space might be attributed to the asymmetry of chemisorption processes, as they occur in completely different fashions from one edge to the other edge.

One O_2 molecule exhibits chemisorption with full dissociation (i.e., on 2 C atoms) whereas the other O_2 molecule alters chemisorption without any dissociation (i.e, on C & B atoms). Figure 2.4 (e) displays a huge peak near Fermi level, which is attributed to the split oxygen atoms as they bind separately to carbon atoms and both possess dangling bonds, with energies at order of Fermi level. One should expect the existence of such dangling bonds because the 2 C atoms underneath the 2 O atoms are still maintaining their coordination in the graphene lattice. Figure 2.3(f) corresponds to the GNR: N after the occurrence of chemisorption processes to 2 SO_3 molecules. Both SO_3 molecules

prefer to bind to C atoms and thus the σ-bond of S-C is strong enough to introduce states at energies of about −0.75 eV and 1.0 eV as shown in Figure 2.4(f).
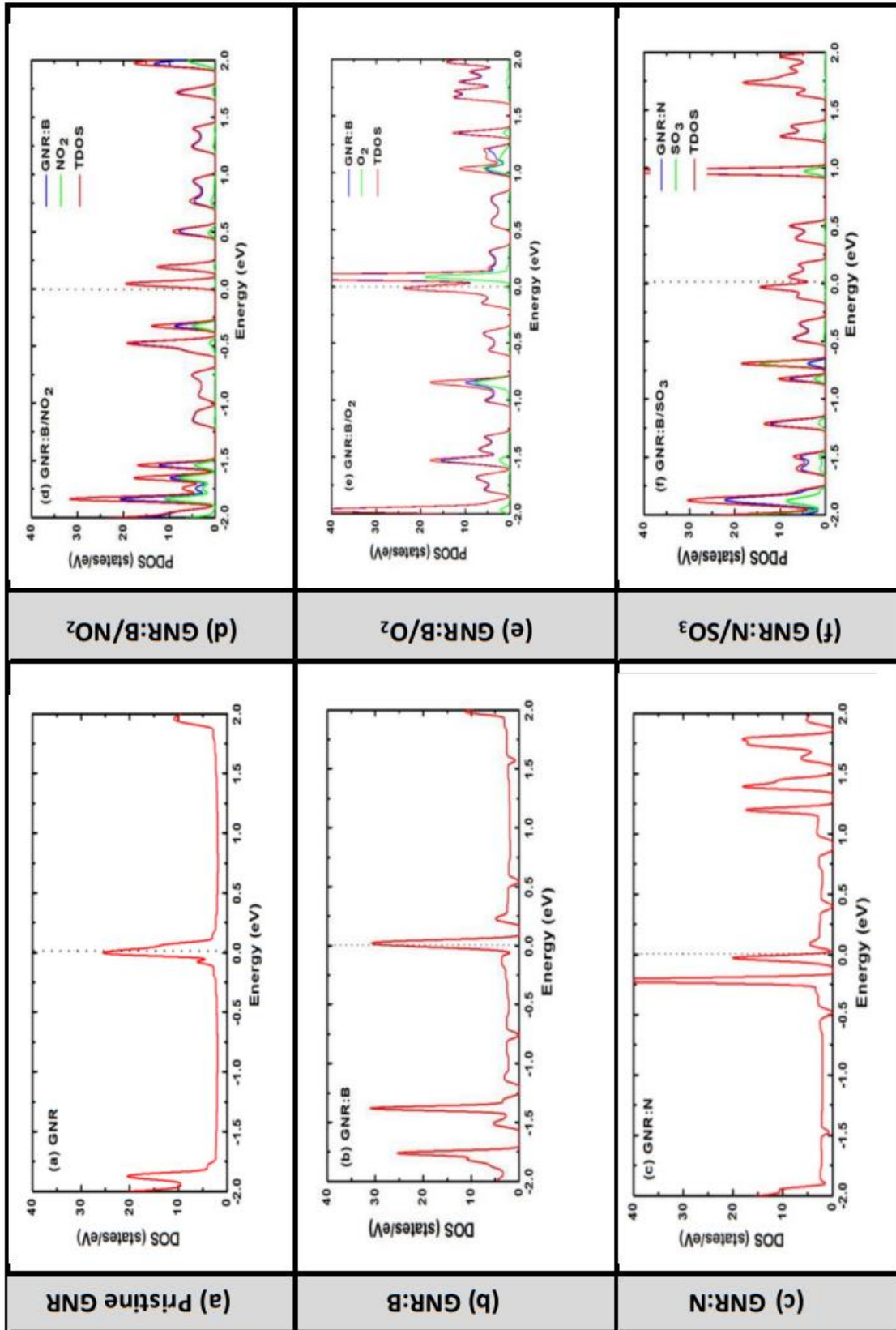
Figure 2.4: Results of PDOS of six periodic relaxed samples.

2.4.4 Charge Density Plots
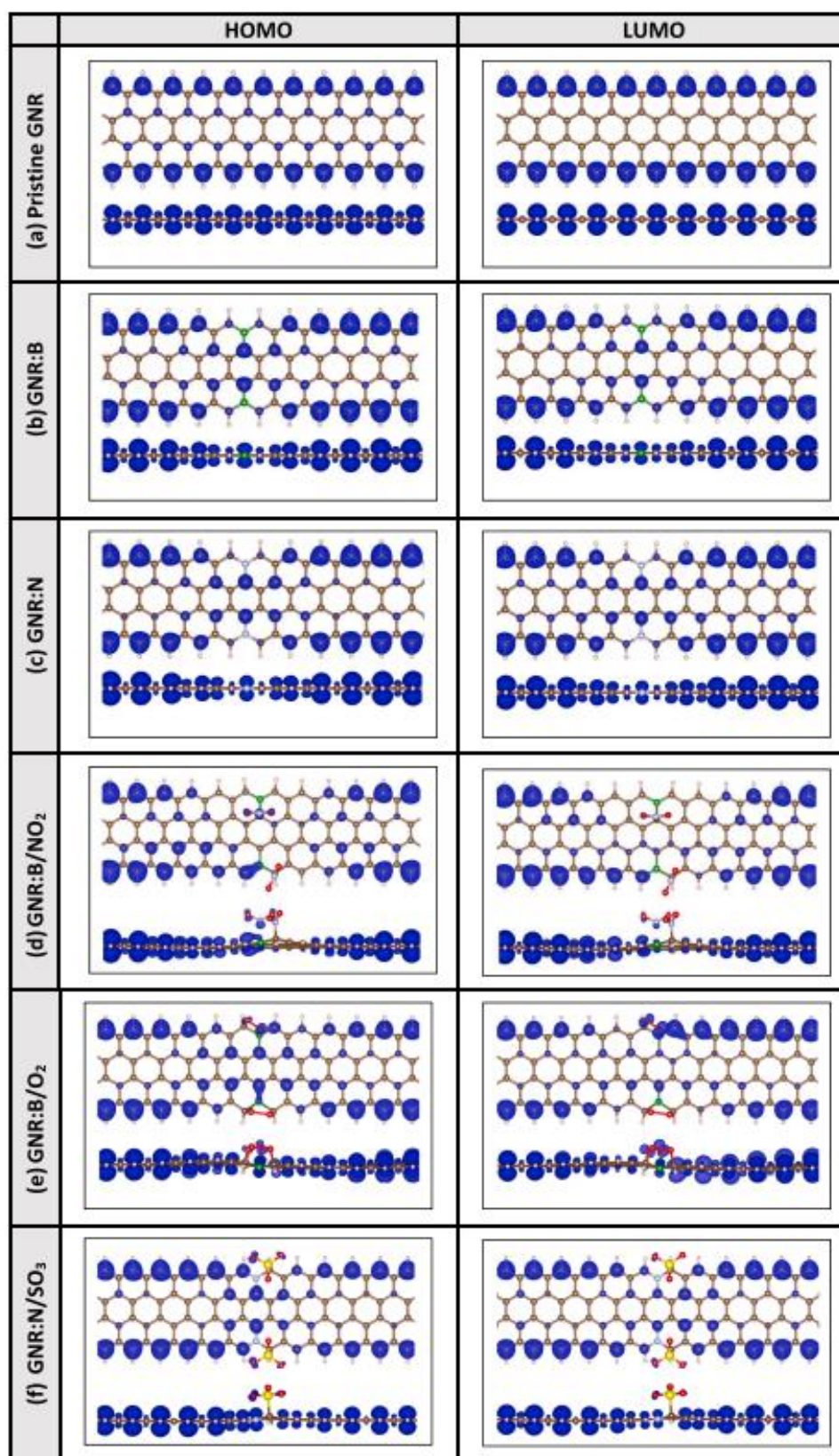
Figure 2.5: Charge density plots of the eigenstates of six periodic relaxed samples.

Figure 2.5 shows charge-density plots of the highest occupied molecular orbital (HOMO) and the lowest unoccupied molecular orbital (LUMO) for each of the six periodic GNR samples described in Figure 2.1. Two different views are displayed for each sub-panel for better clarity (i.e., top and side views are shown). Figure 2.5(a), corresponding to pristine GNR, shows that both HOMO and LUMO states to be supported by C-H bonds at the two edges of GNR. This is in favor of and corroborates the idea that most of the electric current density flows through the edges. Figures 2.5(b) and (c), corresponding to the respective GNR: B and GNR: N, show some interruption/discontinuity of HOMO and LUMO states at the vicinity of the impurity (B and N, respectively).

Yet, these HOMO and LUMO states are shown to still be percolating and conductive and likely to originate from dispersive bands. It is worth emphasizing that for all the samples the eigen-energies of the HOMO/LUMO states are just about within -0.1 eV to $+0.1$ eV around Fermi level.

The occurrences of chemisorption processes of NO_2, O_2 and SO_3 molecules (shown in respective Figures 2.5(d-f)) do cause bit further interruptions to the HOMO/ LUMO states. Nonetheless, in exemption of O_2 molecule, the other molecules (NO_2 and SO_3) would have bigger effects on states far from Fermi level at about ± 0.4 eV and ± 0.75 eV, respectively, as been discussed under the light of bands and DOS in Figures 2.3 and 2.4.

Such effects would not be much pronounced on HOMO/LUMO states but should be detectable in the IV-characteristics when biases are applied at the order of up to 1 Volt.

2.4.5 Transport Properties

Probing the IV-curves requires the use of a device with electrodes. Figures 2.6 shows the results of 5 IV characteristics due to two devices:

(a) Device, composed of GNR: B in its central zone, is used detect NO_2 and O_2 molecules. The IV-curve of the adsorbent bed (i.e., GNR: B), shown in blue solid line, shows the existence of NDR behavior.

(b) Similar NDR trends in the IV-characteristics of GNR: B and GNR: N (blue curves in Figures 2.6 (a) and (b)) exist because of the current blockade caused by

the two dopants (B/N), simultaneously placed at both edges. When dopants get charged, they impede the current by back-scattering [101-102].

(c) The two blue curves show NDR behavior in the energy intervals [0.1,1.0] eV and [0.5,1.0] eV with Top-to-Valley Current Ratios (TVCR) of 1.32 and 1.27, respectively. They have very close TVCR values as their NDR behaviors are attributed to the quantum coherence effects, which are like what happened in Esaki's diode ("tunnel diode") [101].

(d) The adsorbent can alter chemisorption processes with NO_2 and O_2 molecules. After the occurrences of these respective chemisorption processes, the IV characteristics change to the curves shown in red and green colors, respectively. As discussed in Figures 2.4(d) and (e), the NO_2 and O_2 introduce states at about -0.35 and $+0.15$ eV below and above Fermi level, respectively. These states may account for the cross-over of IV-curves between red and blue to take place at about 0.35 eV and between green and blue to occur at about 0.15 eV.

(e) Figures 2.6(a) shows great enhancement in the current after the landing of the NO_2 and O_2 molecules on GNR: B because of passivating the defect states.

(f) On the other hand, Figure 2.6(b) shows the IV characteristics of chemisorption of SO_3 on GNR: N. The 2 SO_3 molecules, absorbed on GNR: N, seem to hamper further the electric current because of introducing defect states near Fermi level. More NDR trends occur with even higher TVCR.

(g) Recalling the band structures of GNR: N before and after the adsorption of SO_3 molecules, presented in Figures 2.3(c) and (f), respectively, one can depict the localization effects on the conduction bands caused by the chemisorption of the molecule (see states at energy of about 0.5 eV and 0.9 eV in Figure 2.3(f)). So, as soon as the bias crosses these energy values, the IV characteristics show NDR behaviors in the red curve corresponding to SO_3@ GNR: N (in Figure 2.6(b)).

(h) The NDR behaviors at biases V = 0.5 V and V = 0.9 V are found to have TVCR = 1.492 and 8.225 values, respectively. The origin of these two NDR behaviors should be attributed to the same reason which caused NDR in Gunn's diode [102] (i.e., when the voltage crosses the energy of flat band, the current reduces drastically).

(i)

(j) Figure 2.6: IV-characteristics of two devices.
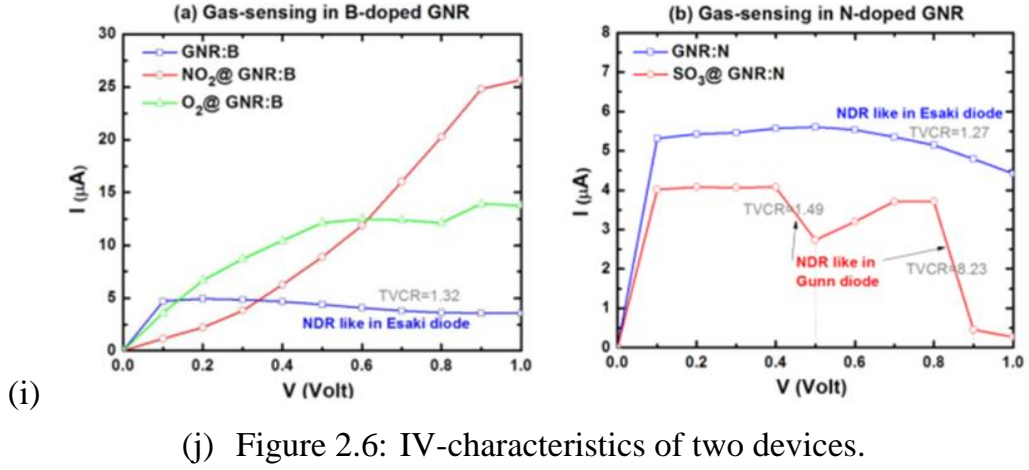
(a) GNR:B and (b) GNR:N before and after the chemisorption of (NO_2, O_2) and SO_3 respectively.

Our argument is based upon the occurrence of NDR in very narrow energy intervals, centered at energies of defect states as mentioned above. It is worth mentioning that SO_3 molecules are found to exhibit physisorption process on GNR: B; whereas both NO_2 and O_2 alter chemisorption processes on GNR: N without molecular dissociations. The obtained electric currents in GNR: N-based devices after the chemisorption of NO_2 and O_2 are found to be vanishingly small and rather below the experimental limit of detection. Hence, while GNR: B is suggested as a good gas sensor of NO_2, GNR: N can be explored in making logical-gate alarm sensor for NO_2 gas.
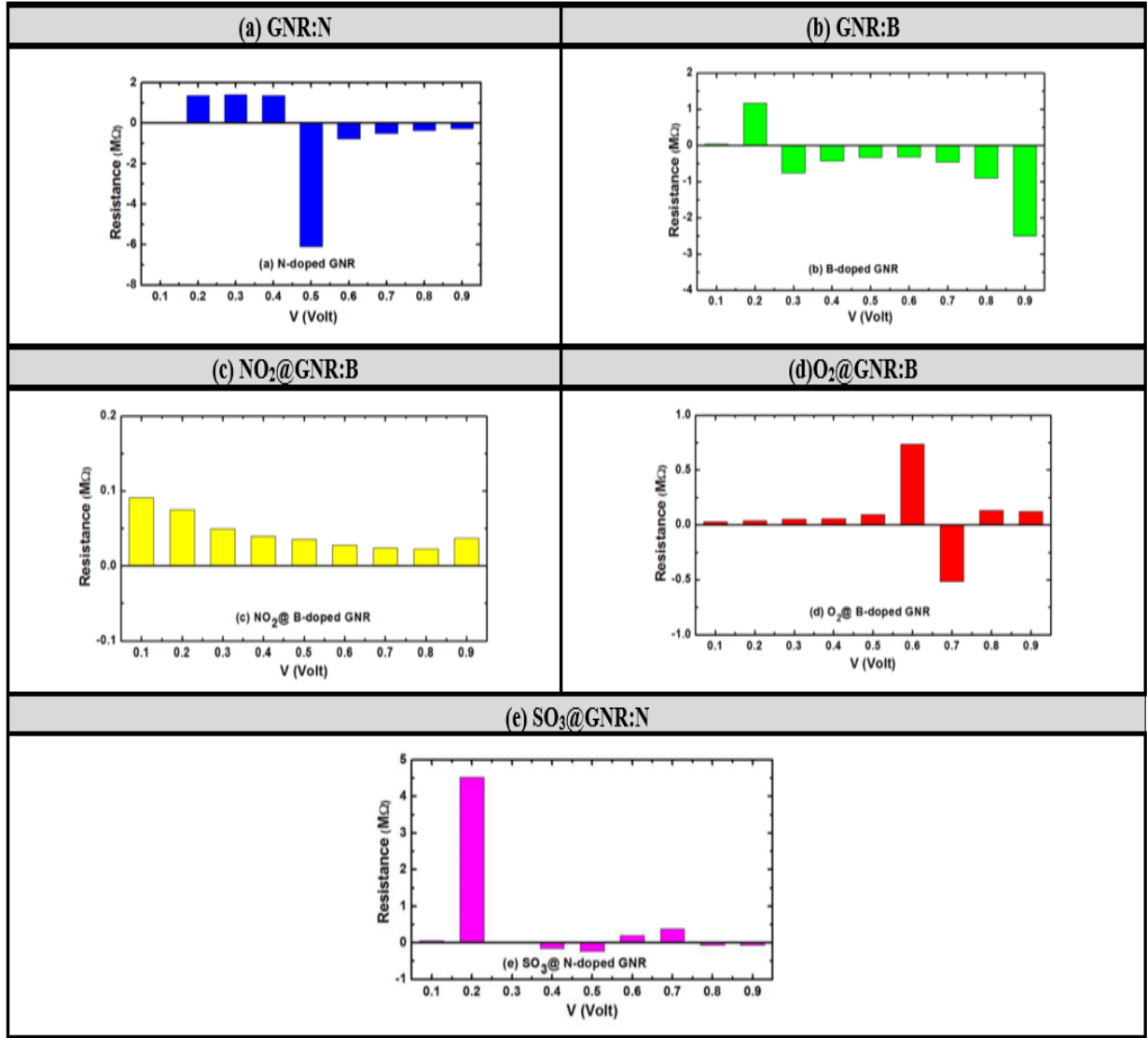
Figure 2.7: Differential resistances versus bias using the five IV-curves.

Figure 2.7 shows the results of differential resistance calculated for all the 5 IV-curves, displayed in Figure 2.6, versus bias up to 1 Volt. As the electric currents in Figure 2.6 are in the order of micro-Ampere (μA), the calculated differential resistances are at the order of mega-Ohm (MΩ). NDR behavior persists in (a) GNR: N and (b) GNR: B devices, specifically at higher voltages than 0.5 V and 0.3 V, respectively. The chemisorption processes of NO_2 and O_2 molecules on GNR: B would rectify the current and sweeps or eliminate most of the NDR behaviors (Figure 2.7(c) and (d)). Whereas the chemisorption of SO_3 on GNR: N device preserves some NDR behaviors (Figure 2.7(e)) because of localized defect states in the DOS, as shown in Figure 2.4(f).

2.4.6 Gas Sensing Properties

Using the results of differential resistance versus bias, one can calculate the Sensor response of the two devices (i.e., GNR:B- and GNR:N based devices). The results corresponding to the absorption of NO_2, O_2 and SO_3 gases are shown in Figures 2.8(a-c), respectively. The average values of Sensor response versus bias for these respective gases are as follows: (a) $S_{ave} = 21.8$, (b) $S_{ave} = 9.86$ and (c) $S_{ave} = 5.94$. It should be emphasized that we have carried out tests for detection of other gases as well (e.g., N_2, H_2, O_3, CO, CO_2, H_2O, H_2S, NH_3, NO, and SO_2) and all of these gases exhibit either physisorption processes on these two devices or having very low electric current much below the threshold for the experimental detection, which we considered to be about $nA=10^{-9}$ Ampere.
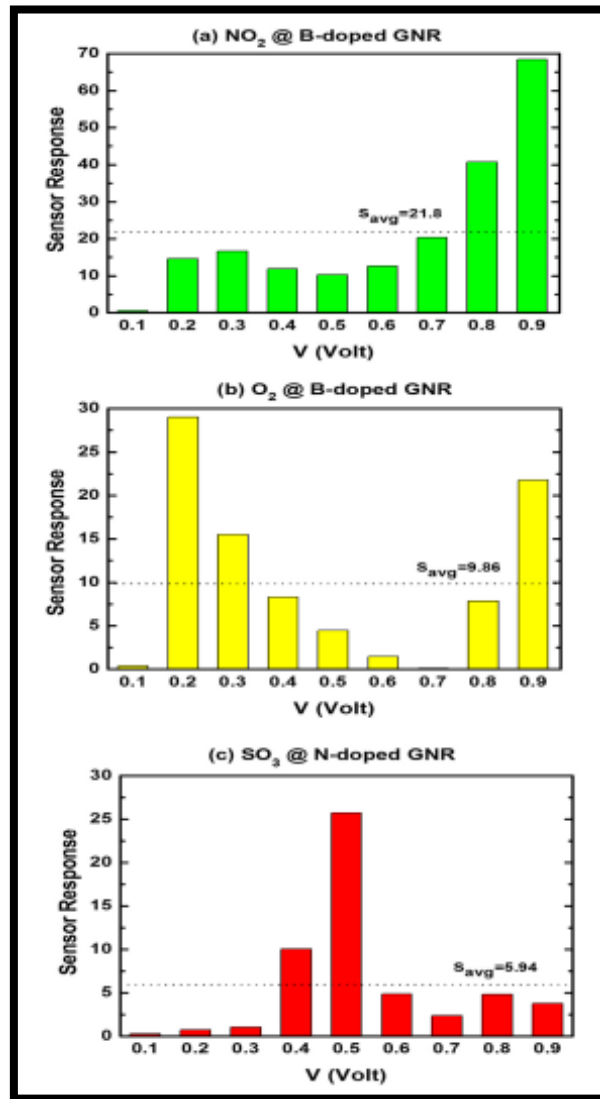
Figure 2.8: Sensor response versus bias are shown for targeted gases on the devices.

Chapter 3: Manganese Embedded C_2N for H_2 Sensing and Storage

3.1 Summary

Density Functional Theory (DFT) has been employed to investigate the effect of magnetic moment on the hydrogen adsorption and gas-sensing properties in Mn-embedded in C_2N. Special focus was given to the effects of both magnetization and dimerization on the adsorption properties. Two distinct configurations of embedment were considered: (i) Single atom catalyst (SAC): Mn@C_2N; and (ii) Dimer atom Catalyst (DAC): Mn_2@C_2N. The results showed that the H_2 molecule exhibits chemisorption processes on both SAC and DAC with weak molecular dissociation. The effect of chemisorption on the electronic structure is so enormous to the extent that the DOS gets fragmented near Fermi level with opening of small gaps of order 0.11 eV and 0.20 eV in SAC and DAC, respectively. Such changes would be manifested in enhanced sensor responses. Based upon the huge changes in electronic and magnetic properties induced by the chemisorption and the low recovery time (i.e., $\tau \ll 1$ s, $\tau = 92$ μs and 1.8 ms, respectively), we concluded that C_2N: Mn should be an excellent candidate for (reusable) hydrogen magnetic gas sensor with high sensitivity and selectivity and rapid recovery time. Our theoretical results were corroborated with good agreement with the available data in literature.

3.2 Introduction

The breakthrough discovery of graphene by Geim and Novoselov [1] not only earned them the Noble prize in physics in the year 2010 but it further paved the way for a new horizon of physics field based on 2D-materials. The expectations of the inventors in graphene were very high and they predicted that it would be the leading and prime material for fabrication of new generation of electronic devices [1-4, 6, 106]. Graphene is a one-atom thick layer with honeycomb structure and is metallic by having two bands linearly crossing each other at the Fermi level at K point in the Brillouin zone to make the so-called Dirac cones (i.e., having high electronic speed at Fermi level and high electronic mobility of about $\mu \sim 2 \times 105$ cm^2/V.s [107] better even than 9200 cm^2/V.s of GaAs [108]). That Fermi speed by itself opened a dialogue between materials science and high-energy physics. These characteristics ranked graphene to be a unique material with multi-functionality, as it can be functionalized to tune its properties to basically any specific task. As a matter of fact, graphene has proven itself to be a multifunctional material for many applications, for instance: (i) In nano-electronics: It was considered for post-silicon electronics as Graphene-based Field-Effect Transistor (G-FET) was fabricated [63, 109]; (ii) In Photonics: Even though pristine graphene has a zero gap, its functionalization and compounds can produce a gap tunable for specific optoelectronic applications. Recent results have shown the application of graphene in optoelectronics ranging from dye-sensitized solar cells to light-emitting diodes to touch screens to photodetectors and to ultrafast lasers [110-113]; (iii) In biomedicine: It was used in biosensors (i.e., to detect glucose, dopamine, proteins and DNA), as well as in bio-imaging, drug delivery and photo-thermal therapy applications [116]; (iv) in strain sensors: Functionalization (e.g., graphene oxide) can reduce the stiffness of graphene and make it suitable for strain sensing [117, 118]; (v) in gas sensing: Perhaps the broadest field of graphene applications is in the arena of gas-sensing. As it was in the original vision of the inventors [2], graphene has shown some superiority over Metal Oxides (MOX) in having high sensitivity towards toxic gases at Room Temperature (RT) [6, 80, 119-120]. Many toxic gases (e.g., H_2S, CO_2 and NO_2) whose detection at RT used to be challenging for MOX were detected at ambient air conditions using graphene-based sensors [121-123]. Recent progress in growth and synthesis has led to

the creation of completely new materials. For instance, the nitrogenated holey graphene "C_2N" was recently successfully synthesized by Mahmood and co-workers in 2015, using a bottom-up wet-chemical reaction [12]. This novel material has been proven to be very thermodynamically stable and possesses potential characteristics to adapt against embedding metal catalysts which normally are used to trigger the selectivity towards certain toxic gases at RT. This new material also demonstrated high competence as suitable material for energy-storage applications [13, 15-16, 124]. C_2N not only it has a uniform distribution of holes, but the holes and phenyl rings are also surrounded by aromatic nitrogen atoms to widen the gap between the valence and conduction bands and, thus, to make itself useful for semiconducting applications (i.e., $E_g \approx 1.90$ eV) [12]. In the case of energy-storage applications, light metal atoms (e.g., Li, Na, K, Ca) can be embedded in the holes or intercalated between layers for Hydrogen adsorption. One must ensure that the binding energy of the metal atom to the substrate is higher than the cohesive energy of the metal itself. This is indeed true in the case of light metal atoms as it should be sufficient to prevent the clustering of the catalyst atoms and to ensure their uniform distribution to enhance/maximize the H_2 uptake capacity. Meanwhile, as a compromise, one must ensure that the adsorption energy of H_2 gas molecule on catalyst atom is within the well-known energy range [0.2, 0.6] eV, as recommended by the International Atomic Energy Agency "IAEA" for hydrogen storage. C_2N has proven its candidature for Calcium-ion Batteries (CIBs) and this would solve the problem of formation of dendrites existing in case of Lithium-ion Batteries (LIBs) [40-41, 125-126]. Meanwhile, it will pave the way for fabrication of low-dimensional batteries for utilization in portable electronic devices. While the embedment of light metal atom(s) in C_2N has shown great relevance in energy-storage applications, these atoms also have a few shortcomings in the case of gas-sensing applications, most likely due to the limitation in coordination number. For gas sensing applications, many researchers reported the importance of utilization of transition metal atoms. Zhao and co-workers reported DFT results of the effect of copper dimer (Cu_2) embedded in C_2N on the CO_2 reduction reaction [125]. They have shown that Cu dimer can be stably embedded in the porous C_2N monolayer because of the formation of strong hybridization between Cu 3d orbitals and N 2p orbitals. Then, $Cu_2@C_2N$ was shown to be efficient for the

electrochemical reduction of CO_2 to hydrocarbons [126]. Ma and co-workers also used DFT to show that 3d Transition Metal (TM) embedded in C_2N are promising Single-Atom Catalyst (SAC) [127]. They included in their study five TM atoms (i.e., Sc, Ti, V, Cr and Mn) and to test their catalytic activity they studied their adsorption with CO and O_2 molecules. The strong adsorption and significant activation of the reactants (i.e., CO and O_2 molecules) were observed for Cr and Mn catalysts. So, they concluded that Cr and Mn embedded C_2N monolayers are the very promising SACs for low-temperature CO and O_2 oxidation reactions [127]. In another related work, Luo and co-workers used Dmol^3 package to study the effect of MnN_4 embedded in several carbon systems (i.e., graphene (MnN_4-Gra), Graphene Nanoribbons (MnN_4-GNR), Graphene Nanosheets (MnN_4-GNS), Carbon Nanotubes (MnN_4-CNT) and C_{60} fullerenes (MnN_4-C_{60})) on the adsorption and capture of numerous toxic gases [128]. The embedment of MnN_4 is done as follows: They removed 1 pair/bond of carbon atoms and replaced them with 1 Mn atom; then they changed the four neighboring carbon atoms with 4-N atoms (like in substitutional doping). The atomic relaxation and binding energy calculations showed that such embedment of MnN_4 is thermodynamically stable. They carried on with adsorption tests of many toxic gases of environmental concern. The list of gases included: CO_x, NO_x, N_2O, H_2S, SO_2, NH_3, O_2 and H_2O. Their results showed that both the dopant and system curvature play a role in enhancing the adsorption properties. Among the five tested systems, MnN_4-C_{60} is found to have the largest adsorption energy for all gases and thus proven suitable for trapping the gases. MnN_4-Gra, MnN_4-GNR and MnN_4-CNT are evaluated as good catalysts for Oxygen Reduction Reaction (ORR). MnN_4-Gra, MnN_4-GNR and MnN_4-CNT are reported as suitable catalysts for CO oxidation. The best temperature intervals for the validity of such characteristics were determined by the Gibbs free energy and Molecular Dynamics (MD) [128]. The same authors also reported the occurrence of chemisorption of the MnN_4-catalyst with CO, NO_x, NH_3 and SO_2 molecules, whereas physisorption processes took place with the other gas molecules [128]. Both electrochemical measurements and DFT calculations reported by Liu and co-workers [129] confirmed the synthesis and catalytic activity of MnN_4 - to be even better than FeN_4-embedded in carbon layers in inducing ORR. Their results strongly suggested that Mn and N (i.e., MnN_4) co-doping in carbon are promising high-

performance catalysts for ORR in acidic medium [129].

In another DFT study, Impeng and coworkers investigated the correlation between magnetic moment and strength of chemisorption of 13 gases on MnN_4-embedded graphene. Only five gases (i.e., NO, NO_2, O_2, CO and SO_2) exhibited strong chemisorption with adsorption energies −2.30, −1.42, −1.32, −1.11 and −0.51 eV, respectively. Moreover, the magnetic moment of MnN_4-Gra drastically changed from 3.01 μB to 0.13, 1.04 and 2.01 μB, after the chemisorption of NO, CO and NO_2 gases, respectively, while it was hardly altered by the other gases. Adding to this, the computed respective recovery times at 423 K were 2.5×10^{14} s, 1.7 s and 8275 s. So, the shortest recovery time for CO detection suggested that MnN_4- Gra is a promising magnetic sensor for CO detection [120]. From energy perceptions, fossil fuel inevitably persists being used while it generates many kinds of toxic gases (e.g., CO_x and NO_x), which destroy the ecological environment and endanger human health. Besides, its reserves are limited, and they will deplete soon with the current energy demands (e.g., within a half century) pushing humans to seek other alternatives to consider as future energy resources. As a matter of fact, hydrogen stands as one of the strongest candidates to act as one clean energy resource and eco-friendly. Research has achieved good progress in exploring hydrogen in energy-storage such as fuel cells and batteries [131]. It is known that fuel cell is an electrochemical cell that converts the chemical energy of hydrogen fuel using oxidizing agent into electricity through a pair of redox reactions [131]. On the other hand, hydrogen is a very explosive gas and very reactive at high temperatures larger than 600 K. Meanwhile, its gas-sensing presented a great challenge to Metal Oxides (MOX) based sensors, such as Pt-doped ZnO whose operating temperature was optimized to 400 K [132,133]. So, many researchers have been searching for other materials convenient for hydrogen storage and gas-sensing such as graphene and its derivatives (e.g., C_2N and C_3N) [12, 15-16, 124, 134]. The scope of the present investigation is to explore the novel C_2N material and its functionalization by embedding Mn atom(s) to study its interaction with H_2 gas molecule. We use the state-of-the-art DFT method based on the Vienna Ab-initio Simulation Package (VASP), while we pay special attention to the effects of magnetic moment of manganese and its clustering on the adsorption of H_2 molecule. Another important issue in our present study is the

contrast between Single Atom-Catalyst (SAC) and Dimer-Atom-Catalyst (DAC) effects on the adsorption properties of H_2 molecules. This Chapter is organized as follows: Section 3.3 gives a detailed description of the computational method. Section 3.4 gives an elaborate discussion of the results. The last Section 3.5 summarizes our main findings.

3.3 Computational Method

It is well established that Density Functional Theory (DFT) is a very appropriate method to predict the ground state characteristics, including the adsorption properties. Perhaps, the most popular and reliable package is the VASP [135], which incorporates all basic interactions, such as spin-polarization, magnetic and dipole-dipole long-range (i.e., van der Waals) interactions. Furthermore, our present study involves magnetic dopants (e.g., manganese "Mn") and its binding with C_2N as well as interaction with gas molecules. Our calculations include atomic relaxation to study the adsorption of H_2 molecule(s), spin-polarized band structures and partial as well as orbital densities of states, difference of charge density plots, Bader-charge analysis, magnetic moments, and recovery time. We use a supercell of size 2×2 primitive cells of C_2N (e.g., the supercell of pristine C_2N contains 48 C and 24 N atoms = total of 72 atoms). Mainly, throughout this work, we have analyzed two compounds: (i) Single-Atom-Catalyst "SAC" Mn embedded in a pore of C_2N (Mn@C_2N); and (ii) Dimer-Atom-Catalyst "DAC" Mn_2 embedded in a pore of C_2N (Mn_2@C_2N). We have studied the interactions of these two systems with H_2 molecules. The calculation employs a plane-wave basis set (with cutoff energy of 500 eV). Within the framework of the Projected-Augmented plane-Waves (PAW) method, the electronic exchange-correlation was treated using the Generalized Gradient Approximation (GGA) along with DFT-D3 method [57, 136] to take care of the van der Waals interactions. In the geometry optimization, all the atoms in the supercell were allowed to relax until the Hellmann Feynman force on each atom became smaller than $0.01 \, eV\text{Å}^{-1}$; whereas the tolerance for the total energy convergence was set to $10^{-4} \, eV$. The sampling of the Brillouin zone was performed using $6\times6\times1$ Monkhorst-Pack (MP) technique [56] for total energy calculations. However, the density of states calculations was performed with a relatively denser $12\times12\times1$ k-mesh. The adsorption energy of hydrogen molecule on Mn-embedded C_2N was evaluated using the formula:

$$E_{ads} = E_{C2N+H_2} - E_{C2N} - E_{H_2} \tag{3.1}$$

where E_{C2N+H2}, E_{C2N}, and E_{H2} are the total energies of the system of Mn embedded C_2N with and without H_2 molecule and the H_2 molecule, respectively.

Furthermore, we emphasize that the charge transfer was estimated using Bader-charge analysis [137]. A critical inspection about various methods to calculate charge transfer has also been discussed in recent reviews [138-139].

3.4 Results and Discussions

3.4.1 Atomic Relaxations

Figure 3.1 shows the relaxed structures using DFT code (VASP). The original supercell contains 2×2 primitive cells of C_2N structure (i.e., each primitive cell has 12 C + 6 N atoms, so the supercell would have 72 atoms). The displayed relaxed structures correspond to the following systems:

(a) Pristine C_2N/H_2: An attempt to relax H_2 molecule on the pore of pristine C_2N yielded physisorption process, where the molecule remained at about $d(H_2\text{-}C_2N) =$ 1.68 Å via van der Waals interaction with a weak adsorption energy of about E_{ads} = - 0.109 eV. The H_2 molecule acts as reducing agent for C_2N with very small charge transferred to C_2N is of order of about thousandths of electron charge $\Delta q =$ - 0.005e. The results of the geometrical parameters are summarized in Table 3.1; whereas the energetic parameters are in Table 3.2. The functionalization of C_2N by embedding Mn atom(s) in the pore changes the behavior from semiconducting to metallic and the adsorption of the H_2 molecule would exhibit chemisorption process, as will be shown in next panels.

(b) System $1Mn@C_2N$: A preliminary assessment of the stability of the Mn catalyst inside the C_2N pore was a necessity prior to the study of adsorption. In this context, the atomic relaxation was attempted from two different perspectives in which two different Mn-catalyst's initial positions were tested as follows:

1. Initially, the Mn atom occupied the center of the pore; and
2. Initially, the Mn atom was put midway between the pore's center and the C-C bond of pore's edge.

After full relaxations in these latter scenarios, the Mn atom found a local-stable position at the pore center (with $E_{bind} = -4.342$ eV) and the global-stable position at off-center by a distance of about 0.38 Å (with $E_{bind} = -4.497$ eV), respectively. Our results are in good agreement with those reported by Ma and coworkers [127], who reported $E_{bind} = -4.28$ eV and Mn SAC to stabilize at off center position with the Mn-N distances of about $d_{Mn-N} = 2.15–2.78$ Å. The most stable position is shown in Figure 3.1(b), which actually show no further distortion was caused on the shape of the pore as it is sufficiently large (diagonal distance d_{N-N} =5.51 Å) to accommodate not only a SAC but a DAC.

(c) System 1Mn@C$_2$N/H$_2$: One H$_2$ gas molecule was relaxed on the metal catalyst (i.e., starting from just above Mn onsite by about 1.5 Å). The molecule stabilized after a chemisorption process, in which both H atoms get split, but they remained attached to the same Mn atom at about $d_{(Mn-H)} = 2.07$ Å. The distance between H atoms is about $d_{(H-H)} = 0.90$ Å which is larger than the hydrogen molecule bond-length of about $b_{(H-H)} = 0.77$ Å. Thus, this configuration is due to the relaxation that was carried out in VASP under the condition of frozen lattice (0 K), (i.e., under the assumption of validity of Born-Oppenheimer approximations). It is noticeable that establishing two bonds with hydrogen atoms, Mn catalyst cut all its bonds with nitrogen atoms but only two bonds were remaining connected. Furthermore, the H$_2$ molecule acts as oxidizing the SAC by draining an amount of charge of order few hundredths of electronic charge $\Delta q = +0.017$ e. The adsorption energy was calculated to be about $E_{ads} = -0.474$ eV, which is at the border value between strong physisorption and weak chemisorption.

(d) System Mn$_2$@C$_2$N: The dimer Mn-Mn was embedded in the pore of C$_2$N, and it seems that the atomic relaxation yielded a thermodynamically stable configuration, in which the dimer is fully buried to remain in the same plane as C$_2$N membrane without any buckling effect. The bond length $d_{(Mn-Mn)} = 1.76$ Å is much shorter than $d_{(Mn-N)} = 2.46$ Å indicating that Mn is a very cohesive metal. It is worth noting that the binding energy of the Dimer Atom Catalyst (DAC) E_{bind} = -3.822 eV/atom is smaller than that of the Single Atom Catalyst (SAC) which is mentioned above (-4.497 eV); but is larger than the Mn cohesive energy $E_{coh} = -$

2.92 eV [140]. This reveals that the DAC is also stable like SAC in the embedment in the pore of C_2N. From perspective of assessment of stability, three different initial configurations of Mn DAC were attempted and the most stable relaxed structure if found to be the one shown in Figure 3.1(d) and is consistent with structure of Cu DAC embedded in C_2N ($Cu_2@C_2N$) which was reported by Zhao and coworkers [126]. Furthermore, the magnetization in case of Mn DAC is much reduced compared to that of Mn SAC (i.e., $M_{(DAC)} = 2.42$ μB $< M_{(SAC)} = 3.60$ μB).

The Mn DAC seems to be in favor of stabilizing inside the pore in an antiferromagnetic state.

(e) System $Mn_2@C_2N/H_2$ onsite: In relaxing the H_2 molecule on the system, only two initial positions were attempted as having the highest potential for the chemisorption occurrence. In Figure 3.1(e), the initial position from which the H_2 molecule started its relaxation was onsite one of the two Mn atoms, starting from a height of about 1.5 Å. The atomic relaxation achieved a stable configuration in which the H_2 molecule exhibited chemisorption process with a weak molecular dissociation. The distance between Mn-H reached a value $d_{(Mn-H)} = 1.64$ Å close to the SAC-H_2 value and even the distance $d_{(H-H)} = 0.92$ Å is also similar. One may think that if temperature were higher than 0 K, then the splitting in the H_2 molecule would be higher than it is presented. This configuration is so as it is within the given conditions of calculation due to frozen lattice implemented within the framework of Born-Oppenheimer approximations. Yet, the adsorption energy $E_{ads} = -0.551$ eV is a bit higher than the case of Mn SAC and H_2 molecule acts as oxidizing Mn DAC with a larger charge transfer $\Delta q = +0.073$ e (Table 3.2). The formation of chemical bonding between Mn-H caused a relief and an elongation of Mn-Mn bond to become $d_{(Mn-Mn)} = 1.97$ Å.

Such elongation further reduces the magnetic moment from $M_{bef(DAC)} = 2.42$ μB to $M_{aft\,(DAC)} = 1.97$ μB from before to after hydrogen chemisorption, respectively. This might be attributed to the role of diversifying the type of species of neighboring atoms and changing the directional cosines of new bonds with hydrogen atoms.

(f) System $Mn_2@C_2N/H_2$ center: In Figure 3.1(f), the starting position of H_2 molecule in the atomic relaxation process was from just above the middle of Mn-Mn bond, from a height of about 1.5 Å. The H_2 molecule passed through a chemisorption process associated with a weak molecular dissociation, after which the H atoms are about to separate and get coupled to two distinct Mn atoms. The distance $d_{(H-H)} = 0.90$ Å, again, since the VASP calculation is carried out at frozen lattice approximation (0 K) and lack of heat has driven the system to such minimum-energy configuration where $d_{(Mn-H)} = 1.65$ Å similar to the previous situation of DAC. Nonetheless, the formation of chemical bonding between Mn-H causes relief or elongation of Mn-Mn bond to have a higher bond-length $d_{(Mn-Mn)} = 1.97$ Å in similar fashion to the previous situation of DAC, including the reduction of magnetization. Yet, the H_2 molecule acts as oxidizing DAC but the amount of transferred charge becomes a bit larger than the previous situation to be $\Delta q = + 0.080$ e. The adsorption energy in this case is also larger $E_{ads} = -0.552$ eV revealing that this configuration is more stable.
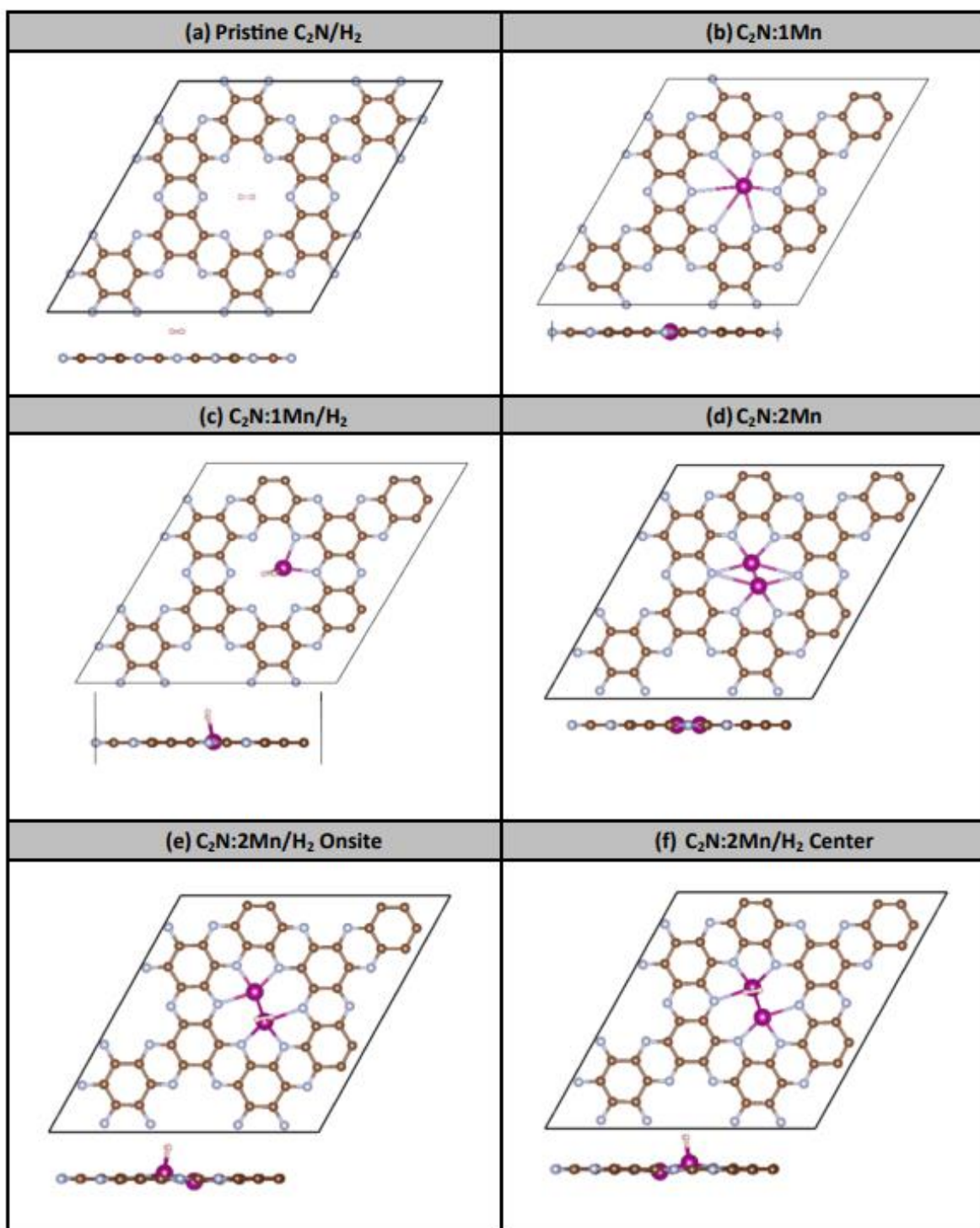
Figure 3.1: Relaxed atomic structures of (a) Pristine C_2N; (b) C_2N:1Mn; (c)C_2N:1Mn/H_2; (d) C_2N:2Mn/H_2(onsite); (f) C_2N:2Mn/H_2(on center).

Table 3.1: Geometrical parameters of DFT-relaxed atomic structures of Mn-embedded (SAC) and Mn_2-embedded (DAC) C_2N before and after the adsorption of H_2 gas molecule.

(a) Pristine C_2N	**(b) Pristine C_2N / H_2**
$d(\text{C-C})$ = 1.43–1.47 Å $d(\text{C-N})$ = 1.34 Å	$d(\text{C-C})$ = 1.43–1.47 Å $d(\text{C-N})$ = 1.34 Å $d(\text{H-H})$ = 0.75 Å $d(H_2\text{-}C_2N)$ = 1.68 Å
(c) C_2N:1Mn	**(d) C_2N:1Mn/H_2**
$d(\text{C-C})$ = 1.43–1.46 Å $d(\text{C-N})$ = 1.34 Å $d(\text{N-Mn})$ = 2.72 Å Ang(N-Mn-N) = 59.97°	$d(\text{C-C})$ = 1.42–1.46 Å $d(\text{C-N})$ = 1.35 Å $d(\text{N-Mn})$ = 2.64 Å $d(\text{Mn-H})$ = 2.07 Å $d(\text{H-H})$ = 0.90 Å Ang(N-Mn-N) = 60.08°
(e) 2Mn@C_2N	**(f) C_2N:2Mn/H_2 @ Onsite**
$d(\text{C-C})$ = 1.42–1.46 Å $d(\text{C-N})$ = 1.35 Å $d(\text{N-Mn})$ = 2.46 Å $d(\text{Mn-Mn})$ = 1.76 Å Ang(N-Mn-N) = 71° Ang(N-Mn-Mn) = 106°	$d(\text{C-C})$ = 1.41–1.47 Å $d(\text{C-N})$ = 1.35 Å $d(\text{N-Mn})$ = 2.15 Å $d(\text{H-H})$ = 0.90 Å $d(\text{Mn-H})$ = 1.65 Å $d(\text{Mn-Mn})$ = 1.97 Å Ang(N-Mn-N) = 72.3° Ang(N-Mn-Mn) = 100.9°
(g) C_2N:2Mn/H_2 @ Center	
$d(\text{C-C})$ = 1.41–1.47 Å $d(\text{C-N})$ = 1.35 Å $d(\text{N-Mn})$ = 2.34 Å $d(\text{H-H})$ = 0.90 Å $d(\text{Mn-H})$ = 1.65 Å $d(\text{Mn-Mn})$ = 1.97 Å Ang(N-Mn-N) = 72° Ang(N-Mn-Mn) = 100.85°	

Table 3.2: Band-gap energy, adsorption energy, charge transfer, magnetic moment. Fermi energy and work function of the studied relaxed structures.

Substrate	E_g (eV)	E_{ads} (eV)	Δq (e)[£]	$M(\mu_B)$[¶]	E_F (eV)[¶]	Φ (eV)[¶]	τ(s)
Pristine C$_2$N	1.66[¶] (1.55)[‡]	N/A	N/A	0	−4.100	5.588	N/A
Pristine C$_2$N/H$_2$	1.66[¶] (1.55)[‡]	−0.109[¶] (−0.0077)[‡]	−0.0047	0	−3.736	5.226	6.8×10^{-11}[¶] (1.5×10^{-12})[‡]
C$_2$N:1Mn	0[¶] (0)[‡]	N/A	N/A	3.60	−2.878	5.111	N/A
C$_2$N:1Mn/H$_2$	0.11[¶] (0)[‡]	−0.474[¶] (−1.021)[‡]	+0.0166	3.40	−2.822	4.364	9.2×10^{-5}[¶] (140.2)[‡]
C$_2$N:2Mn	Half−metal[¶] (0)[‡]	N/A	N/A	2.42	−2.996	4.561	N/A
C$_2$N:2Mn/H$_2$ Onsite	0.20[¶] (0)[‡]	−0.551[¶] (−0.482)[‡]	+0.0726	1.97	−2.990	4.577	1.8×10^{-3}[¶] (1.3×10^{-4})[‡]
C$_2$N:2Mn/H$_2$ On Center	0.06[¶] (0.095)[‡]	−0.552[¶] (−0.507)[‡]	+0.0799	1.97	−2.987	4.575	1.9×10^{-3}[¶] (3.2×10^{-4})[‡]

[¶] VAP Results.
[‡] SIESTA Results.
[£] Bader charge analysis.

3.4.2 Charge Transfer and Recovery Time

Information about charge exchange between adsorbate and absorbent can be extracted by several means. One of them is by using the Bader-charge analysis whose results are already shown in Table 3.2 and discussed in the previous section. Another method is to plot the charge density of the highest occupied molecular orbital (HOMO) and lowest unoccupied molecular orbital (LUMO) states. However, these would only give information about the valence-band (VB) and conduction band (CB) edge states. A third method is to plot the charge density contour plots, which would show the electronic distribution in the ground state. Here, to make a contrast between the charge densities of after and before the occurrence of adsorption, we decided to present the charge-density difference (CDD) plots for C$_2$N-based systems in Figure 3.2. In Figure 3.2, green and yellow colors stand for deficit and gain of charge, respectively. The iso-surfaces of electron density illustrates the overlapping of the electronic wave-functions at the interface region between H$_2$ molecule and substrate, confirming the formation of covalent bonds due to mixing of atomic orbitals, specifically in cases of occurrence of chemisorption.
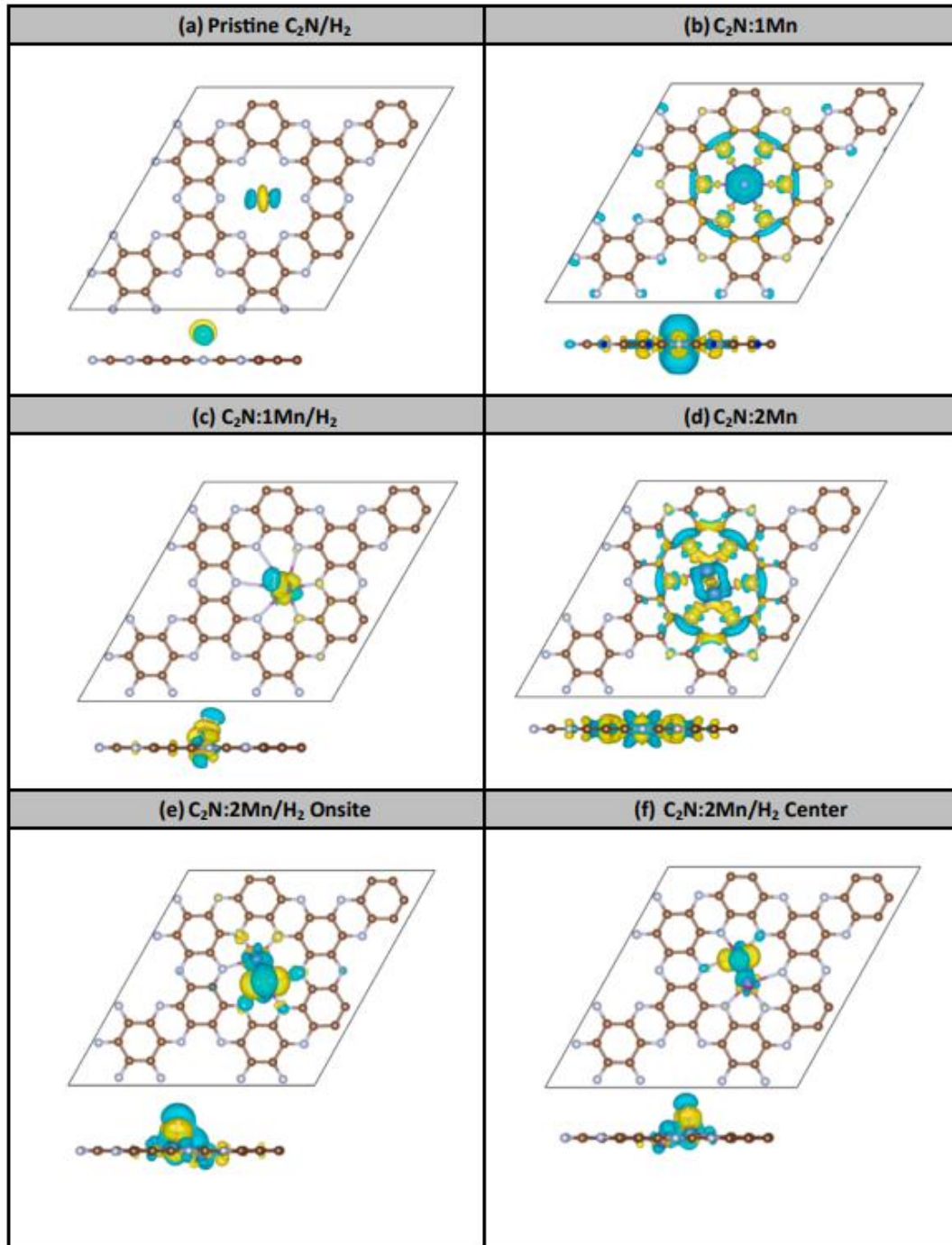
Figure 3.2: CDD for six systems after full atomic relaxations.

a) Pristine C_2N/H_2: Figure 3.2(a) shows the CDD in case of relaxed H_2 molecule on pristine C_2N. The relaxation yielded a physisorption process where the molecule stabilized away from the C_2N layer at a distance at about $d_{(H2\text{-}C2N)} = 1.68$ Å and persisted to interact with the substrate via van der Walls interaction (i.e., dipole-dipole interaction). Within the vicinity of pore of C_2N, the discrepancy in electronegativity between C and N atoms (i.e., $\chi^N = 3.04$ Pauling $> \chi^C = 2.55$

Pauling) [140], would make electric dipoles directed from N to C (N → C). The surface dipoles induce some charge redistribution in the H_2 molecule hung nearby the hole. Figure 3.2(a) shows that the electrons move to accumulate at the center of H-H bond, as an electrostatic effect of getting repelled from the negative charges accumulated on N atoms. Furthermore, the high electronegativity of N atom with respect to H atom (i.e., $\chi^H = 2.20$ Pauling) [141], would make it possible that some charge tunnel from H_2 molecule to the N atoms, of value $\Delta q = 0.0047$ e.

b) $1Mn@C_2N$: Due to the binding of 1 Mn in the pore of C_2N, charge has been displaced from Mn site and C-N bonds to accumulate more on N atoms and N-Mn bonds. It indicates formation of electric dipole moments from N → Mn due to the discrepancy in electronegativity between N and Mn atoms (i.e., $\chi^N = 3.04$ Pauling $> \chi^{Mn} = 1.55$ Pauling) [141].

c) $1Mn@C_2N/H_2$: After the chemisorption process of H_2 on SAC, the molecule acted as oxidizing the SAC with $\Delta q = +0.013$ e. So, the charge looks transferred from Mn to accumulate along the Mn-H chemical bonds. This is also justified by the fact that H atom being more electronegative than Mn atom (i.e., $\chi^H = 2.20$ Pauling $> \chi^{Mn} = 1.55$ Pauling) [141].

d) $Mn_2@C_2N$: The dimer Mn-Mn (DAC) being embedded in the pore of C_2N would cause a similar effect on the charge distribution as that done by single Mn SAC. The charge is displaced from the Mn atomic sites to accumulate along the Mn-N bonds.

e) $Mn_2@C_2N/H_2$ onsite: After the occurrence of chemisorption between H_2 and C_2N, the molecule seemed to have functioned as oxidizing DAC, where the charge is displaced from Mn atoms towards the Mn-H bonds.

f) $Mn_2@C_2N/H_2$ on center: The effect is like the previous case. The charge accumulation on Mn-H is even clearer.

To decide whether the gas sensor should be reusable or disposable, calculation of recovery time becomes necessary. To be categorized reusable, the recovery time must be rapid. Yong and coworkers presented elaborate theoretical work on the absorption of several gas molecules on pristine C_2N [142], including the calculation of recovery time.

Having moderate adsorption energy, of respective values −0.539 eV and −0.438 eV (i.e., at the border between strong physisorption and weak chemisorption, which is about ~0.5 eV), and large effect on the electronic structure but small recovery times of estimated values 1.2 ms and 23 μs at room temperature (RT), NH_3 and NO were found to be the most suitable for detection on C_2N-based sensor. The sensor in that case would be reusable and have high sensitivity and selectivity. Within the framework of the conventional transition state theory [80], the recovery time can be expressed as:

$$\tau = v_0^{-1} e^{(-\frac{E_{ads}}{k_B T})} \tag{3.2}$$

where T is absolute temperature, k_B is the Boltzmann's constant, E_{ads} is the adsorption energy, and v_o is the attempt frequency. Peng and coworkers [143] confirmed the validity of the above formula by using it in fitting experimental data of adsorption of NO_2 gas on single-walled carbon nanotubes (SWCNT). The experimental recovery time of NO_2 on SWCNT was confirmed to be long of about 12h using this above formula. We assume that the attempt frequency of H_2 molecule on all C_2N-systems have same order of magnitude as that of NO_2 molecule (i.e., $v_o = 10^{12} s^{-1}$), which is incidentally also used in the theoretical work of Yong and co-workers on C_2N [142].

Then, we calculated the recovery times of adsorption of H_2 molecule on Mn-doped C_2N at RT and included the results in Table 3.2. To start with pristine C_2N, one can notice that our recovery times 6.8×10^{-11}s and 1.5×10^{-12}s (due to VASP and SIESTA) are a bit smaller than that reported by Yong et al. 4.5×10^{-10}s [142]. This is so because our adsorption energy is underestimated as compared to the one of Yong et al [142].

By comparing our results of adsorption energy between VASP and SIESTA, they all agree to a good extent but only one value is much different, the one corresponding to the chemisorption of H_2 on C_2N:1Mn (i.e., in VASP $E_{ads} = -0.474$ eV whereas in SIESTA $E_{ads} = -1.021$ eV). One possible explanation for this large discrepancy is that in SIESTA the adsorption temperature is RT where the chemisorption was associated with strong molecular dissociation, whereas in VASP T = 0 K was used under the assumption of frozen lattice and validity of Born-Oppenheimer approximations.

In any case, both VASP and SIESTA found good agreement in the adsorption energies of H_2 on DAC (i.e., C_2N:2Mn), where $E_{ads} = -0.551$ eV and −0.507 eV, respectively. Considering the results of VASP, the recovery times of H_2 on SAC and DAC were found

to be about 92 μs and 1.8 ms, respectively. Furthermore, the H_2 molecule acted as oxidizing on both SAC and DAC with drained charges of about 0.013 e and 0.08 e, respectively. Hence, it seems that the more clustering of Mn the more charge transfer, the higher adsorption energy and the higher recovery time. Yet, the recovery times are so small (i.e., $\tau \ll 1$ s).

Considering the huge effect on electronic structures (explained here below) caused by the adsorption of H_2 gas molecule on both SAC and DAC, huge change of magnetic moment, one would expect that C_2N: Mn would be very strong candidate for magnetic gas sensor for detection of H_2 with very high sensitivity and selectivity.

3.4.3 Electronic Structure of Pristine C_2N
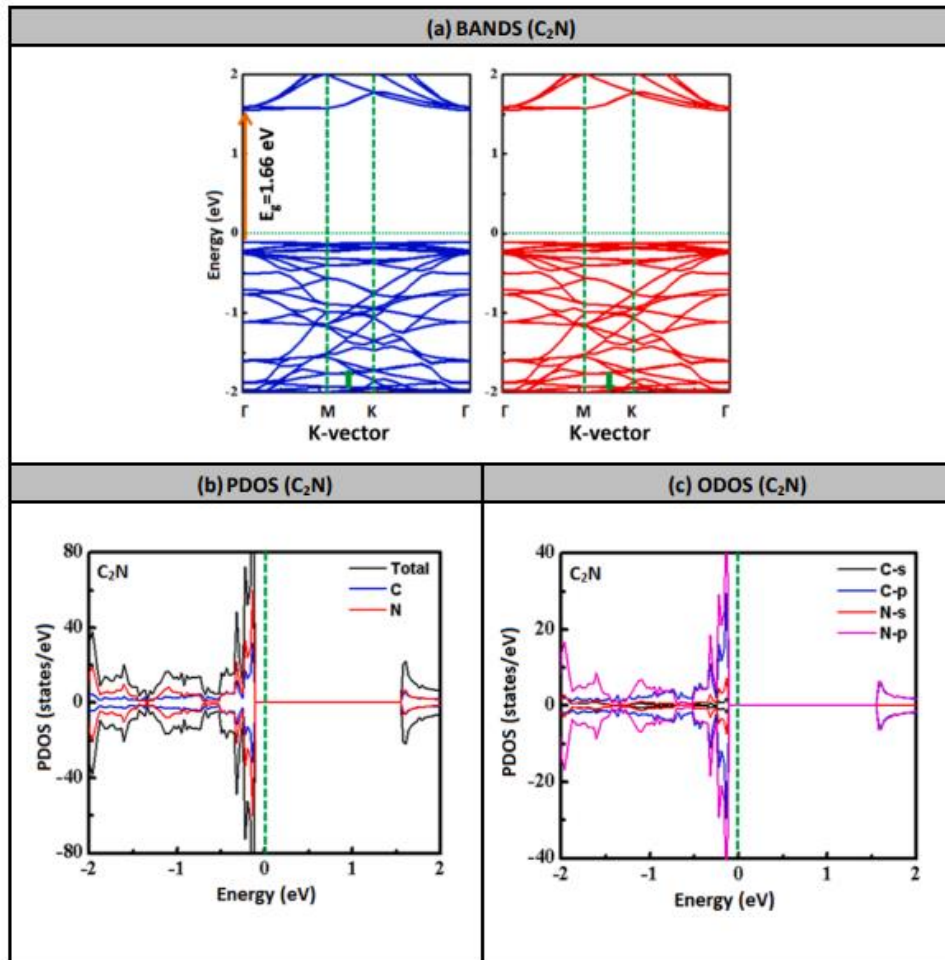
Figure 3.3: Bands (a), PDOS (b) and ODOS (c) of pristine C_2N.

Figure 3.3 shows the spin-polarized electronic structure of pristine C_2N, due to DFT calculation on a xy-periodic sample of size 2×2 primitive cells. The band structures of

spin-up and spin-down are displayed in Figure 3.3(a). It shows clearly no distinction and independence of spin as evidence that C_2N is a non-magnetic material. The band-gap energy is found to be E_g = 1.66 eV, which is in fair agreement with the theoretical one reported in the original paper by Mahmood and coworkers [12] of value 1.70 eV, obtained by DFT method. Panel 3.3(b) shows the spin polarized PDOS of C_2N. Here also, there is no distinction between spin-up and spin down in both PDOS's contributions of C and N atoms. This corroborates the description of bands. Nonetheless, although the weight of N atoms is about one third of the total DOS, the contribution of N atoms to the VB structure is much bigger than the one of C atoms. This is attributed to the fact that the electronegativity of nitrogen atoms being larger than that of carbon atoms (i.e., χ^N = 3.04 Pauling > χ^C = 2.55 Pauling) [141]. Whereas the CB received almost similar contributions from both C and N atoms proportional to the ratio of C:N = 2:1. Panel 3.3(c) shows the orbital-resolved DOS (ODOS) of the same sample of C_2N. One expects a hybridization of sp^2 to take place in both C and N atoms, with p_z to be more delocalized and to contribute to the CB structure. Figure 3.3(c) shows that the main contribution to VB comes from p orbitals of N and C, including near-Fermi level (i.e., near VB and CB edges). The ODOS plot also shows that very high DOS at the VB-edge comes from the p-states of N atoms. Likely this bulged DOS is attributed to the saturated dangling bonds on nitrogen atoms.

3.4.4 Adsorption and Spin Polarized Electronic Structures

(a) Single atom catalyst (Mn@C$_2$N)
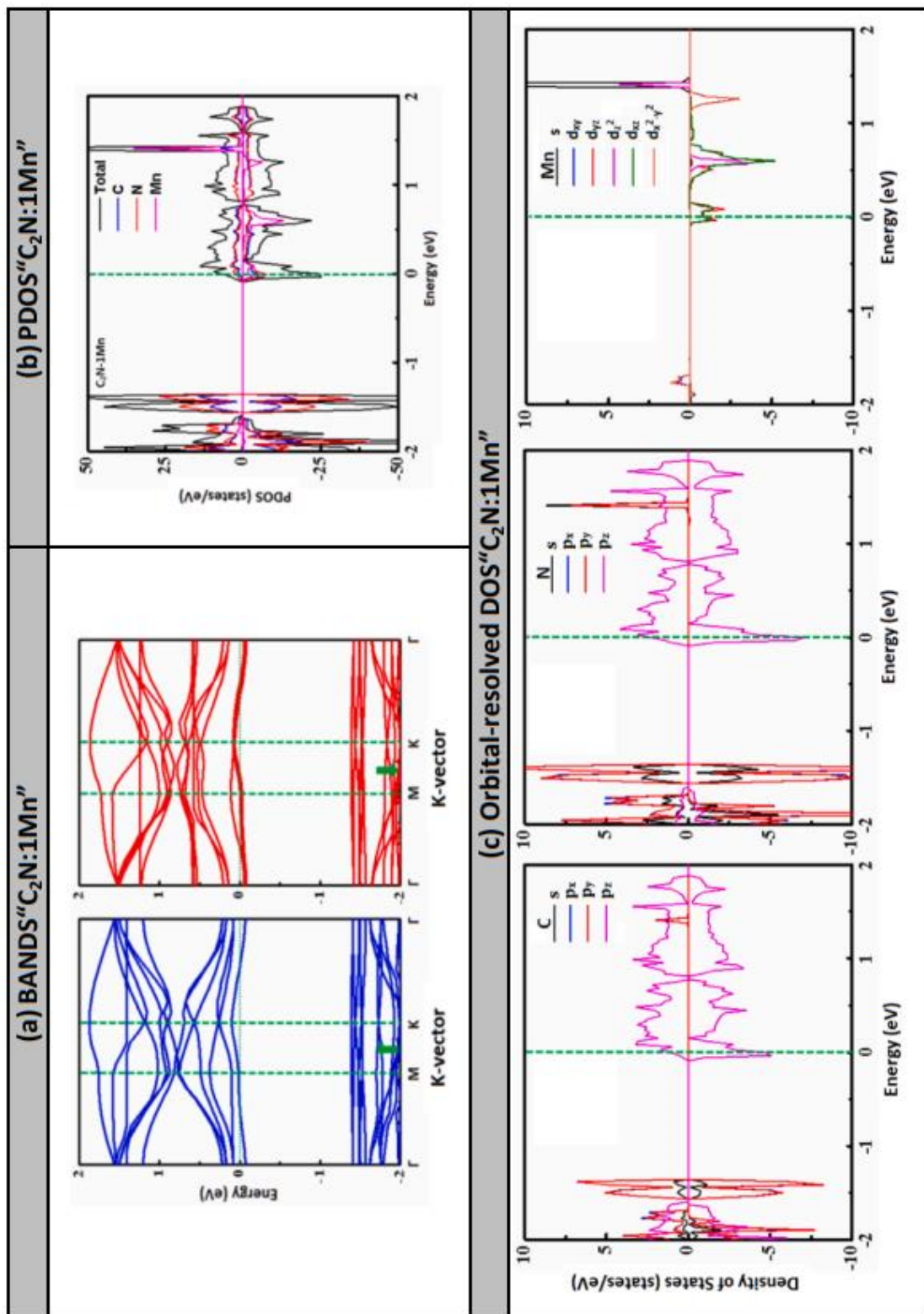
Figure 3.4: Bands (a), PDOS (b) and ODOS (c) of system C$_2$N:1Mn.
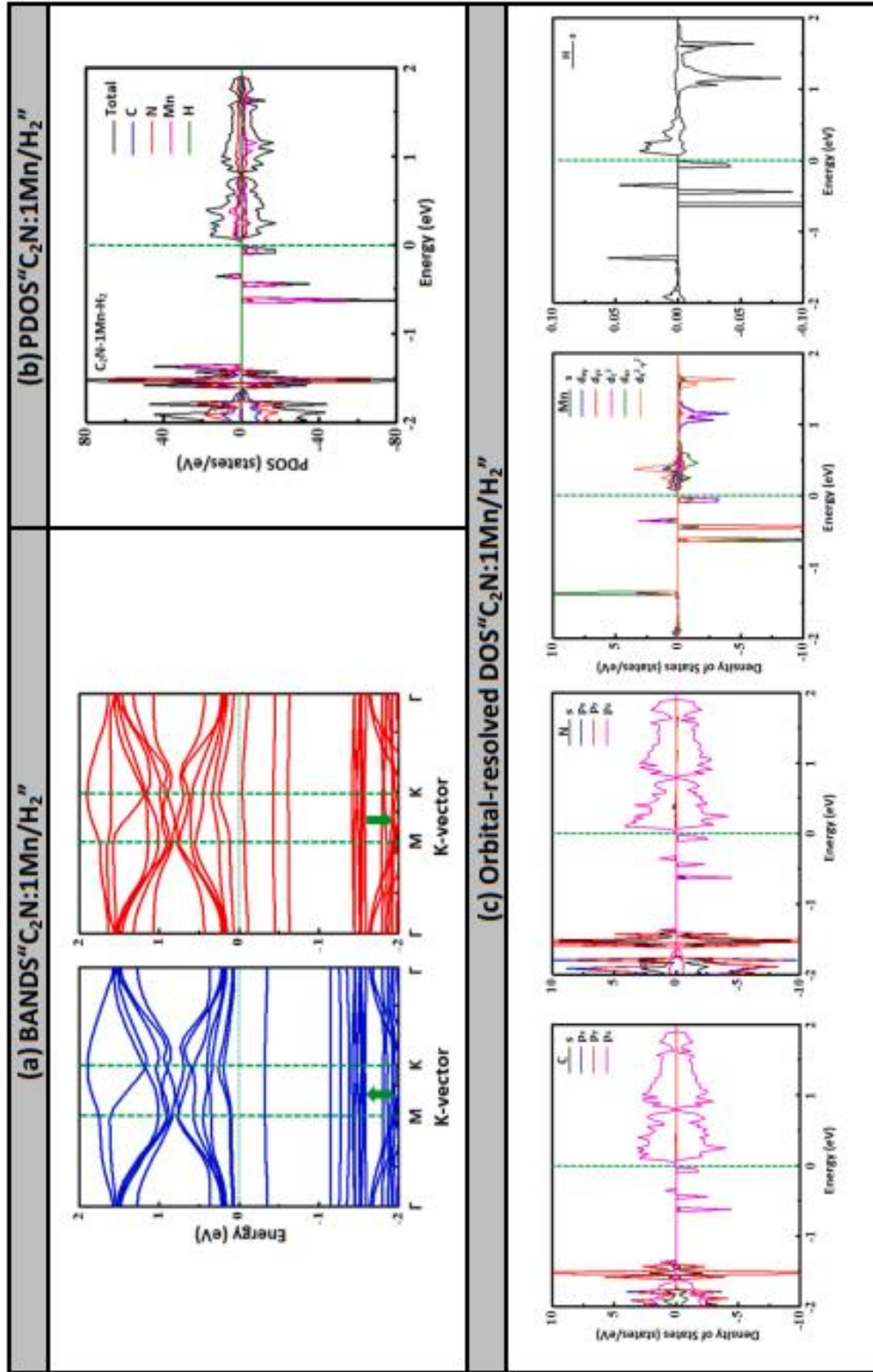
Figure 3.5: Bands (a), PDOS (b) and ODOS (c) of system $C_2N:1Mn:H_2$.

Figure 3.4 shows the electronic structure of the case of a single Mn atom embedded in the pore of C_2N after conducting atomic relaxation and fully achieving the stable

configuration. The addition of a single Mn-atom would be sufficient to transform the host material from semiconductor to a metal. Panel 3.4(a) shows the bands structures corresponding to spin-up and spin-down in blue and red colors, respectively. Both spin-up and spin-down band-structures are not identical and show that Mn introduced resonance states in the CB and dragged Fermi level into there. It revealed also that the material became magnetic and metallic. Likely, the Bohr radius is larger than the system size so that there was formation of dispersive metallic bands at Fermi level. Mn atom contributes with its states to the CB structure and shifts Fermi level to lay above the CB-edge.

Panel 3.4(b) displays the spin-polarized PDOS and shows large discrepancy between spin-up and spin-down and consistently conveys that the magnetization might be huge in the system. As a matter of fact, the calculation of magnetization yielded a value of 3.60 Bohr magneton (μB) (Table 3.2). The contribution to the VB structure coming from N atoms is larger than C atoms due to the electronegativity of N atom being larger than that of C atom. It seems that Mn atom has induced magnetization in the atoms at the neighborhood of the pore where Mn was embedded. Panel 3.4(c) displays the orbital-resolved DOS of C_2N:1Mn system. In the case of C and N atom, the sp^2 hybridization would let the mixing of s, p_x and p_y orbital contribute to the VB structure whereas p_z contributes to the CB structure. There exists a clear asymmetry between ODOS of spin-up and spin-down states as an effect of magnetic induction due to Mn-doping. In the ODOS of Mn atom, within the energy region of Fermi level, it is amazing to see that most contributions come from spin-down states of d_{yz}, d_{zx} and d_{z2} orbitals.

It seems that the CB has contributions from the delocalized states of p_z orbitals of C and N as well as d-orbitals with z projections. Yet, the ODOS of Mn atom clearly shows huge magnetic moment as the calculation confirmed.

Figure 3.5 shows the band-structure of C_2N:1Mn after the adsorption of H_2 via chemisorption. It is very important in the study of gas-sensing properties to be picky on the amendment caused by adsorption on the electronic structure of the system. The primary observation on the bands is the opening of a band gap at Fermi level of energy $E_g = 0.11$ eV. This change in electronic characteristics would be very significant to gas-sensing as it causes a big modification in the conduction properties and consequently

enhances the sensor response. It seems that the chemisorption of H_2 on SAC causes magnetic relaxation so that the magnetic moment reduces to 3.40 μB. Panel 3.5(a) shows the band structures for spin-up and spin-down in blue and red colors, respectively. Just below Fermi level ($E_F = 0$, which was taken as an energy reference), 1 spin-up and 3 spin-down bands are mainly introduced by Mn atom as to be confirmed by PDOS and ODOS in Panel 3.5(b) and 3.5(c). The flat bands in the group at about 1.2 eV below Fermi level are mainly due to the p_x, p_y on C and N atoms after sp^2 (planar) hybridization whereas p_z orbitals of both C and N atoms as well as d_{yz}, d_{zx} and d_{z2} orbitals of Mn atom keep contributing to the construction of CB.

The asymmetry between bands and PDOS of spin-up and spin-down states reveal the existence of magnetic moment in the system. Mn atom can induce magnetization into the atoms after the orbital overlapping. For instance, the ODOS of hydrogen atoms can clearly show contributions to all the total DOS structure because of orbital overlapping.

(b) Dimer atom catalyst (Mn$_2$@C$_2$N)
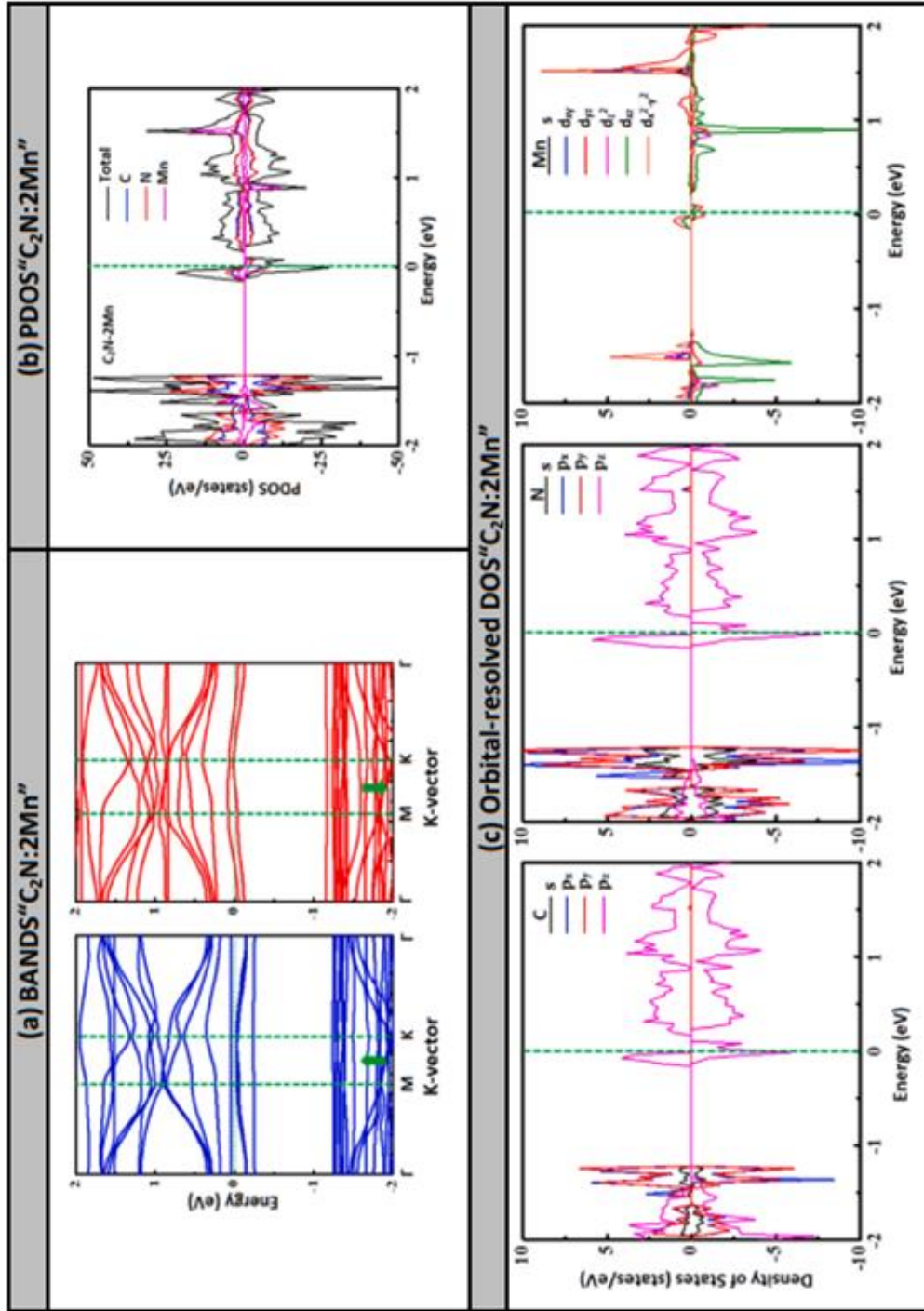
Figure 3.6: Bands (a), PDOS (b) and ODOS (c) of system C$_2$N:2Mn.

Figure 3.6 shows the electronic structure in the case of dimer Mn-Mn embedded in the pore of C$_2$N after achieving full atomic relaxation. Here, like in Figure 3.4, the embedment of the dimer Mn$_2$ in the pore of C$_2$N drastically changes the properties from semiconducting to metallic. The asymmetry between bands and PDOS of spin-up and spin-down states reveal the existence of magnetic moment in the system Mn$_2$@C$_2$N. As

we described before, we should mention again here that the hybridization sp^2 taking place in the C and N atoms involves p_x, p_y and s orbitals.

These latter states are the main contributors to the structure of VB. On the other hand, the delocalized states, p_z of C and N atoms, as well as d_{yz}, d_{zx} and d_{z2} orbitals of Mn atom do contribute to the structure of CB. In contrast to SAC, in case of DAC the ODOS of Mn shows a difference between spin-up and spin-down states but less pronounced than the case of SAC.

This would corroborate the reduction of magnetic moment to a value 2.42 μ_B. More importantly, by looking at panel 3.6(b) (Plot of PDOS), one can notice that the spin-up PDOS is showing a semiconducting behavior whereas the spin-down PDOS is showing a metallic behavior. Such characteristics are usually associated with "Half-metal". Hence, the system C_2N:2Mn has characteristics of half metal. Next, we are going to see the effect of chemisorption of H_2 molecule on such characteristics, which gets affected and will have a sound impact on the sensor response.
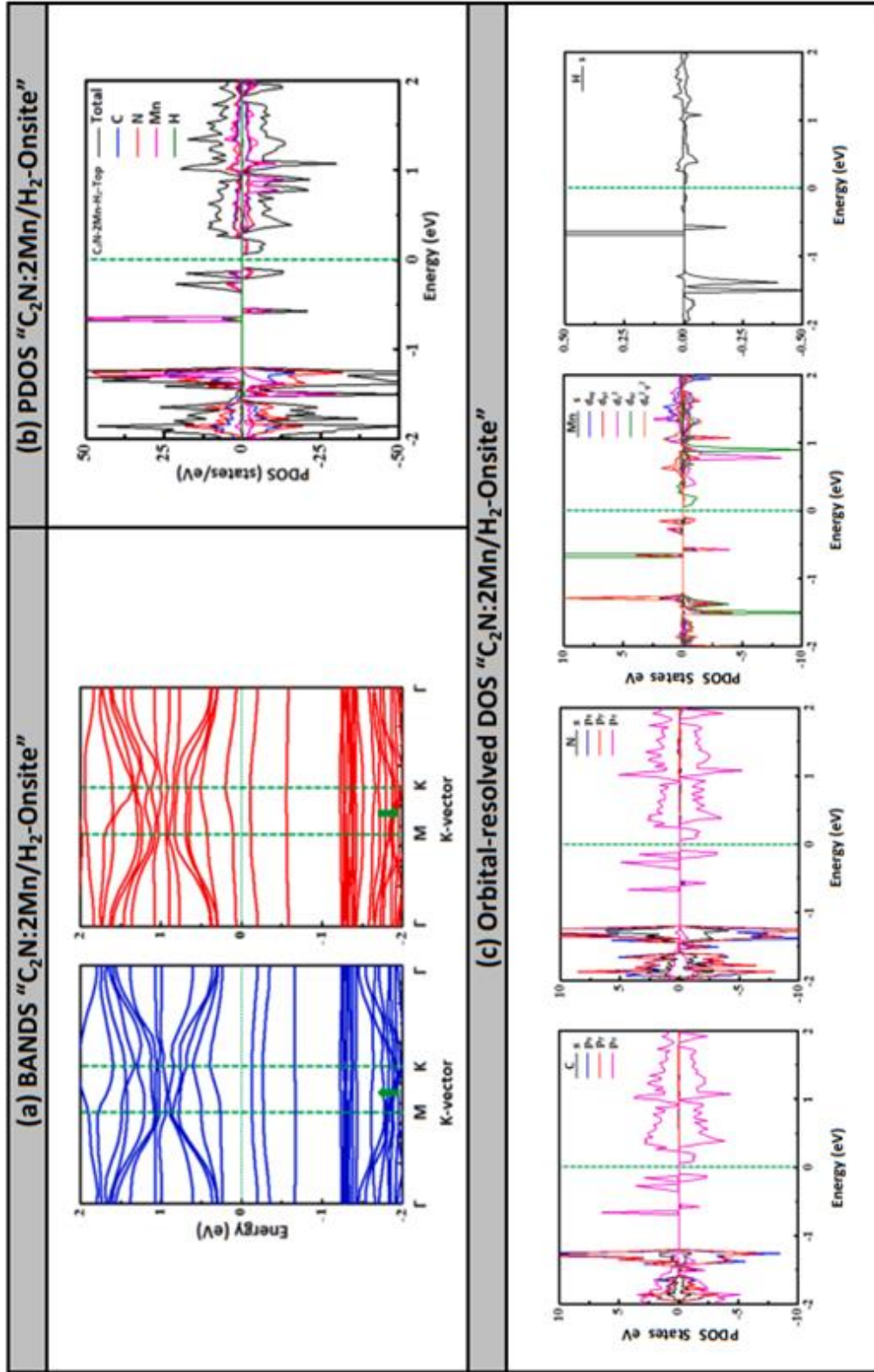
Figure 3.7: Bands (a) PDOS (b) ODOS (c) of system $C_2N:2Mn/H_2$ after chemisorption of H_2 molecule above DAC (onsite).

Figure 3.7 shows the electronic structure of the system $C_2N:2Mn/H_2$-onsite. We have attempted two ways of relaxing H_2 molecule on DAC. (i) The relaxation of H_2 started from

onsite one of the two Mn atoms; and (ii) The relaxation of H_2 started from just above midway between 2Mn atoms. Figure 3.7 shows the results of band-structures due to the relaxed structure of case (i); whereas Figure 3.8 shows the results of band structures due to the relaxed structure of case (ii). Both cases show opening of band gap at Fermi level. However, the gap in Figure 3.7 is larger than the one in Figure 3.8 (i.e., $E_g = 0.20$ eV and 0.06 eV, respectively). Panels 3.7(a) and 3.8(a) show non-identical bands revealing the existence of magnetic moments in both systems (i) and (ii). One more common trend between these two systems is that the total DOS has contributions from all the four atoms (i.e., C, N, Mn, and H atoms) revealing the occurrence of covalent bonding between the dimer Mn_2 and C_2N as well as H-atoms and Mn-dimer. Due to the occurrence of chemisorption with H_2, both systems get magnetic relaxation so that their magnetic moments get drastically reduced to same value 1.97 µB. Now, focusing on Figure 3.7, just below Fermi level, in panel 3.7(a), there are 5 localized states (i.e., 3 spin-up + 2 spin-down states). The lowest one among these five gap states (spin-up state) is very flat/localized and is attributed to Mn atomic orbitals. Furthermore, the huge reduction in magnetic moment is corroborated by the ODOS shown in panels 3.7(b) and 3.8(b) where the conduction band turned to have about equal contributions from spin-up and spin-down states.

66
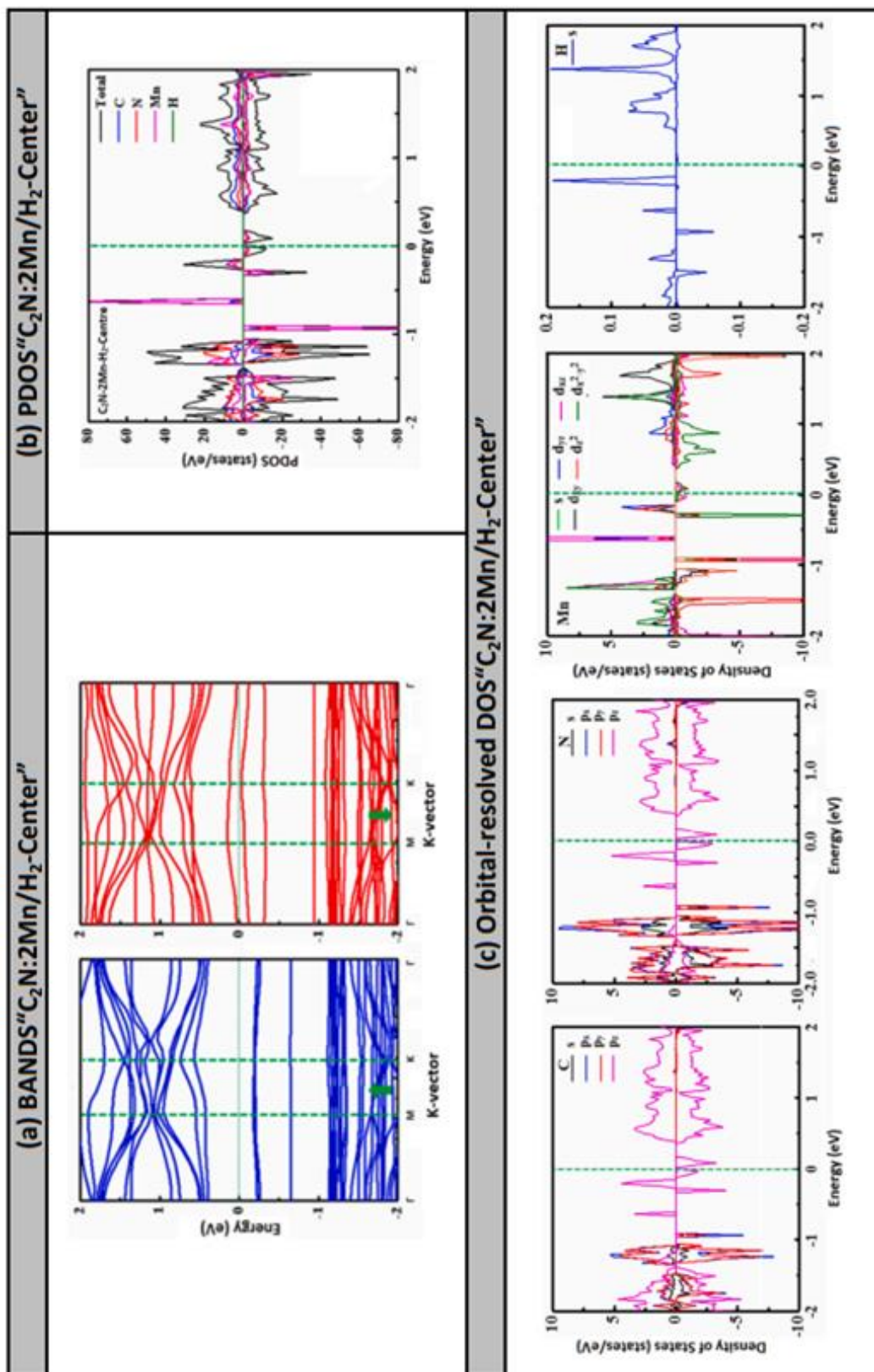
Figure 3.8: Bands (a), PDOS (b) and ODOS (c) of system $C_2N:2Mn/H_2$ after chemisorption of H_2 molecule DAC (center).

Chapter 4: Relevance of Metal Embedded C$_2$N for Energy Storage Applications

4.1 Summary

In this Chapter the suitability of embedding metal atoms (Ca versus Mn) in the pores of C$_2$N to be employed as the anode material for metal-ion battery applications is studied using density functional theory. The effect of single-atom catalyst (SAC) versus dimer-atom catalyst (DAC) on the uptake catalyst capacity is put under focus. Our results show that both metal atoms exhibit very strong interactions with the pyridinic-nitrogen pore and show the ability of the pore to accommodate either a single Ca atom or a dimer of Mn atoms within its membrane-plane. While the theoretical irreducible capacitance in case of SAC Ca catalyst is limited to about 200 mAhg^{-1}, it can exceed this value in case of DAC-Mn catalyst to reach 1110 mAhg^{-1}. Regarding the adsorption, the H$_2$ molecule exhibits strong physisorption on Ca-catalyst and moderate chemisorption on Mn-catalyst, with an adsorption energy increasing from SAC to DAC cases. The SAC of Mn is found not only concurrent candidate to Ca for energy-storage applications but further promising for platform of reusable hydrogen gas-sensors with very low recovery time (i.e., t « 1 s). Our findings are in good agreement with the available experimental data and theoretical results.

Redrafted from

4.2 Introduction

The breakthrough discovery of graphene in 2004 by Geim and Novoselov [1] not only earned them the Noble prize in physics in 2010 but opened a completely new research field on 2D systems with extraordinary properties. Graphene comprises of one atom-thick monolayer of carbon atoms in honeycomb structure with extremely high thermodynamic stability. Another prominent feature of graphene is the presence of Dirac cone where the two bands linearly cross each other at K-corner in the Brillouin zone resulting in exceptionally high mobility (m ~ $2x10^5$ cm^2/Vs) much exceeding the one of GaAs. Such high speeds of ballistic electrons at the Fermi level, in turn, have opened a new dialogue arena between solid-state physics and high-energy physics. Therefore, graphene has an immense potential for developing novel electronic devices with ultrafast response. In the field of gas-sensing, it has achieved the sensitivity to detect a single-gas molecule [1]. The selectivity of graphene-based gas sensors can be improved by chemical functionalization [3-6]. More recently, in 2015, another interesting and thermodynamically stable material based on nitrogenated holey graphene "C_2N" was successfully synthesized by Mahmood and coworkers, via a bottom-up wet-chemical reaction [12]. The periodic distribution of uniform holes makes this material advantageous for several applications such as gas sensing and filtration. Contrary to graphene, the presence of holes and phenyl rings surrounded by aromatic nitrogen atoms creates a finite band gap (Eg ≈ 1.90 eV) which makes this material also suitable for semiconducting applications [12-14]. The functionalization of holey graphene C_2N further advances this material for both selective gas-sensing and energy-storage applications [15-16, 144]. In addition, single- and multi-layered C_2N have potential as anode material for both Lithium-ion Batteries (LIBs) and Sodium-ion Batteries (SIBs) as revealed in recent experiments [15-16, 124].

From perspective of energy-storage applications, light metal atoms (e.g., Li, Na, K, Ca) can be embedded in holes or intercalated between layers of C_2N for hydrogen adsorption. Such light atoms would be able to balance the two key aspects required for practical applications, such as: (i) to have a binding energies greater than the cohesive energies so that the clustering effect is minimal and the atoms can be uniformly distributed over the holes of the layer; and (ii) to adsorb hydrogen molecules on the periphery of the sheet

with an energy that is between strong physisorption and weak chemisorption (i.e., within the range [0.2, 0.6] eV), which is recommended by the International Atomic Energy Agency (IAEA). Incidentally, C_2N can be a strong potential candidate for anode in both SIBs and Calcium-ion Batteries (CIBs) to overcome the long-standing problem of formation of dendrites existing in LIBs. Meanwhile, C_2N would pave the way for fabrication of low-dimensional batteries for utilization in portable electronic devices [7, 35-37]. On the experimental side, single- and multi-layered C_2N have been demonstrated to be promising anode materials for both LIBs and SIBs [15, 124]. Successful experiments aimed at homogeneously embedding Transition-Metal (TM) atoms in the C_2N-pores while fully overcoming the problem of metal clustering have been achieved by Huang and co-workers (i.e., M@C_2N using M = Ru, Pd and Co atoms) [16]. The synthesis was based upon the bottom-up wet-chemical route to achieve the metal catalysts being homogenously embedded in the 2D C_2N network; method was developed from their original growth technique [12]. The morphologies of the M@C_2N (M = Ru, Pd and Co) were characterized using X-Ray diffraction (XRD), Scanning Electron Microscopy (SEM) and Transmission Electron Microscopy (TEM) [16]. Benefiting from their unique structural features (e.g., uniform 2D nanohole distribution, high surface area and enlarged distance between C_2N layers), the M@C_2N electrodes display outstanding lithium storage properties and yield high performance of LIBs [16] (i.e., high specific capacities were achieved: 1104, 1168 and 789 mA h g^{-1} for M = Ru, Pd and Co, respectively) [16]. Incidentally, recent DFT calculations on the same system presented by Liang and coworkers [27] have confirmed the thermodynamic stability of these M@C_2N structures and further shown the catalytic activity towards the Oxygen Reduction Reaction (ORR). Furthermore, the downsizing of these metal nanostructures to singly dispersed metal atoms would be highly desirable for maximizing the efficiency of catalytically active metal sites [27-28, 145-146]. The Single Atom Catalyst (SAC) and Double Atom Catalyst (DAC) nanostructures have been experimentally achieved in metal oxides and in C_2N and shown very enhanced catalytic activity towards several toxic-gas reduction reactions (e.g., CO_x, NO_x and SO_x) of environmental concerns [146-149]. The SAC and DAC were further utilized in enhancing the uptake capacity and in improving the performance of metal-ion batteries [16, 150, 151]. The successful

70

syntheses of SAC and DAC in C_2N also inspired and triggered many theoretical efforts to study the corresponding reaction mechanisms [24, 26, 152]. Furthermore, holey graphene has unique characteristics to make itself suitable for a broad range of applications, including electrical-energy storage (e.g., super-capacitors, LIBs and SIBs), energy conversion (e.g., water splitting in hydrogen production and dye-sensitized solar cells), water desalination, fuel cells, gas sensors, and hydrogen storage [13]. Peculiarity in utilizing light-atoms such as Calcium in gas sensing applications can also happen [154]. Liu and coworkers reported some superiority of $Ca@C_2N$ over TM-atom doping (e.g., Sc, Ti, V, Cr, Mn, Fe, Co) for an efficient and reversible capture of CO_2 gas molecules [154]. A review article on recent achievements in synthesis and functionalization of 2D holey graphene and 3D porous graphene has been reported by Zhang and coworkers [14]. Furthermore, holey graphene demonstrated diversity of applications in the fields of electrochemical sensing, electro-catalysis and electrochemical energy storage [14], hydrogen and solar energy storage [155-158], optical-data storage [159], and gas-sensing [154]. On the computational side, Density Functional Theory (DFT) has always been the most reliable technique to explore the potential of the material for both gas-sensing and energy-storage purposes [160]. Its strength stems from its success in describing the ground-state properties of complex structures. Perhaps the most popular package for using DFT is "Vienna Ab-initio Simulation Package" (VASP) [53]. On one hand, light metal atoms (e.g., Li, K, Na, and Ca) have been shown to bear great potential for energy storage applications, as they yield great balance between adsorption and desorption of hydrogen. For instance, Wu and coworkers proposed $Na@C_2N$ to be used as anode in SIBs [124, 125], and Hussain and coworkers showed the enhancement in uptake capacity by using light-atom catalysts (e.g., Li, Na, and Ca) in C_2N [161]. On the other hand, TM atoms have been shown to possess the ability to act as catalyst in enhancing both the uptake capacity of light-atoms for better performance of batteries [162] and efficiently capturing gas molecules [126-128, 163-164]. TM atom has been proposed as efficient SACs and DACs for reduction reactions of CO and CO_2. For instance, Ma and coworkers studied TM atoms embedded in C_2N monolayer of different valency/ electronegativity (e.g., Sc, Ti, V. Cr, and Mn) as SACs. They concluded that Cr and Mn to be very promising for low temperature CO

oxidation reaction [127]. Some theoretical work went beyond studying the materials'
properties of electrodes and further addressed the issue of electrode/electrolyte charge
exchange, using sophisticated DFT methods, such as quantum-mechanical molecular
dynamics (e.g., "Car-Parrinello Molecular Dynamics" (CPMD)) [165]. For instance,
Mukherjee and coworkers showed a dramatic improvement in the performance of
graphene-based LIB/SIB when suitable electrolytic solvents were used [166]. Pham,
further, used CPMD to study liquid electrolytes for energy conversion and storage,
including aqueous solutions, organic electrolytes, and ionic liquids [167]. Last but not
the least, combined experimental and computational efforts were focused by many
researchers to study the kinetic mechanism for reduction reactions and
hydrogenation/dehydrogenation reactions using metal catalysts aiming for both
environmental and energy-storage applications [128, 167-170]. The results of many of
these studies were in favor of manganese "Mn" as a strong catalyst candidate for oxygen
reduction reaction (ORR) [129, 169], CO reduction reaction [127, 130] and CO_2
reduction reaction [128]. While magnesium "Mg" has experimentally demonstrated its
suitability for application as hydrogen-storage material [167-170], our present work
focuses on testing the suitability of manganese "Mn" for the similar task. The scope of
the present investigation is to use DFT to study the effect of metal catalyst(s) (i.e., Ca
versus Mn), embedded in a pore of C_2N, on the hydrogen adsorption properties at Room
Temperature (RT) with a focus to assess their relevance for energy-storage applications.
Special attention will be given to the effects of magnetism and clustering of catalysts
(i.e., catalysts with/without intrinsic magnetic moment and SAC versus DAC,
respectively) on the energy-storage properties. Our results will show that Calcium would
be more appropriate for the role of catalyst embedded in C_2N for CIBs with enhanced
uptake-capacity with increasing clustering. Whereas Manganese SAC embedded in C_2N
will be shown not only to be concurrent candidate to Ca for energy-storage applications,
but further to be useful as platform for reusable hydrogen gas-sensor at room
temperature with fast recovery time (i.e., t « 1 s). The Chapter is organized as follows.
Details of the computational methods will be presented in section 4.3. The results will be
discussed in section 4.4. The concluding section will summarize our main findings and
future outlooks.

4.3 Computational Method

In our present investigation, spin polarized DFT methods are used for atomic relaxation and calculations of electronic properties. The "Spanish Initiative for Electronic Simulations with Thousands of Atoms" (SIESTA) code [54,55], which is incorporated within the Atomistic Toolkit (ATK) package, was mostly used in the calculations as the code possesses the ability to carry on calculations at Room Temperature (RT). VASP [53, 172] was used for benchmarking the cohesive, binding and adsorption energies, as it is dependable, but it deals only with a frozen lattice (0 K) under the assumption of validity of Born-Oppenheimer approximations. The primitive cell of C_2N consists of 18 atoms (i.e., 12C + 6 N atoms), so a supercell of size 2x2 primitive cells would have 72 atoms (excluding the metal catalyst atoms and molecule), on which periodic boundary conditions are applied along the plane of C_2N monolayer (i.e., x and y directions). Within the framework of SIESTA, the atomic orbitals are expanded in plane-wave basis set within an energy cut-off E_{cut} = 2585 eV. For the exchange-correlation functional, we used the Generalized Gradient Approximation (GGA), parametrized by Perdew-Burke-Ernzerhof (PBE) [173]. All atoms were allowed to relax until Hellmann Feynman forces on all atoms and the total energy becomes less than 0.05 eV/A and 0.1 meV, respectively. The pressure tolerance is set to be 0.1 GPa. For Brillouin-zone sampling, we used the Monkhorst-Pack (MP) technique [56]. A grid of K-mesh = 3x3x1 is used for DFT iterations for atomic relaxations and a finer grid of K-mesh = 7x7x1 was used for the Density of States (DOS) calculations. In SIESTA, calculations take place at RT with smearing or thermal broadening of 0.05 eV. To take account of van der Waals long-range interactions, the DFT-D3 method of Grimme has been incorporated [57]. This interaction is crucially important especially in cases of occurrence of physisorption processes. A vacuum space of about 15 Å is applied in the direction perpendicular to C_2N monolayer (i.e., z-direction) to warrant the isolation of C_2N monolayer and avoid its interactions with images. The charge exchange between gas molecule(s) and doped C_2N monolayer is estimated by means of Bader-charge analysis [58]. For the estimation of the cohesive energy of metal catalyst, we use the total energy calculations of bulk and free metal atom. In solid-state structure, Ca crystallizes in face-centered cubic (i.e., named alpha phase) with 1 atom per basis; whereas Mn crystallizes in body-centered

cubic (i.e., named alpha phase) with complex structure having 19 atoms per basis. So, the cohesive energy is defined as

$$E_{coh} = \frac{E_{tot}(bulk) - N_b E_{tot}(MA)}{N_b} \qquad (4.1)$$

Where N_b is the number of atoms per basis, $E_{tot}(bulk)$ and $E_{tot}(MA)$ are total energies of bulk and single free metal atom, respectively. The results of our calculations of cohesive energies are summarized in Table 4.1. The binding energy of the metal catalyst (e.g., take the case of SAC) embedded in pristine C_2N is evaluated as

$$E_{bind} = E_{C2N-MA} - E_{C2N} - E_{MA} \qquad (4.2)$$

where E_{C2N-MA}, E_{C2N} and E_{MA} stand for the total energy of the system of metal catalyst embedded in pristine C_2N monolayer, pristine C_2N monolayer and free metal atom.

Furthermore, one also can define the recursive binding energy, E_{rec} for the metal catalyst atom as to be the binding energy of the last metal atom to bind to the substrate. It is defined as

$$E_{rec} = E_{(MA_n@Mater)} - E_{(MA_{n-1}@Mater)} - E_{(MA)} \qquad (4.3)$$

where $E_{(MA_n@Mater)}$, $E_{(MA_{n-1}@Mater)}$ and $E_{(MA)}$ stand for total energies of metal atoms in the material after and before adding the n-th atom and single-free atom. In case $|E_{rec}| > |E_{coh}|$ then the metal atom is more stable by its attachment to the substrate; otherwise, if $|E_{rec}| \leq |E_{coh}|$, then the new metal atom has more tendency to cluster with its peers. In the present work, as a reliable reference to judge upon the binding energies, we used the experimental cohesive energies for Ca and Mn to be 1.84 eV and 2.92 eV, respectively [140]. The adsorption energy of the H_2 gas molecule on the substrate is defined as

$$E_{ads} = E_{C2N-gas} - E_{C2N} - E_{gas} \qquad (4.4)$$

where, $E_{C2N-gas}$, E_{C2N} and E_{gas} are total energies of gas molecule adsorbed on functionalized C_2N, functionalized C_2N and free single molecule, respectively. The more negative the adsorption energy (E_{ads}) indicates the stronger the interaction between the molecule and adsorbate. Usually, chemisorption occurs if $|E_{ads}| > 0.5$ eV and

physisorption if 0.5 eV > $|E_{ads}| > 0$. Obviously, the molecule remains free if $|E_{ads}| \geq 0$ (i.e., is positive).

The theoretical specific capacity of an electrode can be calculated using the formula:

$$C = \frac{n_e n_{MA} F}{3.6(n_{MA} m_{MA} + n_N m_N + n_C m_C)} \tag{4.5}$$

where F is Faraday's constant (F= 96486.7 As); m_{MA}, m_N and m_C are the atomic masses of the metal (Ca or Mn), nitrogen (N) and carbon (C) atoms in g/mol; n_{MA} is the number of metal atoms strongly bound to the substrate; n_N and n_C are the numbers of N and C atoms in the supercell (e.g., in our current case: n_N= 24 and n_C= 48); ne is the number of valence electrons (e.g., n_e = 2 for Ca and n_e= 2 - 7 for Mn atoms). The factor 3.6 put in denominator is used to express the units of specific capacity in mAh/g.

As was shown by Mahmood et al. [12], pristine C_2N with uniform distribution of nanopores can be synthesized using wet-chemical reaction between hexaminobenzene trihydrochloride and hexaketocyclohexane octahydrate in N-methyl-2-pyrrolidone in the presence of sulphuric acid. Huang et al. have presented an experimental protocol for creating C_2N material doped with different metal atoms such as Ru, Pd and Co using similar solution-processing methods [16]. We assume that the here studied C_2N monolayers with embedded Ca and Mn atoms can be created using the same synthesis technique presented in Ref. [16].

Table 4.1: Calculated cohesive energies(in eV) of Ca and Mn are compared to experimental data.

Cohesive Energy (eV)	
Ca	Mn
−1.905[a], −1.891[b], −2.102[c], −1.84[d]	−3.874[a], −3.73[b], −2.90[e]-2.92[d]
[a] Present work (VASP with GGA-PBE). [b] Present work (VASP with Full Potential). [c] Present work (SIESTA with GGA-PBE).	

4.4 Results and Discussions

4.4.1 Electronic Properties of Pristine C_2N

The supercell to be used in our adsorption study consists of 2x2 primitive cells of C_2N (i.e., it is composed of 72 atoms = 48 C + 24 N atoms). The fully optimized structure of our model system is shown in Figure 4.1(a). The obtained bond lengths are $b_{(C-C)}$ = 1.43-1.48 Å and $b_{(C-N)}$=1.34 Å, which are in good agreement with those reported in the original experimental work of Mahmood and coworkers [12].
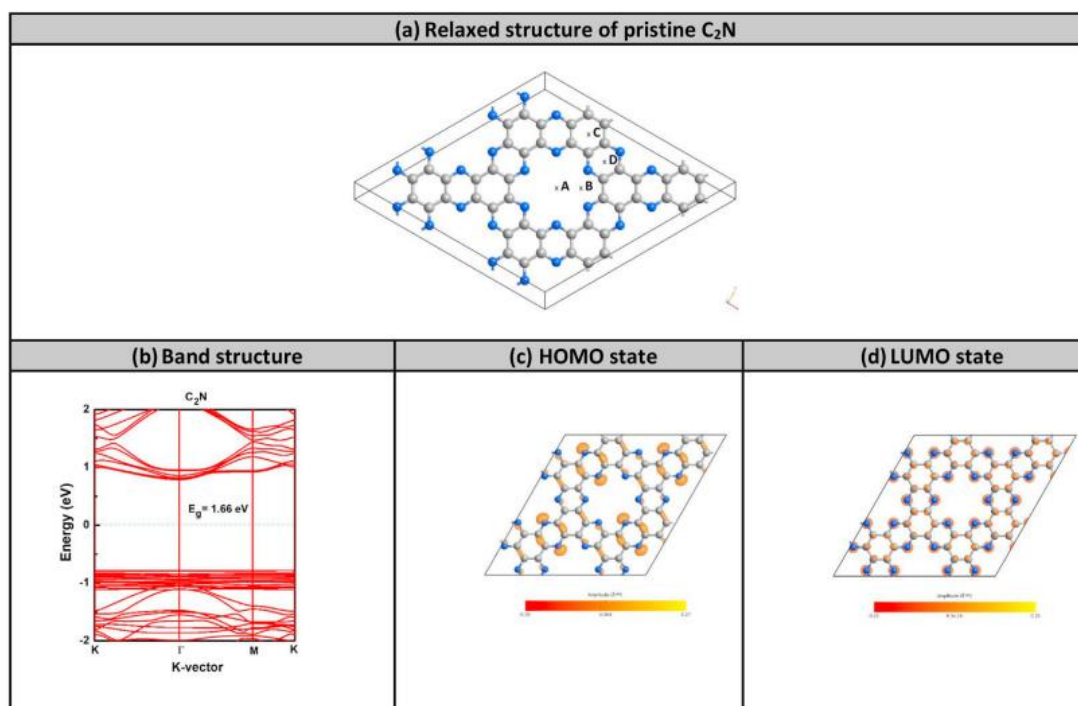
Figure 4.1: Pristine C_2N sample of size 2x2 primitive cells (a) Periodic 2D supercell; (b) Band structure; (c) HOMO and (d) LUMO states.

These results are also in good agreement with many others appeared in literature; for instance, DFT calculations of Yong and coworkers [142] reported the bond-lengths $b_{(C-C)}$ = 1.430 - 1.469 Å and $b_{(C-N)}$ = 1.336 Å. Our optimized lattice constant of primitive cell is a = b = 8.34 Å, which is also in good agreement with the experimental value of 8.30 Å [12] and with results of other DFT methods, such as Liu and coworkers who reported 8.33 Å [154].

Figure 4.1(b) shows the calculated band structure of our reference system (Figure 4.1(a)). The band structure shows too many flat valence-bands attributed to the nitrogen

saturated dangling bonds and dispersive conduction bands due to delocalized states of Bloch-like wave-functions attributed to the C-C and C-N bonds. The band-gap energy E_g=1.66 eV is similar to the one obtained by Liu et al. [154] and is a bit smaller than the experimental value of 1.90 eV reported by Mahmood et al. [12]. This discrepancy is due to the underestimation of DFT-GGA of band-gap energy of semiconductors, unless hybrid functionals are employed. Yet, the obtained results are satisfactory as far as the study of adsorption properties is concerned. Figure 4.1(c) and (d) display the highest occupied molecular orbital (HOMO) and the lowest unoccupied molecular orbital (LUMO) states corresponding to pristine C_2N structure displayed in Figure 4.1(a). The HOMO state clearly indicates the curdling of the valence-band (VB) edge state at both nitrogen atoms and C-C bonds. These are the origins of the flat bands existing at the VB edge. Whereas the LUMO states are clearly delocalized and almost uniformly distributed over all C and N sites, as shown in Figure 4.1(d). Therefore, the conduction-band (CB) edge states are dispersive corroborating the behavior of delocalized nature of the LUMO state.

4.4.2 Catalyst Stability and Irreversible Capacity

To test the suitability of a type of metal catalyst for either gas sensing or battery applications, it is important first to assess its tendency to clustering then subsequently test the uptake capacity whether reversible or irreversible. For such task we used VASP to calculate the binding energy of SAC and DAC of both Calcium (Ca) and Manganese (Mn) embedded in the pore of C_2N. One should recall that Ca and Mn atoms to be our candidates because they have high potential electric and magnetic properties that can be explored in at least one of these two applications (i.e., either gas-sensing or energy storage application). In our strategy, for the assessment of stability of SAC, we carried out relaxations starting from 4 different initial positions, as shown in Figure 4.1(a). Whereas, for the stability of DAC, we used 3 initial configurations as candidates leading to the most stable structure. Figure 4.2 shows the relaxed atomic structures of SAC for both (a) Ca and (b) Mn atoms, respectively. Top and side views together with binding energy are shown in each panel for comparison. The four initial positions used in our testing are shown in Figure 4.1(a) (with letters A, B, C, and D). Position A is located at the center of the pyridinic-nitrogen pore, position B is midway between pore center and

C-C bond located at the edge of the pore, position C is at the center of C_6 hexagon, and position D is at the center of C_4N_2 hexagon (Figure 4.1(a)). In the first two relaxations, the SAC-atom was started from the exact positions A and B, respectively. Whereas, in the last two relaxations, the SAC-atom was started from above the respective positions C and D. The most stable configurations achieved after relaxations for both Ca and Mn are shown in Figures 4.2(a) and (b), respectively (see the binding energy values in respective panels).

The interactions of the SAC-atom on the C_6-hexagon and on the C_4N_2-hexagon are found to be much weaker than its interaction with the pyridinic nitrogen atoms in the pore, as evidenced by their relatively weaker binding energies. So, we will focus on discussing the 2 cases of SAC in the pore. In the case of Ca, it seems that it has tendency to stay at the center of the pore via strong ionic bonding with the nitrogen atoms located at the edge of the pore. Starting the relaxation from either position "A" or position "B" does not matter much as the Ca atom would find its final and most stable equilibrium position to be at the center of the pore. The discrepancy in binding energies between the final states in cases "A" and "B" (i.e., E_{bind}= -6.909 eV and -6.885 eV, respectively) is at the order 24 meV, which might be attributed to the super-cell's primitive-vector relaxations. In any case, the Ca atom prefers to adsorb in the center of the pore and to remain within the membrane plane with binding energy consistent with that reported by Hussain and coworkers -7.04 eV [161]. The barrier for Ca-atom to move out of the pore is higher than 5 eV, so that 1 Ca/pore would contribute to the irreversible uptake capacitance. On the other hand, SAC of Mn atom has tendency to stabilize a bit off the center of the pore (Figures 4.2(b)). In case of starting position from pore center (i.e., position "A"), the final position remained at center with binding energy E_{bind}= - 4.342 eV; whereas in case of starting from position "B", the Mn atom moved from it toward center for a net displacement of about 1.09 Å to stabilize near the pore center but off it by about 0.38 Å and having the strongest binding E_{bind}= -4.497 eV. This latter equilibrium position is in membrane plane and energetically more stable than the center by about 155 meV, in which Mn gets six coordinated with nitrogen atoms. These results are indeed in good agreement with those reported by Ma et al. where E_{bind}= - 4.28 eV and off-center position at the Mn-N distances of about d_{Mn-N} = 2.15-2.78 Å [127]. This equilibrium

78

position of Mn atom is deeper in energy than the center one by about 55 meV and is also consistent with 35 meV of Ma et al [130]. The binding energies of Mn at the locations "C" and "D" are higher than the stable position (i.e., the one at "B") by about 3.966 eV and 3.539 eV, which are consistent with the results of Ma et al. [127] of about 3.99 eV and 3.47 eV, respectively. The diffusion energy barriers of Mn atom to migrate from position "B" to either position "C" or "D" are estimated to be about 4.15 eV and 3.62 eV, respectively [127].
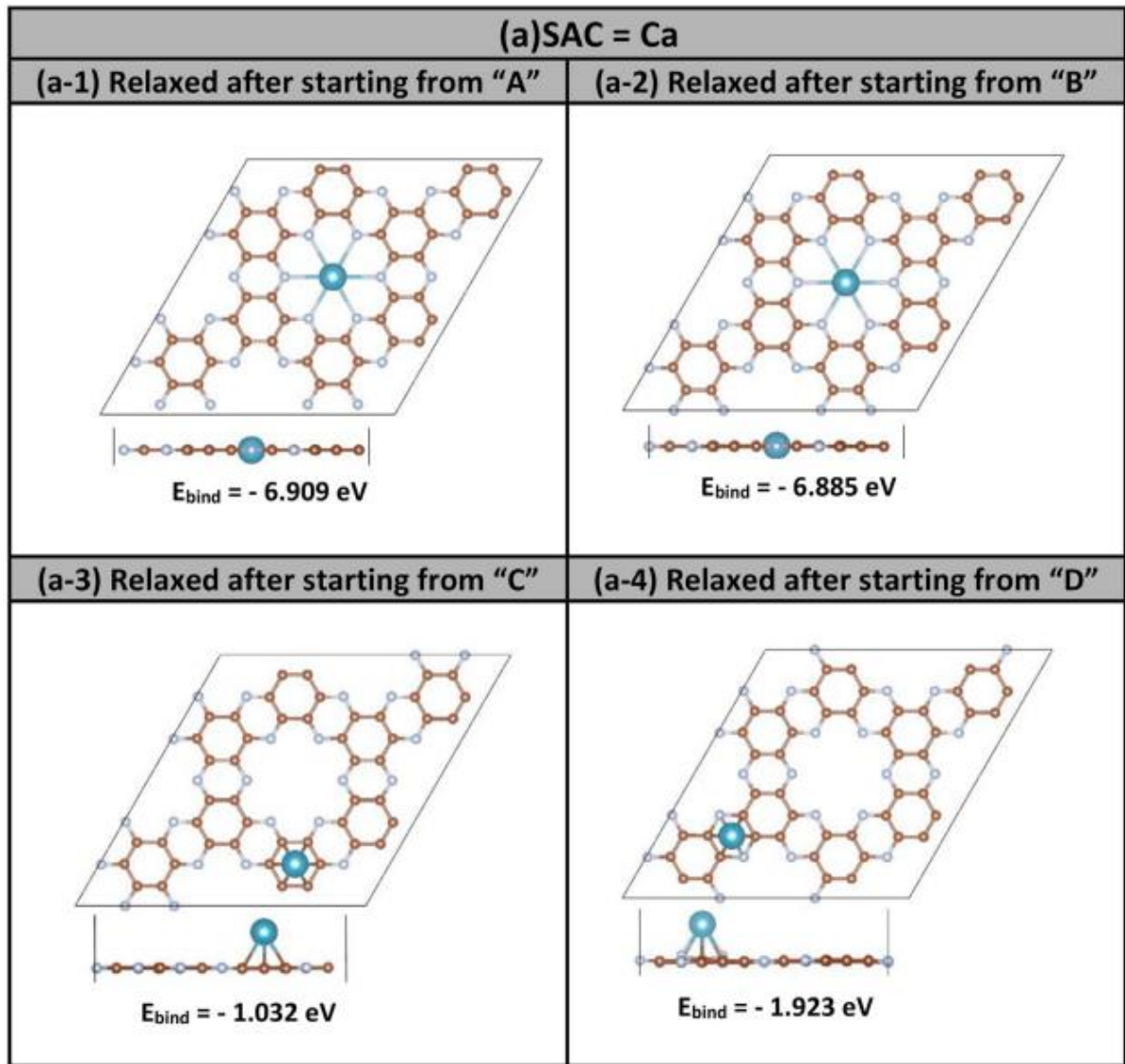
Figure 4.2(a): Relaxed atomic structure of SAC: (a)1Ca@C_2N starting from 4 different initial positions.
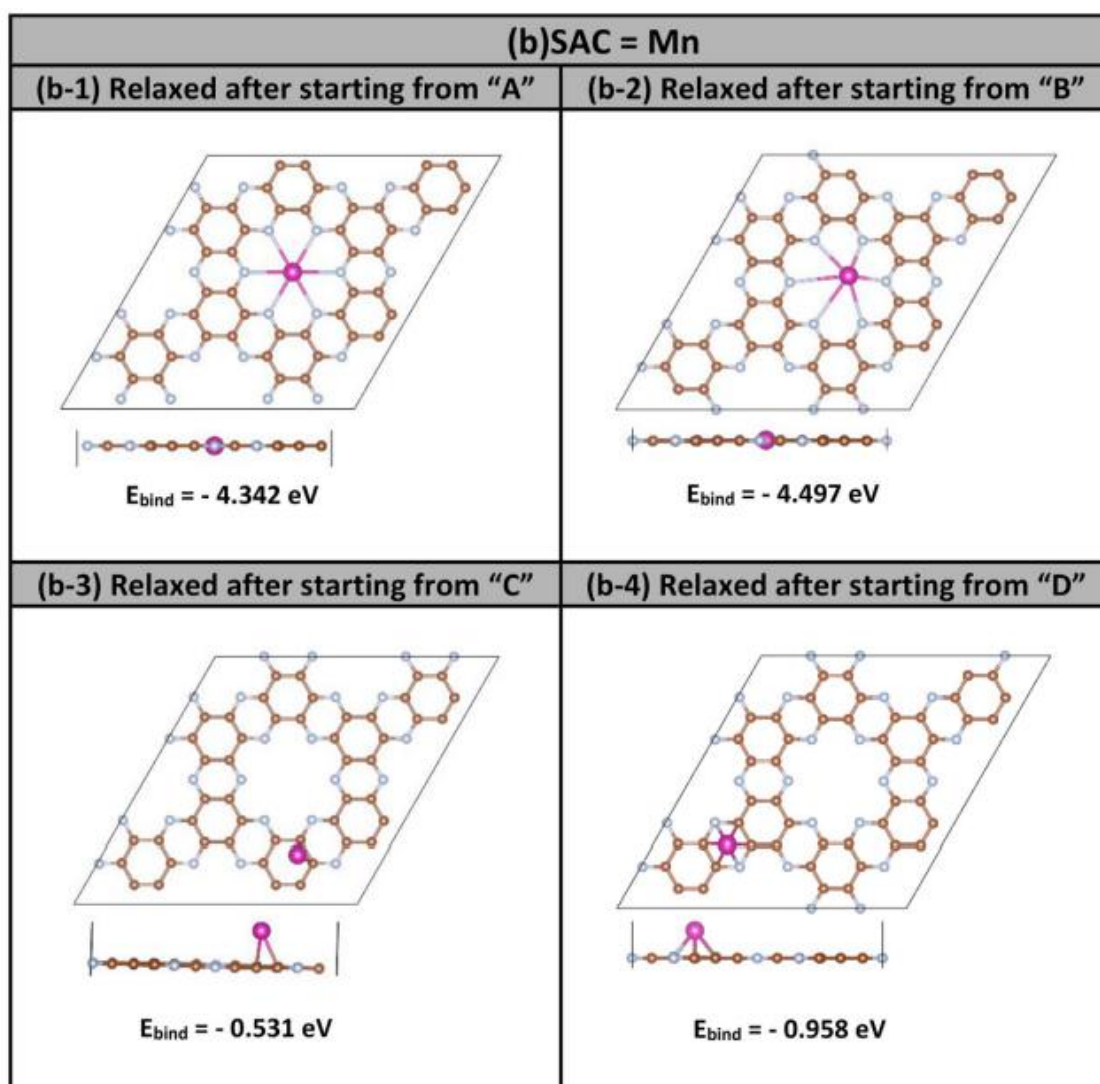
Figure 4.2(b): Relaxed atomic structure of SAC: (a)1Mn@C$_2$N starting from 4 different initial positions.
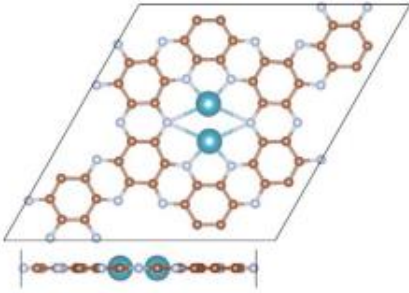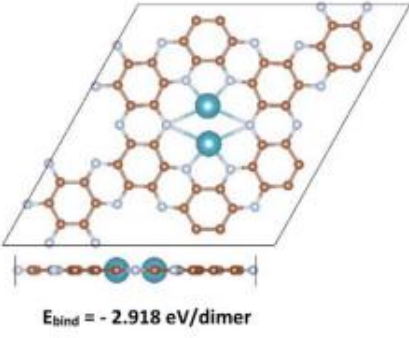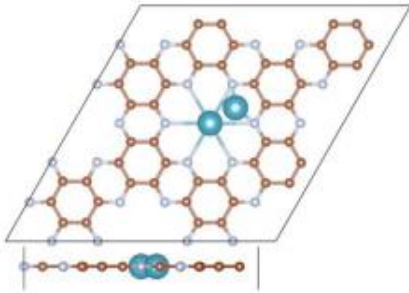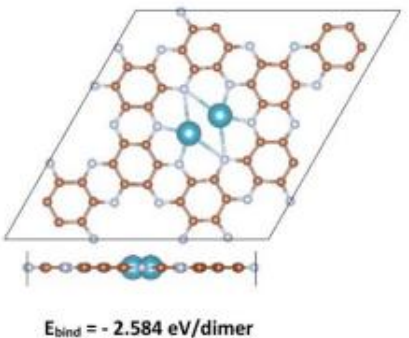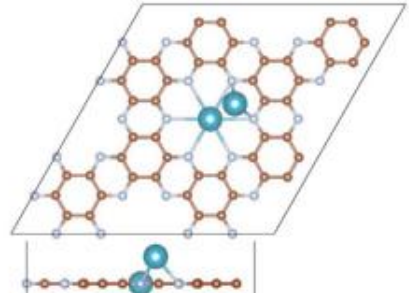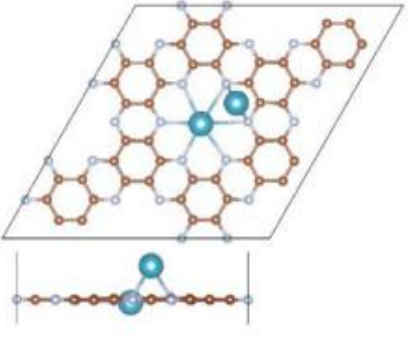
Figure 4.3(a): Initial and final (relaxed) structure of DAC: (a)Ca$_2$@C$_2$N starting for three different configurations.
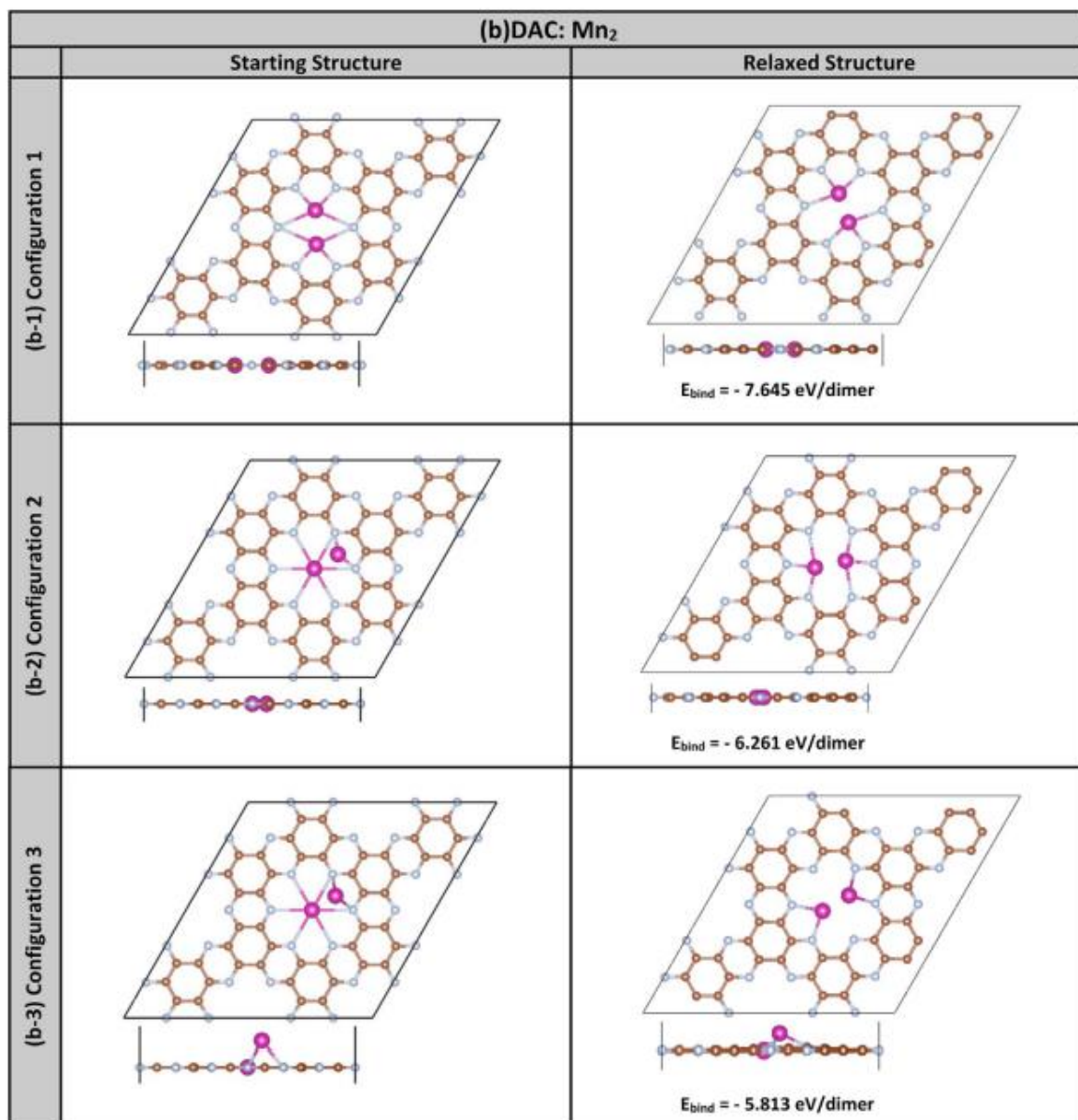
Figure 4.3(b): Initial and final(relaxed) structure of DAC: (a)Mn_2@C_2N starting for three different configurations.

Concerning the case of DAC of both of Ca_2 and Mn_2, we have considered three possible scenarios using three different initial configurations:

- The dimer was initially symmetrically embedded in the pore of C_2N as one body in a similar fashion to the work reported on copper dimer (Cu_2) embedded in C_2N used for the capturing of CO_2 molecule, reported by Zhao et al. [126]. In the other remaining two scenarios, one atom of the catalyst dimer was put at the center of the pore and the second atom was as follows:

- The second atom of dimer was midway between the pore center and C-C bond at the pore edge.

- The second atom of dimer was elevated (like buckled) up the membrane plane from the previous 2nd atom position. Then, the atoms in the three systems undertook processes of full atomic relaxation.

Figure 4.3 shows the atomic structures of the three systems before and after relaxation for both dimers: (a) Ca_2 and (b) Mn_2. The initial dimer bond-lengths were 2.28 Å, 1.84 Å, and 2.49 Å for the three systems, respectively. After relaxation, the new bond lengths became for Ca_2 to be 2.29 Å, 2.25 Å, 3.41 Å and for Mn_2 to be 2.02 Å, 2.07 Å and 2.31 Å, respectively. The most stable dimer for Ca_2 corresponds to configuration #3 with binding energy E_{bind} =-7.180 eV/dimer. In this situation, one Ca atom was found to occupy the center of the pore and the second atom is buckled off the membrane plane along the direction center to C-C bond at the edge of the pore. This is consistent with what was reported by Hussain and coworkers [161].

While the Ca-atom at the center is strongly bound, as described in Figure 4.2(a), the second atom seems to be much weakly bounded and can be mobile to jump, for instance to likely site "D" with diffusion barrier reduced to about 0.2 eV [161]. So basically, only 1 Ca atom can contribute to the irreversible capacitance yielding a capacity of about 200 mAhg^{-1} [161]. On the other hand, DAC of Mn_2 would find its most stable equilibrium state after the relaxation using configuration #1. In such stability, both Mn atoms occupy positions inside the pore at the membrane plane like the case of copper dimer reported by Zhao and coworkers [126]. One should emphasize that configuration #2 would yield a similar relaxed structure to the one obtained in configuration #1 but with less binding energy in magnitude (i.e., $|E_{bind}^{conf2}|$ = -6.261 eV $<$ $|E_{bind}^{conf1}|$= -7:645 eV). Although each Mn atom looks three-fold coordinated but the supercell in configuration #1 is further relaxed from the perspectives of supercell size and pressure. Furthermore, the bond-length of dimer in configuration #1 is 2.02 Å, which is smaller than that in configuration #2 which is 2.07 Å.

The binding energy of the Mn_2 dimer in the relaxed configuration #1 is E_{bind} (2Mn) = -7.645 eV/dimer. Considering the binding energy of the most stable SAC of Mn shown in

Figure 4. 2(b2) to be E_{bind} (1Mn) = - 4.497 eV, then the binding energy of the second Mn atom or the so-called the recursive energy would be E_{rec} = - 3.148 eV, whose magnitude is larger than the Mn-cohesive energy (i.e., E_{coh} = - 2.92 eV [137]). So, it seems that the Mn DAC can be strongly bound in the pore of C_2N, and this would suggest that our current 2x2 sample can accommodate about 8 Mn atoms all embedded within the membrane plane. Therefore, these strongly anchored Mn atoms would contribute to the irreversible capacitance, which would range from 317 to 1110 mAhg^{-1} depending on the valency of Mn atom, as expected, to be ranging from 2 up to 7, respectively. In case of SAC of Mn, the irreducible capacitance would be less and range from 189 to 663 mAhg^{-1}. So, it becomes obvious that if the clustering can be avoided and the interaction between Mn and H_2 will be found moderate (to be discussed next), then Mn embedded in C_2N should be a good candidate for application as anodes in metal-ion battery application.

4.4.3 Atomic Relaxation for Adsorption

The adsorption of H_2 gas molecule on metal embedded C_2N is studied at RT using 6 different scenarios for the initial state of the molecule on 4 different substrates as follows:

   a) H_2 molecule on top of SAC Ca
   b) H_2 molecule on top site of DAC Ca
   c) H_2 molecule on top of center of DAC Ca
   d) H_2 molecule on top of SAC Mn
   e) H_2 molecule on top site of DAC Mn
   f) H_2 molecule on top of center of DAC Mn.

The results shown in Figure 4.4 are as follows:

   (a) 1Ca@C_2N: Without H_2 molecule, the relaxation of 1 Ca atom inside the pore yielded a stable configuration in which Ca atom occupied the center of the hollow site equidistant to the six N atoms $d_{(N-Ca)}$ = 2.72-2.73 Å (Figure 4.2 (a1)). These values are in good agreement with those 2.72-2.74 Å using DFT reported by Liu et al. [154]. Thereafter, the relaxation of H_2 molecule, which was launched to start

from onsite above Ca atom at about 1.5 Å, yielded H_2 molecule to alter physisorption process in which the molecule stabilizes above Ca atom at about $d_{(Ca-H)} = 2.56$ Å via van der Waals interaction and having a weak adsorption energy of about -0.167 eV. This adsorption value is not too weak but very close to the lower bound of the range of adsorption energies recommended for storage energy application.

(b) $2Ca@C_2N$: Before studying the adsorption of H_2 molecule, the relaxation of a Ca dimer inside the C_2N pore yielded a stable dimer completely buried in-plane level of C_2N (Figure 4.3(a1)). However, the adsorption of H_2 on Ca-dimer triggered the buckling of the Ca-dimer in two different ways. If the H_2 molecule is put initially on one site of Ca, then both Ca atoms would buckle one upper and one downer plane of C_2N. The molecule displaced farther from the original Ca-site at distance of 3.60 Å and got closer to the other Ca atom which buckles in the direction of the molecule. The molecule seemed to stabilize at closer distance to the latter Ca atom at about 2.56 Å. However, if the H_2 molecule is initially put on the center of the Ca-dimer above it by about 1.5 Å, one of Ca atom buckled out of the C_2N plane while the second Ca atom kept stable inside the pore at the same level of C_2N membrane plane. The stable configuration yielded $d_{(Ca-Ca)} = 3.75$ Å and the H_2 molecule to stabilize opposite to the buckled Ca atom and rather close to the Ca in-plane atom at a distance of about 2.56 Å. It is worth mentioning that the relaxation of H_2 molecule when it started from on-site Ca yielded an adsorption energy - 0.482 eV whereas when it started from Center of Ca-dimer the relaxation yielded an adsorption energy - 0.507 eV. So, the latter physisorption is more stable. Moreover, it is worth emphasizing that the adsorption energy of H_2 molecule on $2Ca@C_2N$ is found to be higher than that of H_2 molecule on $1Ca@C_2N$. This should be considered as improvement for battery application from both perspectives of convenient adsorption energy and an indication for enhancement of uptake capacity.

(c) $1Mn@C_2N$: Before involving the H_2 molecule, the relaxation of Mn inside the C_2N pore yielded stable configuration in which Mn atom occupied the center of the hollow site at equidistance from N atoms of about 2.70-2.71 Å (Figure

4.2(b1)). This result is consistent with the DFT findings of Du et al. [175]. Thereafter, the relaxation of H_2 molecule started from onsite Mn atom at above distance of about 1.5 Å to pass through a chemisorption process, associated with weak splitting of H_2 molecule. The interatomic distance $d_{(H-H)} = 0.92$ Å is larger than the hydrogen molecular bond-length $b_{(H-H)} = 0.77$ Å. Yet both the H atoms are found to stabilize attached to the same Mn site at about $d_{(Mn-H)} = 1.60$ Å, which would make the desorption achievable task. The adsorption energy is found to be about -0.474 eV which is moderate and within the range of energy-storage applications. Toward this possibility, the only challenge remains in the side of growth nanotechnology whether to achieve the synthesis of SAC or not.

(d) 2Mn@C_2N: In absence of H_2 molecule, the relaxation of a dimer of Mn atoms inside the C_2N pore yielded stable configuration in which the dimer remains fully buried inside at the same plane of C_2N monolayer (Figure 4.3(b1)). The DAC also persisted in remaining buried in the pore after the adsorption of H_2 molecule because Mn atom possesses high coordination number by having 5 unpaired d-electrons and 2 s-electrons in the outer electronic shells. Thereafter, in case the relaxation of H_2 molecule starting from above the center of Mn-dimer, it yielded chemisorption with strong molecular dissociation, where the two H atoms ended attached to the 2 Mn atoms separately. The adsorption energy is about - 0.552 eV being a bit larger than the previous case of a single Mn-atom embedded in C_2N. However, if the relaxation of H_2 molecule started from the onsite of Mn-atom, then it would also lead to a weak chemisorption, associated with weak dissociation of the molecule. In this latter case, the molecule remains attached to that Mn site at about 1.64 Å and the inter-atomic distance $d_{(H-H)} = 0.92$ Å being higher than the hydrogen bond-length (0.77 Å). The adsorption energy is -0.551 eV, a bit weaker than the case when the molecule started from the center of Mn-dimer. So, the destiny of the H_2 splitting itself to pave each of the H-atoms to form a single bond with an independent Mn-atom of dimer should be considered more likely to occur as is a more stable configuration. Thus, in the case of Mn-dimer, desorption might not be guaranteed. To computationally check on this requires the use of a sophisticated technique like CPMD method.
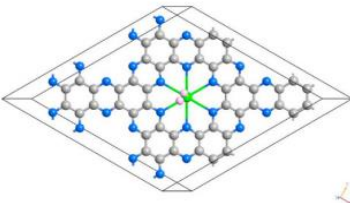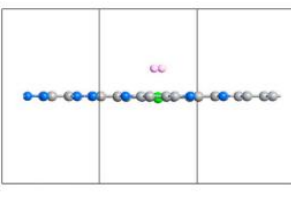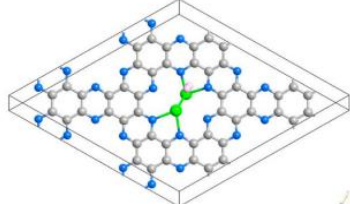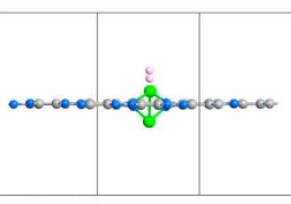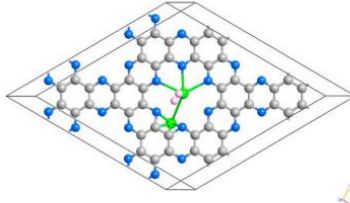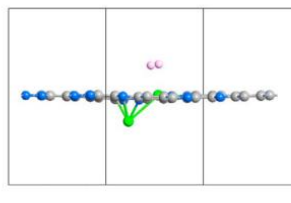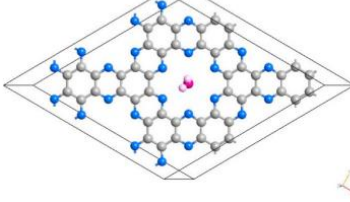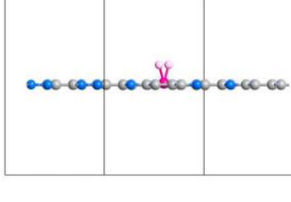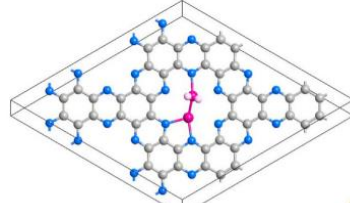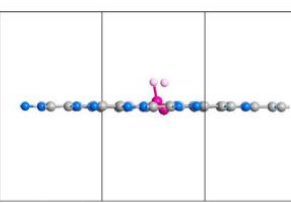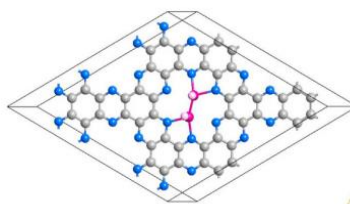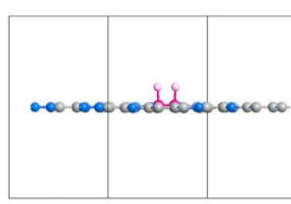
Substrate	Top View	Side View
(a) C$_2$N:1Ca/H$_2$		
(b) C$_2$N:2Ca/H$_2$ Onsite		
(c) C$_2$N:2Ca/H$_2$ On center		
(d) C$_2$N:1Mn/H$_2$		
(e) C$_2$N:2Mn/H$_2$ Onsite		
(f) C$_2$N:2Mn/H$_2$ On center		

Figure 4.4: Adsorption of H$_2$ molecule on the six samples under study.

4.3.4 Spin Resolved Band Structures

We performed DFT calculations of the electronic properties on four samples presented in Figure 4.4 (a,c,d,f). We emphasize that in case of adsorption of H_2 on DAC we selected the starting configuration at center of dimer as it leaded to the most stable adsorption. Within the given size of the computational supercell, it seems that the embedding of even a single metallic atom in the pore of C_2N would be sufficient to change the properties from semiconducting to metallic. Figure 4.5 displays the spin-resolved partial density of states (PDOS). One common trend between all four samples is that Ca- or Mn-doped C_2N make the sample metallic (i.e., in all of which the bandgap closes at Fermi level, $E_g = 0$). Besides, Fermi level is taken as an energy reference (i.e., $E_F = 0$). Several bands below Fermi level persist to be nasty "dispersion-less" and should be attributed to the hybridized orbitals of 6 nitrogen atoms overlapping with metal atom(s). The general trend is that the adsorption of H_2 molecule on the metal atom would passivate those dangling bonds and clear and widen the band gap. For instance, see what happened to the localized states in panels 4.5 (a-b) corresponding to the bands of (a)C_2N:1Ca and (b)C_2N:2Ca. Even though the hydrogen molecule was just under physisorption process and both of these systems are in paramagnetic state (i.e., zero magnetic moment), the inter-band gaps have broadened after the dipole-dipole interaction with the molecule. Furthermore, in panels 4.5(c-d) corresponding to the bands of: (c)C_2N:1Mn and (d)C_2N:2Mn, the H_2 molecule altered chemisorption processes associated with molecular dissociation.
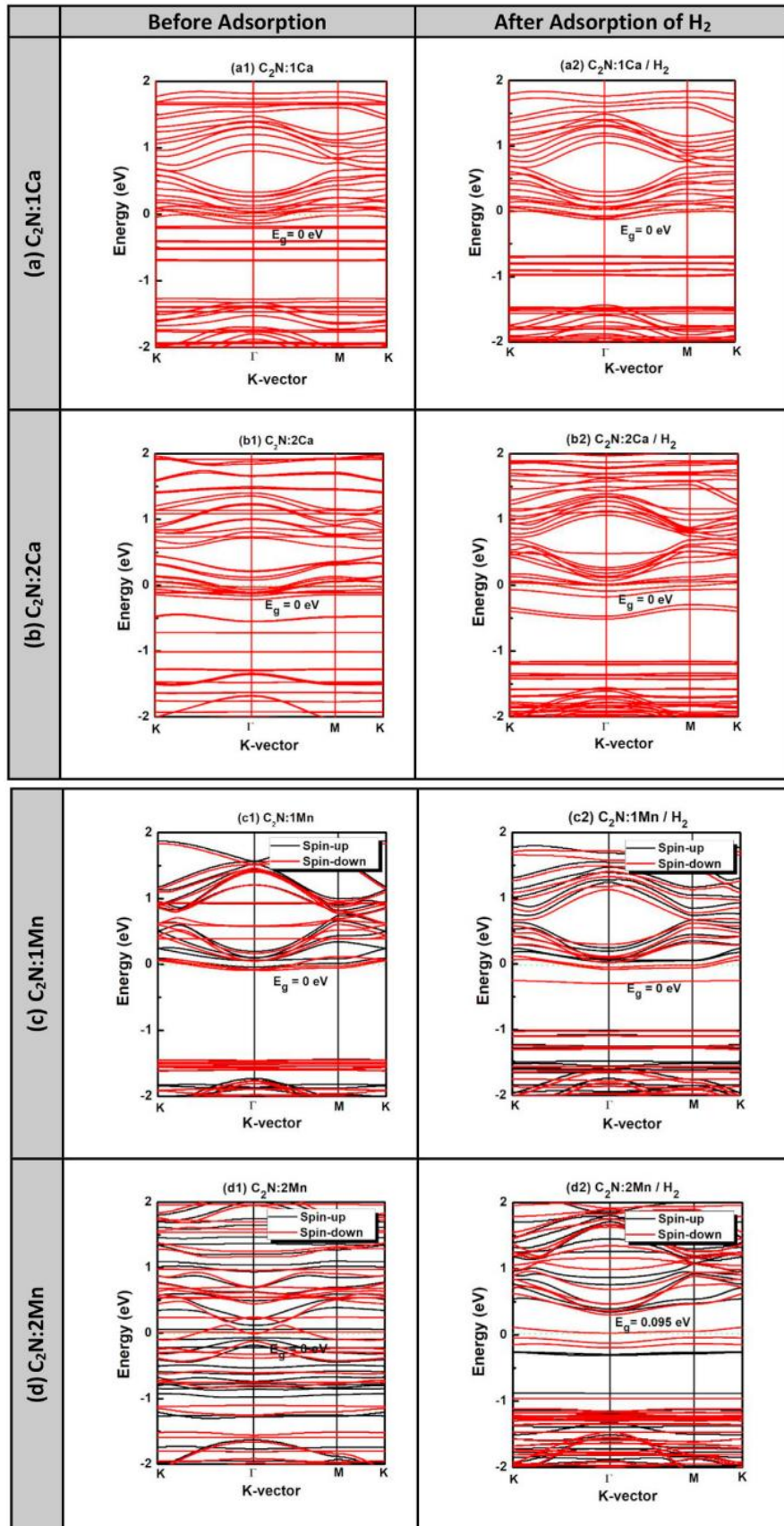
Figure 4.5: Band structures of four samples (a)C_2N:1Ca, (b) C_2N:2Ca,(c) C_2N:1Mn, and (d) C_2N:2Mn before and after H_2 adsorption.

The change is so big in case of $C_2N:2Mn$ that the messy states filling all energy space became grouped again and the inter-band gaps broadened, including the appearance of an optical gap of $E_g = 0.095$ eV. The charge transfers from or to the molecule in the four cases are summarized in Table 4.2. One may notice that H_2 molecule is reducing the Ca-catalyst but oxidizing the Mn-catalyst. Furthermore, regarding the role of magnetism, in case of Ca-dopants, the magnetic moment is always zero regardless of the state before or after the physisorption of H_2 molecule. On the other hand, in case of Mn-doping, the magnetic state matters as it changes through the adsorption process. For instance, (c) $C_2N:1Mn$ has the largest magnetic moment M = 3.60 Bohr Magneton (μ_B) before the adsorption, but it gets reduced to M = 3.40 μ_B after the occurrence of the chemisorption with H_2 molecule. (d) $C_2N:2Mn$ exhibits an even stronger change of magnetic properties. The magnetic moment of the Mn-Mn dimer buried in the pore of C_2N was M = 2.42 μ_B before interaction with H_2 molecule. This magnetic moment gets too much reduced through the chemisorption process, associated with molecular dissociation, to become M = 1.97 μ_B. Hence, from both perspectives of electronic and magnetic properties, it is remarkable that Mn_2 dimer, embedded in C_2N, has higher sensor's response to H_2 gas molecule(s) than that of single Mn-doped C_2N.

4.3.5 HOMO/LUMO States

To inspect the charge transfer between the H_2 molecule and the metal-doped C_2N samples, Figure 4.6((a) and (b)) displays the charge-density plots of the highest occupied molecular orbital (HOMO) and the lowest unoccupied molecular orbital (LUMO) eigen-states, respectively. In the cases of physisorption, such as the interaction of H_2 molecule with Ca doped C_2N, Bader charge analysis predicted mimic transfer of charge (i.e., of order no more that hundredth of electron) from the molecule to substrate, as it is shown in Table 4.2. Figure 4.6(a) (a-b) shows that the HOMO state gets more curdled and fatherly scattered away from the molecule after the occurrence of physisorption.
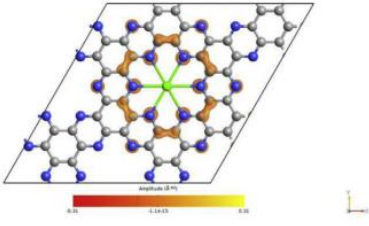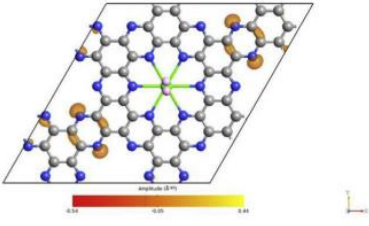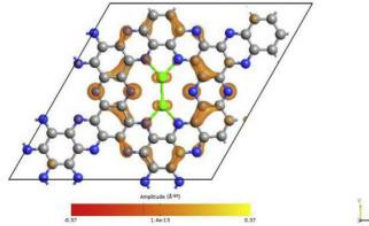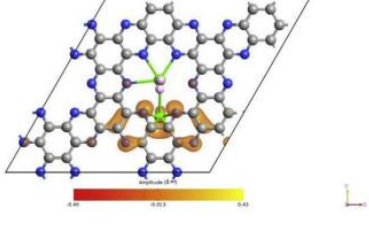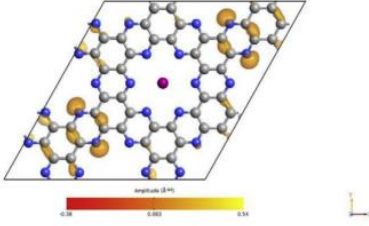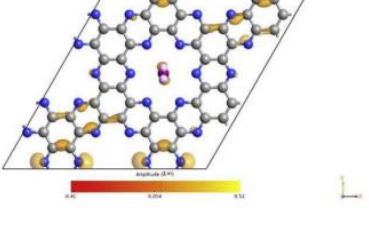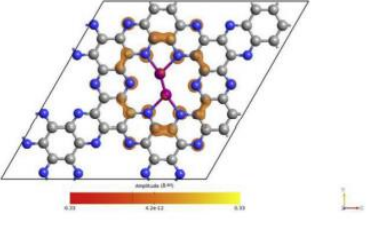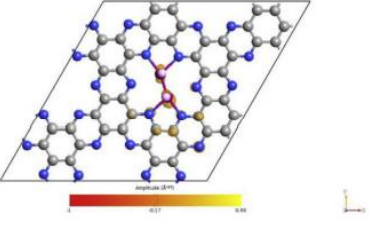
Substrate	HOMO Before Adsorption	HOMO After Adsorption of H_2
(a) C_2N:1Ca		
(b) C_2N:2Ca		
(c) C_2N:1Mn		
(d) C_2N:2Mn		

Figure 4.6(a): Charge density plots for HOMO states corresponding to the four samples under study.
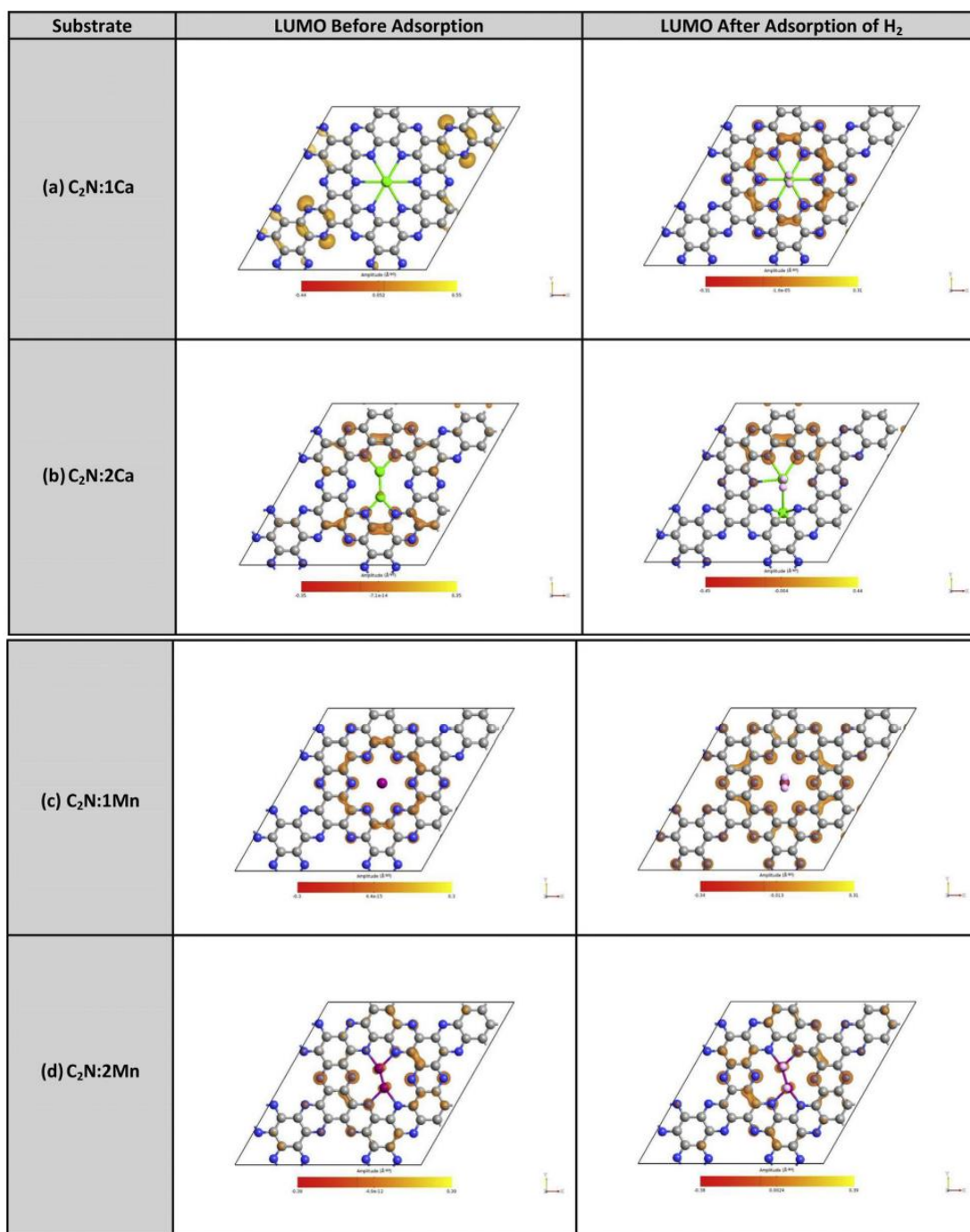
Figure 4.6(b): Charge density plots for LUMO states corresponding to the four samples under study.

Whereas Figure 4.6(b) (a-b) shows that the LUMO state gets more curdled but closer to the location of the molecule after the happening of physisorption. In the cases of chemisorption, such as the interaction of H_2 molecule with Mn-doped C_2N, Bader charge analysis predicted H_2 to be oxidizing the system with draining a charge at the order of 8 hundredths of electron (Table 4.2). Figure 4.6(a) (c-d) shows that the HOMO state experiences an accumulation of charge on Mn-H bonds after the occurrence of

chemisorption with H_2 molecule. Whereas Figure 4.6(b) (c-d) shows that the LUMO state gets rather more extended after the formation of H-Mn bonds, revealing that those states to be permissible and originate from dispersive bands.

4.3.6 Desorption and Recovery Time

Desorption is a plausible task only in cases of physisorption and chemisorption either without molecular dissociation or weak splitting. Such cases are demonstrated in the hydrogen adsorption on Ca-doped C_2N and SAC of Mn in C_2N, respectively. From the perspective of gas-sensing, to decide whether the gas sensor should be reusable or disposable, the calculation of recovery time becomes further necessary. Yong and co-workers presented an elaborate theoretical work on the absorption of several gas molecules on pristine C_2N [145], including the calculation of recovery time. In their study, NH_3 and NO were found to have moderate adsorption energies of values -0.539 eV and -0.438 eV (i.e., having energies laying at the border between strong physisorption and weak chemisorption, of about ~ 0.5 eV), small recovery times of 1.2 ms and 23 ms at RT, and large effects on the electronic structures. So, these two gases were proposed to be the most suitable for detection on C_2N-based sensor. The sensor in that case would be reusable and have high sensitivity and selectivity. Within the framework of the conventional transition state theory [80], the recovery time can be expressed as follows:

$$\tau = v_0^{-1} e^{(-\frac{E_{ads}}{k_B T})}$$
(4.6)

where T is absolute temperature, k_B is the Boltzmann's constant, E_{ads} is the adsorption energy, and v_0 is the attempt frequency. Peng and co-workers [143] confirmed the validity of the above formula after using it in fitting the experimental data of adsorption of NO_2 gas on Single-Walled Carbon Nanotubes (SWCNT). The experimental recovery time of NO_2 on SWCNT was confirmed to be long of about 12 h using this above formula. We assume that the attempt frequency of H_2 molecule on all C_2N-systems have same order of magnitude as that of NO_2 molecule on SWCNT at RT (i.e., $v_0 = 1012$ s^{-1}), which is incidentally also used in the theoretical work of Yong and coworkers on C_2N [142]. Then, we calculated the recovery times of adsorption of H_2 molecule on both Ca-

doped and Mn doped C_2N at RT and included the results in Table 4.2. To start with pristine C_2N, one can notice that our recovery times 6.8×10^{-11} s and 1.5×10^{-12} s (due to VASP and SIESTA, respectively) are a bit smaller than that reported by Yong et al. 4.5×10^{-10} s [142]. This is so because our adsorption energy is underestimated as compared to the one of Yong et al. By comparing our results of adsorption energy between VASP and SIESTA, they all agree to a good extent but only one value is much different, corresponding to the chemisorption of H_2 on C_2N:1Mn (i.e., in VASP E_{ads} = -0.474 eV whereas in SIESTA E_{ads} = -1.021 eV). One possible explanation for this large discrepancy is that in SIESTA the adsorption temperature is RT where the chemisorption was associated with strong molecular dissociation whereas in VASP T = 0 K as was used under the assumption of frozen lattice and validity of Born Oppenheimer approximations. The adsorption cases of H_2 on Ca-doped C_2N are all physisorption type. Having low adsorption energies, the recovery time in all these cases is at the order or below nanosecond (i.e., t ≈ ns). Furthermore, both VASP and SIESTA found good agreement in the adsorption energies of H_2 on Mn-doped C_2N DAC (i.e., C_2N:2Mn), where E_{ads} = - 0.551 eV and - 0.507 eV, respectively.

Table 4.2: Band-gap energy, Adsorption energy, Charge transfer, magnetic moment and recovery time of the studied relaxed structures.

Substrate	E_g (eV)	E_{ad} (eV)	Δq (e)[c]	M (μ_B)[a]	τ(s)
Pristine C_2N	1.66[a] (1.55)[b]	N/A	N/A	0	N/A
C_2N/H_2	1.66[a] (1.55)[b]	−0.109[a] (−0.0077)[b]	−0.0047	0	6.8×10^{-11a} $(1.5x^{-12})^b$
C_2N:1Ca	metallic[a,b]	N/A	N/A	0	N/A
C_2N:1Ca/H_2	metallic[a,b]	−0.1669[a] (−0.0828)[b]	−0.0083	0	6.6×10^{-10a} $(2.5 \times 10^{-11})^b$
C_2N:2Ca	metallic[a,b]	N/A	N/A	0	N/A
C_2N:2Ca/H_2 (H_2 initially @ Onsite)	metallic[a,b]	−0.2081[a] (−0.4821)[b]	−0.0063	0	3.3×10^{-9a} $(1.4 \times 10^{-4})^b$
C_2N:2Ca/H_2 (H_2 initially @ Center)	metallic[a,b]	−0.2088[a] (−0.5065)[b]	−0.0089	0	3.4×10^{-9a} $(3.6 \times 10^{-4})^b$
C_2N:1Mn	metallic[a,b]	N/A	N/A	3.60	N/A
C_2N:1Mn/H_2	0.11[a] (metallic)[b]	−0.4739[a] (−1.0206)[b]	+0.0131	3.40	9.2×10^{-5a} $(140.2)^b$
C_2N:2Mn	Half-metal[a] (metallic)[b]	N/A	N/A	2.42	N/A
C_2N:2Mn/H_2 (H_2 initially @ Onsite)	0.20[a] (metallic)[b]	−0.5509[a] (−0.4821)[b]	+0.0726	1.97	1.8×10^{-3a} $(1.3 \times 10^{-4})^b$
C_2N:2Mn/H_2 (H_2 initially @ Center)	0.06[a] (0.095)[b]	−0.5518[a] (−0.5065)[b]	+0.0799	1.97	1.9×10^{-3a} $(3.2 \times 10^{-4})^b$

[a] VASP Calculations.
[b] SIESTA Calculations.
[c] Bader-charge Analysis.

Considering the results of VASP, the recovery times of H_2 on SAC and DAC were found to be about 92 ms and 1.8 ms, respectively. Furthermore, the H_2 molecule acted as oxidizing on both SAC and DAC with drained charges of about 0.013e and 0.08e, respectively. Hence, it seems that with increased clustering of Mn more charge transfer

would occur, therefore the higher adsorption energy and recovery time would be. Yet, the recovery times are so small (i.e., t « 1 s).

Considering the huge effect on the electronic structures (explained in the Chapter above) caused by the adsorption of H_2 gas molecule on both SAC-Mn and DAC-Mn, huge change of magnetic moment, one expects that C_2N: Mn would be very strong candidate for magnetic gas sensor for the detection of H_2 with very high sensitivity and selectivity.

Chapter 5: Transition-Metal SAC Embedded in C_2N-NR for Toxic-Gas Reduction Reaction and Selective Gas-Sensing Applications

5.1 Summary

Exploring advanced materials for detecting noxious gases is a key requirement for maintaining healthy air quality in the environment. The catalytic activity of four magnetic Transition Metal (TM) elements (e.g., Mn, Fe, Co and Ni) embedded in C_2N pores, as Single-Atom Catalysts (SAC), has been tested towards detecting toxic oxidizing gases. As a model, we tested the sensing efficiency of these catalysts towards two toxic gases, namely NO and NO_2. For our calculations, we have used a formalism based on the combination of Density Functional Theory (DFT) and Non-Equilibrium Green's Function (NEGF). From our findings we have drawn a strong correlation between the sensor response and the reduction in magnetization ($\Delta M \cong -1.40$ to -0.55 μB). The results of spin polarized transport properties showed that Ni- and Fe-embedded C_2N are the most efficient in detecting NO/ NO_2 and NO_2 molecules (with $\Delta M/M_0 = -98\%$, -38% to -18%, respectively). The main reason for the magnetization reduction was the formation of chemical bonds between SAC and molecules thereby causing an enormous reduction in the number of unpaired d-electrons. Thus, Fe- and Ni-C_2N are recommended for either toxic-gas reduction reactions or platform materials in disposable gas sensors for efficient capturing of toxic gases.

Redrafted from

5.2 Introduction

The graphene discovery in 2004 by Konstantin Novoselov and Andre Geim had not only fetched them the Nobel prize in Physics in 2010, but also opened the door for the creation of a new horizon in the physics of 2D systems, with promising capabilities for various practical applications [1-6]. In 2015, following a more sophisticated synthesis technique compared to the one used by the graphene inventors [1], Mahmood and coworkers utilized bottom-up wet-chemical reaction to fabricate nitrogenated holey graphene "C_2N" [12]. The uniform-hole periodic distribution makes C_2N advantageous for various applications including gas filtration and sensing. In contrast to graphene, a finite band gap (i.e., $E_g \cong 1.90$ eV) is created due to the existence of phenyl rings and holes that are surrounded by aromatic nitrogen atoms, which makes C_2N also appropriate for semiconducting applications [12]. The functionalization of the holey graphene C_2N has been achieved experimentally which further enhances its capabilities for various applications such as energy storage and selective gas-sensing [87]. Furthermore, recent experimental investigations explored the relevance of C_2N, both in monolayer and multilayer forms as possible anode candidates in Sodium-ion batteries (SIBs) and Lithium-ion Batteries (LIBs) applications [15-16, 27]. Focusing on gas-sensing applications, successful experimentalists have been successful at homogeneously embedding Transition Metal (TM) atoms in the C_2N-pores while overcoming the metal clustering issue. Huang and coworkers [16] used a bottom-up wet-chemical approach to achieve metal embedment (i.e., M@C_2N, where M = Co, Ru, and Pd atoms). Furthermore, to enhance the catalytic capabilities of these active metal sites, these metal nanostructures were downsized to singly dispersed metal atoms [27, 148-153]. Experimentally, the nanostructures of Single Atom Catalyst (SAC) and Double-Atom Catalyst (DAC) have been achieved in C_2N and metal oxides. These nanostructures have shown improved catalytic activity towards various toxic gas reduction reactions (e.g., NO_x, SO_x, CO_x and H_2S) [149-150, 183-184] and for detecting biomolecules such as blood sugar macromolecules [185]. The successful syntheses of SAC and DAC in C_2N have triggered several theoretical efforts to investigate the reaction mechanisms and the possible functionalizing catalysts that tune its properties for niche applications [24, 26, 153]. From the perspective of environmental protection, diverse experimental techniques

have been developed for the detection and removal of NO_2 toxic gases; most of which are based on catalytic reductions at relatively high temperatures, while few are at ambient conditions [186]. Porous materials have demonstrated tremendous potential for NO_2 removal applications due to their high capacity in the pristine form which can be further enhanced upon functionalization. Recently, Shang and coworkers used the uncalcined TM-based layered double hydroxides (TM-Al-CO_3 LDHs) as ambient NO_2 adsorbents [186]. An adsorption capacity exceeding 5.3 mmolg^{-1} and the lowest NO generation ratio was reported with lowest degradation performance after six adsorption–desorption cycles [186]. Along the same trend, the Metal–Organic Framework (MOF) materials have been proven to be highly efficient for ambient detection of NO_2 gas [187–188]. Han and coworkers reported their success in fabricating the reactive adsorption of NO_2 in a redox-active MOF, MFM-300(V), associated with the reduction of NO_2 into NO and water. They reported an extraordinary NO_2 uptake of 13.0 mmolg^{-1} at Room Temperature (RT = 298 K) with a reproducibility of cycles (i.e., the absorbent can be used in a reusable detector) [187–188]. In this perspective, the novel material of C_2N should be considered as candidate for ambient capture of NO_2, based on its porous morphology, thermal stability, and hydrophobic character [189]. The idea of embedding of transition metal atoms (in "SAC" form) in C_2N pores has been attempted by many groups (i.e., M@C_2N, with M = Ru, Pd, and Co done in the experimental group of Huang et al. [16]; and M = Sc, Ti, V, Cr, Mn done in the theoretical group of Ma et al. [127]). Furthermore, Huang and coworkers employed M@C_2N as an anode platform in lithium-ion battery applications [16]. Whereas Ma and coworker designed a theoretical model based on SAC M@C_2N to study gas adsorption and they found Cr and Mn to be promising SAC for CO reduction reactions at low temperature [127]. A lot of credit should go to the successful experimental synthesis of SAC M@C_2N by Huang group in 2019 [16], which inspired many theoretical efforts to dig deeper to understand the science behind the reaction mechanisms and functionalization possibilities for C_2N [189]. Actually, the embedment of transition metal atoms as SAC and DAC in C_2N has demonstrated a very enhanced catalytic activity towards toxic-gas reactions (e.g., CO_X, NO_X, and SO_X) [144-146,183], non-toxic-gas reduction reaction [190], hydrogen evolution reaction [25, 191], photo-catalysis for water splitting [192,193], energy storage

[88, 178, 194] and metal-ion batteries [161]. Focusing on the reduction of toxic gases, He and coworkers have used ab-initio method to show that an Iron SAC embedded in C_2N (i.e., Fe@C_2N) is very stable and efficient for CO and O_2 reduction reactions [148]. Cui et al. used ab-initio method and screened twelve metal SAC embedded in C_2N (i.e., M@C_2N) and found 6 amongst them to be efficient in CO_2 reduction reactions (i.e., they are namely: M = Ti, Mn, Fe, Co, Ni, Ru) [149]. Using the first principles method, Zhao et al demonstrated the efficiency of DAC Cu embedded in C_2N (i.e., Cu_2@C_2N) towards CO_2 R-R [126]. Geo and coworkers used ab-initio method to study the adsorption characteristics of toxic gases (NO_2, NH_3, SO_3 and H_2S) on Iron-SAC-doped graphene [150]. Another toxic gas SF_6 has been theoretical simulated using first-principles method and shown to be detectable using DAC (i.e., M_2@C_2N, with M = Co, Ni) [164]. This study is beneficial to our current investigation as we will screen four ferromagnetic TM atoms and use them in both SAC and DAC embedded in C_2N to assess their effectiveness in capturing NO and NO_2 gases. Many other computational simulations have further corroborated the great catalytic activity of TM atoms in the capture of gas molecules [128, 195-197]. In a recent effort, the catalytic activity of Mn as SAC and DAC embedded in C_2N has been tested for gas sensing of several gas molecules (e.g., O_2, N_2, H_2S, H_2O, H_2, CO_2, and CO) [197]. The results have shown strong chemisorption to occur with the oxidizing gases in a clear distinction from the weak chemisorption which occurred with the reducing gases. Strong correlation was shown between the strength of the chemisorption and the change of magnetization [197]. Furthermore, it is expected that such a change in magnetization (in magnitude and direction) would affect both gas-sensing sensitivity and selectivity. This hypothesis will be tested in the current investigation by involving many ferromagnetic TM atoms as SAC embedded in C_2N (e.g., namely, Mn, Fe, Co and Ni). Special target gases will be the hazardous gases (e.g., NO_x, CO_x, SO_x), which are oxidizing. The scope of the current study is to inspect the correlation between gas sensor response and the change in magnetization due to adsorption of toxic gases (e.g., NO and NO_2). To achieve this aim, we tested four ferromagnetic TM elements (i.e., Mn, Fe, Co, and Ni), embedded in C_2N pore as SAC. We used sophisticated Density-Functional Theory (DFT) packages (e.g., Atomistic Tool-Kit "ATK" and Vienna Ab-initio Simulation "VASP" packages).

The results would clarify the following: (i) The effect of change in magnetization on the sensor response of the toxic gases such as NO and NO_2; and (ii) The correlation between strength of chemisorption and the sensor response. This Chapter is organized as follows: Section 5.3 will describe the models and the computational methods. Section 5.4 will show an elaborate analysis and discussion of the findings. The final section will illustrate our main conclusions.

5.3 Computational Model and Method

As computational models, we used two types of supercells.

- The first supercell, used for electronic structure calculations, contains the C_2N Nanoribbon (NR), shown in Figure 5.2, where periodic boundary conditions are applied. The used supercell's dimensions were A = L = 29.51 Å, B = C = 20 Å to make sure that the nanoribbon is periodic along the x-direction as a 1D lattice; besides B and C are set to be large enough to isolate the NR to interact with its mirror images along y, z directions. Without counting the TM-SAC and the molecule, the pristine C_2N-NR is composed of three primitive cells. Each primitive cell has 50 atoms (i.e., NR would have 150 atoms).

- The second supercell, used for calculation of transport properties, is composed of 2 electrodes (i.e., source and drain) and a central zone consisting of the C_2N-NR like those shown in Figure 5.2. Each electrode is composed of 1 primitive cell of C_2N-NR. It must be noted that the central zone should be kept at least 3 times longer than the electrode size to avoid interference effects due to reflections from electrodes.

As computational techniques, two Density-Functional Theory (DFT) packages have been used. The "Spanish Initiative for Electronic Simulations with Thousands of Atoms" (SIESTA) code [54,55], which is incorporated within the Atomistic Toolkit (ATK) package, was mostly used in the atomic relaxation and the calculations of the electronic structures and transport properties, as it possesses the ability to handle large systems. The incorporation of the Non-Equilibrium Green's Functions (NEGF) formalism into SIESTA has further paved the way for the calculation of the transport properties, which are essential in the study of gas-sensing. Besides, the Vienna Ab-initio Simulation

Package (VASP) [53] was also used for the calculation of Charge Difference Density (CDD) and the benchmarking of adsorption energy and magnetization, as it is known to be reliable but also limited with system size.

Using the results of total energy calculation, the adsorption energy of a gas molecule on the adsorbent (i.e., metal-doped C_2N-NR) is defined as:

$$E_{ads} = E_{tot}^{Sub/gas} - E_{tot}^{Sub} - E_{tot}^{gas} \qquad (5.1)$$

where $E_{tot}^{Sub/gas}$, E_{tot}^{Sub}, and E_{tot}^{gas} stand for total energies of substrate with and without gas molecule and the isolated gas molecule itself. The charge transfers between substrate and molecule are calculated using the Mulliken population charge analysis in SIESTA and the Bader-charge analysis in VASP [58]. The magnetization can be calculated using the spin-polarized total DOS as follows:

$$M = \mu_B \int_{-\infty}^{E_F} [G_{tot}^{Up}(E) + G_{tot}^{Down}(E)] dE \qquad (5.2)$$

where μ_B is the Bohr magneton, E_F is Fermi energy, $G_{tot}^{Up}(E)$ and $G_{tot}^{Down}(E)$ are the total densities of states of the system with spin-up and spin-down polarizations. It should be emphasized that $G_{tot}^{Down}(E)$ is presented to be negative and the total density of states $G_{tot}(E) = G_{tot}^{Up}(E) - G_{tot}^{Down}(E)$ is normalized to yield the total number of valence electrons in the system (N):

$$N = \int_{-\infty}^{E_F} [G_{tot}^{Up}(E) - G_{tot}^{Down}(E)] dE \qquad (5.3)$$

For instance, without the incorporation of the catalyst, the 1D-periodic supercell of 150 atoms, mentioned above, contains a total of 558 electrons: (96C+30 N+24H atoms = 96× 4+30×5+24×1 = 558 electrons). It should be further emphasized that for the TM-SAC atoms in ATK calculations would include the shell before the outer one (e.g., Mn, Fe, Co, and Ni are assumed to have: $3s^2$, $3p^6$,$3d^X$,$4s^2$ states; with X = 5,6,7,8, respectively). So, the number of electrons corresponding to these 4 catalysts would be: 2+6+X+2 = 15, 16, 17, and 18, respectively. Therefore, the total number of electrons in the system (i.e., filled states in TDOS) should be 573–576 electrons, respectively.

Concerning the transport and gas-sensing properties, the IV-curves are calculated by ATK package using the device configuration, where the TM-catalyst-embedded into the

pore of C$_2$N-NR, which consists of the central region. The calculation of the current versus bias is performed using the two-terminal Landauer-Buttiker formula [59] given by

$$I(V_b) = \frac{2e}{h} \int_{-\infty}^{+\infty} T(E, V_b)[f_L(E - \mu_L) - f_R(E - \mu_R)]dE \tag{5.4}$$

where V$_b$, T(E,Vb), $\mu_{L/R}$ and f$_{L/R}$ are the applied forward bias, bias-dependent transmission coefficient, electro-chemical and Fermi-Dirac distribution function of the left/right electrode respectively.

Based on the IV results, the differential resistance versus bias is evaluated (R = ΔV/ΔI), using the finite-difference method.

The sensor response of the device [60, 61] is defined as

$$S = \frac{|G_g - G_o|}{G_o} = \frac{|R_g - R_o|}{R_g} \tag{5.5}$$

where G is the conductance (i.e., G=1/R), G$_g$ (G$_o$) and R$_g$ (R$_o$) are the conductance and resistance in presence (absence) of gas molecule on the C$_2$N:TM device, respectively. In order to decide about whether the sensor should be reusable or disposable, one may estimate the recovery time [80] given by

$$\tau = \upsilon_o^{-1} \exp\left[-\frac{E_{ads}}{k_B T}\right] \tag{5.6}$$

where υ_0 is the attempt frequency, E$_{ads}$ is the adsorption energy, k$_B$ and T are the Boltzmann constant and the absolute temperature, respectively.

In this Chapter, we have tested 4 different TM-SAC atoms (i.e., Mn, Fe, Co, and Ni) embedded in C$_2$N-NR to search for the efficient adsorption of two toxic gases (i.e., NO and NO$_2$), and the results of spin polarized PDOS, CDD, I(V) characteristics, and sensor response will be discussed next.

5.4 Results and Discussions

5.4.1 Atomic Relaxations

As a starting point, it is essential to assess the stability of the embedded TM catalyst on various sites on the C$_2$N nanoribbon. Of course, the system is one dimensional and should lead to different results than the case of 2D C$_2$N monolayer. To make a clear contrast, in our previously reported results [196], we used VASP-package to study the

stability of manganese SAC on 2D-periodic sample of C_2N containing 2×2 primitive cells (i.e., composed of 72 atoms).
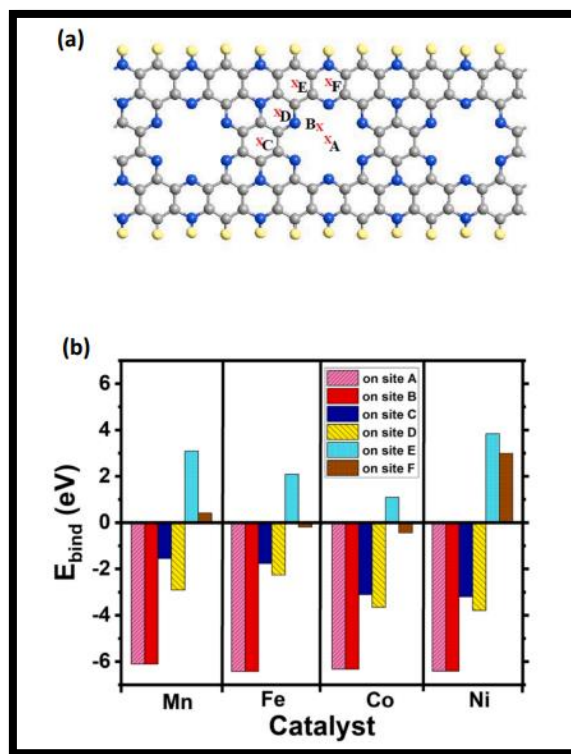
Figure 5.1: Embedding positions tested for metal atoms in the C_2N-NR.

In the case of C_2N ML, four different potential initial sites to deposit Mn catalyst were tested. Namely, they were as follows: (i) center of big pore, (ii) off-center of big pore, (ii) above the center of benzene ring, and (iv) above the center of pyridine ring. Our results have shown that the most stable position for Mn SAC corresponds to a global energy minimum which is located at off center position in the big pore. Our results were in line with many other ab-initio results such as those reported by Ma and coworkers [127].

As far as this present work is concerned with studying the gas-sensing properties, in which spin-polarized transport calculations are essential, the system in focus here is C_2N Nanoribbon (C_2N-NR). Here the system to be studied is different from the case of ML, and the C_2N-NRs in our present investigation consists of a relatively large system comprising of about 150 atoms. Furthermore, to assess the stability of TM catalyst, we explored 6 different sites (Figure 5.1), which are more than the case of C_2N ML. Besides, we have 4 ferromagnetic TM atoms to inspect (i.e., Mn, Fe, Co, and Ni) as these atoms intrinsically can induce magnetism into the system and the theme of our investigation is

to correlate the change in magnetization and the gas-sensing selectivity towards the oxidizing toxic gases (e.g., NO and NO_2 gases). Furthermore, in our previous study [197], we had fixed the TM catalyst on "Mn" embedded in C_2N and studied its interaction and magnetic effects on gas-sensing properties for many toxic oxidizing gases (e.g., CO_x, NO_x, SO_x, H_2S). Here, in our current study, we are fixing the toxic oxidizing gas molecules (namely, NO_x) and screening the ferromagnetic TM SAC atoms.
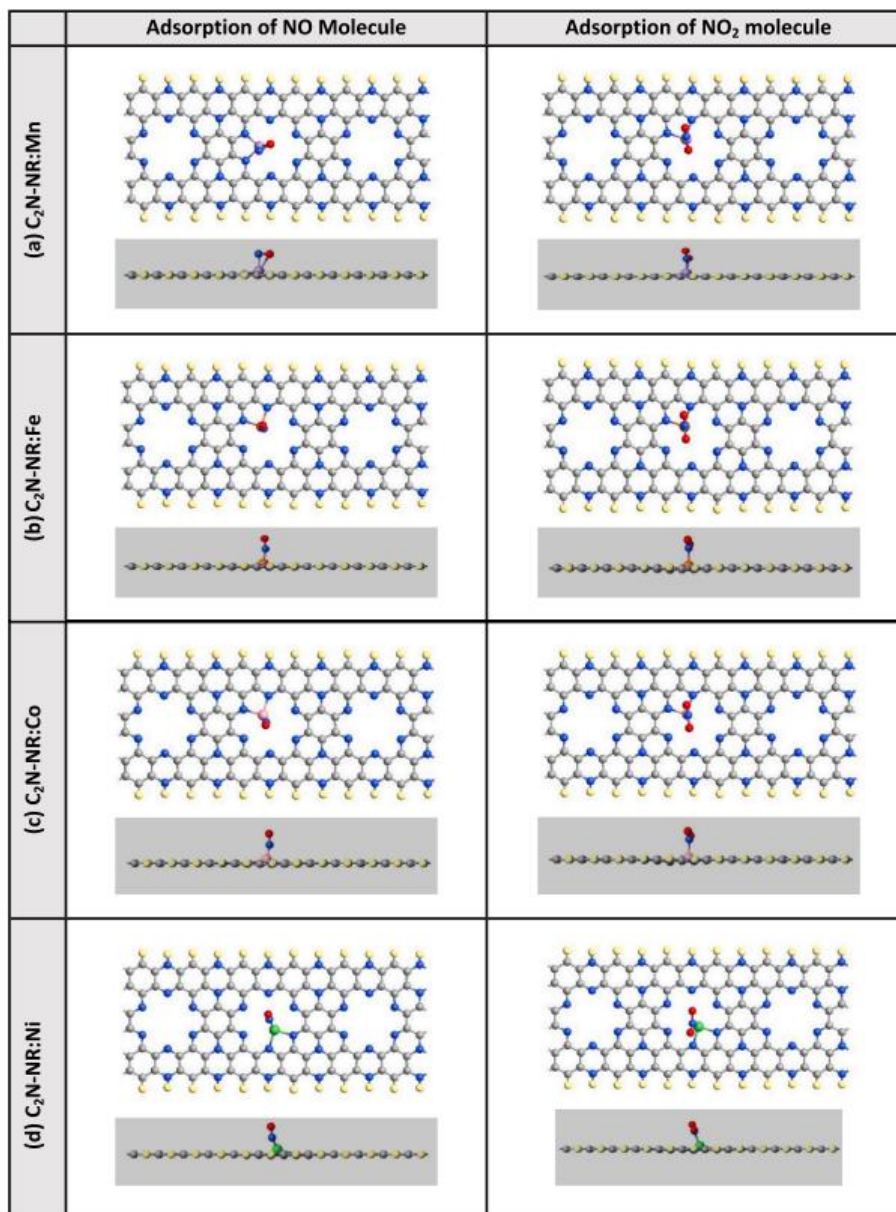
Figure 5.2: Relaxed structures after the chemisorption of NO and NO_2 on the four samples tested.

Having said all the above, we decided to use SIESTA for relaxations and total energy calculations of each of the four TM SAC atoms on each single site amongst the six

104

locations shown in Figure 5.1(a). The results of total and binding energies are shown in Table 5.1 and in Figure 5.1(b). The results of the atomic relaxations of the four different TM-SAC atoms share some common trends. Namely:

- the atomic relaxation starting at point "A" (center of big pore) always converges to point "B", located at off-center of big pore by about 1.2 Å.

- Point "B" is the local minimum-energy for all catalysts with a very strong binding energy E_{bind} = -6.104, -6.426, -6.329, and -6.406 eV corresponding to Mn, Fe, Co, and Ni, respectively.

- The TM-SAC atoms seem to bind well on sites C and D as well but in local minima having binding energies in the following order in terms of algebraic negative values: $E_{bind}^{B} < E_{bind}^{D} < E_{bind}^{C}$. One can notice the pyridine hexagon ring of center "D" provides more stability to all catalysts than the benzene ring of center "C" does.

- Basically, the remaining tested locations at points "E" and "F" are not quite stable destinations for all the 4 catalysts as the binding energies are found to be positive (in kind of exception of the pyridine ring of center "F" to accommodate Fe and Co atoms with very small negative binding energies of E_{bind} = - 0.194 and - 0.449 eV, respectively.

In brief, the most stable configuration of embedding the TM-SAC is found to be in position "B" for all the 4 catalysts. So, we decided to use the fully relaxed TM-SAC configurations (@ site B) as our adsorbent bed to study the adsorption and gas sensing properties toward the toxic gas molecules (NO and NO_2). Moreover, one has to emphasize that without the catalyst (i.e., Mn, Fe, Co, and Ni), the gas molecules are found to exhibit physisorption processes on the pristine C_2N-NR. Hence, the improvement of interaction of the gas molecules with the C_2N-NR required the functionalization of the substrate by TM catalyst.

The embedment of TM-SAC into the big pores of C_2N-NR did not only reach the most thermodynamically stable structures but also the achievement of chemisorption processes with both NO and NO_2 molecules.

Table 5.1: Total-energy optima corresponding to relaxations of TM atoms(Mn, Fe, Co, Ni) starting from four different sites (A,B,C and D).

Metal	@A (eV)	@B (eV)	@C (eV)	@D (eV)	@F (eV)	@G (eV)
Mn	→B	-6.104	-1.545	-2.906	+3.089	+0.409
Fe	→B	-6.426	-1.769	-2.262	+2.091	-0.194
Co	→B	-6.329	-3.105	-3.652	+1.089	-0.449
Ni	→B	-6.406	-3.204	-3.792	+3.842	+2.984

Figure 5.2 displays the relaxed structures of the four TM-SAC catalysts (e. g., Mn, Fe, Co, Ni) embedded in C_2N-NR pore after the occurrence of chemisorption with NO and NO_2 molecules. The geometrical parameters are summarized in Table 5.2. The most stable location for the TM atom embedded in the C_2N pore is found to be off-center and closer to the 2N atoms at the side of the pore, which is consistent with all first-principal predictions [127]. The agreement was taken as a confirmation of our good choices of pseudopotentials and Hubbard U parameters. For instance, in case of Mn atom, its globally stable position is found to be off center by about 0.38 Å, which is in excellent agreement with the results of ab initio calculations reported by Ma and coworkers [127]. Both NO and NO_2 molecules exhibit chemisorption processes with all the four TM SACs but are not associated with molecular dissociation.

Figure 2a displays the strongest chemisorption bonding between Mn and NO and NO_2 molecules. As it is clearly shown that the NO molecule is attached to Mn through both its ends. The molecular bond length of NO became longer than that in free molecule (i.e., $d_{N-O} = 1.27$ Å $> b_{N-O} = 1.15$ Å). The weakening of N–O bond occurred in order to pave the way for both N and O atoms to make new covalent bonds with Mn catalyst. Furthermore, the interaction between Mn and NO_2 is also stronger than the other cases of catalysts. One of two oxygen atoms of NO_2 got attached to Mn. The molecular bond lengths became larger than those in free molecule (i.e., $d_{N-O} = 1.22$-1.32 Å $> b_{N-O} = 1.19$ Å) and the molecular angle became larger than that in free molecule (i.e., $Ang_{(N–O–N)} = 127.59°$). Such provisions were taken to allow two atoms in the molecule (N and O atoms) to get attached to the Mn catalyst.

The interactions of both NO and NO_2 molecules with the remaining three TM catalysts were almost similar, one to another, and not as strong as that of Mn catalyst. (b-d) Concerning the chemisorption of NO molecule on the SAC Fe, Co, and Ni, it seems that

the N atom takes the lead in making just one chemical bond with the SAC with a perpetual bond-length of $d_{SAC-N}^{molecule} \cong$ 1.64–1.65 Å. The attachment to N-atom into NO molecule is favored because N atom is trivalent and has the capacity to make three bonds. So, to some extent, a double bond is maintained with O atom to keep the molecule cohesive, and 1 electron can be engaged to make the bonding with the SAC. The NO molecule maintains its bond length close to the equilibrium one (i.e., d_{N-O} = 1.18–1.19 Å $\cong b_{N-O}$), as π-bond is preserved. Furthermore, in the case of chemisorption of NO_2 molecule on the SAC (i.e., Fe, Co, and Ni), although the electronegativity of O atom is greater than that of N atom (i.e., χ^O= 3.44 $>\chi^N$ = 3.04 Pauling) [55], the N atom is again responsible for making the bond with SAC as it is trivalent. The NO_2 molecule breaks its π-bonds to pave the way for N atom to make that covalent bond with SAC (i.e., the N–O bond becomes larger than the case of the free molecule: d_{N-O} = 1.22–1.24, 1.26–1.27 Å $> b_{N-O}$ = 1.18 Å). The two N–O bonds in NO_2 molecules are a bit different due to the asymmetry in their orientations with respect to the lattice so the electrons in the bonds exhibit different charge exchange and van de Waals interactions with the lattice.

Table 5.2: Geometric parameters for the relaxed atomic structures of four samples after chemisorption of NO and NO_2 molecules.

	NO molecule		NO_2 molecule	
	Bond length (Å)	Angle (degrees)	Bond length (Å)	Angle (degrees)
Free Molecule	1.150	N/A	1.197	134.3°
M@C$_2$N	Adsorption of NO molecule		Adsorption of NO_2 molecule	
	Bond length (Å)	Angle (degrees)	Bond length (Å)	Angle (degrees)
Mn@C$_2$N	d_{Mn-N} = 1.91,1.95 Å (lattice) d_{Mn-N} = 1.74 Å (molecule) d_{Mn-O} = 1.99 Å (molecule) d_{N-O} = 1.27 Å (molecule)	(Mn—N—O) = 81.07° (Mn—O—N) = 59.70° (N—Mn—O) = 39.23°	d_{Mn-N} = 1.93,1.94 Å (lattice) d_{Mn-N} = 1.75 Å (molecule) d_{Mn-O} = 2.08 Å (molecule) d_{N-O} = 1.22,1.32 Å (molecule)	(O—N—O) = 127.59°
Fe@C$_2$N	d_{Fe-N} = 1.92,1.96 Å (lattice) d_{Fe-N} = 1.65 Å (molecule) d_{N-O} = 1.19 Å (molecule)	(Fe—N—O) = 157.66°	d_{Fe-N} = 1.92 Å (lattice) d_{Fe-N} = 1.78 Å (molecule) d_{N-O} = 1.24,1.27 Å (molecule)	(O-N-O) = 125.76°
Co@C$_2$N	d_{Co-N} = 1.96,1.97 Å (lattice) d_{Co-N} = 1.64 Å (molecule) d_{N-O} = 1.18 Å (molecule)	(Co—N—O) = 162.35°	d_{Co-N} = 1.94 Å (lattice) d_{Co-N} = 1.79 Å (molecule) d_{N-O} = 1.24,1.26 Å (molecule)	(O—N—O) = 125.58°
Ni@C$_2$N	d_{Ni-N} = 1.97,1.98 Å (lattice) d_{Ni-N} = 1.65 Å (molecule) d_{N-O} = 1.18 Å (molecule)	(Co-N-O) = 159.30°	D_{Ni-N} = 1.97,1.99 Å (lattice) D_{Ni-N} = 1.80 Å (molecule) d_{N-O} = 1.24,1.26 Å (molecule)	(O—N—O) = 125.15°

5.4.2 Spin-Polarized DOS
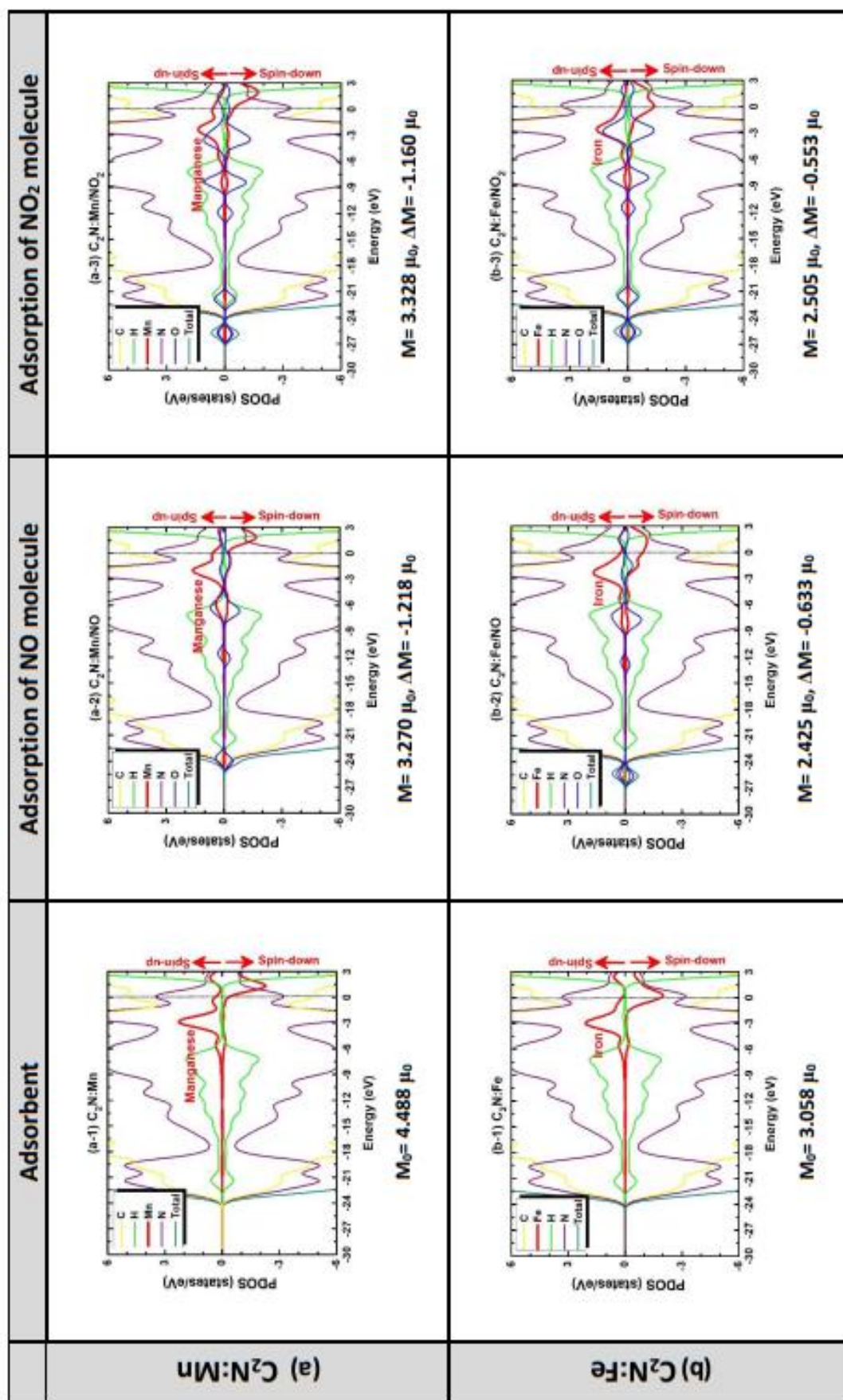
Figure 5.3: Spin polarized PDOS and TDOS for the 4 samples before and after NO and NO$_2$ chemisorption processes.
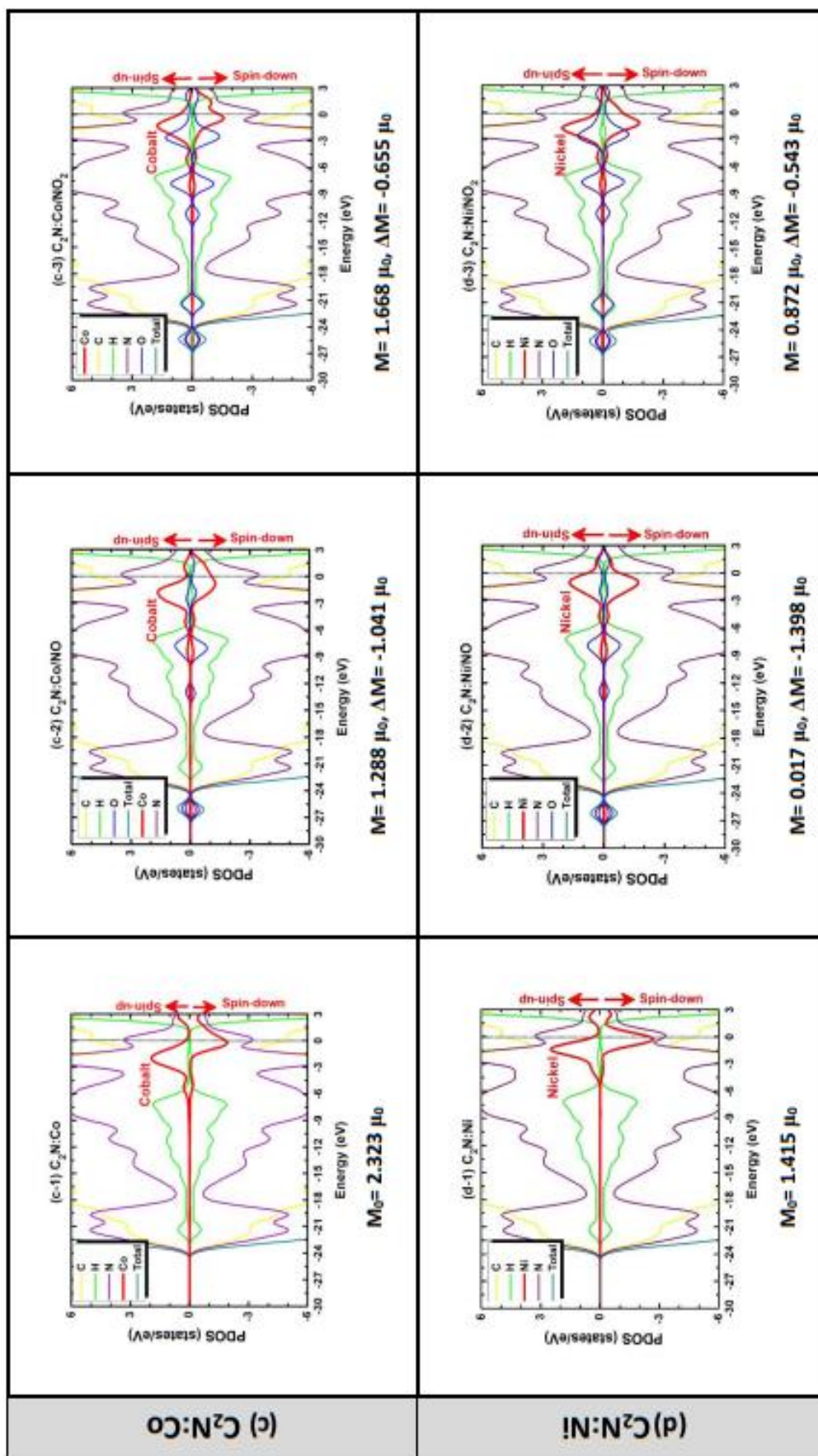
Figure 5.3: Spin polarized PDOS and TDOS for the 4 samples before and after NO and NO$_2$ chemisorption processes (continued).

The spin-polarized Partial Density of States (PDOS) can reveal information about the magnetic states (i.e., the magnetization). We have used GGA+U to probe the PDOS for the structures presented in Figure-5.2 before and after the occurrence of chemisorption with either NO or NO_2 molecules. Of course, it is crucially important to make sure that the Total Density of States (TDOS), including both spins, should be normalized to the total number of electrons existing in the Supercell. i.e.: Without SAC, the C_2N-NR contains a total of 150 atoms (96C+30 N+24 H atoms = 96×4+30×5+24×1 = 558 electrons). The incorporation of TM SAC (e.g., Mn, Fe, Co, or Ni) would raise the total number of electrons in the system into 573–576 electrons, respectively. Due to such a large number of electrons, the spin-polarized TDOS was spread in energy within a range [-100, +100] eV and in magnitude within a range [− 35, +35] (states/eV-spin). As we are selective about the interaction between the TM-SAC and either NO or NO_2 molecules, we decided to zoom in into the energy range [−15, +6] eV and show only the PDOSs due atoms contributing to the magnetization in order to understand effectively the origins of variation of magnetization from before to after the occurrence of gas chemisorption [198-199]. The energy region near Fermi level would give us more relevant physical trends concerning the changes in magnetization due to the interaction between molecules and TM-SAC. Figure 5.3 shows the results of spin polarized PDOS in the studied four samples before and after the occurrence of chemisorption with either NO or NO_2 molecules. The PDOS of TM-SAC is shown in thick red curve to make it well distinct as being the main contributor to the built-in magnetization.

Furthermore, we show the PDOSs of atoms considered as second-order contributors to the magnetization, such as the 6 nitrogen atoms as First Nearest Neighbors (FNN) of the TM atom; besides the PDOS of the whole molecule. The asymmetry between two PDOSs of spin-up and spin-down of the TM-SAC is very pronounced.

Table 5.3: Effect of chemisorption of NO and NO_2 molecules in four samples on the adsorption energy, recovery time, magnetization and charge transfer.

TM-Catalyst	E_{ads} (eV) per Molecule		τ (s)		M_0 (μ_B)	M (μ_B)		ΔM (μ_B) of system		Δq (e) of Molecule	
	NO	NO_2	NO	NO_2		NO	NO_2	NO	NO_2	NO	NO_2
Mn	-3.625^a	-3.611^a	$6 \times 10^{48(a)}$	$3.5 \times 10^{48(a)}$	$4.488^a, 4.868^b$	3.27^a	3.33^a	$-1.22\ (-27\%)^a$	$-1.16\ (-26\%)^a$	$-0.31^{(c)}$	$0.44^{(c)}$
	-2.299^b	-2.130^b	$3.5 \times 10^{26(b)}$	$5.2 \times 10^{23(b)}$	$4.62^e, 4.3^f$	2.74^b	3.04^b	$-2.13\ (-43\%)^b$	$-1.83\ (--37\%)^b$	$-0.51^{(d)}$	$0.63^{(d)}$
Fe	-3.974^a	-3.235^a	$4.3 \times 10^{54(a)}$	$1.7 \times 10^{42(a)}$	$3.058^a, 3.884^b$	2.43^a	2.51^a	$-0.63\ (-21\%)^a$	$-0.55\ (-18\%)^a$	$-0.137^{(c)}$	$-0.423^{(c)}$
	-3.038^b	-2.828^b	$8.7 \times 10^{38(b)}$	$2.6 \times 10^{35(b)}$	$3.48^e, 3.4^f$	3.03^b	2.59^b	$-0.85\ (-22\%)^b$	$-1.08\ (-27\%)^b$	$-0.37^{(d)}$	$-0.55^{(d)}$
Co	-3.608^a	-2.827^a	$3.2 \times 10^{48(a)}$	$2.5 \times 10^{35(a)}$	$2.323^a, 2.342^b$	1.29^a	1.67^a	$-1.04\ (-45\%)^a$	$-0.66\ (-28\%)^a$	$-0.13^{(c)}$	$-0.42^{(c)}$
	-3.299^b	-2.858^b	$2.1 \times 10^{43(b)}$	$8.4 \times 10^{35(b)}$	$2.12^e, 2.6^f$	1.08^b	2.05^b	$-1.26\ (-54\%)^b$	$+0.29\ (+12\%)$	$-0.34^{(d)}$	$-0.50^{(d)}$
Ni	-4.517^a	-3.630^a	$5.5 \times 10^{63(a)}$	$7.4 \times 10^{48(a)}$	$1.415^a, 1.321^b$	0.02^a	0.87^a	$-1.40\ (-98\%)^a$	$-0.54\ (-38\%)^a$	$-0.09^{(c)}$	$-0.43^{(c)}$
	-3.049^b	-2.791^b	$1.3 \times 10^{39(b)}$	$6.3 \times 10^{34(b)}$	$1.06^e, 1.7^f$	0.00^b	0.98^b	$-1.32(-100\%)^b$	$-0.34\ (-26-\%)^b$	$-0.19^{(d)}$	$-0.51^{(d)}$

(a) SIESTA Calculations.
(b) VASP Calculations.
(c) Calculations using "Mullikan Population" in SIESTA (i.e., ATK).
(d) Calculations using "Bader-Charge Analysis" in VASP.

In the case of Mn embedded in C_2N, in absence of molecules, the initial magnetization of Mn is large $M_0 = 4.488\ \mu_B$. The position of the Mn within the pore can also affect the magnetization; for instance, when Mn is located at the center of the pore (i.e., point A in Figure 5.1), the magnetization was found to be $4.868\ \mu_B$ [196]; then when Mn occupies the global energy minimum energy at the off-center position and establishes bonds with 2 N atoms of the lattice (i.e., point B in Figure 5.1), its magnetization decreases to become equal to M_0 shown above, due to the interaction which would keep some electrons busy in establishing those bonds and consequently reduces the number of unpaired electrons. On the same line, after chemisorption with either NO or NO_2 molecules, the number of unpaired electrons get further reduced and the magnetization is decreased.

As a matter of fact, after the interactions with NO and NO_2 molecules, the magnetization reduces to: $M_1 = 3.270\ \mu_B$ and $M_2 = 3.328\ \mu_B$ with reductions of $\Delta M = -1.218\ \mu_B$ (-27%) and - 1.160 μ_B (-26%), respectively. The data are summarized in Table 5.3. On the other hand, one should further emphasize the asymmetry existing between spin-up and spin-down of the PDOS of molecule (i.e., more asymmetry in case of NO than that in NO_2), which reveals the induced magnetism into the molecule(s) while the total magnetization gets reduced.

In the case of Fe embedded in C_2N pore, the magnetization is large but a bit smaller than the case of Mn as the number of unpaired d electrons is reduced to four instead of five in case of Mn. So, in its initial off-center position, the iron possesses a total magnetization

$M_0 = 3.058 \mu_B$. Again, the occurrence of chemisorption processes with NO and NO_2 molecules would reduce the magnetization to $M_1 = 2.425 \mu_B$ (i.e., $\Delta M = -0.633 \mu_B = -21\%$) and $M_2 = 2.505 \mu_B$ (i.e., $\Delta M = -0.553 \mu_B = -18\%$), respectively. The relative changes in magnetization are relatively smaller in case of iron than those in case of manganese and such a trend might be attributed to the relatively weaker bonding between Fe and molecules (e.g., in case of Mn, two covalent bonds Mn-N and Mn-O are established with each molecule). Figure 5.3(b) shows the spin-polarized PDOSs of these molecules to have more asymmetry in case of NO than NO_2 to reveal the magnetic-induction responses.

The spin polarized PDOSs in the case of Cobalt are shown in Figure 5.3(c). The larger the asymmetry between the spin-up PDOS and the spin-down PDOSs is, the larger the magnetization would be. Such asymmetry is larger in absence of molecules and gets reduced by the occurrence of chemisorption with the molecules because of reduction in the number of unpaired electrons. Cobalt as a free atom has 7 electrons in its d-shell; and only 3 electrons among these 7 electrons are unpaired. The embedment of Co into the C_2N-pore has cost the Co atom to use 2 electrons (amongst 2s and 3d electrons) to establish the 2 bonds with the lattice. The initial magnetization while Co embedded in the lattice is $M_0 = 2.323 \mu_B$. The interactions of Co atom with the NO and NO_2 molecules cause the reduction of magnetization to $M_1 = 1.288 \mu_B$ (i.e., $\Delta M = -1.041 \mu_B = -45\%$) and $M_2 = 1.668 \mu_B$ (i.e., $\Delta M = -0.655 \mu_B = -28\%$), respectively. Figure 5.3(c) shows the huge relative change in magnetization in case of the interaction with NO molecule (i.e., -45%), which should affect enormously the passage of the current and consequently would enhance the gas sensitivity.

Last remark about Figure 5.3(c) is that the spin polarized PDOSs of NO molecule show more asymmetry than those of NO_2 molecule. This trend reveals a stronger magnetic induction taking place in NO molecule.

The case of Nickel embedment in C_2N as it interacts with NO molecule is really the most amazing. In the state of free atom, Ni atom possesses 2s and 2d unpaired electrons. But after the embedded in the C_2N big pore, two of these unpaired electrons are shared with the lattice in establishing the covalent chemical bonds with N atoms. The remaining 2 valence electrons in Nickel atom, that could be of d-type, would form an initial

magnetization $M_0 = 1.415$ μ_B. It is amazing to see that the chemisorption of NO molecule would reduce the magnetization to a vanishingly small value $M_1 = 0.017$ μ_B (i.e., $\Delta M = -1.398$ $\mu_B = -98\%$).

Quote the minimal discrepancy between spin-up and spin-down PDOSs of "Nickel" in interacting with NO molecule, presented in Figure 5.3(d), which reveals the vanishing of magnetization. This might be attributed to the formation of a double bond between "Nickel" and "Nitrogen" of NO molecule (i.e., Table 5.2 reports the bond length $d_{(Ni-N)} =$ 1.65 Å, between Ni and NO molecule, which is much smaller than the bond length of Ni-lattice and even Ni-NO$_2$). Furthermore, the chemisorption of NO$_2$ molecule reduces the magnetization enormously as well to the value $M_2 = 0.872$ μ_B (i.e., $\Delta M = -0.543$ $\mu_B = -38\%$). Based on the physical concept that the magnetization (both in magnitude and direction) can affect the passage of the electric current [62], so one should expect "Co" and "Ni" to play a major role in achieving large not only sensitivity but rather selectivity towards especially NO gas molecule (see gas-sensing properties in sections below)

5.4.3 Probability Density of Fermi Eigenstates and Recovery Time

In the case of Mn catalyst (Figure 5.4(a)), its charge state changes from $\Delta q_{Mn} = +0.562$ e to +0.631 e and to +0.683 e in going from the situation before the adsorption to the situations after the chemisorption of NO and NO$_2$ molecules, respectively. This reveals its high electropositive character and the charge donated should get distributed on the lattice (evenly between spin-up and spin-down) and into the molecules. Indeed, the molecules are oxidizing and drain the following amounts of charges $\Delta q_{NO} = -0.308$ e and $\Delta q_{NO2} = -0.432$ e. In consistency with the results of PDOS shown in Figure 5.3, Figure 5.4 displays that loss of charge from Mn and this latter gets distributed on the lattice sites (C and N atoms) and drained by the molecules.

In case of Fe catalyst (Figure 5.4(b)), the charge state of this catalyst changes from Δq_{Fe} $= +0.585$ e to +0.557 e and to +0.645 e. On the other hand, both molecules NO and NO$_2$ are oxidizing in nature, and they acquire the charges of $\Delta q_{NO} = -0.137$ e and $\Delta q_{NO2} = -$ 0.423 e from TM-SAC, respectively. By inspecting the results of PDOS presented in Figure 5.3(b), one can clearly notice that spin down PDOS of Fe has a large value at Fermi level. This is consistent with the accumulation of spin down (light blue cloud) at

the Fe site which can be attributed to the electronegative (oxidizing) character of the NO and NO$_2$ molecules.
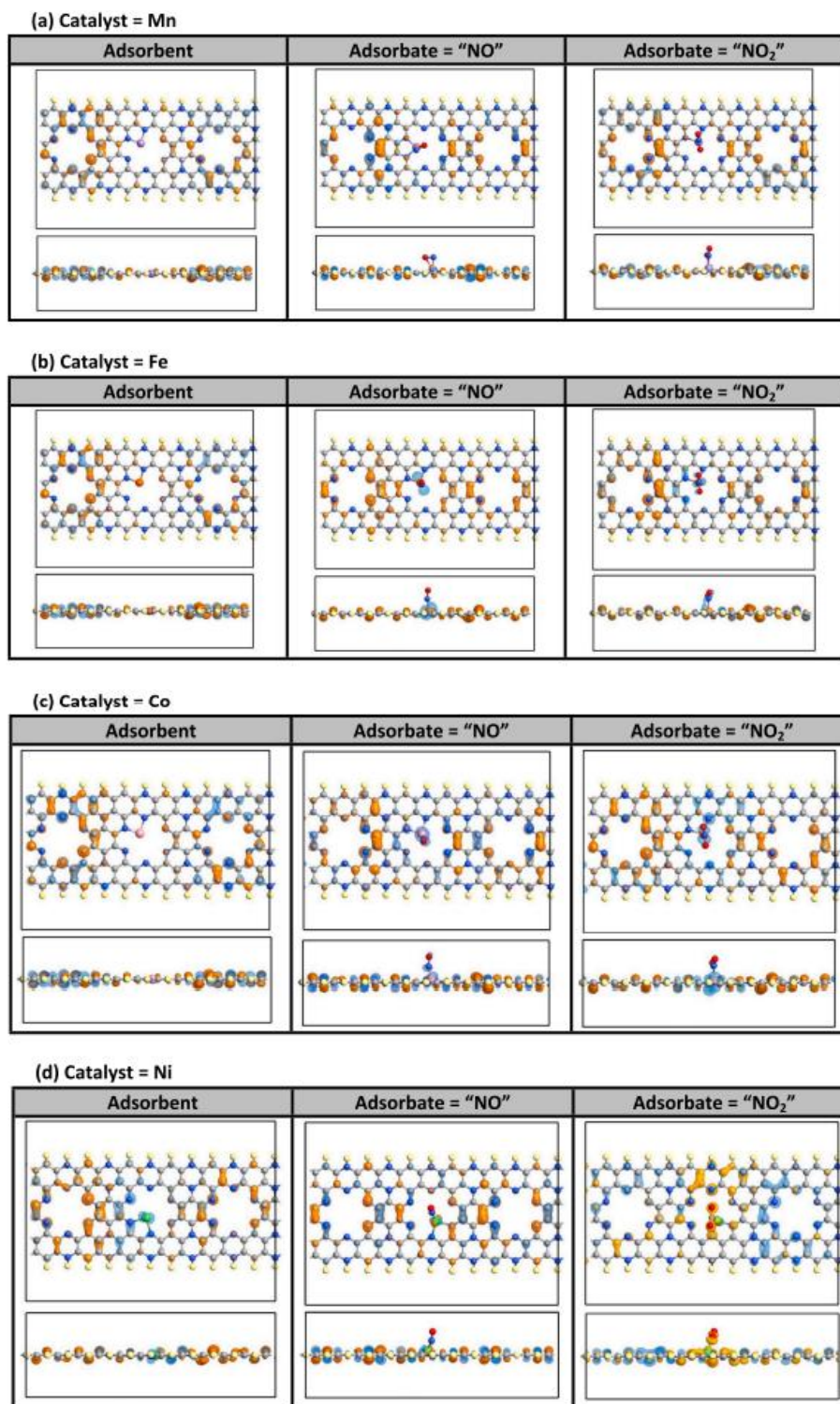
Figure 5.4: Probability density of Fermi Eigenstates of metallic C$_2$N:M(with M= Mn, Fe, Co or Ni).

In case of Co catalyst (Figure 5.4(c)), the charge state of Cobalt changes from $\Delta q_{Co} =$ +0.610 e to +0.526 e and to +0.679 e. Whereas, the molecules get oxidized by acquiring

the charge $\Delta q_{NO} = - 0.126$ e and $\Delta q_{NO2} = - 0.416$ e from catalyst atom, respectively. In similar way to Fe catalyst, the Eigenstate at Fermi level is metallic where Co play, the role of an electropositive (positively charged) and the given charge is distributed over the lattice irrespective of spin-state in even fashion between C and N atoms. By inspecting the spin-polarized PDOS presented in Figure 5.3(c), one may further notice that spin-down PDOS of Co atom has largest at Fermi level. This is consistent with the blue cloud around the Co catalyst shown in Figure 5.4(c), which can be attributed to the electronegativity and oxidizing characters of the NO and NO_2 molecules, as well.

In the last case of Ni catalyst (Figure 5.4(d)), the charge state of Ni atom changes from $\Delta q_{Ni} = +0.779$ e to $+0.560$ e and to $+0.685$ e. On the other side, the molecules of NO and NO_2 persist in their oxidizing behaviors and accumulate charges of $\Delta q_{NO} = - 0.083$ e and $\Delta q_{NO2} = - 0.424$ e from the catalyst atom, respectively. However, the trends in this case of Ni are different from the previous ones. First, notice that spin-down PDOS of Ni atom are the largest at Fermi level in absence of molecules (shown in Figure 5.3(d)) and this is consistent with the accumulation of light-blue cloud at Ni-site in Figure 5.4(d). Then, in case of NO chemisorption, the state gets mixed with both spin at Fermi level and this is again consistent with Figure 5.4(d) as both orange light-blue clouds are on the catalyst site. Last, in case of NO_2 chemisorption, the spin up PDOS of Ni atom predominates the Fermi level. In turn, this is consistent with Figure 5.4(d), where the orange cloud accumulates at the catalyst site.

Regarding the response time and recovery time of a gas sensor, one should make a clear distinction between both as follows. The response time is defined as the time required for a sensor to reach 90% of the total response of the signal such as resistance upon exposure to the target gas. The recovery time is defined as the time required for a sensor to return to 90% of the original baseline upon removal of the target gas [60]. Furthermore, the recovery time is a parameter that quantifies the utility of the gas sensor so it can be categorized either as reusable or disposable. While the response time can be easily determined experimentally, the recovery time can also theoretically be estimated and is strongly related to the adsorption energy (equation (5.6)).

Both VASP and SIESTA methods predicted strong chemisorption processes to occur for both NO and NO_2 gas molecules on $M@C_2N$ without molecular dissociation. Yet, the

adsorption energies are estimated to be very large expressing the strength of chemisorption(s) (i.e., $E_{ads} \geq 3.0$ eV for NO molecule and $E_{ads} \geq 2.1$ eV for NO_2 molecule). Consequently, the recovery time is estimated to be very large for both molecules on all the TM-SACs (Table 5.3). Hence, the results are in favor of proposing M@C_2N to be relevant for either efficient toxic-gas degradation/reduction reaction or to be used as platform in a disposable chemical sensor for toxic gases (e.g., namely, NO and NO_2 gases).

5.4.4 Transport Properties

The calculation of IV-characteristics requires the use of a device with two electrodes and the sample consisting of the central zone. To carry on reliable calculations, the sample must be long enough to avoid interference effects due to the reflections which were expected to occur at the interfaces with electrodes. In our present case, our sample is the C_2N-NR shown in Figure 5.2, doped with TM-SAC, in which IV-curves are to be calculated and assessed before and after the capture of NO and NO_2 molecules. Usually, the length of the sample must be at least three times bigger than the width of the electrode. So, we have set the device to comprise 3 primitive cells of C_2N-NR along the x-axis (i.e., $3\times50 = 150$ atoms without counting the TM-SAC atom), as shown in Figure 5.2, and the electrode to consist of just 1 primitive cell (i.e., $1\times50 = 50$ atoms). Biases are to be applied between the 2 electrodes (i.e., Source and Drain) and electric current to be collected at Drain electrode. To make sure that IV-curves achieved convergence, we kept observing the transmission coefficient for each bias and made sure to include sufficient k-points [203]. One more remark about the magnitude of collected current, for sake of practical measurement, the currents must be larger than order of tenth of micro-Ampere (μA) (i.e., above the minimum metallic conductivity) in order to yield electrical resistance less than 10 mega Ohm (MΩ), to avoid the experimental measurement challenges.
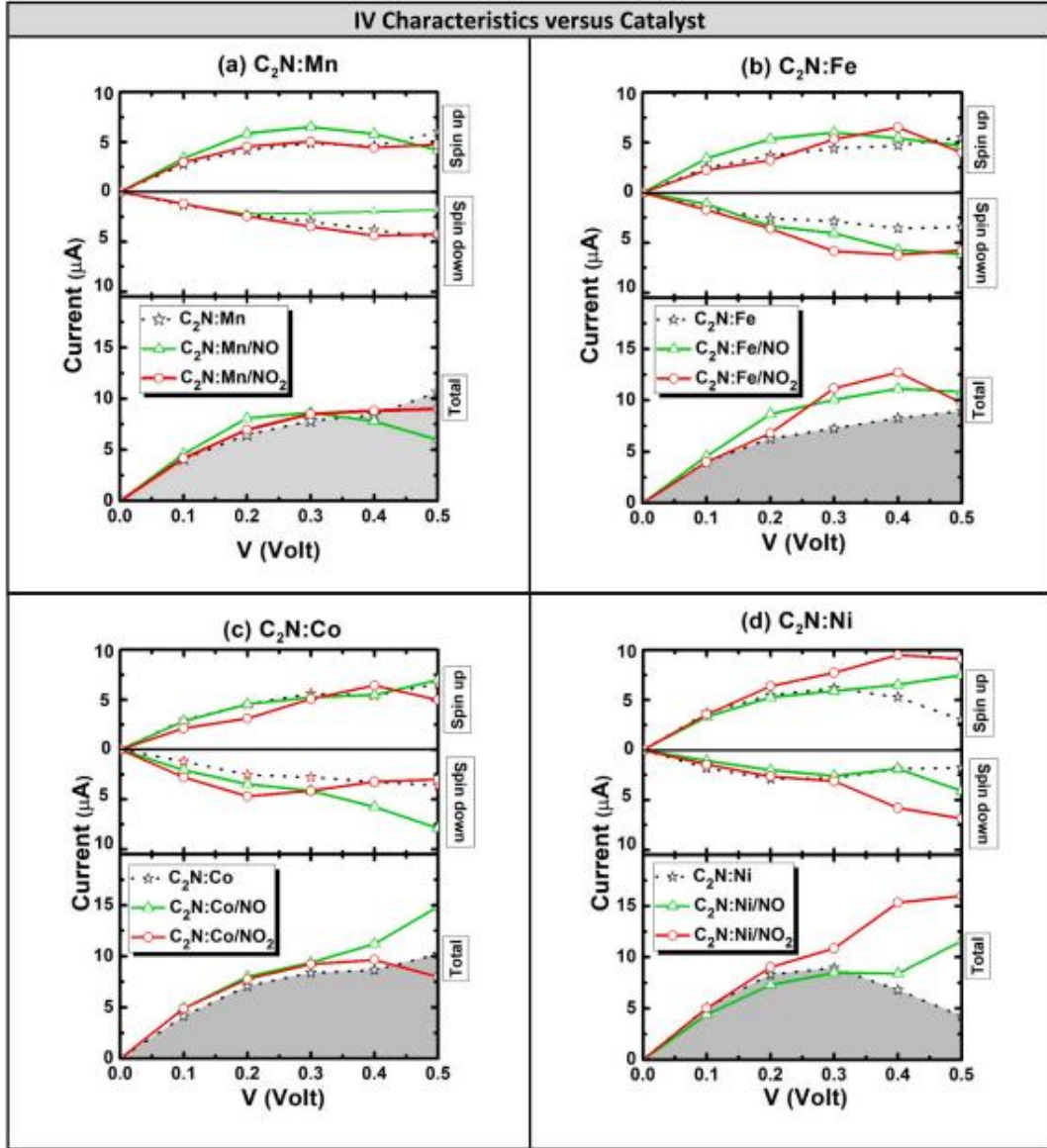
Figure 5.5: Spin polarized IV-characteristics of the four samples before and after the chemisorption of NO molecule and NO_2 molecule.

One further important remark is that spin-polarized transport calculation is not only important but rather a necessity in our present case because the inclusion of TM-SAC obviously induces magnetization and Spin–Orbit Coupling (SOC) effects in the system. Figure 5.5 displays the IV-curves for 4 devices whose central regions consisting of: (a) C_2N-NR: Mn, (b) C_2N-NR: Fe, (c) C_2N-NR: Co, and (d) C_2N-NR: Ni, in three states before gas exposure (dotted black curve) and after the occurrence of chemisorption of NO (green solid curve) and NO_2 molecules (red solid curve).

Convergence of IV-curves was achieved for 6 biases [0,0.5] Volt with a step of $\Delta V = 0.1$ V. The results of IV-curves corresponding to each device are split into two sub-panels.

The upper sub-panel includes the results of IV-curves spin-up and spin-down split into two sides for clarity purpose. The lower sub-panel includes the total current versus bias (i.e., $I_{tot} = I_{up} + I_{down}$). Of course, the lower subpanel would matter for the further calculation of differential resistance and sensor response versus bias and recommend focusing more upon it in our next discussions. In the total current sub-panel, the more deviation of IV-curve occurs after the chemisorption of the molecule the higher the sensitivity toward that gas would be.

By observing the IV characteristics displayed in Figure 5.5 (total current sub-panel), one may see the following trends:

- The only case where the adsorbent yields Negative-Differential Resistance (NDR) is the case of Ni@C_2N. It seems that both the chemisorption processes of NO and NO_2 molecules would yield a serious rectification to the NDR and induce large deviations in IV characteristics. Such large deviations would primarily select Ni to have the largest gas responses toward both NO and NO_2. Using the upper subpanel in Figure 5.5(d), both spins do contribute to the deviations especially at relatively higher voltages (V ≥ 0.3 Volt).

- In all the four samples, deviations of IV-characteristics are shown to start at relatively high voltages, similarly to the case of Ni but the strength of deviation is smaller. To the naked eye, the deviations should be ranked as: $\Delta I_{(Ni)} > \Delta I_{(Fe)} > \Delta I_{(Mn)} \approx \Delta I_{(Co)}$ for sensing NO_2 gas (see red curves in lower sub-panels of Figure 5.5); whereas for sensing NO gas all the four samples look having comparable sensor responses unless rigorous calculations are carried out which we present next.

Figure 5.6 shows chart diagrams representing the calculated differential resistance for each IV-curve presented in the previous Figure 5.5 (lower subpanels). Similar colors as in Figure 5.5 are used and do correspond to: adsorbent (grey), adsorbent interacting with NO molecule (green), and adsorbent interacting with NO_2 molecule (red). All our catalysts are tested: (a) Mn@C_2N, (b) Fe@C_2N, (c) Co@C_2N, and (d) Ni@C_2N.

118
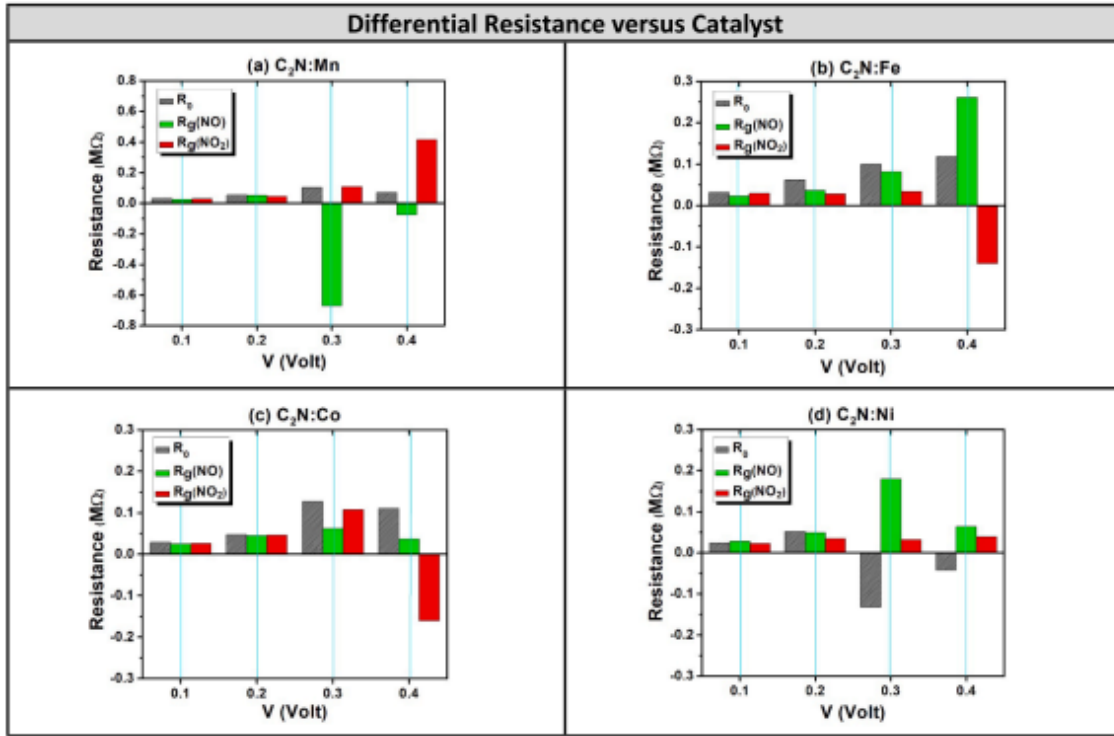
Figure 5.6: Differential resistance versus bias for the four samples.

By looking at Figure 5.6, one can observe the following trends:

- The only adsorbent sample which possesses native NDR behavior is Ni@C_2N (Figure 5-d). The chemisorption of both NO and NO_2 gas molecules would remove the NDR behavior and rectify the IV-characteristics.

- All the other three samples do not exhibit NDR behavior but the adsorption of NO on Mn@C_2N sample and NO_2 on Fe@C_2N and Co@C_2N samples would induce an NDR regime at certain biases (Figure 5.6(a), (b), and (c), respectively).

5.4.5 Sensor Response

Based on the results of differential resistance presented in Figure 5.6, the gas sensitivity (i.e., sensor response) was calculated for each sample per individual gas. Figure 5.7 shows the results of sensor responses versus the bias. The common trend between the results of Figure 5.7 is that they show the gas sensitivity to be larger when $V \geq 0.3$ Volt (in exception of Fe@C_2N, where $V \geq 0.2$ Volt). The averages of sensor responses in each panel corresponding to the chemisorption of NO and NO_2 molecules are shown in Figure 5.7 in green and red dotted lines, respectively. Figure 5.7(a) presents the results of averages of sensor response of both NO and NO_2 gases for all the four TM-SACs for

sake of comparison, as calculated using SIESTA-package. One can notice in Figure 5.7(a) the following trends:

- Ni seems to have the largest sensor responses for both NO and NO_2 gases, simultaneously. These trends are consistent and well correlated to the enormous reductions in magnetization displayed in Figure 5.2(d).

- For NO_2 detection, Fe catalysts can be a second candidate after Ni.

- The trend of sensor responses to NO gas presented in Figure 5.8 is consistent with both trends of relative reductions of magnetization ($|\Delta M|/M_0$) obtained in both VASP and SIESTA (i.e., ATK) and which are shown in both Table 5.3 and Figure 5.8(b). In case of NO detection, the relative change of magnetization seems well behaved and follows a concave parabolic trend versus the occupancy of the d-shell.
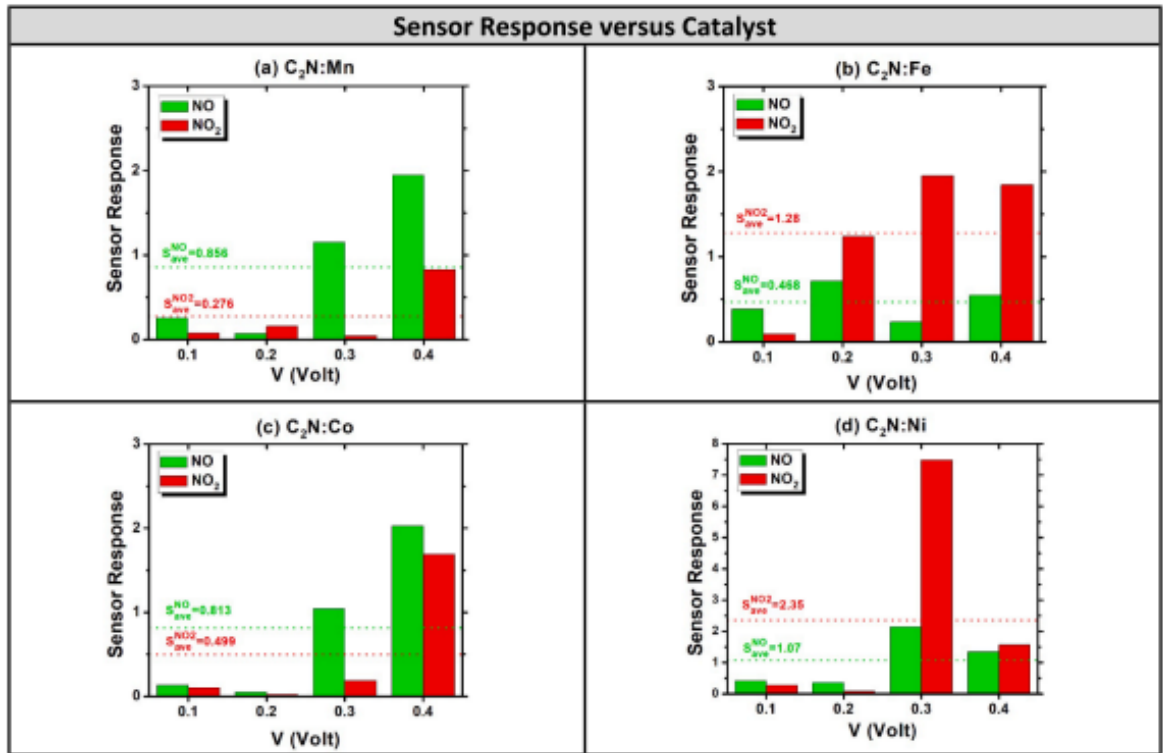
Figure 5.7: Sensor response due to the adsorption of NO and NO_2 gases on the four samples of interest versus bias.

Although there exist minor discrepancies in the values of $|\Delta M|/M_0$, both VASP and SIESTA do agree on predicting almost the same trend whose profile is, in turn, in good agreement with the sensor response shown in green histograms in Figure 5.8(a). Such

consistent trends should reveal the existence of a correlation between the change of magnetization and the sensor response.

Chapter 6: Synergetic Effects of Combining TM Single- and Double-Atom Catalysts Embedded in C₂N on Inducing Half-Metallicity

6.1 Summary

Designing 2D-materials that exhibit half-metallic properties is crucially important in spintronic devices that are used in low-power high-density logic circuits. The large pores in the C_2N morphology can stably accommodate various configurations of Transition-Metal (TM) atoms that can lead to Ferromagnetic (FMC) and Anti-Ferromagnetic Coupling interactions among them, and thus paving the way for achieving half-metallic characteristics. In the present study, we use manganese 'Mn' as a promising catalyst and the spin-polarized density-functional theory to search for suitable configurations of metal atoms that yield half-metallicity. Test samples comprised of Single-Atom Catalyst (SAC) and Double-Atom Catalyst (DAC) of Mn embedded in a C_2N sample of size 2×2 primitive cells as well as their combinations in neighboring large pores (i.e., SAC–SAC, SAC–DAC, and DAC–DAC). Tests were extended to screen many other TM catalysts and the results showed the existence of half metallicity in just five cases: (a) C_2N:Mn (DAC, SAC–SAC, and SAC–DAC); (b) C_2N:Fe (DAC); and (c) C_2N:Ni (SAC–DAC). Our results further showed the origins of half-metallicity to be attributed to FMC interactions between the catalysts with the six mirror images, formed by the periodic-boundary conditions. The FMC interaction is found to have strength of about 20 meV and critical length scale up to about ~21–29 Å, dependent on both the type of magnetic impurity and the synergetic effects. The potential relevance of half-metallicity to spintronic device application is discussed. Our theoretical results have been benchmarked to the available data in literature and they were found to be in good agreement.

Redrafted from

6.2 Introduction

The breakthrough discovery of graphene had not only fetched the inventors the Nobel prize in physics in 2010 but more importantly, it has established a new field of research in 2D systems [1, 2, 4]. Thereafter, many fascinating novel 2D materials have been synthesized and functionalized to tune their properties toward numerous applications, such as C_2N and C_3N [12, 15-16], black-phosphorus [212], hexagonal BN [213], Transition-Metal Dichalcogenides (TMD) [214], and MXene [215, 216]. The lack of bandgap in graphene has triggered research, with the aim of designing other 2D materials which possess semiconducting properties. For instance, Mahmood et al in 2015 reported their success in synthesizing the nitrogenated holey graphene 'C_2N' using simple wet-chemical reaction [12]. In C_2N, the presence of the electronegative Nitrogen atoms along with the uniformly distributed pores of 5.5 Å sizes, open up a band gap of 1.97 eV. The reasonably sized pores are suitable sites for stable embedment of Transition Metal (TM) catalysts which can tune the properties of the material. Another subsequent article by the same group of researchers [16] reported their successful embedment of TM atoms into the big pores of C_2N in forms of Single-Atom Catalyst (SAC) and Double-Atom Catalyst (DAC).

The functionalization of C_2N has made this material strategic with potential of applications in several fields comprising (a) nano-electronics: C_2N Monolayer (ML) was proposed for metal-oxide semiconductor field-effect transistor (MOSFET) [217]; (b) photonics: C_2N van der Waals-based heterostructures have been used with enhanced quantum efficiency [218]; (c) batteries: C_2N was found suitable for metal-ion batteries in general and lithium–sulfur batteries in particular [15, 124, 161, 219]; (d) energy-storage: C_2N possesses an enhanced uptake capacity in hydrogen storage [189, 196]; (e) gas-sensing: selective detection of toxic gases [183, 197]; (f) bio-sensing: it was proposed for sensing diabetes mellitus [185]; and (g) spintronics: half-metallicity can be hosted in TM doped C_2N and thus explored in spintronic-device applications [222, 223].

Moore's law had predicted that from 1965 until 2020, the number of transistors on an Integrated Circuit (IC) would double every two years, thereby shrinking the size of computers, and making them more and more portable over time while simultaneously

reducing their price. However, the progress in electronic devices has become saturated by the year 2020.

Thereafter to continue this trend of miniaturization of memory devices, new technologies such as spintronics have to be explored in information storage, processing and communication [222]. The main property that must be desired in the host material for spintronic applications is half metallicity [223]. This occurs when one spin is metallic while the other spin channel is semiconducting, making the overall DC conductivity of the material spin polarized. Recently many efforts have been focused on this direction, toward designing, or searching suitable materials that exhibit half metallic characteristics. Efforts have also been made to understand the underlying physics, in order to explain its mechanism or origin. In the field of 2D or quasi 1D systems, the reported findings in literature can be categorized into three main groups: (a) half metallicity that can be obtained upon functionalization with TM atoms [222, 223]; (b) half metallicity obtained in quasi 1D materials by applying transversal electric field [66, 225]; and finally (c) half metallicity that results due to vacancies and point defects in TMDs [227, 228].

In the present Chapter we have focused our effort on investigating the effects of TM atom doping C_2N (i.e., category #1) on the electronic and magnetic properties while paying special attention to the emergence of half metallicity as attempted to be induced by exploring the Ferromagnetic Coupling (FMC) interactions. In TMDs, half metallicity can be achieved by creating point defects (i.e., category #3) [227, 228]. In our recent research efforts, we have computationally demonstrated that a single Molybdenum vacancy 'V_{Mo}' can trigger half metallicity in 2D $MoSe_2$ periodic samples having dimensions of 4×4 and 5×5 Primitive Cells (PCs) [229]. The cause of this was attributed to occurrence of FMC interactions among the localized magnetic moments (i.e., in the vicinity of the Molybdenum vacancy), and its mirror images, on account of the periodic boundary conditions that apply on the computational supercell. However, this half metallicity vanishes for larger supercells such as those comprising of 6×6 PCs and above, therefore enabling us to determine the critical length for FMC interactions which was found to be about $L_c \approx 16.5$Å. This value was found to be slightly larger than that predicted by Ma et al [227] which was about 12 Å, since they have taken into

consideration only a single sample of 4×4 PCs, while overlooking the scaling effects. Also, Hong et al [230] had experimentally reported a maximum vacancy-defect density of $\rho_{max} \approx 3.5{\times}10^{13}\,cm^{-2}$ which is smaller than the densities estimated in our samples $6.4{\times}10^{13}cm^{-2}$ and $4.2{\times}10^{13}cm^{-2}$. Realistically speaking, experimental efforts based on concrete theory evidence are the only way to achieve novel materials with half metallic characteristics that can be used for robust spintronic applications.

As a matter of fact, TM doping (i.e., category #1) is often a preferred route in achieving the half metallicity. To date, most of the reports in this direction have been based on 3D half-metals and developing their 2D counterparts remains a challenge. The biggest hurdle is to establish FM ordering in low dimensional systems [33]. Many computational efforts have suggested designs or different morphologies of 2D materials that are capable of hosting half metallicity [231-233]. Feng et al reported a thorough revision on spintronics in 2D materials (e.g., TM-functionalized graphene, phosphorus, and TMD-ML) [224]. Ahn discussed the superiority of 2D materials thus proposing a superior way to control the carrier spin. He presented graphene and other 2D inorganic semiconductors. He further highlighted the major challenges in integrating 2D materials into spintronic devices as well as provided a future perspective on 2D materials for spin-logic devices [232]. An overview on the unusual physical properties emerging 2D materials as new platform for novel spintronic devices as well as the challenges and future opportunities was recently addressed by Hu and Xiang [233]. Although metal free planar FM half-metallic systems are more favored in spintronic devices, their task remains very challenging from practicality point of view. These systems are important as they possess long spin relaxation times due to the weakness of spin–orbit-coupling interactions. Many researchers suggested just computer-designed structures where both ferromagnetism and half-metallicity can exist simultaneously. For instance, Choudhuri and Pathak [220] in a Density-Functional Theory (DFT) study suggested C-doped C_2N as a metal-free FM and halfmetallic 2D material. Gong et al [222] showed that the electron-doping via gating in C_2N with moderate density (ρ = 4-8x$10^{13}cm^{-3}$) would not only yield FM but also half-metallicity. Nonetheless, metal-free systems are very challenging for experimental synthesis. Besides, for practical reasons and relying on the successes achieved in TM-embedment in the large pores of C_2N with adequate stability

[16], we decided to explore the opportunity to study the effect of embedment of SAC, DAC and their combinations on the emergence of ferromagnetism and half-metallicity. This Chapter is organized as follows. Next section 6.3 gives details on the computational model and method. Section 6.4 elaborates a discussion on the obtained results. The last section summarizes our main findings.

6.3 Computational Model and Method

From the perspective of top-view, C_2N monolayer has graphitic structure with one benzene ring missing per area of four benzene rings (i.e., porosity = 1:3) and the six carbons most internal in each big pore are converted into nitrogen atoms. The pores are connected just by pyridine rings (i.e., C_4N_2), as shown in Figure 6.1(a). Figure 6.1(a) contains samples that comprise of 2×2 Primitive Cells (PCs). The PC is composed of 12C and 6N atoms and has a lattice constant of a = 8.33 Å, which is in good agreement with the experimental value of 8.30 Å reported by Mahmood et al [12]. Most of our work is done using a computational supercell of size 2×2 PCs (i.e., it contains 48 C + 24 N atoms) and having dimensions A = B = 16.66 Å and C = 20 Å. The latter C value is maintained sufficiently large to ensure the isolation of the monolayer to interact with the mirror images along the c-axis.

The great advantage in studying C_2N, over conventional graphene, is that it has pores which are uniformly distributed and having sufficiently large diameters (5.5 Å) [12], which open up the possibilities of functionalization via embedment of TM atoms in SAC and DAC configurations. These metal atoms are found to be stable inside the pores, and they tune the properties of the host material for specific tasks such as spintronic and selective gas-sensing applications. Regarding the computational method, we used the DFT method as incorporated in the 'Vienna Ab-initio Simulation Package' (VASP) [53]. The ion–electron interaction is treated by projected augmented-wave method [135]. The exchange and correlation interactions were addressed using the generalized gradient approximation with the Perdew-Burke-Ernzerhof (PBE) functional [234]. For structural optimization, the convergence criteria/tolerances for total energy of 10^{-8} eV and atomic force of 0.01 eV^{-1}Å were applied. In sampling the Brillouin zone, a k-mesh of 5×5×1 Gamma-centered Monkhorst–Pack (MP) [56] was utilized in the geometry optimization of the samples 2×2, 3×3 and 4×4 PCs. A denser k-mesh grid of 8×8×1 (or 5×5×1) was

used in the calculations of Density of States (DOS) for the 2×2-PC (or 4×4 -PC) samples. The plane-wave cut-off energy was selected to be 550 eV and on-site U-Hubbard parameter U = 4.5 eV and J = 1.0 eV, which are almost the default values in the VASP-package, and in good agreement with the adjusted values done by Mann et al [211]. The charge exchange between dopant and host crystal is calculated based upon the Bader charge analysis within the framework of VASP package [58]. Curie temperature (T_C) is defined to be the critical temperature above which the FMC interactions would vanish and thus the system exhibits a phase transition to become paramagnetic.

The rigorous calculation of T_C requires either Monte Carlo [235, 236] or ab-initio molecular dynamics [237] simulations. Based upon the DFT study done by Gong et al [222], owing to the prominent van Hove singularity in the band structure of C_2N, this material exhibits spontaneous ferromagnetism at a relatively low doping density. Over the range of carrier density $\rho = 4\text{-}8\times10^{13}\,cm^{-2}$, the system becomes half-metallic with carriers fully spin-polarized. The estimated Curie temperature was about $T_C \approx 320$ K [222]. Many researchers argued that the TM functionalization of for instance graphene can make the Curie temperature much higher than Room Temperature (RT) and rather at order 500– 800 K [237]. As discussed in section 6.2, our doping density should be within the range studied by Gong et al and this would pave an opportunity of the halfmetallicity for room-temperature spintronic device applications. Last but not the least, regarding the potential synthesis of the proposed structures yielding half metallicity, Mahmood et al [12] first reported, in 2015, their successful synthesis of C_2N monolayers using wet-chemical reaction between hexaminobenzene trihydrochloride and hexaketocyclohexane octahydrate in N-methyl-2-pyrrolidone in the presence of sulphuric acid. Thereafter, the same group [15, 16] reported, in 2017 and 2019, more progress through presenting an experimental protocol for creating C_2N material with embedment of some selected metal atoms (like Ru, Pd, and Co) for applications as anodes in lithium-ion batteries. From our theoretical perspectives, searching for 2D materials hosting half metallicity at RT (i.e. with Curie temperature higher than RT) is by itself a formidable task, especially if the synthesis of the predicted structures is potentially plausible.

6.4 Results and Discussions

6.4.1 Atomic Relaxations

In any DFT study, the calculation of the atomic relaxation should be carried out first. Figure 6.1 shows the atomic relaxed structures of supercells of C_2N with a common size of 2×2 PCs. The PC contains 6 N + 12 C atoms (i.e., 18 atoms); so that the pristine supercell would have 72 atoms (i.e., 24 N + 48 C atoms).
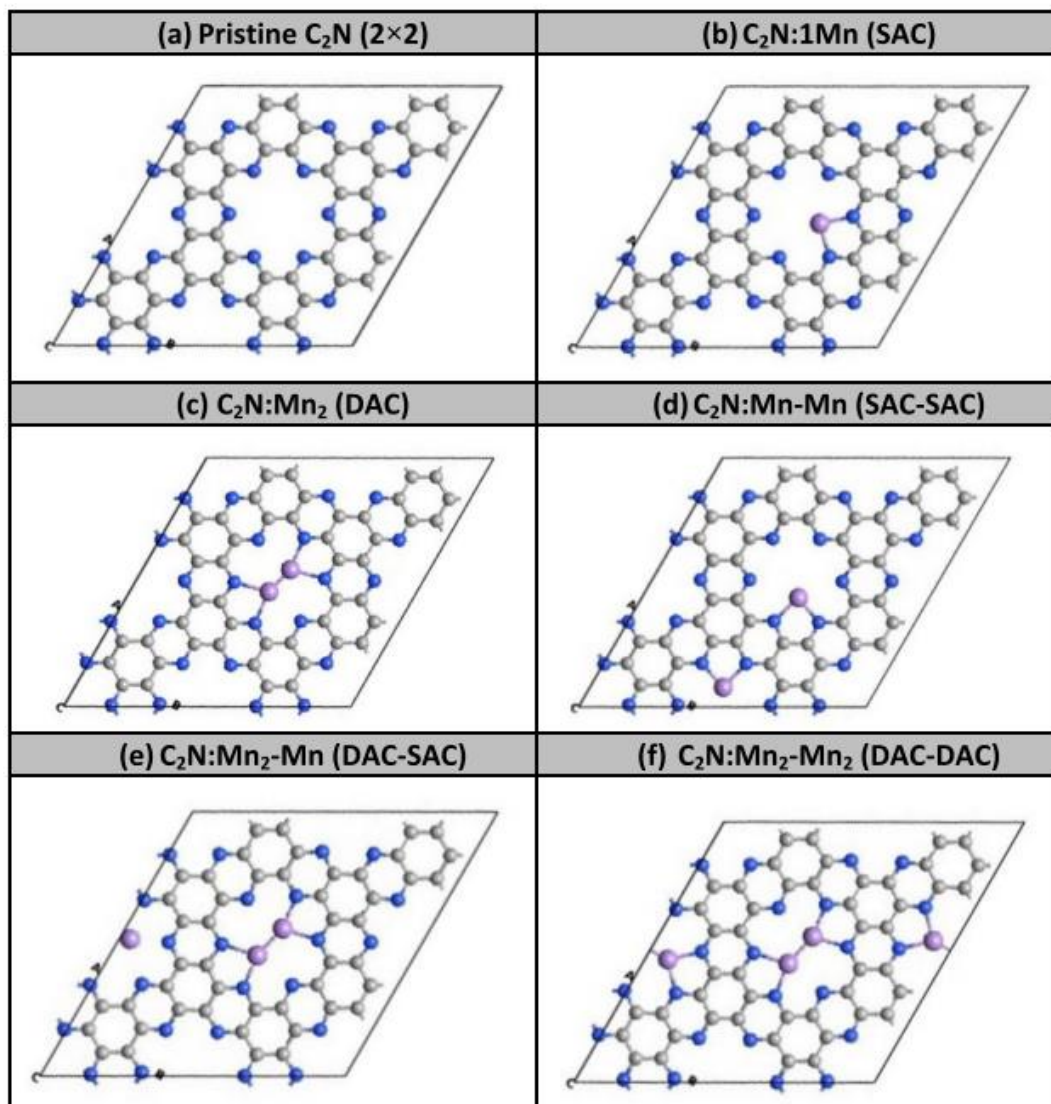
Figure 6.1: Relaxed atomic structures of C_2N 2x2 PCs supercell with and without Mn-atom catalysts.

Table 6.1 shows the geometrical parameters of relaxed structures in the cases yielding the half-metallicity character. Figure 6.1 shows six relaxed structures: (a) Pristine C_2N; (b) C_2N with 1-Mn (SAC) inside the big pore; (c) C_2N with 1 DAC-Mn inside the big

128

pore; (d) C_2N with double SACs Mn inside two neighboring big pores; (e) C_2N with 1 DAC + 1 SAC of Mn atoms embedded inside two neighboring big pores; and (f) C_2N with 2 DACs Mn inside two neighboring big pores.

Table 6.1: Geometrical parameters of relaxed structures of pristine and Mn doped C_2N samples of 2x2.

(a) Pristine C_2N (2×2)	(b) C_2N:1Mn (SAC)
b_{C-C} = 1.43 - 1.47 Å[¶], 1.43-1.47 Å[‡] b_{C-N} = 1.34 Å[¶], 1.34 Å[‡] Ang(C-N-C) = 118[¶], 118°[‡] A = B = 16.685 Å[¶], 16.66 Å[‡], 16.66 Å[†]	b_{Mn-N} = 1.88 – 1.91 Å[¶] Ang(N-Mn-N) = 85.77°[¶] A = B = 16.685 Å[¶]
(c) C_2N:Mn_2 (DAC)	(d) C_2N:Mn-Mn (SAC-SAC)
b_{Mn-N} = 1.93 – 2.03 Å[¶] b_{Mn-Mn} = 2.02 Å[¶] Ang(N-Mn-N) = 82.99° – 83.10°[¶] A = B = 16.685 Å[¶]	b_{Mn-N} = 1.85 – 1.96 Å[¶] Ang(N-Mn-N) = 85.52° – 85.64°[¶] A = B = 16.685 Å[¶]
(e) C_2N:Mn_2-Mn (DAC-SAC)	(f) C_2N:Mn_2-Mn_2 (DAC-DAC)
DAC: b_{Mn-N} = 1.93 – 2.03 Å[¶] b_{Mn-Mn} = 2.02 Å[¶] Ang(N-Mn-N) = 84.29° – 84.97°[¶] **SAC:** b_{Mn-N} = 2.12 – 2.31 Å[¶] Ang(N-Mn-N) = 74.12°[¶] A = B = 16.685 Å[¶]	b_{Mn-N} = 1.92 – 2.02 Å[¶] b_{Mn-Mn} = 2.03 – 2.20 Å[¶] Ang(N-Mn-N) = 84.35° – 89.21°[¶] A = B = 16.685 Å[¶]

The details about the results are summarized in Table 6.1 and should be described as follows:

- Pristine C_2N: The results showing a lattice constant a= 8.34 Å and bond lengths b_{C-C}= 1.43-1.48 Å, b_{C-N} = 1.34 Å, and $angle_{(C-N-C)}$ = 118° are in excellent agreement with the experimental data reported by the inventors Mahmood and et al [12] and the DFT results of Liu et al [239] and Ma et al [127]. In most of the work reported here, we used a supercell of size 2×2 PCs as to be optimally suitable to assess the effects of the embedment of 1–4 TM atoms on the acquisition of half-metallicity within the framework and the capability of VASP-package. Basically, we screened all the ten TM atoms with various combinations of SAC and DAC and found only three elements (Mn, Fe, and Ni) to yield the half metallicity.

- C$_2$N:1Mn (SAC): Figure 6.1(b) shows the case of SAC-Mn embedded in the large pore of C$_2$N. It is very important to emphasize that such embedment is thermodynamically very stable as it indeed corresponds to very strong binding energy (i.e. E$_{bind}$ = −4.497 eV for Mn in Table 6.2).

Table 6.2: Magnetization and properties in 2x2-PC C$_2$N samples with and without Mn, Fe and Ni catalyst cases.

Structure	E_{bind} (eV)	$E_g^{spin-up}$ (eV)	$E_g^{spin-down}$ (eV)	Property	M (μ_B)
(a) Pristine C$_2$N	N/A	1.67	1.67	Semiconductor	0
(b) C$_2$N:Mn (SAC)	−4.497	0	0	Metal	4.33
(c) C$_2$N:Mn (DAC)	−7.645	0.405	0	Half-metal	4.0
(d) C$_2$N:Mn (SAC–SAC)	−9.126	0.20	0	Half-metal	8.004
(e) C$_2$N:Mn (DAC–SAC)	−11.881	0.246	0	Half-metal	7.0
(f) C$_2$N:Mn (DAC–DAC)	−14.597	0	0	Metal	7.575
(g) C$_2$N:Fe (DAC)	−5.885	0	0.368	Half-metal	2.0
(h) C$_2$N:Ni (DAC–SAC)	−10.711	0	0.164	Half-metal	1.999

Table 6.3: Magnetization and properties in 3x3-PC C$_2$N samples with and without Mn, Fe and Ni catalyst cases.

Structure	$E_g^{spin-up}$ (eV)	$E_g^{spin-down}$ (eV)	Property	M (μ_B)
(a) C$_2$N:Mn (DAC)	0.302	0	Half-metal	4.0
(b) C$_2$N:Mn (SAC–SAC)	0	0	Metal	7.533
(c) C$_2$N:Mn (DAC–SAC)	0	0	Metal	7.001
(d) C$_2$N:Fe (DAC)	0.739	0.295	Magnetic semiconductor	2.0
(e) C$_2$N:Ni (DAC)	0.148	0.177	Magnetic semiconductor	2.0
(f) C$_2$N:Ni (DAC–SAC)	0	0.163	Half-metal	1.999

In the relaxation process, the Mn atom was initially placed at the center of the big pore. However, the center seems to be an unstable point and during the relaxation the Mn atom moved closer to make two single covalent bonds with the two nitrogen atoms at the border of the big pore at distance of about 1.88–1.91 Å. This bond length is smaller than the sum of the two atomic radii 2.32 Å [127], revealing the covalent character of the bonding. The final destiny of Mn atom is to stabilize at off center by an off distance of about 0.7 Å with a binding energy deeper than the center by about 55 meV. These results are also in good agreement with those reported by Ma et al [127].

C$_2$N:Mn$_2$ (DAC): Figure 6.1(c) shows the case of DAC-Mn embedded as a dimer in one large pore of C$_2$N. As it is shown, each Mn atom gets attached to two N atoms, with

respective bond length b_{Mn-N} = 1.93 Å and 2.03 Å, while the dimer makes an inter Mn–Mn bond b_{Mn-Mn} = 2.02 Å. The dimer Mn_2 occupies positions inside the big pore at the membrane plane like the case of copper dimer reported by Zhao et al [126]. The relaxed configuration of dimer Mn_2 has a binding energy $E_{bind}(2Mn)$ = -7.645 eV dimer^{-1} (Table 6.2).

Comparing this latter energy value to the binding energy of SAC-Mn, which is $E_{bind}(1Mn)$= -4.497 eV, one can extract the recursive energy of the second Mn-atom to be about E_{rec} = -3.148 eV, whose magnitude is still larger than Mn-cohesive energy (i.e., E_{coh} = 2.92 eV) [126]). So, one can deduce that the DAC-Mn can be very stable inside the pore and contribute to the so-called irreversible capacitance in the language of metal-ion battery perspectives [196].

C_2N: Mn–Mn (SAC-SAC): As initial positions, two Mn atoms were put at the centers of two neighboring big pores of C_2N. Throughout the relaxation process, they move closer so that each Mn atom makes two bonds with the nitrogen atoms at the wall of the pore as shown in Figure 6.1(d). The bond lengths of Mn–N are about b_{Mn-N} = 1.85–1.96 Å and the bond angle is about $Ang_{(N-Mn-N)}$ = 85.52◦–85.64◦ very similar to the case of SAC.

C_2N:Mn_2–Mn (DAC-SAC): After relaxing a dimer of Mn_2 in the central large pore, the third Mn atom was initially placed at the center of the neighboring large pore and the atomic relaxation is again carried out. The results are shown in Figure 6.1(e) and the geometric parameters are displayed in Table 6.1. For SAC-Mn, the bond length Mn–N is about b_{Mn-N} = 2.12–2.31 Å (i.e., a bit larger than the case of single SAC) and bond angle $Ang_{(N-Mn-N)}$ = 74.12◦ (i.e., a bit smaller than the case of single SAC). For DAC-Mn_2, the bond length b_{Mn-N} = 1.92–2.03 Å (i.e. same as in the case of single DAC) and bond angle $Ang_{(N-Mn-N)}$ = 84.29°- 84.97° (i.e. a bit larger than the case of single DAC). The dimer bond-length is about b_{Mn-Mn} = 2.02 Å, smaller than the sum of the two radii (2R=2.56 Å) [146], revealing the covalent-character aspect.

C_2N:Mn_2–Mn_2 (DAC– DAC): Two dimers Mn_2 were atomically relaxed in two neighboring large pores of C_2N. The results of relaxed structure are shown in Figure 6.1(f) and Table 6.1. The obtained values of bond lengths Mn–N are about b_{Mn-N} = 1.92–2.02 Å (i.e., about same as single DAC) and bond angles $Ang_{(N-Mn-N)}$ = 84.35°–89.21° (i.e. a bit larger than the case of single DAC). The dimer bond-length is about b_{Mn-Mn} =

2.03–2.20 Å (i.e., similar to single DAC). So, the dimers should be assumed to alter covalent bonding with the C_2N lattice.

6.4.2 Spin Polarized Partial Density of States (PDOS)

Figure 6.2 shows the spin-polarized PDOS corresponding to the samples shown in the previous Figure 6.1 with basically the Valence-Band Maximum (VBM) energy and Fermi level are taken as an energy reference in cases of pristine and Mn-doped C_2N, respectively.

- Pristine C_2N: Figure 6.2(a) shows the contributions of both C and N atoms to the Total Density of States (TDOS). The results are based on VASP calculations and do yield a bandgap energy of Eg = 1.67 eV, which is a bit less than the experimentally reported one of 1.96 eV [12]. Such underestimation of bandgap energy is expected in case of using DFT with plane wave basis set unless further consideration of hybrid functional for the exchange correlation should be involved. Moreover, the nitrogen atoms are shown to predominantly contribute to the structure of the valence band due to their possession of filled dangling bonds.

- C_2N:1Mn (SAC): The embedment of one Mn atom in the big pore of C_2N sample of size 2×2 PCs would lead to the metallization of the samples. Figure 6.2(b) shows Fermi level shifting up to cross the dispersive bands originating from Mn atoms. Moreover, the asymmetry existing between spin-up and spin-down TDOS should reveal the existence of magnetization (i.e., magnetic moment). Hence the obtained system is FM metal.

- C_2N:Mn$_2$ (DAC): the embedment of DAC-Mn as a dimer in one big pore, proven to be very stable, is shown in Figure 6.2(c) to yield half-metallicity character. Not only does the system get magnetized, as displayed by the asymmetry between spin-up and spin-down TDOS, but Fermi level crosses some spin-down bands while spin-up states behaving semiconducting and having an energy gap of 0.405 eV. It is worth to emphasize some reduction in magnetization from 4.33 μ_B to 4.0 μ_B corresponding to SAC and DAC, respectively (Tables 6.2 and 6.3). Such reduction reveals that the two Mn-atoms stabilize into an Anti-Ferromagnetic (AFM) state. One question should be raised about the origins of 'half metallicity' is whether it will be due to the existence of such AFMC interaction or due to the FMC

132

interactions of the whole magnetic moment with its (six) mirror images, which are expected to be formed by periodic-boundary conditions. Throughout the present investigation we will come up with answers to this question.

- C_2N:Mn–Mn (SAC–SAC): The embedment of two SAC-Mn atoms in neighboring big pores would also induce the half-metallicity character as it is shown in Figure 6.2(d). Like the previous case of C_2N:Mn_2 (DAC), Figure 6.2(d) shows the asymmetry between spin-up and spin-down states' contributions to TDOS revealing the existence of magnetic moment (M = 8.004 μ_B), which is about the double of the value of SAC case shown in Figure 6.2(b). Such huge magnetic moments should reveal that the SAC–SAC configuration has stabilized to yield FM state. The second question one should raise here is about the origins of the 'half-metallicity', was it due to the FMC interaction between SAC–SAC or between the whole magnetic moment and the others due to the (six) mirror images.

- C_2N:Mn_2–Mn (DAC–SAC): Figure 6.2(e) shows another case of realization of 'half-metallicity' character due to the embedment of DAC and SAC Mn atoms in two neighboring big pores of C_2N. Fermi level is shown to cross the spin-down states as becoming metallic while the spin-up states remaining semiconducting with an energy gap of 0.246 eV. The total magnetization of DAC–SAC is shown in Tables 6.2 and 6.3 to be about M = 7.0 μB, which is less than the case of SAC–SAC and thus revealing an AFMC to take place between the two atoms of DAC configuration. The acquisition of the half-metallicity characters in the three cases (c–e) will be proven to originate from the FMC interactions with the six mirror images, formed by the periodic boundary conditions.

- C_2N:Mn_2– Mn_2 (DAC–DAC): Figure 6.2(f) shows that the embedment of DAC–DAC in two neighboring pores of C_2N would result in magnetic metal with a magnetization of about M = 7.575 μ_B, which is larger than the case of DAC–SAC but smaller than the case of SAC-SAC. It might reveal the fact of existence of AFMC interaction within DAC and FMC interaction between DAC–DAC.
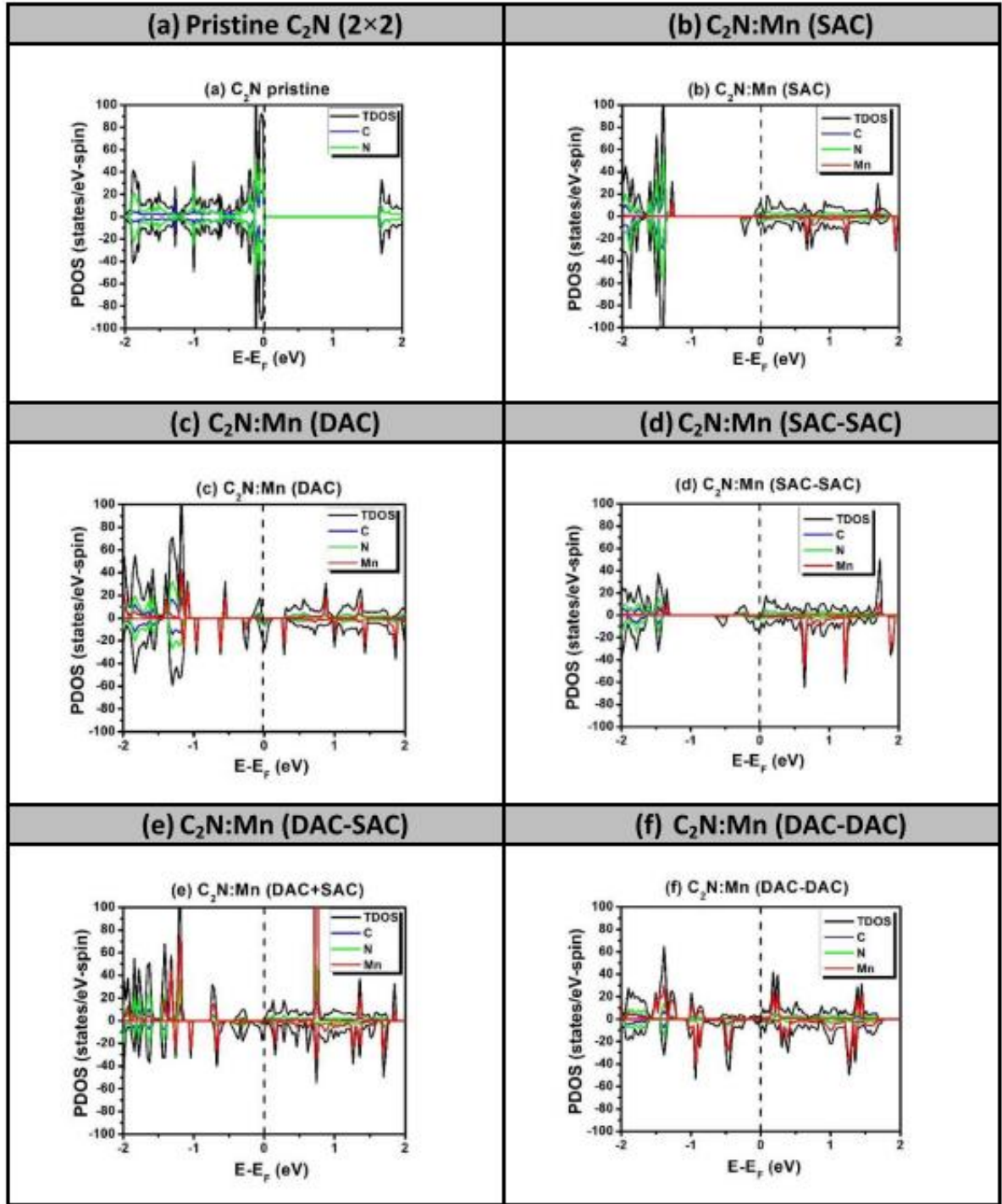
Figure 6.2: Spin polarized PDOS of C_2N 2x2 supercell with and without Mn-atom catalysts.

6.4.3 VBM, CBM and Fermi Eigenstates

In attempting to dig for further understanding of the half-metallicity characteristics, we performed calculations of the VBM, the Conduction Band Minimum (CBM), and the Fermi eigenstates corresponding to semiconducting and metallic behaviors of the two

spin states, respectively. Besides, we performed the calculations of the Orbital Density of States (ODOS). Figure 6.3 shows the eigenstates density plots corresponding to all the samples displayed in the previous Figure 6.2. Of course, only cases (c–e) are previously known to host the 'half-metallicity' character. Details of the distribution of the eigen-states are as follows:
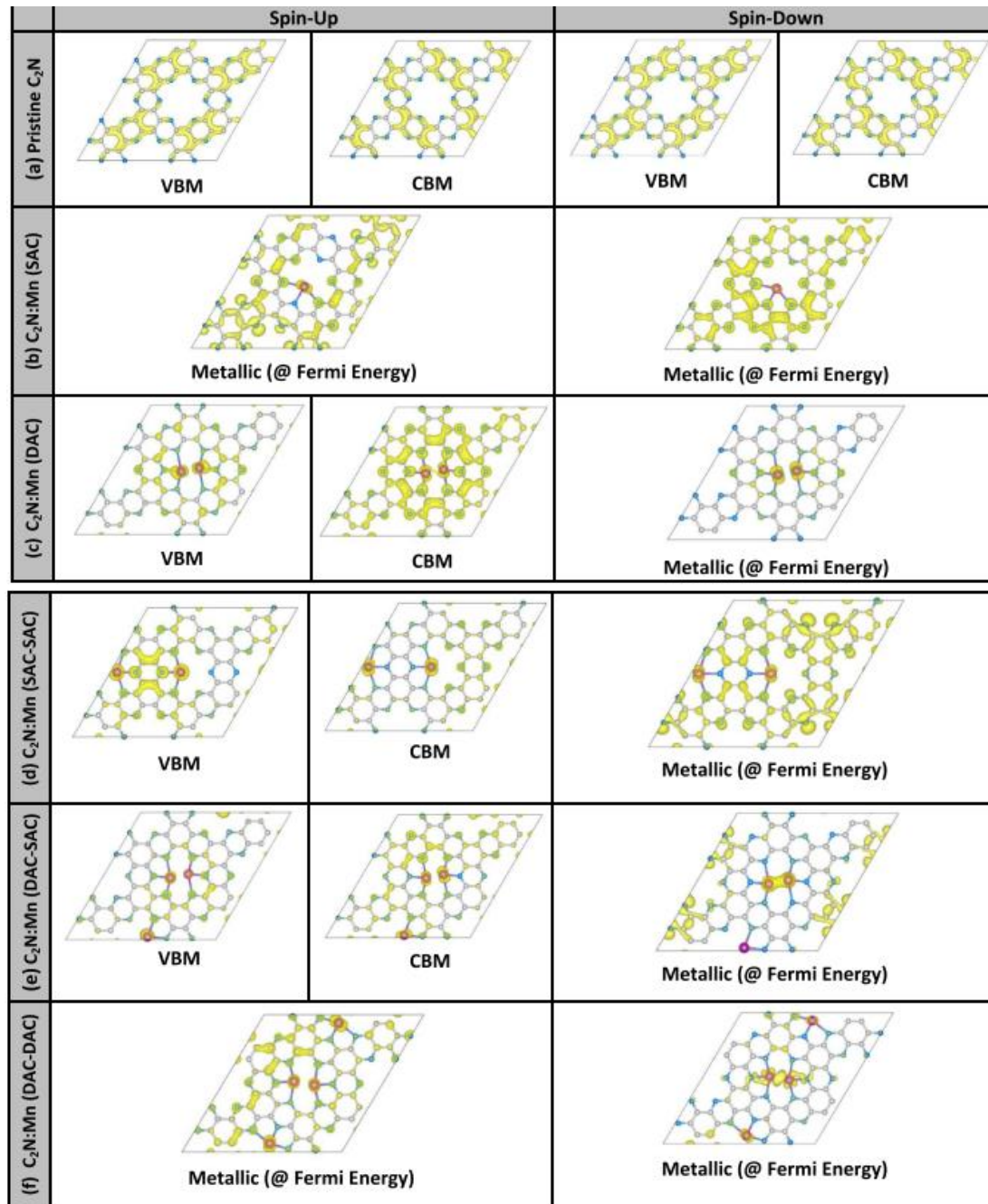
Figure 6.3: Eigen-functions of VBM, CBM and Fermi-level states of C_2N 2x2-PCs supercell with and without embedment of Mn-atom catalysts.

- Pristine C_2N behaves as paramagnetic semiconducting. So, there is no distinction between spin-up and spin-down states. The VBM state and the CBM state are shown to be predominated by the N atoms to corroborate the results of PDOS shown in Figure 6.2(a).

- C_2N:1Mn (SAC): The embedment of SAC-Mn in one big pore of C_2N would yield a magnetic metal, as shown in the previous Figure 6.2(b). The density plots of Figure 6.3(b) shows both spin states behave metallic as their Fermi eigenstates are hosted by all types of atoms and to be percolating from one side to the other.

- C_2N:Mn_2 (DAC): In this case the spin-up states behave semiconducting, and one needs to present both their corresponding VBM and CBM eigenstates; whereas the spin down behaves metallic to yield the 'half-metallicity.' While the VBM/CBM states are hosted by all species in the samples (Figure 6.3(c)), the metallic spin-down states are attributed mainly to the two Mn atoms. So, one would expect some d orbitals mixing to take place in the spin-down states.

- C_2N:Mn-Mn (SAC–SAC): Similarly to the previous case, the spin-down here also behaves metallic to yield 'half-metallicity'. VBM/CBM eigen-states due spin-up sates are attributed basically by all species of atoms in the sample (Figure 6.3(d)), while the metallic spin-down states at Fermi level are shown to kind of repel from the vicinities of two SAC sites but clearly shown to be percolating to yield metallicity. Yet, the mixing of orbitals at Fermi level seems to take place in a fashion different from that of DAC-based half-metallicity.

- C_2N:Mn_2–Mn (DAC–SAC): This is a third case to yield half-metallicity where spin-down states behave metallic while the spin-up remains semiconducting. In this case, the spin-up eigenstates of VBM and CBM are shown in Figure 6.3(e) to be mainly attributed to the host-crystal atoms (i.e., C and N atoms). On the other hand, the metallic spin-down states are shown to have contributions more on DAC than SAC in addition to the C and N atoms of the sample. This might reveal the mixing of d-states of the two Mn atoms of DAC structure.

- C_2N:Mn_2–Mn_2 (DAC–DAC): The embedment of two DACs in two neighboring pores of C_2N would yield magnetic metal where both spin-up and spin down exhibit mixing of d-orbitals of Mn atoms within two DACs. The eigen-states at

Fermi levels corresponding to the two spin-states are shown in Figure 6.3(f) to be attributed to both DACs as well as N and C atoms in the sample.

6.4.5 Screening of TM Doping Versus Half-Metallicity

The selection of manganese in our presented study, so far, is based on its high catalytic activity and FM character as it possesses five unpaired d electrons. We have scanned all the TM atoms ranging from Sc to Zn and searched for possible configurations to obtain half-metallicity. We took the three cases of Mn atoms (DAC, SAC–SAC and SAC–DAC) yielding half-metallicity as model configurations. Nonetheless, we obtained just two further cases exhibiting half metallicity, which correspond to: (a) $C_2N:Fe_2$ (DAC) and (b) $C_2N:Ni_2$–Ni (DAC–SAC). All the results shown in these latter figures show metallic behavior for both spin states. Throughout the present investigation, the occurrence of half metallicity requires the providence of two simultaneous conditions, which are kind of a compromise between synergetic and FMC-interaction effects. The lack of these conditions would affect the occurrence of half-metallicity. So, having said that, the fact that the half-metallicity found to take place only in special cases, specifically when using the FM elements such as Mn, Fe, and Ni, but not to occur in Co is among the wonders. Furthermore, it is important to emphasize the relevance of magnetic semiconductors for spintronic device applications as was recently reported by Anbuselvan et al [240]. Nonetheless, in the current investigation, we would rather focus on cases of half-metallicity.
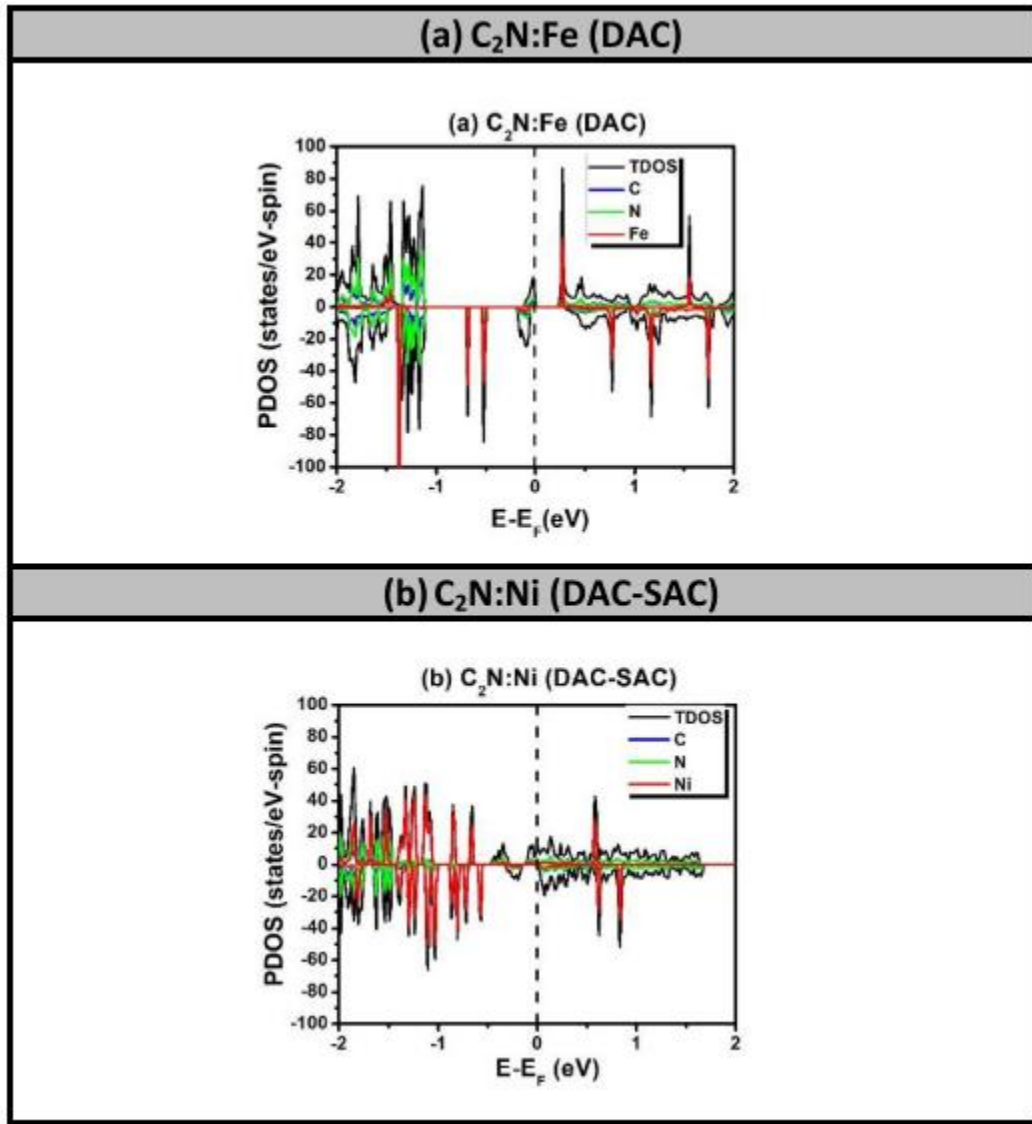
Figure 6.4: Spin-polarized PDOS of C_2N with catalysts Fe and Ni as DACs and SACs respectively.

Figure 6.4 shows the spin polarized PDOS of these samples:

(a) $C_2N:Fe_2$ (DAC): Figure 6.4(a) displays half-metallicity where spin-up states behave as metallic, while the spin-down state remains semiconducting with bandgap energy of about 0.368 eV. The Fe atom is supposed to possess four unpaired d-electrons and 2s-electrons when it is a free atom. In the configuration of DAC-Fe embedded in C_2N, three electrons in each Fe-atom are engaged in the bonding. Yet, Table 6.2 shows that the magnetization of the configuration corresponding to Figure 6.4(a) is about $M = 2$ μ_B. This in turn suggests that the DAC-Fe stabilizes in an AFM configuration (i.e., like Mn_2 DAC).

(b) C_2N:Ni_2–Ni (DAC–SAC): Figure 6.4(b) shows the half-metallicity character when Ni_2–Ni (DAC– SAC) are embedded in two neighboring large pores of C_2N. Fermi level crosses the spin-up states to reveal their metallization while spin-down states remain semiconducting with an energy bandgap of about 0.164 eV. The magnetization value is higher than the case of DAC as FMC between DAC–SAC seems to take place. In a similar way, the trend of half-metallicity seems to remain occurring in similar fashion to Mn embedment in C_2N. We will show below that that trend should rather be attributed to the FMC of the total magnetization with its six mirror images. Figure 6.5 displays the VBM/CBM and Fermi eigen-states corresponding to the two samples whose PDOSs were elaborated in the previous Figure 6.4.
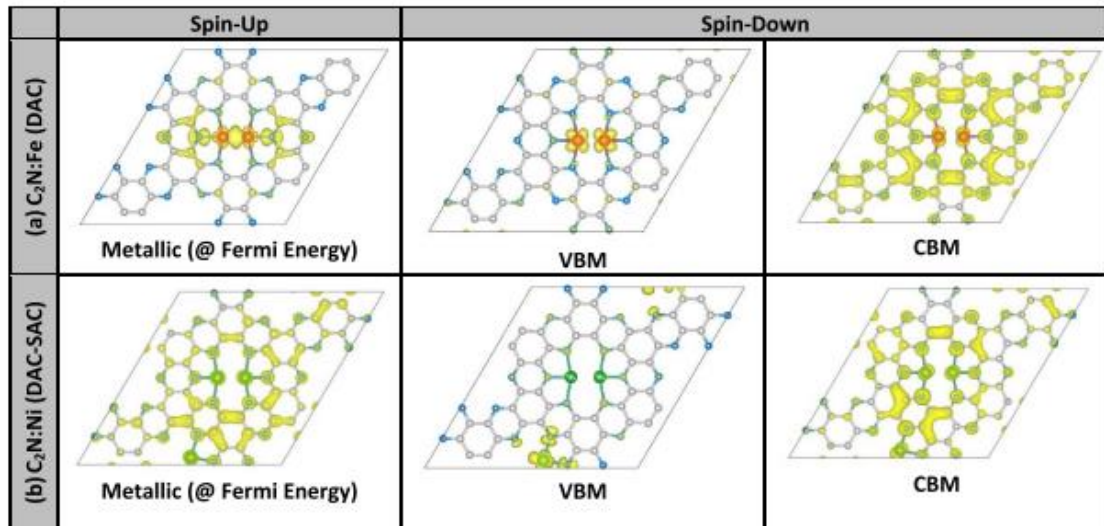
Figure 6.5: Eigenfunctions of VBM, CBM and Fermi level of C_2N 2x2 supercell with Fe and Ni atom catalysts.

Namely, the two structures are as follows:

(a) C_2N:Fe_2 (DAC): It exhibits half-metallicity due to spin-up states becoming metallic. So, Figure 6.5(a) presents the eigen-state at Fermi level associated with spin up states, and the VBM/CBM eigen-states due to the spin-down states exhibiting the semiconducting behavior. The Fe-dimer seems to induce metallization in spin-up states through bands to be carried by C and N atoms around the DAC-Fe. On the other hand, the spin-down states behave semiconducting where the VBM is a very localized state at the DAC-Fe and the CBM is a delocalized state

on all sites but not DAC-Fe. Such behaviors of VBM/CBM states should be good model representation of materials with indirect bandgap transitions (see for instance the band structure in Figure 6.7(e)).

(b) C_2N:Ni_2–Ni (DAC–SAC): This structure behaves as half-metallic with the spin-up states being conductive while spin-down states remain semiconducting. Figure 6.5(b) shows all the eigenstates of spin-up at Fermi level, and spin-down VBM/CBM to be delocalized. The metallization in spin-up states might be caused by FMC interactions between the total magnetic moment at the DAC–SAC complex and its six mirror images, which are formed by the periodic-boundary conditions.

6.4.6 Bands and ODOS

To pursue further analysis about the origins of the 'half-metallicity' Figures 6.6 and 6.7 present the spin-polarized band structures and the ODOS for the pristine C_2N sample of 2×2 PCs in size and the five samples hosting half-metallicity.

In Figure 6.6, the spin-up and spin-down are presented by the green dashed and red-solid curves, respectively.

(a) Pristine C_2N sample of 2×2 PCs shows the evidence of para-magnetism where both spins are indistinguishable. Pristine C_2N is shown to have a direct bandgap of Eg = 1.67 eV at Gamma-point (i.e., as being folded from K-point of Brillouin zone, which is the Wigner–Seitz cell of the reciprocal lattice). All the remaining samples behave FM and whose bands are spin-dependent as follows:

(b) C_2N:Mn_2 (DAC): spin-down bands (red-solid curves) are metallic and spin-up bands (green-dashed curves) are semiconducting with an energy bandgap of 0.405 eV.

(c) C_2N:Mn–Mn (SAC–SAC): spin-down (red-solid curves) are dispersive at Fermi level and thus metallic; whereas the spin-up bands (green-dashed curves) are semiconducting with an energy bandgap of about 0.20 eV.

(d) C_2N:Mn_2–Mn (DAC–SAC): spin-down bands (red-solid curves) are metallic as crossing Fermi level in dispersive fashion. The spin up bands (green-dashed curves) are semiconducting having an energy bandgap of 0.25 eV.

(e) C$_2$N:Fe$_2$ (DAC): spin-up states (green-dashed curves) behave metallic while spin-down states (red-solid curves) are semiconducting with an energy bandgap of 0.37 eV.

(f) C$_2$N:Ni$_2$–Ni (DAC–SAC): spin-up states (green dashed curves) behave metallic while the spin-down states (red-solid curves) are semiconducting with an energy bandgap of 0.16 eV.
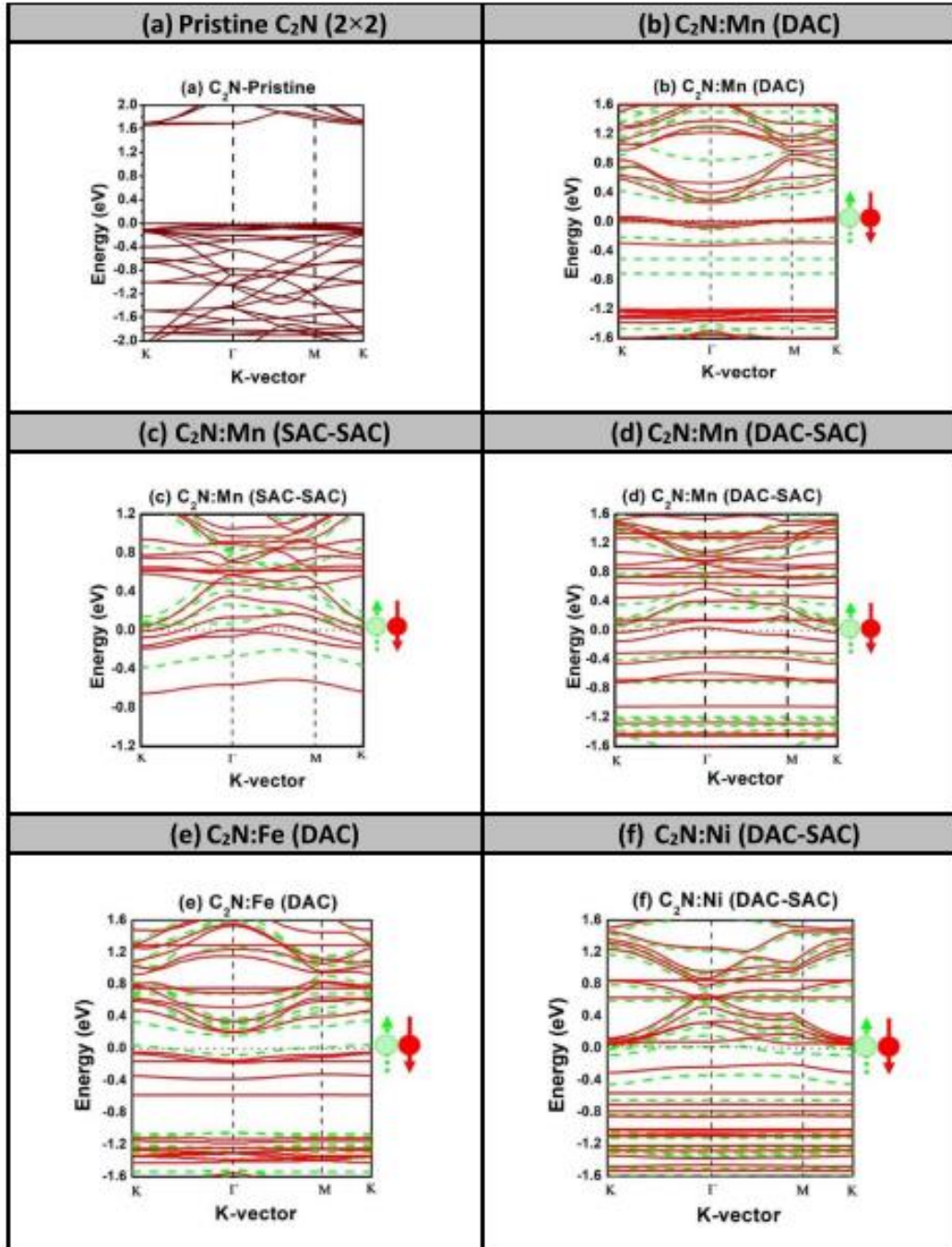
Figure 6.6: Spin polarized band structures of C$_2$N with TM atom catalysts yielding half metallicity.

Figure 6.7 displays the results of spin-polarized ODOS for all the six samples including the pristine C_2N 2×2-PC sample and all the five samples hosting half-metallicity. Figure 6.7(a) presents the case or pristine sample and shows the contributions from the s and p orbitals on each C and N atom. The valence band seems to be predominantly composed of C(p) and N(p) orbitals and more specifically attributed to the filled dangling orbitals residing on the N atoms at the big pores.

In the case of Mn-doped C_2N with the catalysts in configurations of DAC, SAC–SAC, and DAC–SAC, shown in Figures 6.7(b)–(d), respectively, the metallization occurs in the spin-down states. The contributions to the spin-down metallic bands are shown to be attributed mainly to the metal catalyst 'Mn' and the neighboring C and N atoms at the perimeter within the big pore containing the catalysts.

In the cases of Fe and Ni catalysts, the DAC and DAC–SAC configurations are found to host the halfmetallicity, as shown in Figures 6.7(e) and (f). In both these latter cases, the metallization takes place in the spin-up states and attributed to the metal atom and its surrounding C and N atoms located at the perimeter of the large pore.
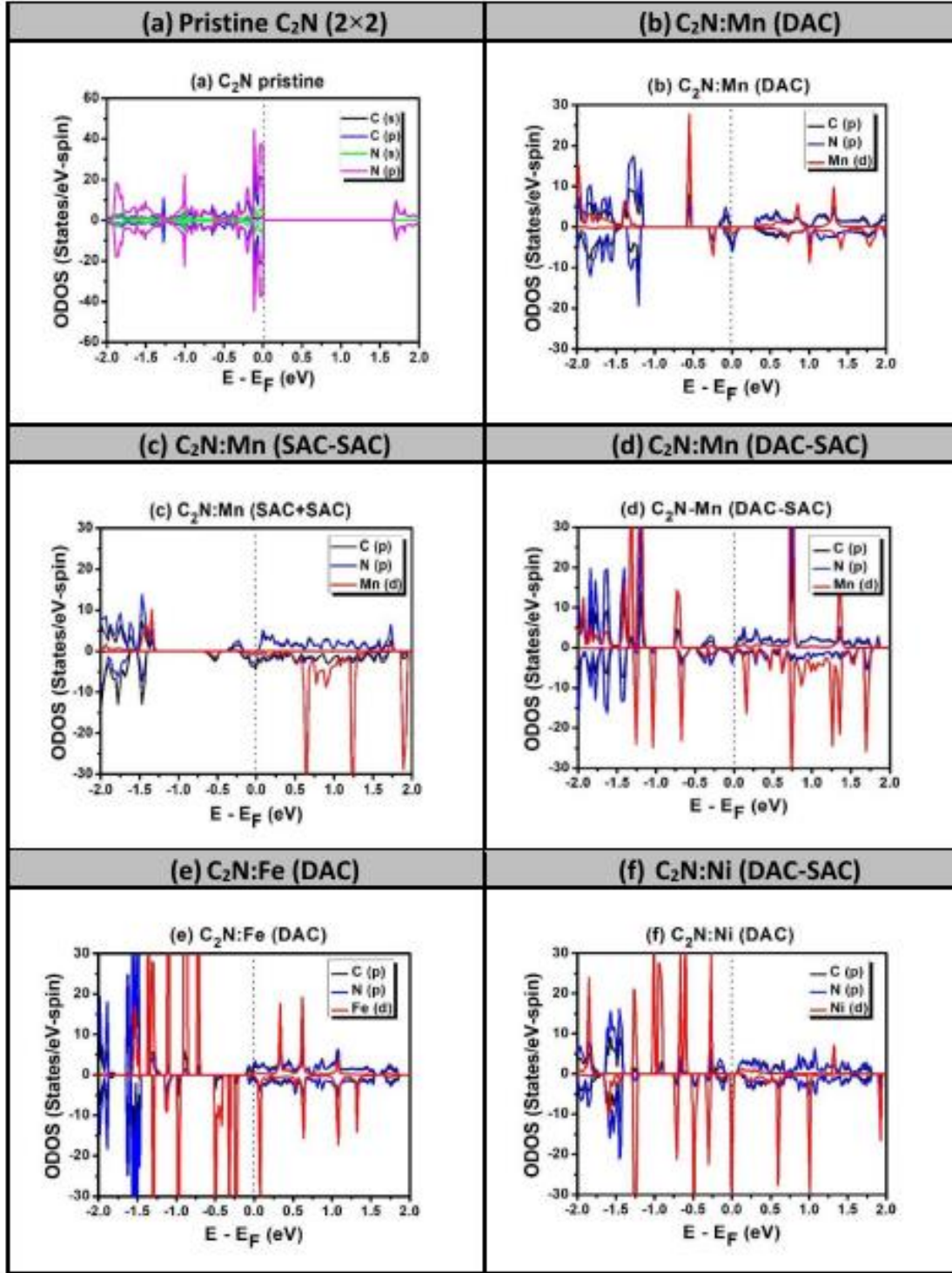
Figure 6.7: Spin polarized ODOS of cases of C_2N with embedment of TM-atom catalysts yielding half metallicity

6.4.7 FMC versus Sample Scaling

Focusing on the origins of half-metallicity in TM doped C_2N, it is due to synergetic effects of incorporating more than one dopant in adjacent locations. SAC-TM alone cannot make it happen.

143

Table 6.4: The variation of magnetization, spin polarized band gap and FMC potential "V_{FMC}" versus distance between M centers.

Host	Sample 2x2				Sample 3x3				Sample 4x4			
	$d_{M\text{-}M}$ (Å)	M (μ_B)	Property BW (eV), V_{FMC} (meV)	E_g^{Up} E_g^{Down} (eV)	$d_{M\text{-}M}$ (Å)	M (μ_B)	Property BW (eV), V_{FMC} (meV)	E_g^{Up} E_g^{Down} (eV)	$d_{M\text{-}M}$ (Å)	M (μ_B)	Property BW (eV), V_{FMC} (meV)	E_g^{Up} E_g^{Down} (eV)
Pristine C_2N	N/A	0	S/C	1.67 1.67	N/A	0	S/C	1.67 1.67	N/A	0	S/C	1.67 1.67
C_2N:Mn (DAC)	16.66	4.0	Half Metal 0.150 (12.5)	0.405 0	25.0	4.0	Half Metal 0.050 (4)	0.302 0	33.33	4.33	S/C	0.64 0.55
C_2N:Mn (SAC-SAC)	16.66	7.0	Half Metal 0.240 (20)	0.20 0	25.0	7.533	Metal	0.0 0.0	.....	.....	.....	.....
C_2N:Mn (DAC-SAC)	16.66	7.0	Half Metal 0.230 (19)	0.25 0	25.0	7.001	Metal	0.0 0.0	.....	.....	.....	.....
C_2N:Fe (DAC)	16.66	2.00	Half Metal 0.122 (10)	0.0 0.368	25.0	2.00	Magnetic S/C	0.739 0.29	.....	.....	.....	.....
C_2N:Ni (DAC-SAC)	16.66	1.999	Half Metal 0.185 (15.4)	0.0 0.164	25.0	1.999	Half Metal 0.105 (9)	0.0 0.163	33.33	1.9224	S/C	0.25 0.504

Now, the next decisive question is whether the half-metallicity is a product of an internal FMC/AFMC interactions within the group of TM dopants or external FMC interactions of the group with its six mirror images, formed on the xy-plane by the periodic boundary conditions.

In order to assess this latter hypothesis, we have tested the existence of 'half-metallicity' in the case of larger samples while keeping the group of TM atoms robust. Furthermore, one should focus on both the existence of 'half-metallicity' and more specifically on the width of the band at Fermi level of the metallic spin. So, we have basically five cases to inspect, for which we calculated the spin polarized PDOS and bands. The resulting data are extracted and summarized in Table 6.4.

(a) C_2N:Mn_2 (DAC): For the sample of size 3×3 PCs, Figures 6.8(a) and 6.9(a) show the existence of metallic (dispersive) band crossing Fermi level for spin-down states while the other spin is semiconducting with bandgap energy of 0.302 eV. The half-metallicity in such system disappears in the sample of size 4×4 PCs, which becomes semiconducting.

(b) C_2N:Mn-Mn (SAC–SAC): For the sample of size 3×3 PCs, Figures 6.8(b) and 6.9(b) show the disappearance of 'half-metallicity' as both spin states becoming metallic. The bands of both spin up and spin-down states shown in Figure 6.9(b) are dispersive.

(c) $C_2N{:}Mn_2$-Mn (DAC–SAC): For the sample of size 3×3 PCs, Figures 6.8(c) and 6.9(c) confirm the disappearance of 'half-metallicity' as both spin states becoming metallic with dispersive bands crossing Fermi level.

(d) $C_2N{:}Fe_2$ (DAC): For the sample of size 3×3 PCs, Figures 6.8(d) and 6.9(d) show the disappearance of 'half-metallicity' as both spin up and spin-down states becoming semiconducting.

(e) $C_2N{:}Ni_2$–Ni (DAC–SAC): For the sample of size 3×3 PCs, Figures 6.8(e) and 6.9(e) show the half metallicity to still exist and is due to the metallization of spin-up states while the spin-down states behave as semiconducting with bandgap energy of about 0.163 eV. Nonetheless, for larger sample size 4×4 PCs, the 'half-metallicity' disappears as both spins becoming semiconducting. In brief, the disappearance of 'half-metallicity' for larger samples is confirming that it originates from the FMC interactions of the magnetization of the group of dopants with the six mirror images, formed on xy-plane by the implementation of the periodic-boundary conditions.
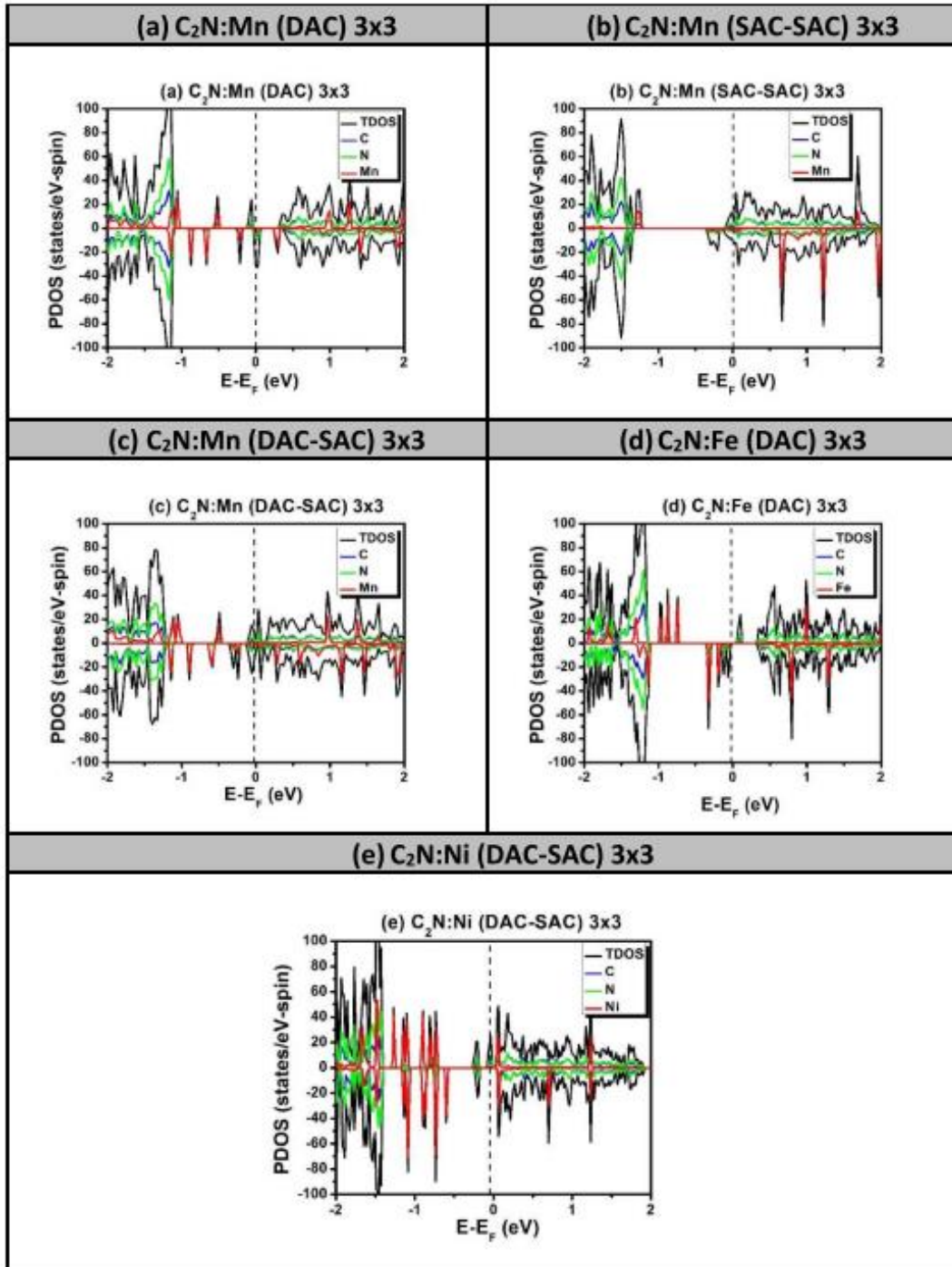
Figure 6.8: Spin polarized PDOS of 3x3 scaled up samples of C_2N with TM catalysts that exhibited half metallicity in 2x2 sample size.

The FMC interaction, inducing the half metallicity, have potential energies of magnitude up to 20 meV and spatially ranging up to critical lengths of order Lc ~ 21–29 Å, as shown in Table 6.4.

146
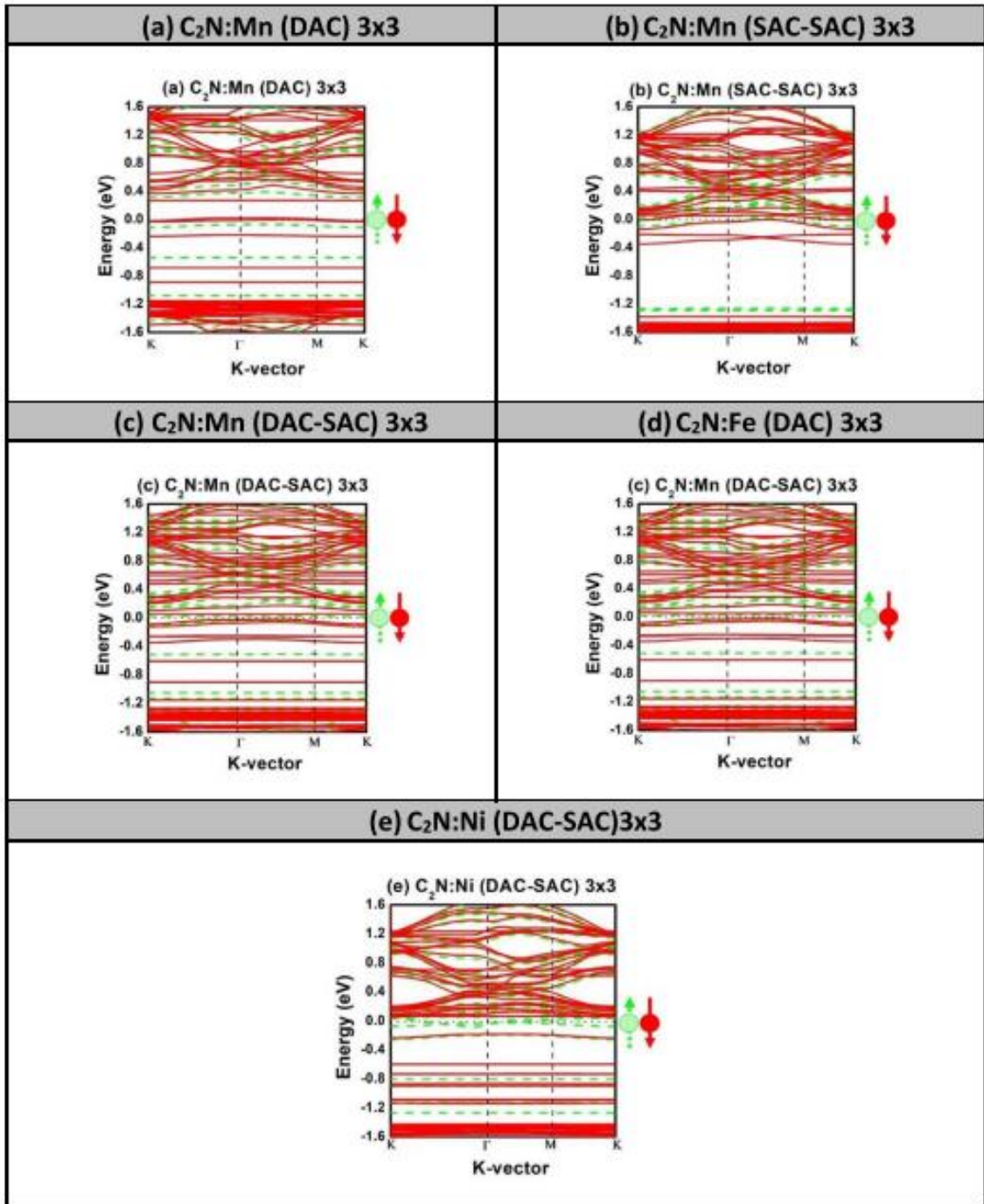
Figure 6.9: Spin polarized band structures of 3x3 scaled up samples of C_2N with TM atom catalysts that exhibited half metallicity in 2x2 sample size.
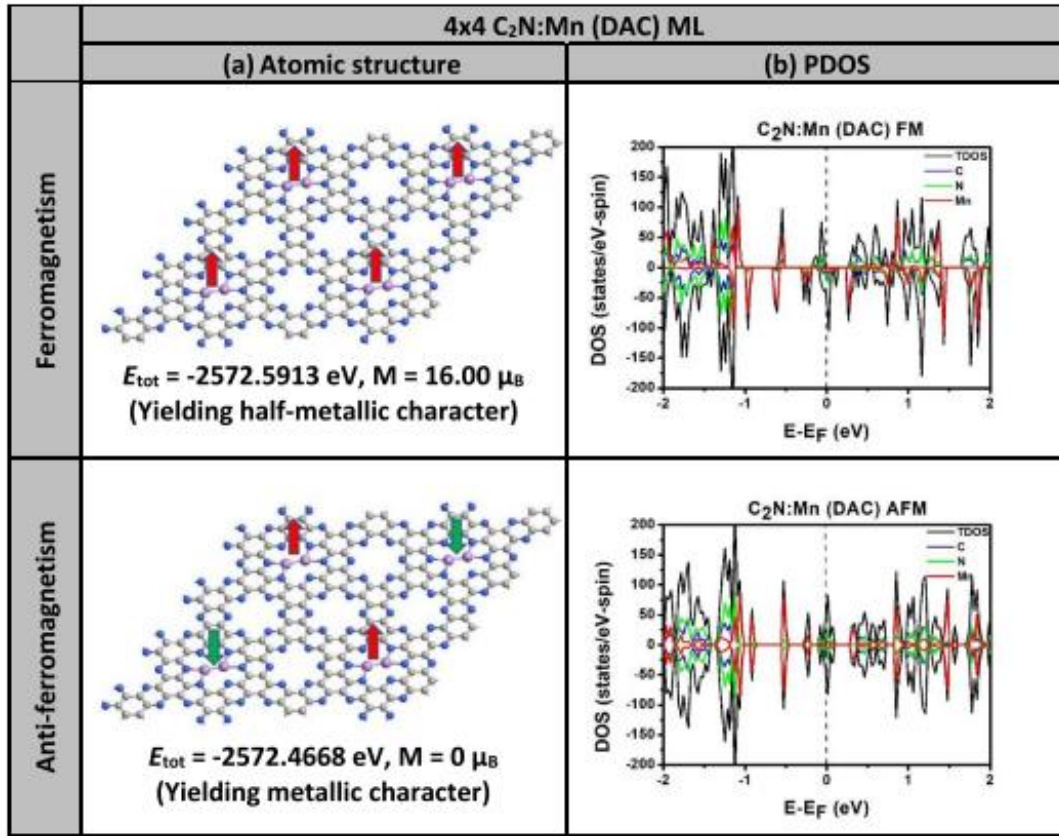
Figure 6.10: Comparison between the effects of FMC and AFMC interactions on the half metallicity in 4x4 sample size.

6.4.8 Ferromagnetism and Anti-Ferromagnetism versus Half Metallicity

To assess the nature of magnetism taking place in case of occurrence of half-metallicity, it is more convenient to use a larger computational supercell such as 4×4 PC of C_2N (i.e. in case of pristine, it contains 288 atoms = 192C + 96N atoms and in case DAC–SAC the supercell should contain $288+4\times3 = 300$ atoms). This supercell should comprise four weights of repetition of the 2×2-PC sample (i.e., two simultaneous repetitions along each x and y direction). We have used this large supercell for two tasks.

In task #1, we tested to double check the existence of half-metallicity in the case of large 4×4-PC samples corresponding to five cases: (a) $C_2N:Mn$ (SAC), (b) $C_2N:Mn$ (DAC), (c) $C_2N:Mn$ (SAC–SAC), (d) $C_2N:Mn$ (DAC–SAC), and (e) $C_2N:Mn$ (DAC–DAC). The results of the spin polarized TDOS are shown in the appendix. The results are consistent with those obtained using the smaller supercell of size 2×2 PCs, displayed in Figures 6.2(b)– (f), approving the metallicity in the two cases of (a) SAC and (e) DAC–DAC;

148

and confirming the half metallicity in the other three cases (b) DAC, (c) SAC– SAC, and (d) DAC–SAC revealing the half-metallicity to be attributed to the FMC interactions. In task #2, the large-sized sample of 4×4 PCs is explored to carry out a comparison between the effects of FMC and AFMC interactions on the halfmetallicity. For demonstration, we took the case of DAC, which yields half-metallicity in the 2×2-PC sample, and we assessed the effects of both FMC and AFMC interactions on the half-metallicity in the large 4×4-PC sample. The results of relaxed atomic structures and spin polarized PDOS and TDOS are shown in Figure 6.10. It is remarkable that the total energy in the sample exhibiting FMC interactions is lower than that of the sample exhibiting AFMC interactions (i.e., $\Delta E = E_{tot}^{FMC} - E_{tot}^{AFMC} = -0.125 eV$). Consequently, the ground state should correspond to the existence of the FMC interactions. The second interesting trend shown in Figure 6.10 is that the FMC interactions do yield half metallicity whereas the AFMC interactions yield metallic state. The magnetization in the latter case seems to vanish as the AFMC interactions cannot even exist at that range of distance (which is about 16.6 Å). In our simulations, we have considered each DAC as a unity having one magnetic moment as presented in Figure 6.10, and we turned on the magnetic interactions with results displayed therein. Throughout our discussions of various combinations of SACs and DACs and various types of magnetic interactions, it should be concluded that the existence of the half-metallicity requires a compromise between synergetic and FMC effects.

Chapter 7: Functionalized Hf₃C₂ and Zr₃C₂ MXenes for Suppression of Shuttle Effect to Enhance the Performance of Sodium-Sulfur Batteries

7.1 Summary

Sodium-sulfur batteries show great potential for storing large amounts of energy due to their ability to undergo a double electron- redox process, as well as the plentiful availability of sodium and sulfur resources. However, the shuttle effect caused by intermediate sodium polysulfides limits their performance and lifespan. To address this issue, here we propose using $Hf_3C_2T_2$ and $Zr_3C_2T_2$ (T= F, O), two functionalized MXenes, as cathode additives to suppress the shuttle effect. By using density-functional theory calculations, we investigate nature of the interactions between Na_2S_n and MXene, such as strength of adsorption energy, electronic density of states, charge exchange, and dissociation energy of the Na_2S molecule. They find that both $Hf_3C_2T_2$ and $Zr_3C_2T_2$ systems inhibit the shuttle effect by binding to Na_2S_n with a binding energy higher than the electrolyte solvents. They retain their metallicity during this process and the decomposition barrier for Na_2S_n on the O functionalized MXenes gets reduced which enhances the electrochemical process. Among the MXene systems studied, $Zr_3C_2O_2$ shows the best performance in suppressing the shuttle effect and increasing the battery's reversible capacity and lifespan.

7.2 Introduction

In the last few decades, Lithium-ion Batteries (LIBs) have been the leading energy storage devices available for usage of portable electronics and Electric Vehicles (EV) [35, 241-242]. Amongst the obvious disadvantages in LIBs is the sustainability issue of lithium's resources as it is depleting in an accelerated way from the earth's crust due to the high augmenting consumption. Alternative batteries based on other materials have recently been explored, such as sodium-ion batteries [243], potassium-ion batteries [244], aluminum-ion batteries [245], zinc-air batteries [246], and Sodium-Sulfur Batteries (NaSBs) [247-248]. Recently, many researchers focused their efforts on NaSBs which demonstrated to be reliable to work at Room Temperature (RT) with high energy density. The biggest advantage of these batteries is the abundance of both sodium and sulfur in nature [247-248].

150

At higher temperatures, the NaSBs' performance reduces due to a reduction in the energy density caused by the formation of NaS_2 product instead of Na_2S_2 [249-250]. Even at RT, some constraints exist, which hamper the performance of NaSBs such as the poor cycling stability attributed to low electric conductivity and the large volume expansion of the sulfur cathode [251]. In addition, there is recursive redox transformation of sulfur to sodium polysulfides (Na_2S_n) which get dissolved in the common electrolyte solvents, such as 1,2-dimethoxyethane (DME) and 1,3-dioxolane (DOL), a phenomenon commonly known as shuttle effect, causing the gradual depletion of cathode material and anode passivation [248, 252].

The idea of physical confinement and chemical adsorption was explored by many researchers for the effective suppression of the shuttle effect [248, 252]. The idea of chemical adsorption requires a cathode-additive material to be used as an anchor to passivate the Na_2S_n by chemisorption interaction with the anchoring material. To state a few examples of anchoring materials, one mentions for instance: (i) Graphene/N-doped carbon [253], (ii) MOF-derived S, N-doped porous carbon [254, 255], (iii) N and O-codoped carbon composites [256], and (vi) $Ti_3C_2T_x$ MXenes Mono Layer (ML) [257]. The role of the additive anchoring electrode is to prevent the dissolution of Na_2S_n in the electrolyte. So, it must provide a chemical binding with Na_2S_n stronger than those with the electrolytes. On the other hand, these interactions should not be too strong to restrict the reversibility of Na_2S_n during the charging process. Meanwhile, another role of the anchoring material is to enhance the electrical conductivity of the sulfur cathode.

To provide such moderate interaction between the Na_2S_n and the cathode-additive anchor, it would be interesting to consider the materials with large surface areas, such as MXenes [258]. For instance, in several MXene based gas-sensing studies, selectivity was achieved in case of ammonia (NH_3) with physisorption and an adsorption energy which do not exceed 0.51 eV [259]. MXenes are novel 2D materials which were originally synthesized as van der Waals nanolayers [258 - 262]. They have been demonstrated to have applications in batteries, gas-sensing, and biosensing biomedical molecules such as those attributed to lung cancer and Alzheimer's diseases [263 - 264]. Usually MXenes are metallic, however their electronic properties could be tuned upon passivation with various functional groups, such as oxygen, sulfur, and halogens (group VI or VII). So,

MXenes have the ability to maintain their interactions with most molecules at the range of intermediate strength like a strong physisorption or a weak chemisorption, which is beneficial to be explored in fabricating reusable sensors.

In literature, many types of anchoring materials have been proposed as an additive on top the sulfur cathode of NaSBs [255, 265 - 269]. For instance, the proposed materias have been ranging from Nano Porous Graphene (NPG) [255], to N-doped NPG [256], to MN_4-doped graphene (M = Cr, Mn, Fe, Co, Cu) [265], to sulfur-doped $Ti_3C_2T_x$ MXenes [266], to CoP-Co composite [267], to C_2N ML [268], and to As_3S_3 ML [269]. Amongst all these 2D materials the performance of MXenes has been shown to be either superior or at par with the other candidates, in order to inhibit the shuttle effect in NaSBs (e.g., using $Ti_3C_2T_x$ [257, 266]). Owing to their huge diversity, outstanding metallic conductivity, tunable surface chemistry, and 2D layered structure, MXenes exhibit enormous potential which can be explored for battery applications in general and NaSBs in particular [270, 271].

The scope of the present Chapter is to investigate the adsorption of Na_2S_n on the two selected MXenes $Hf_3C_2T_2$ and $Zr_3C_2T_2$. Also, the role of the different passivation was analyzed from the perspective of developing a superior anchoring material. Successful syntheses of these MXenes were recently reported [17, 18]. Namely, Zhou and coworkers [17] reported the successful growth of $Hf_3C_2T_x$ and showed their potential for lithium and sodium ion batteries with reversible volumetric capacities of 1567 and 504 $mAhcm^{-3}$, respectively. The same group [18] also reported the successful synthesis of $Zr_3C_2T_x$ and they found them more stable than $Ti_3C_2T_x$ at high temperature.

Here, we applied the Density Functional Theory (DFT) method to study the adsorption of Na_2S_n on $Hf_3C_2T_2$ and $Zr_3C_2T_2$ functionalized with F and O passivation. We calculated the binding energies of Na_2S_n with the studied MXenes and compared the results with those on the electrolytes (DME and DOL) Further, we studied the spin-polarized Partial (PDOS) and Total (TDOS) Density of States to evaluate the effect of Na_2S_n adsorption on the electronic and magnetic properties of $Hf_3C_2T_2$ and $Zr_3C_2T_2$. We thereafter have presented an elaborated discussion on the charge transfer mechanism using Charge Density Difference (CDD) profile and Bader charge analysis. Climbing Image-Nudged Elastic band (CI-NEB) method was used to assess the kinetics of Na^+ ion's dissociation

from Na_2S and its diffusion during the charging process. The Chapter is organized as follows. The model and method will be described in next Section 7.3. Section 7.4 shows a discussion of our DFT-obtained results. The last section summarizes our main findings.

7.3 Computational Model and Method

In crystalline structure, $M_3X_2T_x$ MXenes are layered hexagonal (belonging to the space group P63/mmc) [272], with two formu la units per primitive cell. So, as a model, we considered a computational supercell of size 3×3 primitive cells (i.e., containing 63 atoms). Such a supercell would be sufficient to investigate the adsorption properties of Na_2S_n (n = 1, 2, 4, 6, 8) on $Hf_3C_2T_2$ and $Zr_3C_2T_2$ (T= F, O). One should expect the computations to be spin-polarized and rather demanding as they involve heavy transition metal elements (Hf and Zr), where f-electrons should be included in the calculations. The relaxed atomic structures will be discussed in the next section. The supercell dimensions are set to be (A=B, C), with A = 3×a, a is the lattice constant shown in Table 7.1. So, A and B are set in a fashion to yield periodic slab in xy-direction; whereas C = 20 Å is set large enough to ensure the isolation of the slab from interacting with its mirror images along the z-direction.

Concerning the computational method, we used the state-of-the-art Density Functional Theory (DFT), as incorporated in the "Vienna Ab-initio Simulation Package" (VASP) [53]. The ion-electron interaction is treated by the Projected Augmented Wave (PAW) method [135]. The exchange and correlation interactions were addressed using the Generalized Gradient Approximation (GGA) with the Perdew-Burke-Ernzerhof (PBE) functional [234]. We used an energy cut-off of 500 eV. In sampling the Brillouin zone, a k-mesh of 5×5×1 (12×12×1) under Monkhorst-Pack scheme [56] was utilized for geometry optimization (DOS calculations). We took as convergence criteria of 10^{-6} eV and 10 meV/Å for total energy and force per atom, respectively. Furthermore, it is crucially important to incorporate the Van der Waals (vdW) interactions as they alter the adsorption of Na_2S_n. The vdW interactions are included using the DFT-D3 method of Grimme scheme [57]. The charge exchange between molecule and substrate is calculated based upon the Bader charge analysis within the framework of VASP package [58].

7.4 Results and Discussions

7.4.1 Structural and Electronic Properties

Atomic relaxation always comes first in any DFT study. Figure 7.1(a) shows the results of four MXenes structures, comprising of $Hf_3C_2F_2$, $Hf_3C_2O_2$, $Zr_3C_2F_2$, and $Zr_3C_2O_2$ monolayers. The optimized geometries have been presented in Figure 7.1(a) and their corresponding parameters are summarized in Table 7.1. Each passivated F(O) atom is surrounded by inner two metal Hf/Zr atoms with the bond lengths F - Hf= 2.319 Å, O - Hf = 2.105 Å, F - Zr = 2.333 Å and O - Zr = 2.13381 Å. The obtained lattice parameters are a = b = 3.291 Å for $Hf_3C_2F_2$, a = b = 3.270 Å for $Hf_3C_2O_2$, a = b = 3.342 Å for $Zr_3C_2F_2$ and a = b = 3.319 Å for $Zr_3C_2O_2$, which are found to be consistent with the experimental data [17,18] and in good agreement with the ab-initio results [272, 273]. The bond angles of both metal (Hf, Zr) and carbon atoms are shown in Table 7.1 to be about 90º, which are consistent with what is reported in literature [17, 18, 272, 273].

	Side View	Top view
Hf$_3$C$_2$F$_2$		
Hf$_3$C$_2$O$_2$		
Zr$_3$C$_2$F$_2$		
Zr$_3$C$_2$O$_2$		
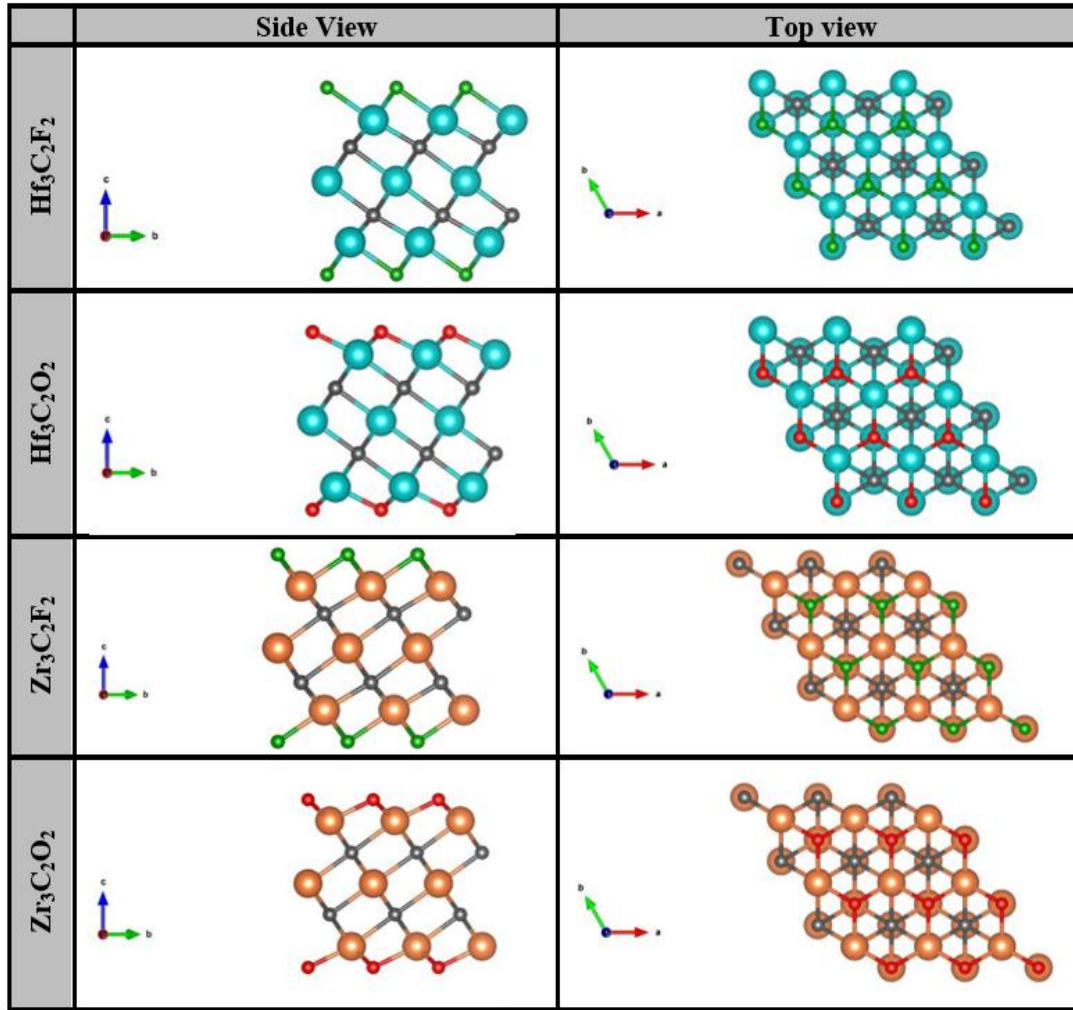
Figure 7.1(a): Side and top view of crystal structure of MXenes Hf$_3$C$_2$X$_2$ and Ti$_3$C$_2$X$_2$ (X=F/O) using 3x3-PC supercell.

Having transition-metal atoms in composition, the inclusion of spin-polarization in the electronic structures of these MXenes becomes necessary. Figure 7.1(b) shows the Projected spin-polarized Density of States (PDOS) of Hf$_3$C$_2$X$_2$ and Zr$_3$C$_2$X$_2$ (X=F/O) as calculated by GGA-PBE. Fermi level is taken as an energy reference (i.e., $E_F = 0$) while the PDOS and TDOS are displayed in energy range [-2, +2] eV around E_F. The results reveal that all the four MXenes are paramagnetic metals (i.e., the PDOSs having similarity between the spin up and the spin down states to yield vanishing magnetization, M = 0, and exhibit finite value at the Fermi energy). The metallic nature can be predominantly attributed to the d states in the metals (Hf/Zr).

155

Table 7.1: Geometrical Parameters of the MXenes Hf_3C_2 and Zr_3C_2 after the two passivations(F/O)

MXene	Hf_3C_2		Zr_3C_2	
Passivation	Passivation F	Passivation O	Passivation F	Passivation O
Lattice Constant DFT	3.291 Å	3.269 Å	3.342 Å	3.319 Å
Lattice Constant Exp.	3.290 Å(*)	3.27 Å(*)	3.332 Å(**)	3.314 Å(**)
Geometry	b_{C-Hf} = (2.19, 2.37) Å b_{Hf-F} = 2.319 Å Slab thickness = 7.66 Å Ang C = 87.1° Ang Hf = 90.59°	b_{C-Hf} = (2.36, 2.32) Å b_{Hf-O} = 2.105 Å Slab thickness = 7.32 Å Ang C = 90.54° Ang Hf = 91.63°	b_{C-Zr} = (2.23, 2.38) Å b_{Zr-F} = 2.333 Å Slab thickness = 7.75 Å Ang C = 87.50° Ang Zr = 90.89°	b_{C-Zr} = (2.36, 2.34) Å b_{Zr-O} = 2.319 Å Slab thickness = 7.43 Å Ang C = 90.90° Ang Zr = 90.03°
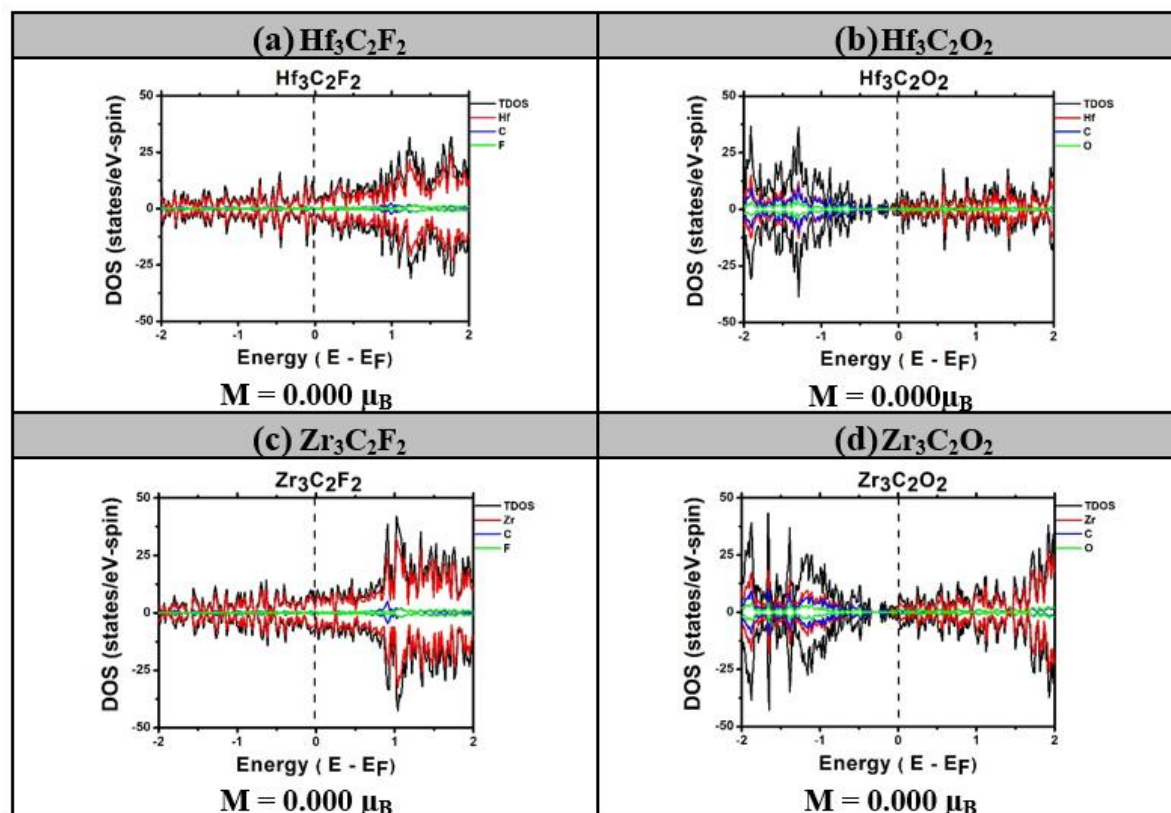
Figure 7.1(b): Spin-polarized PDOS of monolayer MXenes $Hf_3C_2X_2$ and $Zr_3C_2X_2$ (X=F/O) using 3x3-PC supercell.

7.4.2 Adsorption of Na_2S_n

Na_2S_n molecules were introduced on the surfaces of four MXenes to quantify the anchoring capabilities of the latter. The results of binding energies are shown in Figure 7.2(a) and compared with those of electrolytes (DOL and DME). The results of the binding energies of the Na_2S_n are presented in Figure 7.2(b) in a comparative fashion amongst all the four studied MXenes. Whereas Table 7.2 shows an extended comparison of our results of binding energies to others existing in literature. The oxygen passivated

MXenes display the strongest binding energies which are competitive to those displayed for C_2N-based anchoring material [255, 265 - 269].
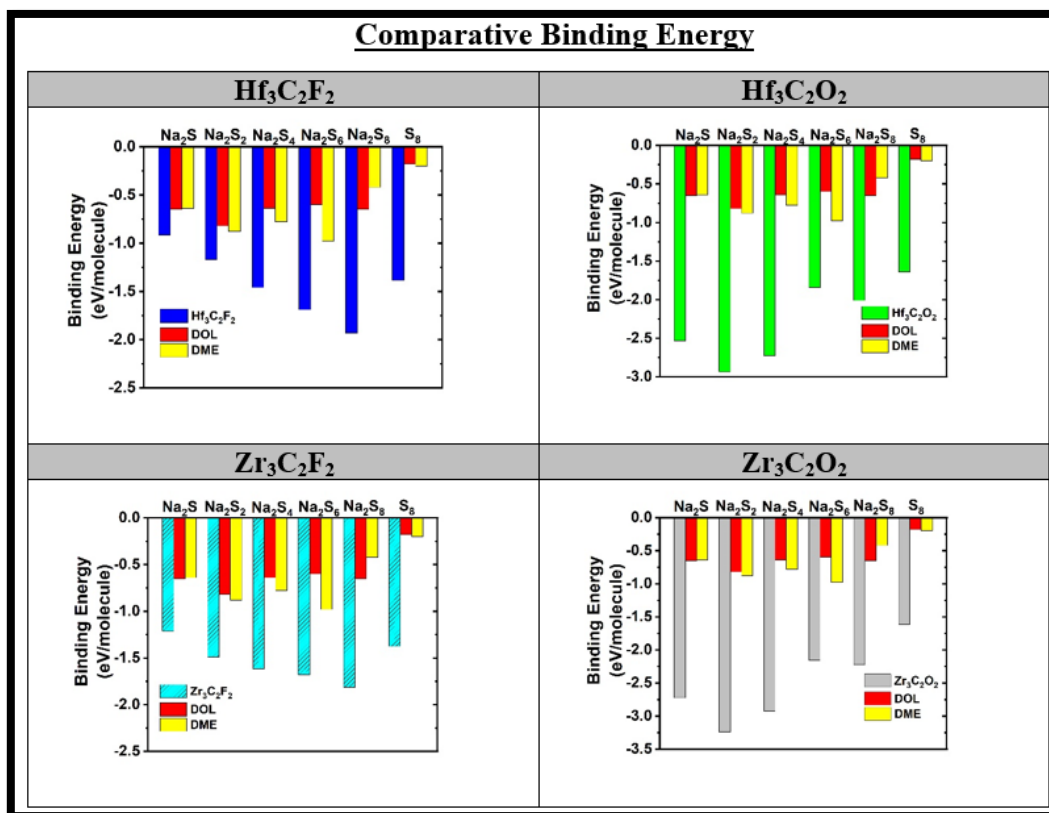
Figure 7.2(a): Comparative binding energies of the 4 MXenes with the 6 sodium polysulfides.

In the atomic relaxation processes, several configurations and orientations were explored and studied to examine the energetically favorable sites and positions and Figure 7.3 (a-d) show the strongest binding configurations of Na_2S_n on $Hf_3C_2F_2$, $Hf_3C_2O_2$, $Zr_3C_2F_2$ and $Zr_3C_2O_2$, respectively.

Table 7.2: Comparison of Binding Energies of the MXenes under study with existing literature for inhibition of shuttle effect.

System	Na$_2$S	Na$_2$S$_2$	Na$_2$S$_4$	Na$_2$S$_6$	Na$_2$S$_8$	S$_8$
Hf$_3$C$_2$F$_2$	-0.92	-1.17	-1.46	-1.69	-1.93	-1.38
Hf$_3$C$_2$O$_2$	-2.53	-2.93	-2.73	-1.84	-2.01	-1.64
Zr$_3$C$_2$F$_2$	-1.21	-1.49	-1.62	-1.68	-1.81	-1.37
Zr$_3$C$_2$O$_2$	-2.73	-3.24	-2.92	-2.16	-2.23	-1.62
DOL	-0.65	-0.82	-0.64	-0.60	-0.65	-0.18
DME	-0.64	-0.88	-0.78	-0.98	-0.42	-0.20
Graphene	-0.82	-0.67	-0.51	-0.43	-0.33	--
N-NPG	-2.77	-1.77	-1.37	-1.43	-1.66	-0.76
FeN$_4$@graphene	-1.09	-1.36	-1.07	-1.16	-1.35	--
Ti$_3$C$_2$T$_x$	--	-1.89	-2.88	-4.72	--	--
CoP-Co	-1.66	-1.74	-2.43	-2.66	--	--
C$_2$N	-3.09	-3.13	-2.51	-2.39	-2.33	--
As$_3$S$_3$	-3.26	-2.41	-1.94	-1.49	-1.52	--

After relaxation, S$_8$ prefers a horizontal alignment over the substrate, for all the four functionalized MXenes. This has also been observed for other 2D materials (e.g., As$_2$S$_3$ [269], black phosphorene [274], Ti$_3$C$_2$T$_x$ [275], graphene [276]). The molecular distances from S$_8$ to the MXenes are as follows: Hf$_3$C$_2$F$_2$ (O$_2$): 3.24 Å (3.542 Å) and Zr$_3$C$_2$F$_2$ (O$_2$): 3.29 Å (3.51 Å), which are greater than the combination of the atomic radii of and S (1.00 Å) and F (0.42 Å)/O (0.66 Å) atoms. Thus, the binding is weak and mainly attributed to the vdW interactions.
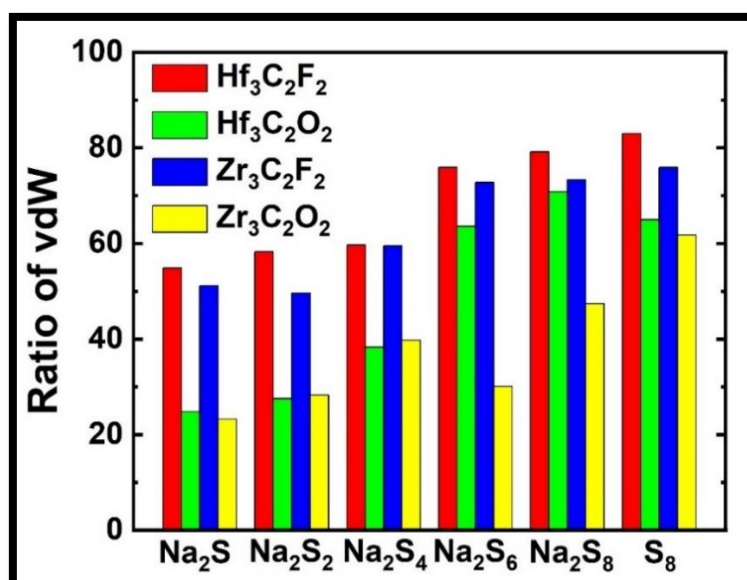
Figure 7.2(b): Ratio of vdW interactions in the adsorption energies of Na$_2$S$_n$ adsorbed on Hf$_3$C$_2$F$_2$, Hf$_3$C$_2$O$_2$, Zr$_3$C$_2$F$_2$ and Zr$_3$C$_2$O$_2$.

The Na atoms in the text are moving towards the surface's F (O) atoms, and the distances between the Na and F(O) atoms are shown in Table 7.3. It is worth mentioning that the atomic radii of Na, F, and O are 1.80, 0.42, and 0.48 Å, respectively. The distances between Na_2S_n and $Hf_3C_2F_2/Hf_3C_2O_2/Zr_3C_2F_2/Zr_3C_2O_2$ are close to the sum of the radii of Na and F (O), which explains the strong chemical bonds that can be observed through X-ray photoelectron spectra (XPS). This is further supported by the calculated binding energies (E_b) shown in Figure 7.2(a).

Table 7.3: Distance between the MXenes and the Na_2S_n after relaxation.

System	Na_2S	Na_2S_2	Na_2S_4	Na_2S_6	Na_2S_8	S_8
$Hf_3C_2F_2$	2.121 Å	2.238 Å	2.326 Å	2.263 Å	2.226 Å	3.243 Å
$Hf_3C_2O_2$	2.279 Å	2.284 Å	2.282 Å	2.363 Å	2.393 Å	3.542 Å
$Zr_3C_2F_2$	2.293 Å	2.326 Å	2.363 Å	2.274 Å	2.384 Å	3.298 Å
$Zr_3C_2O_2$	2.001 Å	2.117 Å	2.178 Å	2.199 Å	2.236 Å	3.490 Å

The E_b values are compared with those of polysulfides adsorbed by the commonly used electrolyte molecules, such as 1,2-dimethoxyethane (DME) and 1,3-dioxolane (DME) [256], and the other 2D materials that have been proposed as anchoring materials in literature. The interaction of all four MXenes are found to be much stronger than the Na_2S_n-electrolyte interactions. This should justify the suppression of the dissolution of Na_2S_n in these electrolytes. Most importantly, the moderate strength of interactions between the Na_2S_n and studied MXenes ensures reversibility of the redox reaction. The immense E_b values are attributed to the polarities of surface O and F atoms. The electronegativities of F (χ^F = 4.0 Pauling) [140] and O (χ^O = 3.5 Pauling) are drastically greater than that of Hf (χ^{Hf} = 1.3 Pauling) / Zr (χ^{Zr} = 1.33 Pauling). Electrons are thus migrated to F and O surfaces atoms, resulting in the negatively charged ions to directly attract polar Na_2S_n analytes. Hence, the presence of the $Hf_3C_2F_2/O_2$ and $Zr_3C_2F_2/O_2$ on the cathode adequately anchor the Na_2S_n molecules and conclusively eliminate the shuttle effect.

It is challenging to analyze the chemical bonding between Na_2S_n and the studied MXenes that is responsible for the suppression of Na_2S_n molecules. However, we have determined that the van der Waals physical interactions play a significant role in the magnitude of the binding energies (E_b), as reflected by the following equation:

$$R = \frac{E_b^{vdW} - E_b^{novdW}}{E_b^{vdW}} \times 100\% \tag{7.1}$$

where E_b^{vdW}, E_b^{novdW} denote the binding energies of Na$_2$S$_n$ including and excluding the vdW interactions, respectively. Figure 7.2(b) shows the ratio of the vdW energies of Na$_2$S$_n$ adsorbed on the surfaces of Hf$_3$C$_2$F$_2$, Hf$_3$C$_2$O$_2$, Zr$_3$C$_2$F$_2$ and Zr$_3$C$_2$O$_2$ MXenes. Interestingly, intrinsic vdW interactions are the predominant contributors to the binding energy of S$_8$ on all the four MXenes which accounts for 83%, 64.96%, 75% and 62% of the binding energy for Hf$_3$C$_2$F$_2$, Hf$_3$C$_2$O$_2$, Zr$_3$C$_2$F$_2$ and Zr$_3$C$_2$O$_2$, respectively. Moreover, in the fluorine passivated MXenes, Hf$_3$C$_2$F$_2$ and Zr$_3$C$_2$F$_2$ the van-der-Waals interactions seem to be the controlling attractive force which accounts for the major contribution in the binding energies. This thereby justifies their weaker interactions in comparison to their Oxygen-functionalized counterparts where the chemical binding energies seem to be significantly higher. Another key point to be noted, is that the vdW contributions appear to reduce with reductions in the sulfur content of the polysulfides, and therefore for Na$_2$S they reduce to only 54%, 25%, 51% and 23% for Hf$_3$C$_2$F$_2$, Hf$_3$C$_2$O$_2$, Zr$_3$C$_2$F$_2$ and Zr$_3$C$_2$O$_2$, respectively. This is justified by the presence of strong chemical bonds, and thereby an enhanced charge exchange between the Na$_2$S moiety and the MXenes as can be seen in the Bader charge transfer of Table 7.4. The transferred charge Δq from Na$_2$S$_n$ to the passivation layer of MXenes increases with the reducing sulfur content of molecules and is also remarkably higher on oxygen passivation than fluorine passivation.
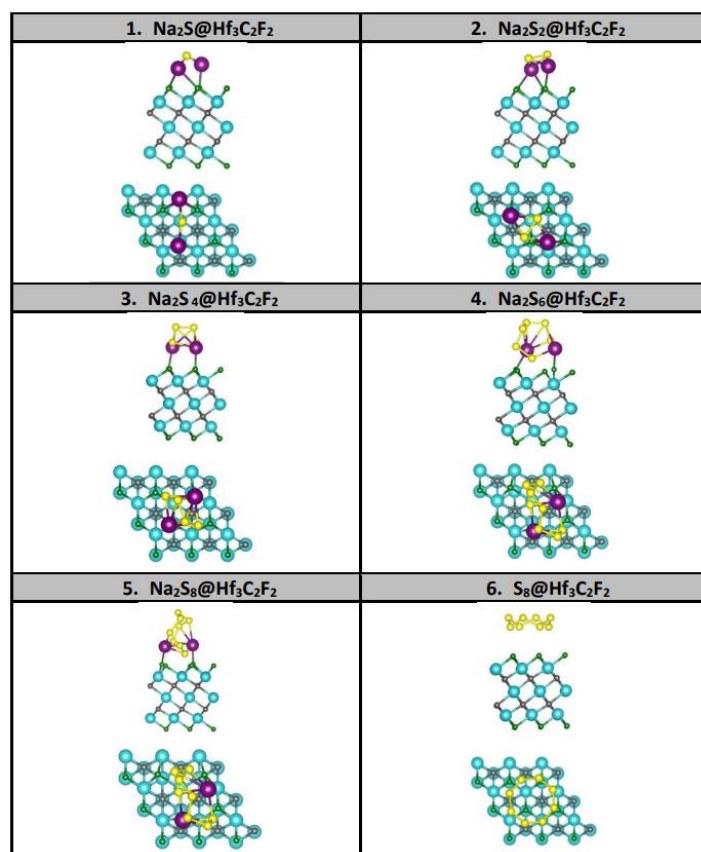
Figure 7.3(a): Relaxed structures of the Na_2S_n on the surface of MXenes ($Hf_3C_2F_2$).
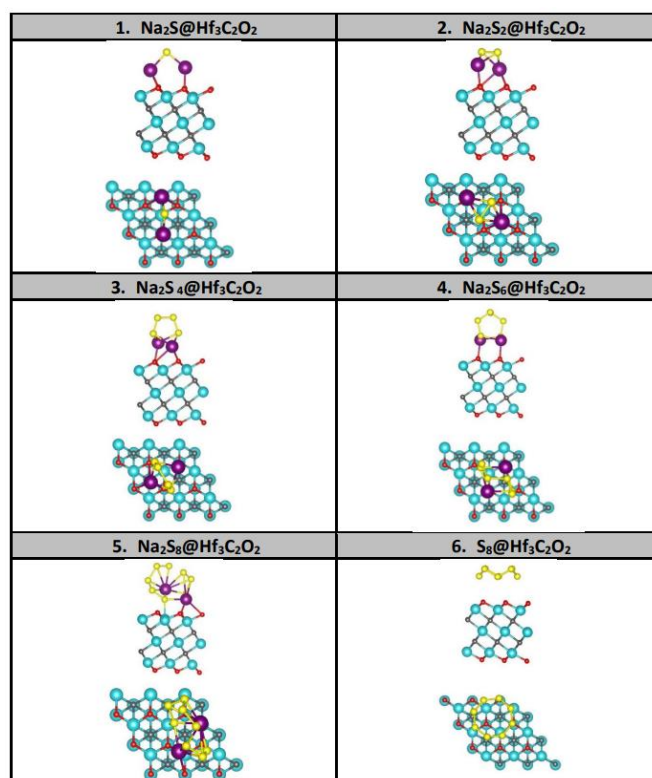
Figure 7.3(b): Relaxed structures of the Na_2S_n on the surface of MXenes ($Hf_3C_2O_2$).
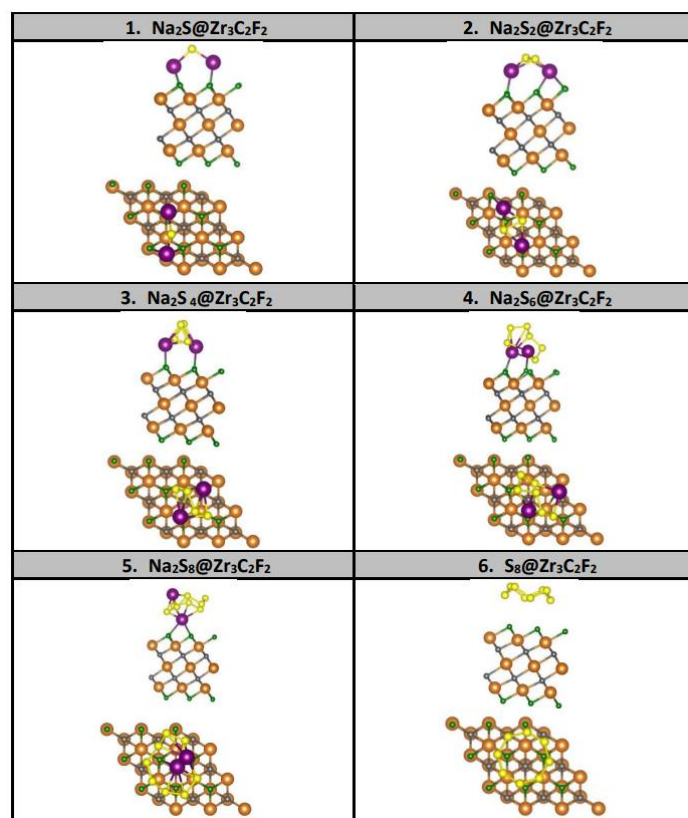
Figure 7.3(c): Relaxed structures of the Na_2S_n on the surface of MXenes ($Zr_3C_2F_2$).
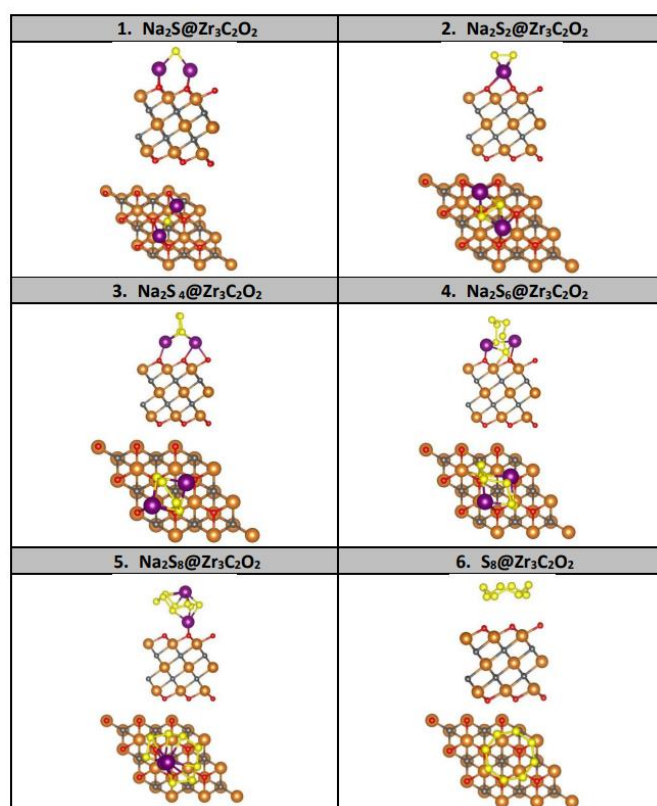
Figure 7.3(d): Relaxed structures of the Na_2S_n on the surface of MXenes ($Zr_3C_2O_2$).

162

Aside from the physisorption of S_8 molecule on all the surfaces of studied MXenes, the common trend amongst the adsorptions of the other five Na_2S_n is that they all exhibited chemisorption processes but not associated with molecular dissociation. Furthermore, in all cases both sodium atoms establish chemical bonds with the passivation layer of MXene except in three cases, corresponding to Na_2S_8 on $Zr_3C_2T_2$ (T=F/O) and Na_2S_6 on $Zr_3C_2O_2$ shown in Figures 7.3(c) and (d), respectively.

Thereafter, we analyzed the electronic properties of $Hf_3C_2F_2/O_2$ and $Zr_3C_2F_2/O_2$ to unravel how the presence of Na_2S_n alters their intrinsic features. Figure 7.4(a-d) shows the spin-polarized PDOS and TDOS of Na_2S_n adsorbed on MXenes. The adsorption of S_8 molecule, does not alter the TDOS of the MXenes noticeably, especially in the range close to the Fermi energy, indicating minor change in the electronic properties (e.g., electronic transport). This is in support of the weak vdW-type physisorption. On the other hand, there are drastic changes in the TDOS, upon the adsorption of Na_2S_n, supporting the immense binding energies and manifesting the chemical bonding. Yet, the electronic properties of MXenes remain metallic after adsorption.

There are additional peaks at the Fermi energy, meaning there are more electronic states available for conduction. Also, some changes can be noted between the spin up and spin down states in some cases: $Hf_3C_2F_2:Na_2S$, $Hf_3C_2O_2:Na_2S$, Na_2S_2, Na_2S_4, Na_2S_6, $Zr_3C_2F_2:Na_2S$, Na_2S_2 and $Zr_3C_2O_2:Na_2S$, Na_2S_2, Na_2S_4 and Na_2S_8. However, the value of the total magnetic moment remains small when compared to the large sample size. Thus overall, the adsorption of Na_2S_n can possibly enhance the electronic transport of the hosts. Moreover, the metallic feature is preserved during the entire course of polysulfide adsorption. The increased electronic population at the Fermi energy and the maintained metal character ensure the conductive anchoring that accelerates the electrochemical process during the battery operation.

1. $Na_2S@Hf_3C_2F_2$	2. $Na_2S_2@Hf_3C_2F_2$
M = 0.2928 μ_B	M = 0.00 μ_B

3. $Na_2S_4@Hf_3C_2F_2$	4. $Na_2S_6@Hf_3C_2F_2$
M = 0.00 μ_B	M = 0.0015 μ_B

5. $Na_2S_8@Hf_3C_2F_2$	6. $S_8@Hf_3C_2F_2$
M = 0.0048 μ_B	M = 0.0059 μ_B
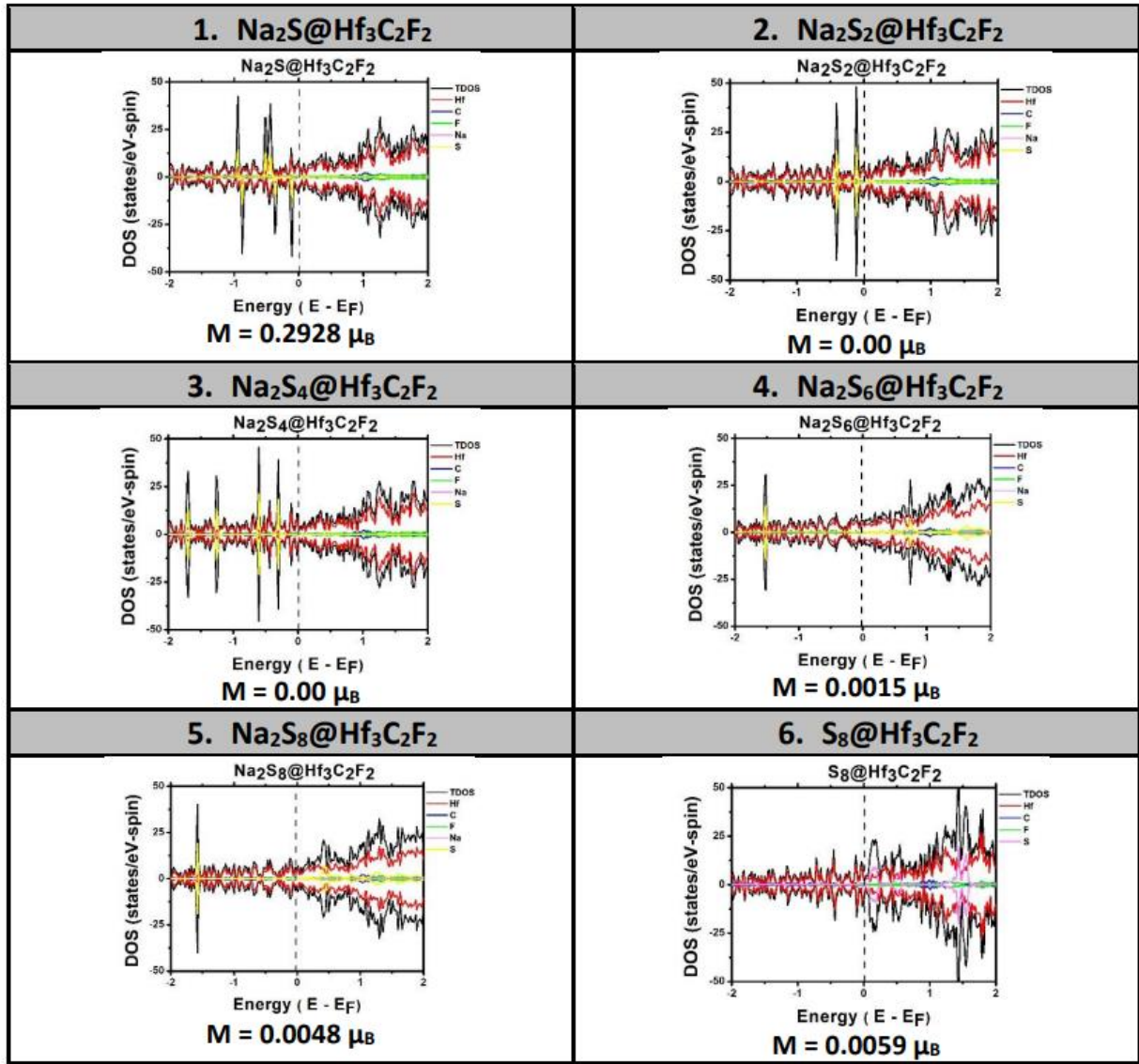
Figure 7.4(a): PDOS of Na_2S_n on the surface of $Hf_3C_2F_2$.

164

1. $Na_2S@Hf_3C_2O_2$	2. $Na_2S_2@Hf_3C_2O_2$
$Na_2S@Hf_3C_2O_2$ M = 0.9343 μ_B	$Na_2S_2@Hf_3C_2O_2$ M = 0.9324 μ_B
3. $Na_2S_4@Hf_3C_2O_2$	4. $Na_2S_6@Hf_3C_2O_2$
$Na_2S_4@Hf_3C_2O_2$ M = 0.9976 μ_B	$Na_2S_6@Hf_3C_2O_2$ M = 0.8337 μ_B
5. $Na_2S_8@Hf_3C_2O_2$	6. $S_8@Hf_3C_2O_2$
$Na_2S_8@Hf_3C_2O_2$ M = 0.00 μ_B	$S_8@Hf_3C_2O_2$ M = 0.00 μ_B
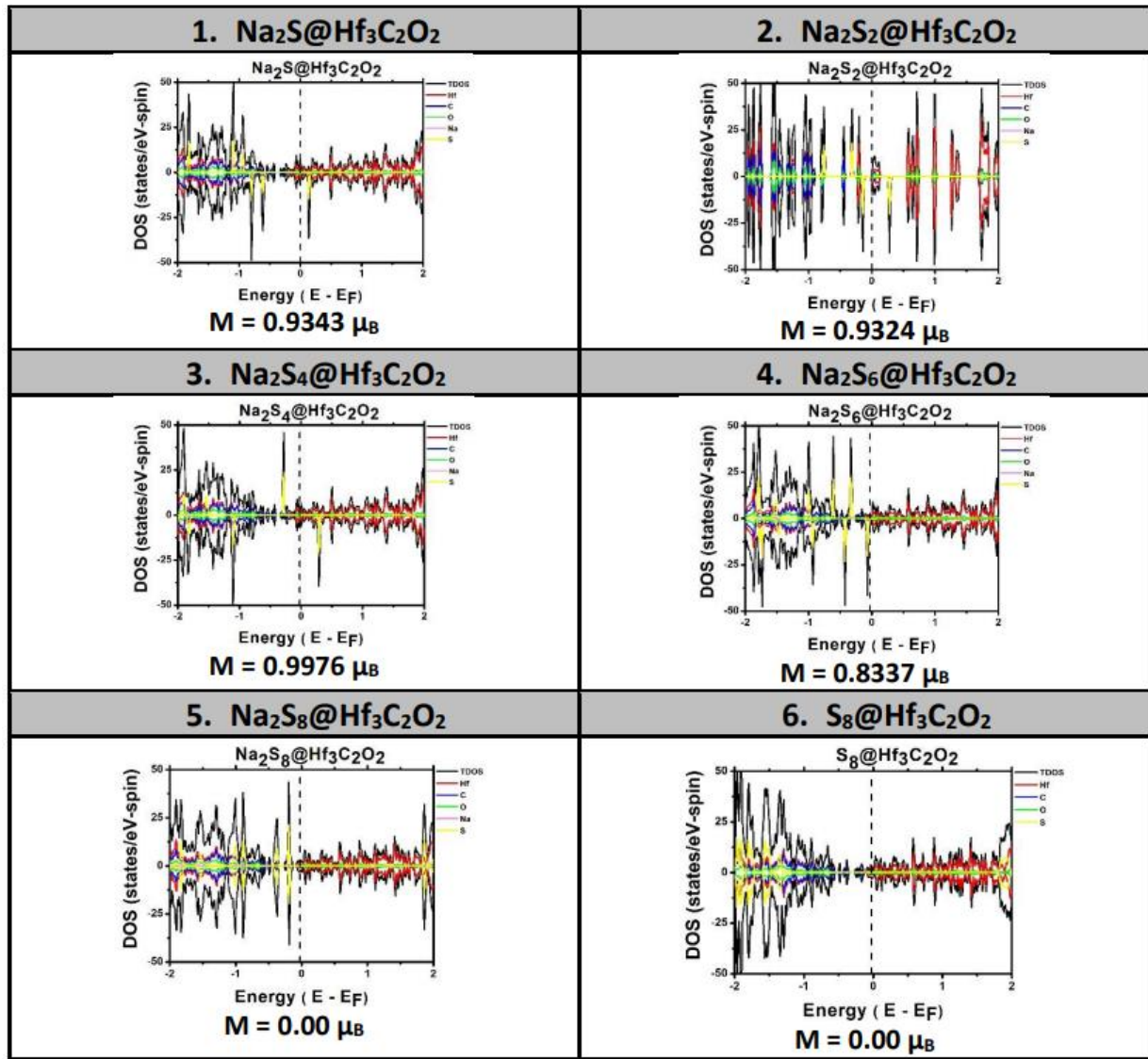
Figure 7.4(b): PDOS of Na_2S_n on the surface of $Hf_3C_2O_2$.

1. $Na_2S@Zr_3C_2F_2$	2. $Na_2S_2@Zr_3C_2F_2$
$M = 0.5913\ \mu_B$	$M = 0.5903\ \mu_B$
3. $Na_2S_4@Zr_3C_2F_2$	4. $Na_2S_6@Zr_3C_2F_2$
$M = 0.000\ \mu_B$	$M = 0.000\ \mu_B$
5. $Na_2S_8@Zr_3C_2F_2$	6. $S_8@Zr_3C_2F_2$
$M = 0.000\ \mu_B$	$M = 0.000\ \mu_B$
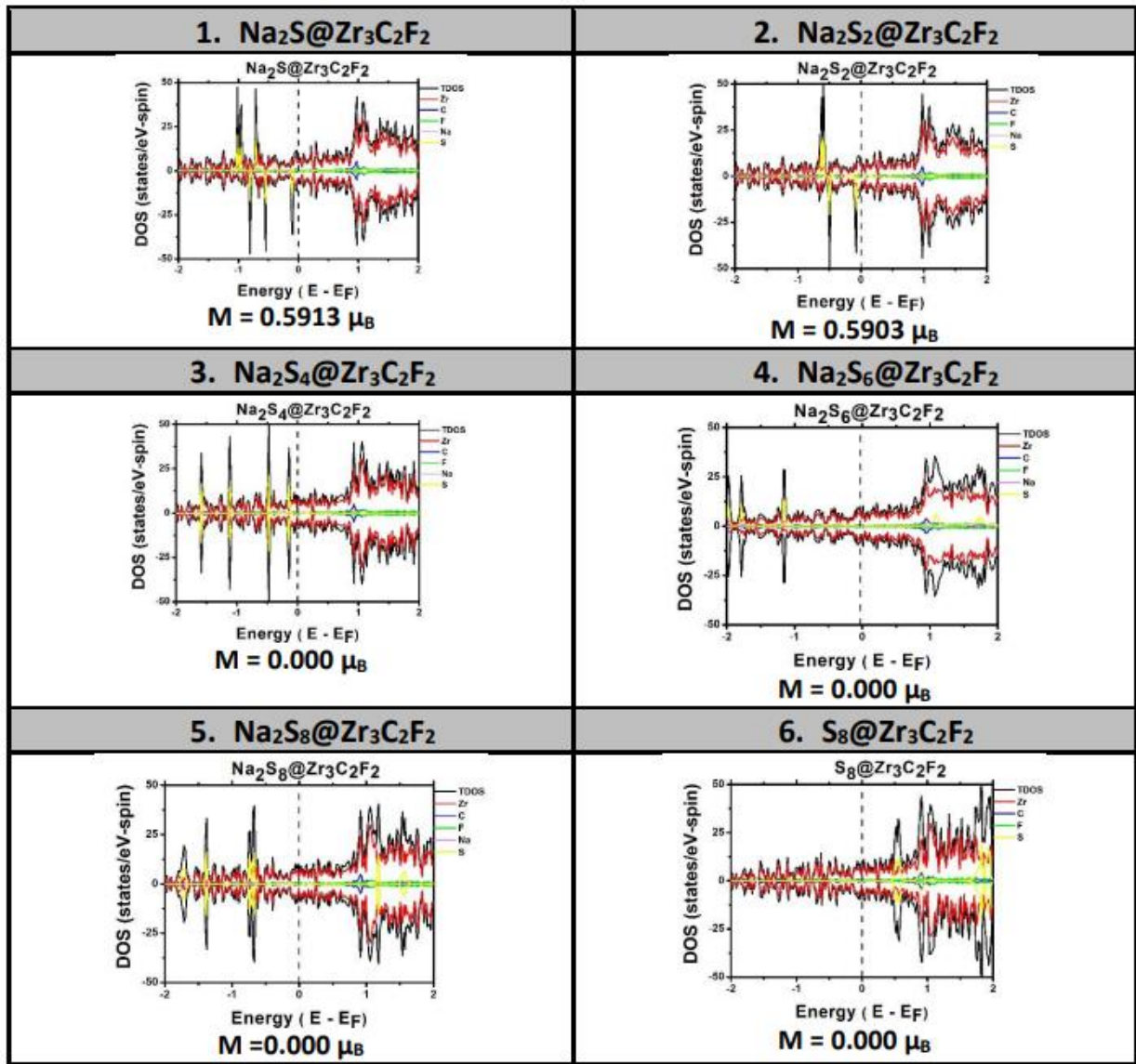
Figure 7.4(c): PDOS of Na_2S_n on the surface of $Zr_3C_2F_2$.
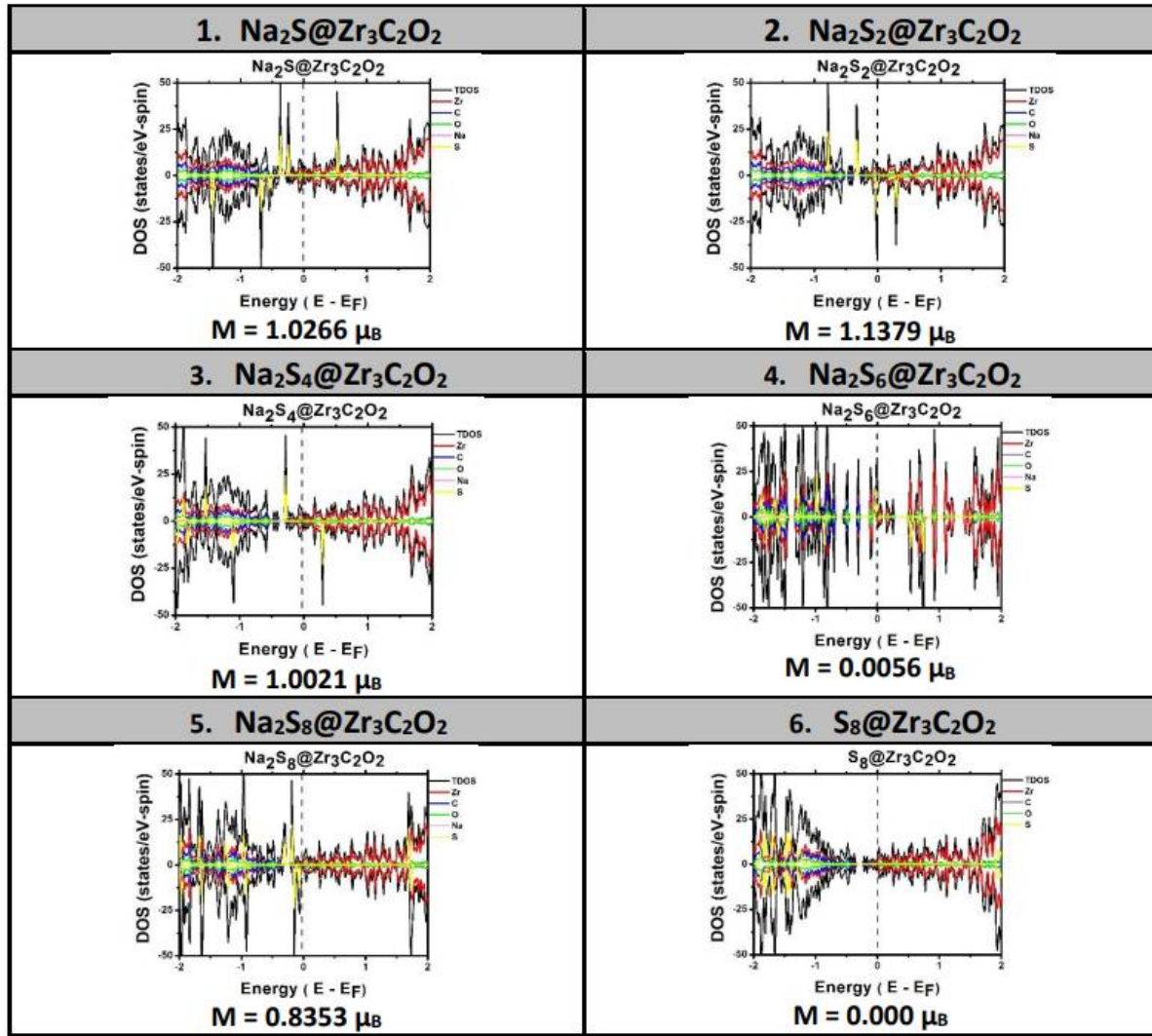
Figure 7.4(d): PDOS of Na_2S_n on the surface of $Zr_3C_2O_2$.

7.4.3 Charge Density Difference (CDD)

Charge transfer is calculated by using Bader analysis with results shown in Table 7.4. As shown in this Table, the charge is donated from the Na_2S_n to the MXenes. This charge donation was higher in case of O_2 functionalization of the Mxenes, in cases of chemisorption processes, which agrees with their stronger binding energies. In the case of S_8 molecules, charge transfer was negligible owing to their weak interaction and insignificant change on the density of states after adsorption. Moreover, we calculated the charge density difference($CDD = \Delta\rho$), based on the following equation:

$$\Delta\rho = \rho_{MXene+NPSs} - (\rho_{MXene} + \rho_{NPSs}) \tag{7.2}$$

167

of the four MXenes upon adsorption of Na_2S_n as depicted in Figure 5(a-d). Here, NPSs refer to Na_2S_n. In Figure 7.5, we display the charge density in both 3D and its projection (1D) on the z-axis.

Table 7.4: Charge transferred between the Na_2S_n and MXene.

System	Na_2S	Na_2S_2	Na_2S_4	Na_2S_6	Na_2S_8	S_8
$Hf_3C_2F_2$	-0.38504	-0.37148	-0.06916	-0.17986	-0.174753	-0.02685
$Hf_3C_2O_2$	-0.876345	-0.87019	-0.8738503	-0.497036	-0.194004	-0.01494
$Zr_3C_2F_2$	-0.55453	-0.54979	-0.14118	-0.19513	-0.04056	-0.03028
$Zr_3C_2O_2$	-0.88898	-0.99504	-0.88124	-0.74342	-0.37673	-0.01511

It seems that there is an accumulation of charge (represented by yellow) on the MXenes surface, and a decrease in charge (represented by the color cyan) on polysulfide clusters. This transfer of electrons is due to the movement of electrons from Na2Sn's Na-3s to the partially filled O-2p (F-2p) orbitals of the anchoring groups. It's important to note that the charge transfer is greater with oxygen passivation and decreases as the sulfur content in sodium polysulfides increases. Furthermore, the charge transfer is nearly negligible in the case of S8 adsorption, which is in line with the results of Bader analysis and can be attributed to weak vdW-like interactions with the substrate. Finally, the fluctuations seen in the $\rho(z)$ plots in Figure 7.5 at the interface between the molecule and MXene's surface show the formation of covalent bonds.
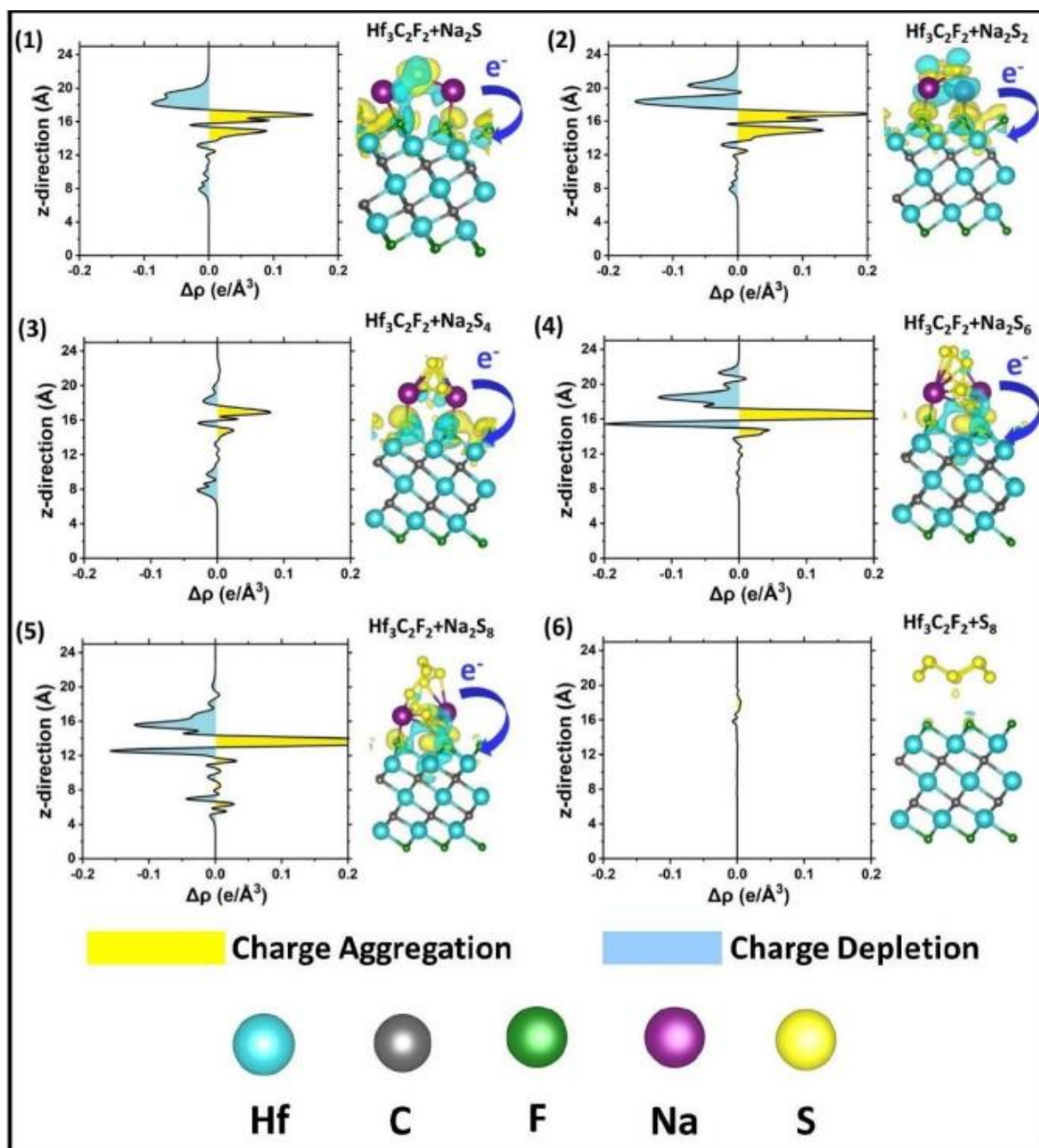
Figure 7.5(a): Charge Density Difference plots between $Hf_3C_2F_2$ and the six Na_2S_n.
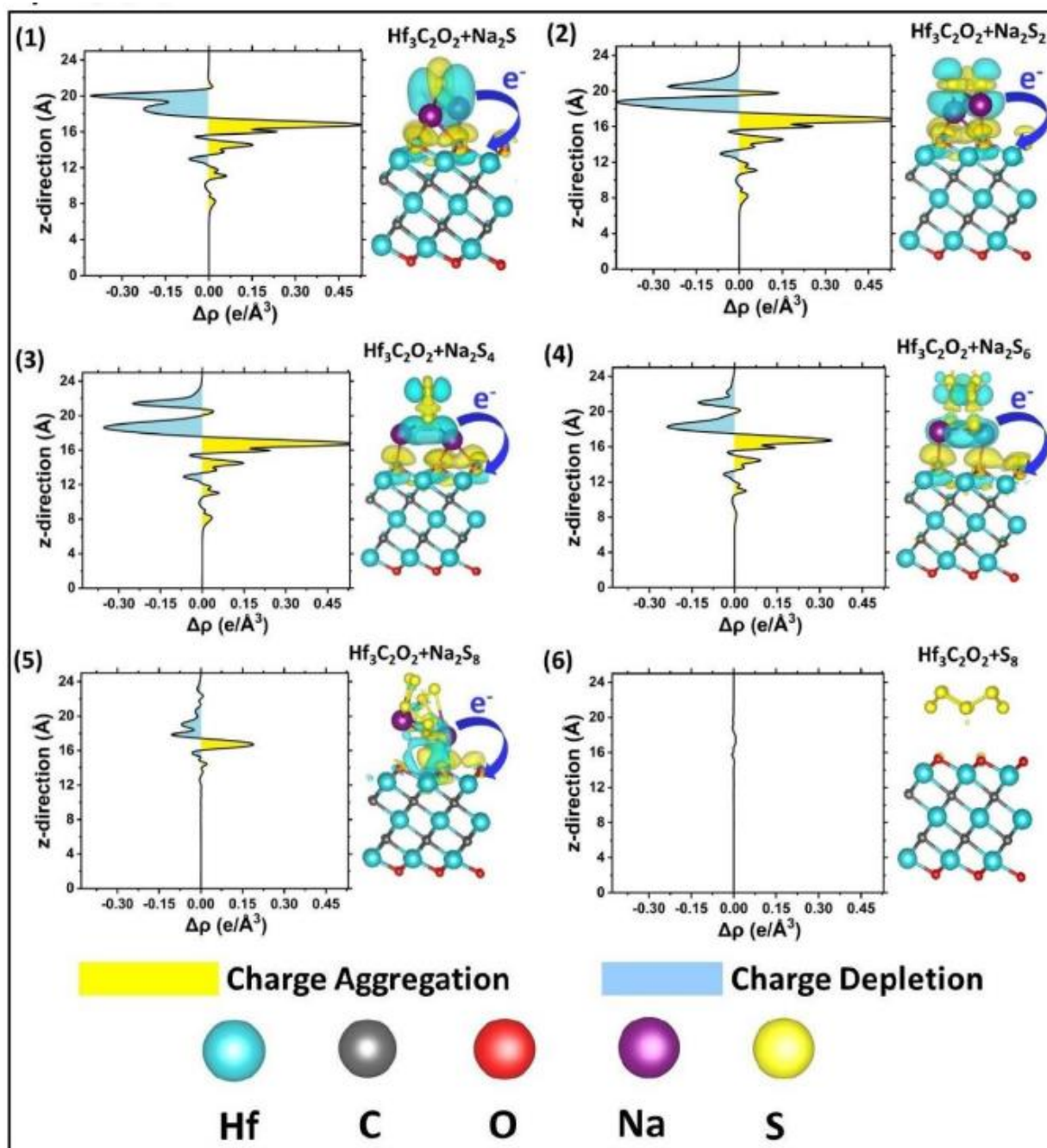
Figure 7.5(b): Charge Density Difference plots between $Hf_3C_2O_2$ and the six Na_2S_n.
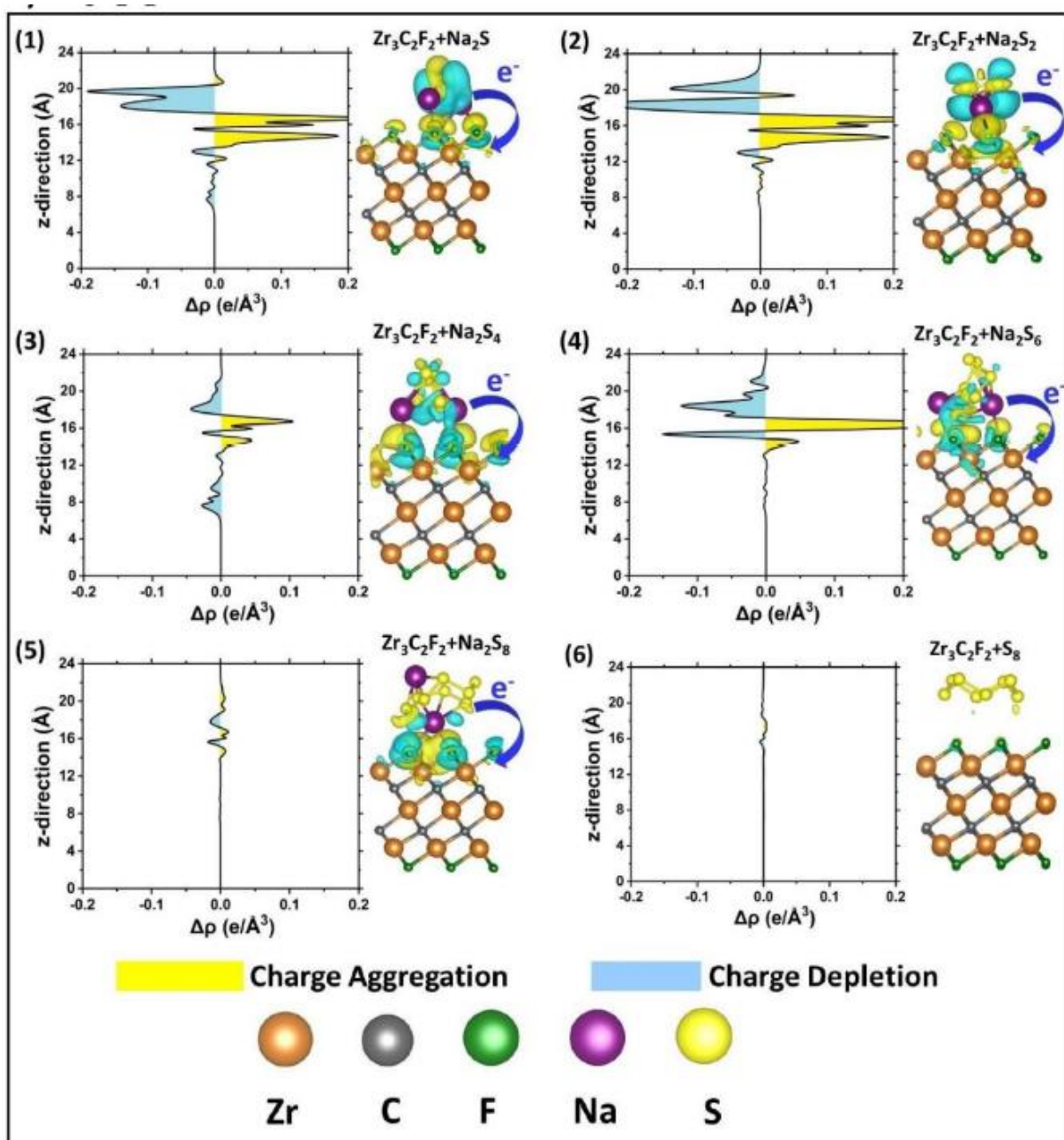
Figure 7.5(c): Charge Density Difference plots between $Zr_3C_2F_2$ and the six Na_2S_n.
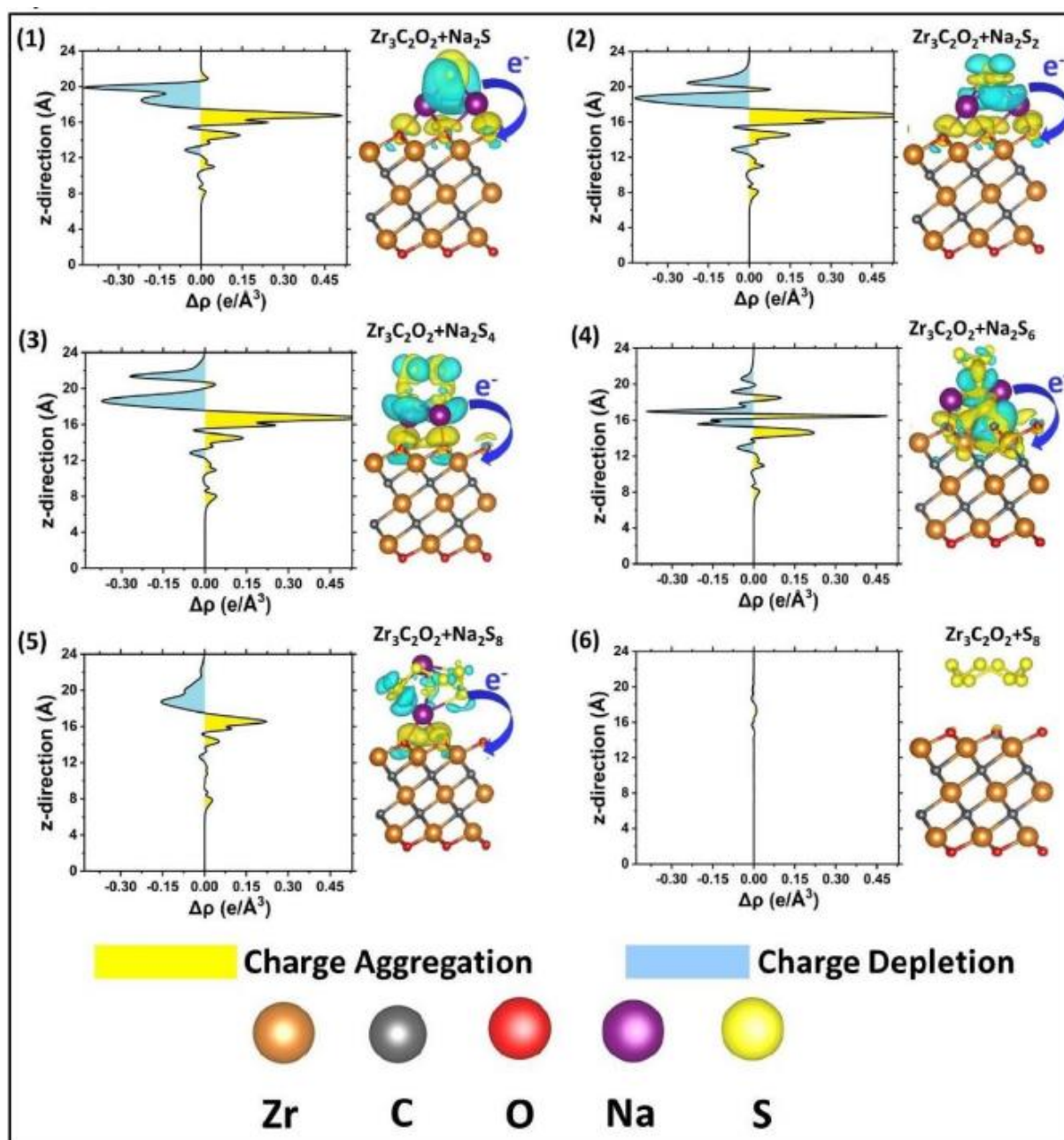
Figure 7.5(d): Charge Density Difference plots between $Zr_3C_2O_2$ and the six Na_2S_n.

7.4.4 Activation Barrier

The key factor in enhancing the reversible capacity and prolonging the battery life during the charging phase is the oxidation of the insoluble Na2S by-product through a catalytic process. To speed up the reaction kinetics, efforts are being made to reduce the dissociation barrier. This is achieved by using the climbing image-nudged elastic band (CI-NEG) method [277].

172
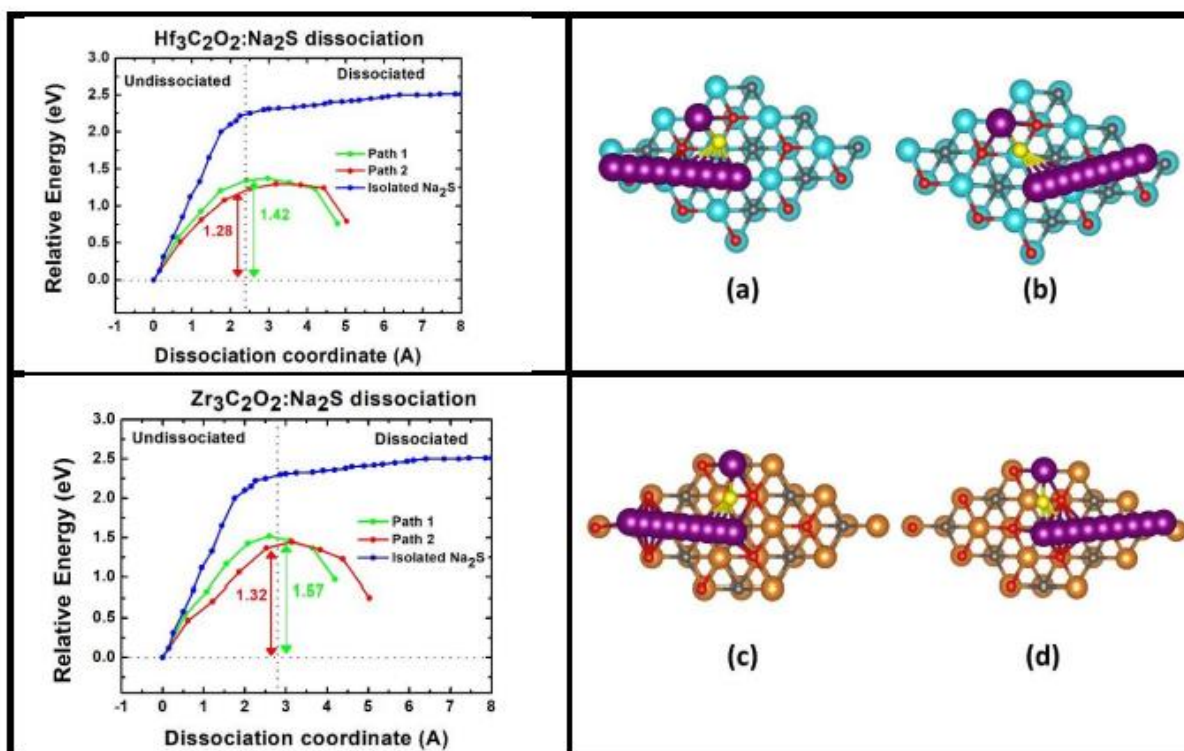
Figure 7.6: NEB Calculations for Dissociation of Na_2S on the surface of the MXene.

The speed at which Na_2S breaks down on the anchors (i.e., by dissociating the Na-S bonds) plays a crucial role in the dissociation process. The high decomposition barrier hinders the electrocatalytic performance of RT-NSBs. The study focused on the decomposition barriers of Na_2S on the most likely meta-stable states of the MXenes, specifically $Hf_3C_2O_2$ and $Zr_3C_2O_2$. The Na_2S molecule is separated into a NaS cluster and a Na+ ion ($Na_2S \rightarrow NaS + Na^+ + e^-$). Then, the freed Na^+ ion can move along two different paths on $Hf_3C_2O_2$ and $Zr_3C_2O_2$, and the potential barriers were determined, as shown in Figure 7.6. The dissociation barrier of a single Na_2S is used as a reference, with the released Na^+ ion considered to be at the zero of the dissociation coordinates (x-axis). The ion is considered to be completely freed when the dissociation coordinate reaches 2.25 Å [257]. The results show that Na_2S is much more energetic to dissociate on $Hf_3C_2O_2$ than $Zr_3C_2O_2$ due to its lower potential barrier (1.28 eV, 1.42 eV and 1.32 eV, 1.57 eV for $Hf_3C_2O_2$ and $Zr_3C_2O_2$, respectively). Both $Hf_3C_2O_2$ and $Zr_3C_2O_2$ greatly reduce the energy required for Na_2S dissociation as compared to an isolated Na_2S. Additionally, dissociating Na_2S is a spontaneous process on both $Hf_3C_2O_2$ and $Zr_3C_2O_2$ without the need for energy absorption. The obtained barriers are similar to those of 2D

materials like chromium nitrogen-doped graphene (Cr@NG) 1.54 eV [278], pristine graphene 1.94 eV, Fe-N$_4$@ graphene 1.05 eV [279], and single-layer vanadium disulfide (VS$_2$) 0.53 eV [19]).

Chapter 8: Conclusion and Future Perspectives

The results presented in this thesis presents the DFT study of functionalization of well-known synthesized 2D materials in order to tune their properties for specific applications, namely gas sensing, energy storage and spintronics. In each stage we have checked the stability of the structures, via total/binding energy calculations to ensure that our proposed solutions are stable and viable options that can be explored for experimental synthesis/applications.

In Chapter 2, we started by studying the adsorption, transport and gas-sensing properties of B/N edge-doped GNRs using the state-of-art computational technique, based on the usage of both VASP and ATK packages. The results have been summarized below.

The location of dopants with respect to the edges of GNR matters a lot for the IV-characteristics. Bilaterally edge-doped GNR with either B or N atoms would yield a blockade of current and creation of NDR behavior, due to back-scattering events. Such NDR is beneficially explored in inducing the selectivity in gas-sensing. So, we decided to consider two samples to investigate the gas-sensing properties:

(i) GNR bilaterally edge-doped with B (so named GNR:B); and

(ii) GNR bilaterally edge-doped with N (so named GNR:N);

Our results of adsorption show the occurrence of chemisorption processes of NO_2 and O_2 molecules on GNR:B and SO_3 molecule on GNR:N. The IV characteristics of both GNR:B- and GNR-N-based devices got very much rectified after the adsorption processes of (NO_2, O_2) and SO_3 molecules, respectively. The deviations of IV curves were so large so that the calculated bias-averaged sensor responses were: 21.8%, 9.86% and 5.94%, respectively.

1. Having tested the adsorption and sensor responses of these two devices (i.e., GNR:B and GNR:N) to many other gases (e.g., N_2, H_2, O_3, CO, CO_2, H_2O, H_2S, NH_3, NO, and SO_2), the results showed that all of these gases do exhibit either physisorption processes or chemisorption processes but with undetectable electric current (i.e., below nA). So, we concluded that GNR:B has an exceptionally high sensitivity (i.e., in other words selectivity) to detect NO_2 gas molecules.

2. Two kinds of NDR behaviors were obtained in case of GNR:N nanodevices. Before the adsorption of SO_3 molecules, the NDR existing in a broad bias range [0.5,1.0] Volt with Top to Valley Current Ratio (TVCR) is 1.32 has been attributed to Esaki-diode effects (i.e., quantum coherence effects). Whereas the two NDR behaviors in the IV-characteristics after the chemisorption of SO_3 molecules occurring at biases 0.5 V and 0.9 V are attributed to Gunn-diode effects (i.e., bias crossing energies of defects states).

3. While SO_3 molecule exhibits physisorption process on GNR:B, both NO_2 and O_2 molecules alter chemisorption processes on GNR:N. However, the produced currents on GNR:N-based devices after NO_2 and O_2 chemisorption processes are found to be vanishingly small and below the detection limit. Hence, it is suggested to use the combination of GNR:B and GNR:N to make gas-sensor and logical-gate alarm sensor for NO_2 gas, respectively.

Our theoretical results find support by experimental work done by Cho and coworkers [77]. The B/N edge-doping should be considered in fabricating GNR-based nano-devices to reach high gas-sensing selectivity towards detecting toxic NO_2 and SO_3 gases, respectively.

In the third Chapter, we moved on to studying the adsorption properties of H_2 molecule on Mn-embedded C_2N. Special attention was paid to the effects of dimerization and magnetization on the adsorption properties. So, a clear comparison is made between two cases of embedment: (i) Single Atom Catalyst "SAC" (i.e., C_2N:1Mn) and (ii) Dimer Atom Catalyst "DAC" (i.e., C_2N:2Mn). The relaxation of H_2 molecule on these two systems always yielded chemisorption processes associated with weak molecular dissociation. Further details about the results of our investigation can be summarized as follows:

- The relaxation of H_2 on pristine C_2N yielded physisorption with weak adsorption energy of about $E_{ads} = -0.109$ eV. The situation can be changed to chemisorption through the functionalization of C_2N, such as embedding Mn atom(s) in the pore of C_2N; and in that case special attention was paid to the effects of magnetic moment and catalyst clustering (e.g., dimerization) on the adsorption properties.

- In the case of SAC (i.e., $1Mn@C_2N$), originally the system had high magnetic moment of about 3.60 μB. The relaxation of H_2 molecule on SAC yielded chemisorption associated with weak molecular dissociation. The adsorption energy was estimated to be about $E_{ads}=-0.474$ eV. The chemisorption process modified many characteristics; for instance, the appearance of a bandgap opening of about $E_g = 0.11$ eV and the reduction in magnetic moment to about 3.40 μB;

- In case of DAC (i.e., $Mn_2@C_2N$), this system behaved as half-metal with magnetization of about 2.42 μB. The relaxation of H_2 molecule on DAC yielded chemisorption associated with weak molecular dissociation. The adsorption energy was found to be about $E_{ads} = -0.551$ eV. The chemisorption of H_2 opened a band gap at Fermi level of energy up to $E_g = 0.20$ eV and reduced the magnetic moment to about 1.97 μB;

- As far as the recovery time is concerned, SAC had less adsorption energy and thus shorter recovery time than DAC (i.e., 92 μs and 1.8 ms, respectively). So, the clustering of Mn in the pore of C_2N increased the adsorption energy and recovery time. In any case, the recovery time is still very small (i.e., $\tau \ll 1$ s). So, the C_2N:Mn based gas sensor would be of reusable type.

As a matter of fact, the H_2 chemisorption on Mn-doped C_2N caused enormous changes in the electronic and magnetic properties, and the adsorption energy is moderate (E_{ads} lies in between strong physisorption and weak chemisorption; as having values around 0.5 eV), the recovery time is at the order of μs – ms. Mn is a unique element by having an intrinsic magnetization.

The chemisorption of H_2 on such catalyst would modify the net magnetization and thus the electronic structure of the system; for instance, by opening small energy gap at Fermi level and thus modifying the transport properties. Therefore, one can conclude that C_2N:Mn should be an excellent candidate for platform of a reusable magnetic gas-sensor with high performance to detect H_2 gas, and having high stability, sensor response and rapid recovery time.

In the fourth Chapter, the suitability of metal (Ca versus Mn) embedded C_2N as a promising ion in metal-ion batteries (MIB) was investigated. Special attention was given to the effect of type of catalyst, magnetism, and clustering (SAC versus DAC) on the

specific capacity and relevance for energy-storage and/or gas-sensing applications. The results showed the following:

1. C$_2$N:Ca always exhibited physisorption with H$_2$ molecule with an increasing adsorption energy with the clustering of Ca atoms in the pore. These indicators corroborate the candidature of C$_2$N:Ca to be used as platform-based anode material in CIBs.

2. Mn doped C$_2$N exhibited chemisorption with H$_2$ molecule, associated with molecular dissociation. SAC-Mn embedded C$_2$N exhibited chemisorption with H$_2$ molecule, associated with a weak molecular splitting and a moderate adsorption energy (i.e., E$_{ads}$=- 0.474 eV laying within the energy range acceptable for energy-storage applications). C$_2$N:SAC-Mn can have dual applications. It shows potential to be used as a reusable hydrogen gas sensor gas with high sensitivity and very low recovery time (t « 1 s). It should further be considered as a strong concurrent candidate to Ca for anode material in metal-ion battery application with even higher irreversible capacity of up to 663 mAhg^{-1}.

For future work, the uptake capacity of Ca catalysts per single pore of C$_2$N as well as the optimization of number of H$_2$ molecules to remain adsorbed are still unchecked. Similarly, if the experimental challenge of achieving the synthesis of SAC/ DAC of Mn-doped C$_2$N were overcome, then one also needs to find out the hydrogen uptake capacity there. The desorption procedure in cases of Mn-doping requires sophisticated computational technique such as CPMD method. If the desorption is found plausible on DAC-Mn embedded C$_2$N, then it would be better candidate than SAC-Mn for platform-based cathode material for MIB applications with a capacity that can theoretically reach 1110 mAhg^{-1}.

In the fifth Chapter, the effectiveness of catalytic activity of four magnetic TM-SAC atoms (i.e., Mn, Fe, Co, and Ni) toward the adsorption and gas-sensing properties of two toxic gases (e.g., NO and NO$_2$) has been theoretically investigated.
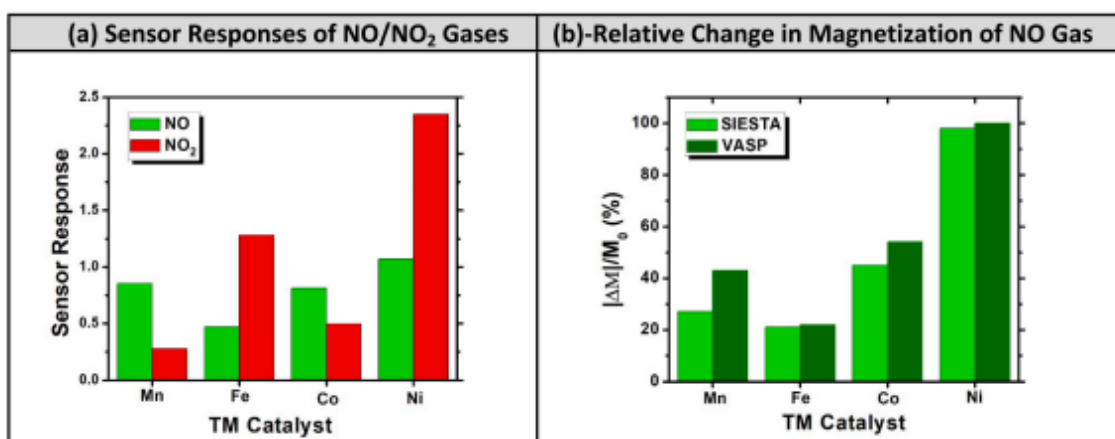
Figure 8.1: Bias averaged Sensor response and relative change in magnetization versus catalyst for NO and NO_2 adsorption.

While all the four catalysts yield strong chemisorption states with both gas molecules, two main trends are worth quoting:

(a) It should be inferred that the strength of the adsorption, E_{ads} and Δq, (e.g., like in C_2N:Mn case) should not necessarily imply to yield the highest sensor response. But what matters more in case of magnetic TM catalyst is, rather, the associated change in magnetic state (i.e., change of magnetization in both magnitude and direction)

(b) Our results demonstrated that the highest sensor responses (i.e., cases Ni for NO/NO_2 molecules and Fe for NO_2 molecule) are found to correlate very nicely to the optimal relative changes in magnetization. This is attributed to the engagement of their unpaired d-electrons into the bonding with the molecule (e.g., in case of NO/Ni, all the unpaired d-electrons of Nickel are engaged in the bonding, so its magnetization vanishes).

Obviously, magnetization would directly affect the IV characteristics to yield optimal sensor response. Our presented results have been benchmarked with the available data in literature for authenticity purposes. The results showed the relevance of magnetic SAC@C_2N-NR for toxic-gas reduction reactions. Furthermore, as the synthesis of C_2N and its doping with TM atoms have been experimentally realized, we expect our work to be further explored in the fabrication of sensor platform based on Ni- and Fe-embedded C_2N for an enhanced performance of gas sensing both NO and NO_2 toxic gases.

In Chapter 6, we have used spin-polarized DFT calculations to search for the existence of 'half-metallicity' in C_2N functionalized by embedding various configurations of TM-atom such as SACs, DACs, and their combinations. We scanned all possible catalysts comprising of the 3d block of TM elements ranging from Sc to Zn.

We were limited by the system size, due to computational constraints but luckily, the task was completely achieved as the 'half-metallicity' was proven to originate from FMC interactions between the group of TM-dopants and its six mirror images, formed by the periodic-boundary conditions. So, the needed samples are of sizes 2×2, 3×3, and at most 4×4 PCs (i.e., comprising four-TM atoms at maximum, and 72, 162, 288 atoms, respectively). The results can be summarized as follows:

(a) Pristine C_2N is paramagnetic semiconductor with bandgap energy of about 1.67 eV a bit underestimated compared to the experimental data of inventors 1.96 eV.

(b) Three TM atoms (i.e. Mn, Fe and Ni) are found to induce the 'half-metallicity' in C_2N sample of size 2×2 PCs in five different configurations, namely:

        i) C_2N:Mn_2 (DAC),

        ii) C_2N:Mn–Mn (SAC–SAC),

        iii) C_2N:Mn_2–Mn (DAC–SAC),

        iv) C_2N:Fe_2 (DAC), and

        v) C_2N:Ni_2–Ni (DAC– SAC).

(c) The calculations of binding energies confirmed that the embedment of both SAC and DAC were thermodynamically very stable. The recursive energy in DAC is even higher than the cohesive energy in strength.

(d) The calculations of the magnetization revealed that the DAC in one large pore of C_2N exchange AFMC interaction, whereas the inter-pore magnetic interaction between SAC–SAC, or DAC– SAC, or DAC–DAC to be FMC interaction. Yet, such FMC/AFMC intra-group interaction should be the driving force for the induction of the 'half-metallicity'.

(e) The scaling of sample size to comprise the 3×3- PC and 4×4-PC samples has shown the disappearance of the half-metallicity and confirmed that its existence would be attributed not to the intra-magnetic coupling interactions but rather to the FMC

interactions of the group of TM dopants with its six mirror images, formed via the implementation of the periodic-boundary conditions.

Thus, our work showed the design of 2D functionalized materials (e.g., TM-catalysts embedded in large pores of C_2N as SAC–DAC combinations) hosting 'half-metallicity'. The results further showed that the origins of existence of 'half-metallicity' to be attributed to the existence of FMC interactions between the group of TM-dopants and its six mirror images. Half metallicity is a fundamental pillar in spintronics, and our results should be very relevant to spintronic device applications.

Finally in the seventh Chapter, we have used spin polarized-DFT calculation to study the suppression of shuttle effect in sodium-sulfur batteries for the enhancement of their performance and the lifetime. MXenes ($Hf_3C_2T_2$ and $Zr_3C_2T_2$ with T = F/O) were proposed as promising candidates for additive-cathodes (anchors) and found to be efficient for both suppressing the shuttle effect and catalyzing the electrochemistry process. The binding energies of sodium polysulfides (Na_2S_n) on all the studied MXenes are found to be stronger than those with electrolytes (e.g., DOL and DME). The oxygen passivation was further shown to have greater chemical binding to polysulfides and lower activation energy for ion kinetics during the discharging process. Thus, our results are in favor of candidature of using MXenes as additive-cathodes (anchors) in room-temperature sodium-sulfur batteries to warrant better performance and longer lifetime.

Overall, we have proposed solutions to critical problems by tailoring the properties of existing materials, by functionalizing them. The state-of-the-art computational packages used by us, VASP and QuantumATK are powerful packages for investigating the properties of these materials and can provide insights for future research.

References

1. K.S. Novoselov, A. K. Geim, S. V. Morozov, D. Jiang, Y. Zhang, S. V. Dubonos, I. V. Grigorieva and A. A. Firsov, "Electric field effect in atomically thin carbon films," Science, vol. 306, pp. 666-669, 2004.

2. F. Schedin, A. K. Geim, S. V. Morozov, E. W. Hill, P. Blake, M. I. Katsnelson and K. S. Novoselov, "Detection of individual gas molecules absorbed on graphene," Nature Materials, vol. 6, pp. 652-655, 2007.

3. A. K. Geim and K.S. Novoselov, "The rise of graphene," Nature Materials, vol. 6, pp. 183-191, 2007.

4. A. H. Castro Neto, F. Guinea, N. M. R. Peres, K. S. Novoselov and A. K. Geim, "The electronic properties of graphene," Reviews of Modern Physics, vol. 81, pp. 109-162, 2009.

5. M. J. Allen, V. C. Tung and R. B. Kaner, "Honeycomb carbon: A review of graphene," Chemical Reviews, vol. 110, pp. 132-145, 2010.

6. S. S. Varghese, S. Lonkar, K. K. Singh, S. Swaminathan and A. Abdala, "Recent advances in graphene-based sensors," Sensors Actuators B, vol. 218, pp. 160-183 2015.

7. R. Mas Balleste, C. Gomez-Navarro, J. Gomez-Herrero and F. Zamora, "2D materials: to graphene and beyond," Nanoscale, vol. 3, pp. 20-30, 2011.

8. C. M. Fang, G. A. De Wijs and R. A. De Groot, "Spin polarization in half-metals," Journal of Applied Physics, vol. 91, pp. 8340-8344, 2002.

9. Y. W. Son, M. L. Cohen and S. G. Louie, "Half-Metallic Graphene Nanoribbons," Nature, vol. 444, pp. 1717-1724, 2006.

10. N. Mohanty, D. Moore, Z. Xu, T. S. Sreeprasad, A. Nagaraja, A. Alexander Rodriguez and V. Berry, "Nanotomy-based production of transferable and dispersible graphene nanostructures of controlled shape and size," Nature Communications, vol. 3 pp. 844-848, 2012.

11. C. Wang, Y. Zhao, Y. Zhang, L. Miao, J. Wu, Y. Yang, Z. Xu, Q. Peng, X. He and C. Sui, "Partially unzipping carbon nanotubes: "A route to synchronously improve fracture strength and toughness of nanocomposites inspired by pinning effect of screw," Materials Today Communications, vol. 25, pp. 1013-25, 2020.

12. J. Mahmood, E. K. Lee, M. Jung, D. Shin, I. Y. Jeon, S. M. Jung, H. J. Choi, J. M. Seo, S. Y. Bae, S. D. Sohn, N. Park, J. H. Oh, H. J. Shin and J. B. Baek, "Nitogenated holey two-dimensional structures," Nature Communications, vol. 6, pp. 646-658, 2015.

13. A. C. Lokhande, I. A. Qattan, C. D. Lokhande and S. P. Patole, "Holey graphene: an emerging versatile material," Journal of Material Chemistry A, vol. 8, pp. 918-977, 2020.

14. Y. Zhang, Q. Wan and N. Yang, "Recent advances of porous graphene: Synthesis, functionalization, and electrochemical applications," Small, vol. 15, pp. 1903-1916, 2019.

15. J. Xu, J. Mahmood, Y. Dou, S. Dou, F. Li, L. Dai and J. B. Baek, "2D frameworks of C2N and C3N as new anode materials for lithium batteries," Advanced Materials, vol. 29, pp. 1702-1707, 2017.

16. C. Huang, J. Mahmood, Z. Wei, D. Wang, S. Liu, Y. Zhao, H. J. Noh, J. Ma, J. Xu, J. B. Baek, "Metal (M = Ru, Pd and Co) embedded in C2N with enhanced lithium storage properties," Materials Today Energy, vol. 14, pp. 1030-1059, 2019.

17. J. Zhou, X. Zha, X. Zhou, F. Chen, G. Gao, S. Wang, C. Shen, T. Chen, C. Zhi, P. Eklund, S. Du, J. Xue, W. Shi, Z. Chai and Q. Huang, "Synthesis and electrochemical properties of two-dimensional Hafnium Carbide," ACS Nano, vol. 11, pp. 3841-3850, 2017.

18. J. Zhou, X. Zha, F. Y Chen, Q. Ye, P. Eklund, S. Du and Q. Huang, "A new two-dimensional Zirconium Carbide MXene by selective etching of Al3C3 from nanolaminated Zr3Al3C5," Angewandte Chemie, vol. 55, pp. 5008-5013, 2016.

19. R. Jayan and M. M. Islam, "Mechanistic Insights into Interactions of Polysulfides at VS2 Interfaces in Na−S Batteries: A DFT Study," ACS Applied Material Interfaces, vol. 13, pp. 35848-35855, 2021.

20. M. S. Nahian, R. Jayan, T. Kaewmaraya, T. Hussain, M. M. Islam, "Elucidating Synergistic Mechanisms of Adsorption and Electrocatalysis of Polysulfides on Double-Transition Metal MXenes for Na−S Batteries," ACS Applied Material Interfaces, vol.14, pp. 10298-10307, 2022.

21. US-EPA Integrated Science Assessment for Oxides of Nitrogen – Health Criteria (2016 Final Report). US Environmental Protection Agency, Washington, DC. EPA/ 600/R-15/068.

22. R. Kikuchi, "Environmental management of sulfur trioxide emission: Impact of SO3 on human health," Environment Management, vol. 27, pp. 837-844, 2001.

23. H. Li, J. Zhong, H. Vehkamaki, T. Kurten, W. Wang, M. Ge, S. Zhang, Z. Li, X. Zhang, J. S. Francisco and X. C. Zeng, "Self-catalytic reaction of SO3 and NH3 to produce sulfamic acid and its implication to atmospheric particle formation," Journal of American Chemical Society, vol. 140, pp. 11020-11028, 2018.

24. A. Shaheen, M. Ali, W. Othman and N. Tit, "Origins of negative differential resistance in N-doped ZnO nanoribbons: Ab-initio investigation," Scientific Reports, vol. 9. pp. 9914-9938, 2019.

25. Z. D. Zheng, X. C. Wang and W. B. Mi, "Tunable electronic structure and spin splitting in single and multiple Fe-adsorbed g-C2N with different layers: A first-principles study," Journal of Physics and Chemistry of Solids, vol. 115, pp. 221-227, 2018.

26. Y. Ding, "A combined theoretical and experimental study on the oxygenated graphitic carbon nitride as a promising sulfur host for lithium–sulfur batteries," Journal of Power Sources, vol. 373, pp. 218-232, 2018.

27. S. Liang, C. Hao and Y. Shi, "The power of single-atom catalysis," Chem Cat Chem, vol. 7, pp. 2559-2567, 2015.

28. B. Bayatsarmadi, Y. Zheng, A. Vasileff and S. Z. Qiao, "Recent advances in atomic metal doping of carbon-based nanomaterials for energy conversion," Small, vol. 13, pp. 1700-1719, 2017.

29. B. L. He, J. S. Shen and Z. X. Tian, "Iron-embedded C2N monolayer: a promising low-cost and high-activity single-atom catalyst for CO oxidation," Physical Chemistry Chemical Physics, vol. 18, pp. 24261-24269, 2016.

30. A. A. Banu, S. Z. Karazhanov, K. V. Kumar and S. P. Jose, "Platinum doped iron carbide for hydrogen evolution reaction: The effects of charge transfer and magnetic moment by first-principle approach," International Journal of Hydrogen Energy, vol. 45, pp. 31825-31840, 2020.

31. R. A. de Groot, F. M. Mueller, P. G. Van Engen and K. H. J. Buschow, "New class of materials: half-metallic ferromagnets," Physical Review Letters, vol. 50, pp. 2024-2027, 1983.

32. J. H. Park, "Direct evidence for a half-metallic ferromagnet," Nature, vol. 392, pp. 794-796, 1998.

33. S. A Wolf and A. Anthony, "Spintronics: A spin-based electronics vision for the future," Science, vol. 294, pp. 1488-1495, 2001.

34. H. Han, K. Umemoto, Z. Wu and R. M. Wentzcovitch, "An adaptive genetic algorithm for crystal structure prediction," Reviews in Mineralogy and Geochemistry, vol. 71, pp. 169-199, 2010.

35. V. Etacheri, R. Marom, R. Elazari, G. Salitra and D. Aurbach, "Challenges in the development of advanced Li-ion batteries: A Review," Energy & Environmental Science, vol. 4, pp. 3243-3262, 2011.

36. M. Armand and J. M. Tarascon, "Building better batteries" Nature, vol. 451, pp. 652-657, 2001.

37. J. M. Tarascon and M. Armand, "Issues and challenges facing rechargeable lithium batteries," Nature, vol. 414, pp. 359-367, 2001.

38. Y. Qie, J. Liu, S. Wang, S. Gong and Q. Sun, "C3B monolayer as an anchoring material for lithium-sulfur batteries," Carbon, vol. 129, pp. 38-44, 2019.

39. H. J. Noh, J. Ma, J. Xu and J. B. Baek, "Metal (M = Ru, Pd and Co) embedded in C2N with enhanced lithium storage properties," Materials Today Energy, vol. 14, pp. 1003-1059, 2019.

40. M. Armand and J. M. Tarascon, "Review of the future perspectives of metal-ion batteries," Nature, vol. 552, pp. 789-808, 2011.

41. R. M. Balleste, C. G. Navarro, J. G. Herrero and F. Zamora, "2D materials: to graphene and beyond," Nanoscale, vol. 3, pp. 20-30, 2011.

42. J. M. Tarascon, "The rise of metal-ion batteries," Nature, vol. 414, pp. 859-867, 2012.

43. S. Lin, Q. Qiao, X. Chen, R. Hu and N. Lai, "Transition metal atom doped C2N as catalyst for the oxygen reduction reaction: A density functional theory study," International Journal of Hydrogen Energy, vol. 45, pp. 27202-27209, 2020.

44. C. Huang, J. Mahmood, Z. Wei, D. Wang, S. Liu, Y. Zhao, H. J. Noh, J. Ma, J. Xu and J. B. Baek, "Experimental realization of singly dispersed metal atoms in C2N with enhanced lithium storage properties" Materials Total Energy, vol. 18, pp. 1253-1279, 2021.

45. B. Dunn , H Kamath and J. M. Tarascon, "Electrical energy storage for the grid: a battery of choices," Science, vol. 334, pp. 928-935, 2011.

46. T. Zhou, W. Liv, J. Li, G. Zhou, Y. Zhao, S. Fan, B. Liu, B. Li, F. Kang and Q. H. Yang, "Twinborn TiO2-TiN heterostructures enabling smooth trapping-diffusion-conversion of polysulfides towards ultralong life lithium sulfur batteries," Energy and Environmental Science, vol. 10, pp. 1694-1703, 2017.

47. Z. L. Xu, J. Q. Huang, W. G. Chong, X. Qin, X. Wang, L. Zhou and J. K. Kim, "In Situ TEM study of volume expansion in porous carbon nanofiber/Sulfur cathodes with exceptional high-rate performance," Advanced Energy Materials, vol. 7, pp. 1620-1678, 2017.

48. L. Li, K. H. Seng, D. Li, Y. Xia, H. K. Liu and Z. Guo, "SnSb@carbon nanocable anchored on graphene sheets for sodium ion batteries," Nano Research, vol. 7, pp. 1466-1476, 2017.

49. K. B. Hueso, M. Armand and T. Rojo, "High temperature sodium batteries: status, challenges and future trends," Energy and Environmental Science, vol. 6, pp. 734-749, 2013.

50. A. A. Koenig and J. R. Rasmussen, "Development of a high specific power sodium sulfur cell," Proceedings of the 34th International Power Sources Symposium Electrochemical Society, pp. 30-34, 1990.

51. W. Auxer, "The PB sodium sulfur cell for satellite battery applications," Proceedings of the International Power Sources Symposium. Electrochemical Society, pp. 49–54, 1989.

52. S. Wei, S. Choudhury, J. Xu, P. Nath, Z. Tu and L. A. Archer, "Highly stable sodium batteries enabled by functional ionic polymer membranes," Advanced Materials, vol. 29, pp. 1605-1612, 2017.

53. G. Sun, J. Jurti, P. Rajczy, M. Kertesz, J. Hafner and G. Kresse, "Performance of the Vienna ab-initio simulation package (VASP) in chemical applications," Journal of Molecular Structure Theochem, vol. 624, pp. 37-45, 2003.

54. J. M. Soler, E. Artacho, J. D. Gale, A. Garcia, J. Junquera, P. Ordejon, S. Sanchez Portal, "The SIESTA method for ab-initio order -N materials simulation," Journal of Physics: Condensed Matter, vol. 14, pp. 2745-2756, 2002.

55. M. Brandbyge, J. L. Mozos, P. Ordejon, J. Taylor and K. Stokbro, "Density functional method for non-equilibrium electron transport," Physical Review B, vol. 65, pp. 165-182, 2002.

56. H. J. Monkhorst and J. D. Pack, "Special points for Brillouin-zone integrations," Physical Review B, vol. 13, pp. 5188-5192, 1976.

57. S. Grimme, J. Antony, S. Ehrlich and H. Krieg, "A consistent and accurate ab initio parametrization of density functional dispersion correction (DFT-D) for the 94 elements H-Pu," Journal of Chemical Physics, vol. 132, pp. 18-32, 2010.

58. G. Henkelman, A. Arnaldsson and H. Jonsson, "A fast and robust algorithm for Bader decomposition of charge density," Computational Material Science, vol. 36, pp. 354-360, 2006.

59. M. Buttiker, Y. Imry, R. Landauer and S. Pinhas, "Generalized many-channel conductance formula with application to small rings," Physical Review B, vol. 31, pp. 6207-6215, 1985.

60. A. I. Ayesh, A. F. S. Abu-Hani, S. T. Mahmoud and Y. Haik, "Selective H2S sensor based on CuO nanoparticles embedded in organic membranes," Sensors Actuators B. vol. 231, pp. 593-600, 2016.

61. K. S. Novoselov, V. I. Fal, L. Colombo, P. R. Gellert, M. G. Schwab and K. Kim, "Roadmap of graphene," Nature, vol. 490, pp. 192-200, 2012.

62. W. Lu, P. Soukiassian and J. Boeckl, "Graphene: Fundamentals and functionalities," MRS Bulletin, vol. 37, pp. 1119-1124, 2012.

63. F. Schwierz, "Graphene transistors," Nature Nanotechnology, vol. 5, pp. 487-496, 2010.

64. X. Yang, X. Dou, A. Rouhanipous, L. Zhi, H. J. Rader and K. Mullen, "Two-dimensional graphene nanoribbons," Journal of American Chemical Society, vol. 130, pp. 421-426, 2008.

65. J. Cai, P. Ruffieux, R. Jaafar, M. Bieri, T. Braun, S. Blankenburg, M. Muoth, A. P. Peitsonen, M. Saleh, X. Feng, K. Mullen and R. Fasel, "Atomically precise bottom-up fabrication of graphene nanoribbons," Nature, vol. 22, pp. 466-470, 2010.

66. Y. W. Son, M. L. Cohen and S. G. Louie, "Energy gaps in graphene nanoribbons," Physical Review Letters, vol. 97, pp. 216-223, 2006.

67. L. Ci, L. Song, C. Jin, D. Jariwala, D. Wu, Y. Li, A. Srivastava, Z. F. Wang, K. Storr, L. Balicas, F. Liu and P. M. Ajayan, "Atomic layers of hybridized boron nitride and graphene domains," Nature Materials, vol. 9, pp. 430-435, 2006.

68. D. Soriano, F. Munoz-Rojas, J. Fernandez-Rossier and J. J. Palacios, "Hydrogenated graphene nanoribbons for spintronics," Physical Review B, vol. 81, pp.165-189, 2010.

69. H. Huang, S. Su, N. Wu, H. Wan, S. Wan, H. Bi and L. Sun, "Graphene-based sensors for human health monitoring," Frontiers in Chemistry, vol. 7, pp. 399-413, 2019.

70. H. J. Yoon, D. H. Jun, J. H. Yang, Z. Zhou, S. S. Yang and M. M. C. Cheng, "Carbon dioxide gas sensor using a graphene sheet," Sensors Actuators B: Chemistry, vol. 157 pp. 310–313, 2011.

71. Y. Zhao, X. G. Li, X. Zhou and Y. N. Zhang, "Heterogeneous precipitation behavior and stacking-fault-mediated deformation in a Co Cr Ni-based medium-entropy alloy," Sensors Actuators B: Chemistry, vol. 231, pp. 72-82, 2016.

72. S. Kumar, V. Pavelyev, P. Mishra and N. Tripathi, "A review on chemiresistive gas sensors based on carbon nanotubes: device and technology transformation," Sensors Actuators A: Physics, vol. 283, pp. 174-186, 2018.

73. S. W. Chiu and K. T. Tang, "Towards a chemiresistive sensor-integrated electronic nose: a review," Sensors, vol. 13, pp. 14214-14247, 2013.

74. J. L. Johnson, A. Behnam, S. J. Pearton and A. Ural, "Hydrogen sensing using Pd-functionalized multi-layer graphene nanoribbon networks," Advanced Materials, vol. 22, pp. 4877-4880, 2010.

75. S. Yuan and S. Zhang, "Recent progress on gas sensors based on graphene-like 2D/2D nanocomposites," Journal of Semiconductors, vol. 40, pp. 111-116, 2019.

76. N. Joshi, T. Hayasaka, Y. Liu, H. Liu, O. N. Oliveira Jr and L. Lin, "A review on chemiresistive room temperature gas sensors based on metal oxide nanostructures, graphene and 2D transition metal dichalcogenides," Microchimica Acta, vol. 185, pp. 213-228, 2018.

77. K. M. Cho, S. Y. Cho, S. Chong, H. J. Koh, D. W. Kim, J. Kim and H. T. Jung, "Edge-functionalized graphene nanoribbon chemical sensor: Comparison with carbon nanotube and graphene," ACS Applied Material Interfaces, vol. 10, pp. 42905-42914, 2018.

78. B. Huang, Z. Li, Z. Liu, G. Zhou, S. Hao, J. Wu, B. L. Hu, W. Duan, "Adsorption of gas molecules on graphene nanoribbons and its implication for nanoscale molecule sensor," Journal of Physical Chemistry C, vol. 112, pp. 13442-13446, 2018.

79. A. Saffarzadeh, "Modeling of gas adsorption on graphene nanoribbons," Journal of Applied Physics, vol. 107, pp. 1143-1149, 2010.

80. Y. H. Zhang, Y. B. Chen, K. G. Zhou, C. H. Liu, J. Zeng, H. L. Zhang and Y. Peng, "Improving gas sensing properties of graphene by introducing dopants and defects: a first-principles study," Nanotechnology, vol. 20, pp. 1855-1896, 2009.

81. F. Banhart, J. Kotakoski, A. V. Krasheninnikov, "Structural defects in graphene," ACS Nano, vol. 5, pp. 26-41, 2011.

82. N. Tit, K. Said, N. M. Mahmoud, S. Kouser and Z. H. Yamani, "Ab-initio investigation of adsorption of CO and CO2 molecules on graphene: Role of intrinsic defects on gas sensing," Applied Surface Science, vol. 394, pp. 219-230, 2017.

83. N. Baildya, N. N. Ghosh and A. P. Chattopadhyay, "Tailoring electronic and transport properties of edge-terminated armchair graphene by defect formation and N/B doping," Physics Letters A, vol. 81, pp. 1261-1294, 2018.

84. C. Ataca, E. Akturk and S. Ciraci, "Hydrogen storage of calcium atoms absorbed on graphene: first-principles plane wave calculations," Physical Review B, vol. 79, pp. 41-46, 2009.

85. T. Hussain, B. Mortazavi, H. Bae, T. Rabczuk, H. Lee and A. Karton, "Enhancement in hydrogen storage capacities of light metal functionalized Boron-Graphdiyne nanosheets," Carbon, vol. 147, pp. 199-205, 2019.

86. K. Alhameedi, T. Hussain, H. Bae, D. Jayatilaka, H. Lee and A. Karton, "Reversible hydrogen storage properties of defect-engineered C4N nanosheets under ambient conditions," Carbon, vol. 152, pp. 344-353, 2019.

87. T. Hussain, M. Hankel and D. J. Searles, "Computational evaluation of Lithium functionalized carbon nitride (g-C6N8) monolayer as an efficient hydrogen-storage material," Journal Physical Chemistry C, vol. 120, pp. 25180-25188, 2016.

88. G. Qin, Q. Cui, B. Yun, L. Sun, A. Du and Q. Sun, "High capacity and reversible hydrogen storage on two dimensional C2N monolayer membrane," International Journal of Hydrogen Energy, vol. 43, pp. 9895-9901, 2018.

89. Y. Su, Z. Ao, Y. Ji, G. Li and T. An, "Adsorption mechanisms of different volatile organic compounds onto pristine C2N and Al-doped C2N monolayer: A DFT investigation," Applied Surface Science, vol. 450, pp. 484-491, 2018.

90. M. Eslami, M. Moradi and R. Moradi, "DFT investigation of hydrogen adsorption on the C3N nanotube," Vacuum, vol. 133, pp. 7-12, 2016.

91. M. Zhou, Y. H. Lu, Y. Q. Cai, C. Zhang and Y. P. Feng, "Adsorption of gas molecules on transition metal embedded graphene: a search for high-performance graphene-based catalysts and gas sensors," Nanotechnology, vol. 22, pp. 3855-3872, 2011.

92. A. K. Mishra and S. Ramaprabhu, "Carbon dioxide adsorption in graphene sheets," AIP Advances, vol. 1, pp. 321-333, 2011.

93. A. K. Mishra and S. Ramaprabhu, "Nano magnetite decorated multiwalled carbon nanotubes: a robust nanomaterial for enhanced carbon dioxide adsorption," Energy and Environmental Science, vol. 4, pp. 88-92, 2011.

94. H. P. Zhang, X. G. Luo, X. Y. Lin, X. Lu, Y. Leng and H. T. Song, "Density functional theory calculations on the adsorption of formaldehyde and other harmful gases on pure, Ti-doped, or N-doped graphene sheets," Applied Surface Science, vol. 283, pp. 559-565, 2013.

95. J. D. Durbin and C. Malardier-Jugroot, "Density functional theory analysis of metal/ graphene systems as a filter membrane to prevent CO poisoning in hydrogen fuel cells," Journal of Physical Chemistry C, vol. 115, pp. 808-815, 2011.

96. L. Wang, Q. Luo, W. Zhang and J. Yang, "Transition metal atom embedded graphene for capturing CO a first-principles study," International Journal of Hydrogen Energy, vol. 39, pp. 20190-20196, 2014.

97. Y. Tang, D. Ma, W. Chen and X. Dai, "Improving the adsorption behavior and reaction activity of CO and O2 molecules," Sensors Actuators B, vol. 211, pp. 227-234, 2015.

98. A. Shaheen, M. Ali, W. Othman and N. Tit, "Origins of negative differential resistance in N-doped ZnO nanoribbons: Ab-initio investigation," Scientific Reports, vol. 9914, pp. 1-8, 2019.

99. N. Tit, W. Othman, A. Shaheen and M. Ali, "High selectivity of N-doped ZnO nanoribbons in detecting H_2, O_2 and CO_2 molecules: effect of negative-differential resistance on gas-sensing," Sensors Actuators B, vol. 270, pp. 167-178, 2018.

100. M. Abu-Haija, A. F. S. Abu-Hani, N. Hamdan, S. Stephen, and A. I. Ayesh, "Characterization of H2S gas sensor on CuFe2O4 nanoparticles," Journal of Alloys and Compounds, vol. 690, pp. 461-468, 2017.

101. N. F. Mott, "Conduction in non-crystalline systems: IX The minimum metallic conductivity," Philosophical Magazine, vol. 26, pp. 1015-1026, 1972.

102. E. A. Davis and W. D. Compton, "Compensation dependence of impurity conduction in antimony-doped germanium," Physical Review B, vol. 140, pp. 2183-2194, 1965.

103. N. Tit, P. Pradhan and N. Kumar, "Length-scale dependent ensemble-averaged conductance of a 1D disordered conductor conductance minimum," Physical Review B, vol. 27, pp. 14715-14717, 2017.

104. G. Wisz, I. Virt, P. Sagan, P. Potera and R. Yavorskyi, "Structural, optical and electrical properties of zinc oxide layers produced by pulsed laser deposition method," Nanoscale Research Letters, vol. 12 pp. 253-261, 2017.

105. N. H. Al-Hardan, M. J. Abdullah, A. Abdul Aziz, H. Ahmad and L.Y. Low, "ZnO thin films for VOC sensing applications. Vacuum 85, pp. 101-106, 2010.

106. S. D. Sarma, S. Adam, E. H. Hwang and E. Rossi, "Electronic transport in two-dimensional graphene," Reviews in Modern Physics, vol. 83, pp. 407-470, 2011.

107. K. I. Bolotin, K. J. Sikes, Z. Jiang, M. Klima, G. Fudenberg, J. Hone, P. Kim and H. L. Stomer, "Ultrahigh electron mobility in suspended graphene," Solid State Communication, vol. 146, pp. 351-355, 2008.

108. P. Arifin, E. M. Goldys and T. L. Tansley, "Electron mobility in low temperature grown gallium arsenide," Material Science and Engineering B, vol. 35, pp. 330-333, 1995.

109. L. Liao, Y. C. Lin, M. Bao, R. Cheng, J. Bai, Y. Liu, Y. Qu, K. L. Wang, Y. Huang and X. Duan, "High-speed graphene transistors with a self-aligned nanowire gate" Nature, vol. 467, pp. 305-308, 2010.

110. F. Bonaccorso, Z. Sun, T. Hasan and A. C. Ferrari, "Graphene photonics and optoelectronics," Nature Photonics, vol. 4, pp. 611-622, 2010.

111. X. Wang, L. Zhi and K. Mullen, "Transparent, conductive graphene electrodes for dye-sensitized solar cell," Nano Letters, vol. 8, pp. 323-327, 2008.

112. D. I. Son, B. W. Kwon, D. H. Park, W. S. Seo, Y. Yi, B. Angadi, C. L. Lee and W. L. Choi, "Emissive ZnO-graphene quantum dots for white-light-emitting diodes," Nature Nanotechnology, vol. 7, pp. 465-471, 2012.

113. A. I. Vlasov, D. S. Terent'ev and V. A. Shakhnov, "Graphene flexible touchscreen with integrated analog-digital converter," Russian Microelectronics, vol. 46, pp. 192-199, 2017.

114. T. Mueller, F. Xia and P. Avouris, "Graphene photodetectors for high-speed optical communications," Nature Photonics, vol. 4, pp. 297–301, 2010.

115. Z. Sun, T. Hasan, F. Torrisi, D. Popa, G. Privitera, F. Wang, F. Bonaccorso, D. M. Basko and A. C. Ferrari, "Graphene mode-locked ultrafast laser," ACS Nano, vol. 4, pp. 803-810, 2010.

116. Y. Yang, A. Asiri, Z. Tang, D. Du and Y. Lin, "Graphene based materials for biomedical applications," Materials Today, vol. 16, pp. 365-373, 2010.

117. S. H. Bae, Y. Lee, B. K. Sharma, H. J. Lee, J. H. Kim, J. H. Ahn, "Graphene-based transparent strain sensor," Carbon, vol. 51, pp. 236-242, 2013.

118. Z. Jing, Z. Guang-Yu, S. Dong-Xia, "Review of graphene-based strain sensors," Chinese Physics B, vol. 22, pp. 577-592, 2013.

119. A. Ilnicka and J. P. Lukaszewicz, "Graphene-based hydrogen gas sensors: A review," Processes, vol. 8, pp. 633-638, 2020.

120. J. H. Choi, J. Lee, M. Byeon, T. E. Hong, H. Park and C. Y. Lee, "Graphene-based gas sensors with high sensitivity and minimal sensor-to-sensor variation," ACS Applied Nano Materials, vol. 3, pp. 2257-2265, 2020.

121. Z. Song, Z. Wei, B. Wang, Z. Luo, S. Xu, W. Zhang, H. Yu, M. Li, Z. Huang, J. Zang, F. Yi and H. Liu, "Sensitive room-temperature H2S gas sensors employing SnO2 quantum wire/reduced graphene oxide nanocomposites," Chemistry of Materials, vol. 28, pp. 1205-1212, 2016.

122. A. D. smith, K. Elgammal, X. Fan, M. C. Lemme, A. Delin, M. Rasander, L. Bergqvist, S. Schroder, A. C. Fischer, F. Niklaus and M. Ostling, "Graphene-based CO2 sensing and its cross-sensitivity with humidity," RSC Advances, vol. 7, pp. 22329-22339, 2017.

123. R. Pearce, T. Iakimov, M. Andersson, L. Hultman, A. Lloyd Spetz and R. Yakimova, "Epitaxially grown graphene-based gas sensors for ultra-sensitive NO2 detection," Sensor Actuators B, vol. 155, pp. 451–455, 2011.

124. D. Wu, B. Yang, H. Chen and E. Ruckenstein, "Nitrogenated holey graphene C2N monolayer anodes for lithium- and sodium-ion batteries with high performance," Energy Storage in Materials, vol. 16, pp. 574-58, 2016.

125. D. Wu, B. Yang, E. Ruckenstein and H. Chen, "Functionalization: An efficient approach to open and close channels for electron transfer in nitrogenated holey graphene C2N anodes in sodium-ion batteries," Journal of Physical Chemistry Letters, vol. 10, pp. 721-726, 2019.

126. J. Zhao, J. X. Zhao, F. Li, Z. Chen, "Copper dimer supported on a C2N layer as an efficient electro-catalyst for CO2 reduction reaction: A computational study," Journal of Physical Chemistry C, vol. 122, pp. 19712-19721, 2012.

127. D. W. Ma, Q. Wang, X. Yan, X. Zhang, C. He, D. Zhou, Y. Tang, Z. Lu and Z. Yang, "3d transition metal embedded C2N monolayers as promising single-atom catalysts: A first-principles study." Carbon, vol. 105, pp. 463-473, 2016.

128. M. Luo, Z. Liang, S. G. Peera, M. Chen, C. Liu, H. Yang, J. Liu, U. P. Kumar and T. Liang, "Theoretical study on the adsorption and predictive catalysis of MnN4 embedded in carbon substrate for gas molecule detection," Applied Surface Science, vol. 525, pp.146-162, 2020.

129. K. Liu, Z. Qiao, S. Hwang, Z. Liu, H. Zhang, D. Su, H. Xu, G. Wu and G. Wang, "Mn- and N-doped carbon as promising catalysts for oxygen reduction reaction: Theoretical prediction and experimental validation," Applied Catalysis B: Environmental, vol. 243 pp. 195-203, 2019.

130. S. Impeng, A. Junkaew, P. Maitarad, N. Kungwan, D. Zhang, L. Shi and S. Namuangruk, "A MnN4 moiety embedded graphene as a magnetic gas sensor for CO detection: A first principles study," Applied Surface Science, vol. 473, pp. 820-827, 2019.

131. K. Schmidt-Rohr, "How batteries store and release energy: Explaining basic electrochemistry," Journal of Chemistry and Education, vol. 95, pp. 1801-1810, 2018.

132. Q.A. Drmosh, Z. H. Yamani and M. K. Hossain, "Hydrogen gas sensing performance of low partial oxygen-mediated nanostructured zinc oxide thin film," Sensors Actuator B, vol. 248, pp. 868-877, 2017.

133. Q.A. Drmosh and Z. H. Yamani, "Hydrogen sensing properties of sputtered ZnO films decorated with Pt nanoparticles," Ceramics International, vol. 42, pp. 12378-12384, 2012.

134. S. G. Chalk and J. F. Miller, "Key challenges and recent progress in batteries, fuel cells, and hydrogen storage for clean energy systems," Journal of Power Sources, vol. 159, pp. 73-80, 2006.

135. J. Hafner, "Ab-initio simulations of materials using VASP: Density-functional theory and beyond," Journal of Computational Chemistry, vol. 29, pp. 2044-2078, 2008.

136. M. Ali and N. Tit, "Adsorption of NO and NO2 molecules on defected-graphene and ozone-treated graphene: First-principles analysis," Surface Science, vol. 684, pp. 28-36, 2019.

137. R. F. W. Bader, P. J. MacDougall and C. D. H. Lau, "Bonded and non-bonded charge concentrations and their relation to molecular geometry and reactivity," Journal of American Chemical Society, vol. 106, pp. 81-90, 1984.

138. L. Casillas-Trujillo, G. Baldinozzi, M. K. Patel, H. Xu and K. E. Sickafus, "Comparison of bonding and charge density in δ-UO3, γ-UO3, and La6UO12," Physical Review of Materials, vol. 1, pp. 654-662, 2017.

139. A. Qteish, "Electronegativity scales and electronegativity-bond ionicity relations: A comparative study," Journal of Physics and Chemistry in Solids, vol. 124, pp. 186-191, 2012.

140. C. Kittel, "Introduction to solid state physics," 8th edition Wiley, New York, 2005.

141. L. Pauling, "The energy of single bonds and the relative electronegativity of atoms," Journal of American Chemical Society, vol. 54, pp. 3570-3582, 1932.

142. Y. Yong, H. Cui, Q. Zhou, X. Su, Y. Kuang and X. Li, "C2N monolayer as NH3 and NO sensors: A DFT study," Applied Surface Science, vol. 487, pp. 488-495, 2019.

143. S. Peng, K. Cho, P. Qi and H. Dai, "Ab-initio study of CNT NO2 gas sensor," Chemical Physics Letters, vol. 387, pp. 271-276, 2004.

144. A. Guirguis, J. W. Maina, X. Zhang, L. C. Henderson, L. Kong, H. Shon and L. F. Dumee, "Applications of nano-porous graphene materials: critical review on performance and challenges," Materials Horizon, vol. 7, pp. 1218-45, 2020.

145. S. Yadav, J. Tam and C. V. Singh, "A first-principles study of hydrogen storage on lithium decorated two-dimensional carbon allotropes," International Journal of Hydrogen Energy, vol. 40, pp. 6128-6136, 2015.

146. J. Liu, "Catalysis by supported single-metal atoms," ACS Catalysis, vol. 7, pp. 34-59, 2017.

147. Z. Shen, X. Fan, S. Ma, Y. An, D. Yang, N. Guo, Z. Luo and Y. Hu, "3D transitional-metal single atom catalysis toward hydrogen evolution reaction on MXenes supports," International Journal of Hydrogen Energy, vol. 45, pp. 14396-406, 2020.

148. B. L. He, J. S. Shen and Z. X. Tian, "Iron-embedded C2N monolayer: a promising low-cost and high-activity single-atom catalyst for CO oxidation," Physical Chemistry Chemical Physics, vol. 18, pp. 24261-24269, 2016.

149. X. Cui, W. An, X. Liu, H. Wang, Y. Men and J. Wang, "C2N-graphene supported single-atom catalysts for CO2 electrochemical reduction reaction: mechanistic insight and catalyst screening," Nanoscale, vol. 10, pp. 15262-72, 2010.

150. Z. Gao, W. Yang, X. Ding, G. Lv and W. Yan, "Support effects in single-atom iron catalysts on adsorption characteristics of toxic gases (NO_2, NH_3, SO_3 and H_2S)," Applied Surface Science, vol. 23, pp. 4585-4595, 2018.

151. C. Lin, H. Zhang, X. Song, D. H. Kim, X. Li and Z. Jiang, "2D-organic framework confined metal single atoms with the loading reaching the theoretical limit," Material Horizons, vol. 7, pp. 2726-2733, 2020.

152. Q. Zhang and J. Guan, "Single-atom catalysts for electrocatalytic applications," Advanced Functional Materials, vol. 30, pp. 20760-20768, 2020.

153. R Guerrero-Aviles and W. Orellana, "Hydrogen storage on cation decorated biphenylene carbon and nitrogenated holey graphene," International Journal of Hydrogen Energy, vol. 43, pp. 22966-22975, 2018.

154. Y. Liu, Z. Meng, X. Guo, G. Xu, D. Rao, R. Wang, K. Deng and R. Lu, "Ca-embedded C2N: an efficient adsorbent for CO_2 capture," Physical Chemistry Chemical Physics, vol. 19, pp. 28323-28329, 2017.

155. A. Gross, "Ab-initio modeling of microscopic structures and processes in hydrogen storage and electrochemical energy conversion," 239th ACS national meeting & exposition, San Francisco, 2010.

156. M. H. Braga, A. Debski, S. Terlicka, W. Gasior and A. Goral, "Experimental and ab-initio study of the Ag-Li system for energy storage and high-temperature solders," Journal of Alloys and Compounds, vol. 817, pp. 1520-167, 2020.

157. M. Z. Kassaee and E. Vessally, "Solar energy storage in norbornadiene-quadricyclane system: electronic effects via ab-initio computations," Journal of Molecular Structure Theochem, vol. 716, pp. 159-63, 2005.

158. S. Hayashi, E. Tajkhorshid, H. Kandori and K. Schulten, "Role of hydrogen-bond network in energy storage of bacteriorhodopsin's light-driven proton pump revealed by ab-initio normal-mode analysis," Journal of American Chemical Society, vol. 126, pp. 1051-1057, 2005.

159. P. O. Astrand, P. Sommer-Larsen, S. Hvilsted, P. S. Ramanujam, K. L. Bak and S. P. A. Sauer, "Five-membered rings as diazo components in optical data storage devices: an ab-initio investigation of the lowest singlet excitation energies," Chemical Physics Letters, vol. 325, pp. 115-119, 2000.

160. W. E. Pickett, "Pseudopotential methods in condensed matter applications," Computational Physics Reports, vol. 9, pp. 115-118, 1989.

161. T. Hussain, D. J. Searles and M. Hankel, "Insights into the trapping mechanism of light metals on C2N-h2D- utilization as an anode material for metal-ion batteries," Carbon, vol. 160, pp. 125-132, 2020.

162. H. Lin, R. Jin, A. Wang, S. Zhu and H. Li, "Transition metal embedded C2N with efficient polysulfide immobilization and catalytic oxidation for advanced lithium-sulfur batteries: a first principles study," Ceramics International, vol. 45, pp. 17996-18002, 2019.

163. B. L. He, J. S. Shen and Z. X. Tian, "Iron-embedded C2N monolayer: a promising low-cost and high-activity single-atom catalyst for CO oxidation," Physical Chemistry Chemical Physics, vol. 18, pp. 24261-24269, 2016.

164. W. Peng, Y. Guo, Y. Zhang, W. Wu, Y. Liu and Z. Zhou, "A first principles investigation of double transition metal atoms embedded C2N monolayer as a promising SF6 gas adsorbent and scavenger," Materials Chemistry and Physics, vol. 240, pp. 122-136, 2020.

165. R. Car and M. Parrinello, "Unified approach for molecular dynamics and density-functional theory," Physical Review Letters, vol. 55, pp. 2471-2474, 1985.

166. S. Mukherjee, L. Kavalsky, K. Chattopadhyay and C. V. Singh, "Dramatic improvement in the performance of graphene as Li/Na battery anodes with suitable electrolytic solvents," Carbon, vol. 161, pp. 570-576, 2020.

167. T. A. Pham, "Ab-initio simulations of liquid electrolytes for energy conversion and storage," International Journal of Quantum Chemistry, vol. 119, pp. 25-42, 2019.

168. Q. Luo, J. Li, B. Li, B. Liu, H. Shao and Q. Li, "Kinetics in Mg-based hydrogen storage materials: enhancement and mechanism," Journal of Magnetic Alloys, vol. 7, pp. 58-71, 2019.

169. Y. Pang and Q. Li, "A review on kinetic models and corresponding analysis methods for hydrogen storage materials," International Journal of Hydrogen Energy, vol. 41, pp. 18072-18087, 2016.

170. Q. Luo, Y. Guo, B. Liu, Y. Feng, J. Zhang, Q. Li and K. Chou, "Thermodynamics and kinetics of phase transformation in rare earth-magnesium alloys: a critical review," Journal Materials Science and Technology, vol. 44, pp. 171-190, 2020.

171. J. Jin, X. Liu, S. Chen, A. Vasileff, L. Li, Y. Jiao, "Heteroatom-doped transition metal electrocatalysts for hydrogen evolution reaction," ACS Energy Letters, vol. 4, pp. 805-810, 2019.

172. M. Ali, N. Tit and Z. H. Yamani, "Role of defects and dopants in zinc oxide nanotubes for gas sensing and energy storage applications," International Journal of Energy Research, vol. 44, pp. 10926-10936, 2020.

173. J. P. Perdew, K. Burke and M. Ernzerhof, "Generalized gradient approximation made simple," Physical Review Letters, vol. 77, pp. 3865-3868, 1996.

174. Y. M. Kim, Y. M. Shin and B. J. Lee, "Modified embedded-atom method interaction potentials for pure Mn and the Fe-Mn system," Acta Materialia, vol. 57, pp. 474-482, 2009.

175. J. Du, C. Xia, W. Xiong, X. Zhao, T. Wang and Y. Jia, "Tuning the electronic structures and magnetism of two-dimensional porous C2N via transition metal embedding," Physical Chemistry Chemical Physics, vol. 18, pp. 22678-22686, 2016.

176. V. Dhinakaran, M. Lavanya, K. Vigneswari, M. Ravichandran and M.D. Vijayakumar, "Review on exploration of graphene in diverse applications and its future horizon," Materials Today, vol. 27, pp. 824-828, 2020.

177. D. Singh, V. Shukla and R. Ahuja, "Optical excitations and thermoelectric properties of two-dimensional holey graphene," Physical Review B, vol. 102, pp. 744-754, 2020.

178. R. Varunaa and P. Ravindran, "Potential hydrogen storage materials from metal decorated 2D–C2N: Ab-initio study," Physical Chemistry Chemical Physics, vol. 21, pp. 25311-25322, 2011.

179. D. H. Wang, Y. Hu, J. J. Zhao, L. L. Zeng, X. M. Tao, W. Chen, "Holey reduced graphene oxide nano-sheets for high performance room temperature gas sensing," Journal of Materials Chemistry A, vol. 2, pp. 17415-17420, 2011.

180. Y. Lei, J. Zhang, X. Chen, W. Min, R. Wang, M. Yan and J. Xu, "From spent lithium-ion batteries to high performance sodium-ion batteries: A case study," Materials Today: Energy, vol. 26, pp. 1009-1016, 2022.

181. W. Zhong, G. Zhang, Y. Zhang, C. Jia, T. Yang, S. Ji, O. V. Prezhdo, J. Yuan, Y. Luo, J. Jiang, "Mesoporous silica-coated gold nanorods as a light-mediated multifunctional theranostic platform for cancer treatment," Journal of Physical Chemistry Letters, vol. 10, pp. 7009-7014, 2019.

182. P. M. Krzwda, A. P. Rodriguez, L. Cino, N. E. Benes, B. T. Mei and G. Mul, "Electroreduction of NO3 on tubular porous Ti electrodes," Catalysis Science and Technology, vol. 12, pp. 3281-3296, 2022.

183. H. Liu, Q. Huang, W. An, Y. Wang, Y. Men and S. Liu, "Dual-atom active sites embedded in two-dimensional C2N for efficient CO2 electroreduction: A computational study," Journal of Energy Chemistry, vol. 61, pp. 507-516, 2021.

184. A. Ngoipala, T. Kaewmaraya, T. Hussain and A. Karton, "Scavenging properties of yttrium nitride monolayer towards toxic sulfur gases," Applied Surface Science, vol. 537, pp. 147-162, 2021.

185. P. Panigrahi, M. Sajjad, S. Singh, T. Hussain, J. Andreas Larsson, R. Ahuja and N. Singh, "Two-dimensional nitrogenated holey graphene (C2N) monolayer-based glucose sensor for diabetes mellitus," Applied Surface Science, vol. 573, pp. 14-22, 2022.

186. S. Shang, C. Yang, Y. Tian, Z. Tao, A. Hanif, M. Sun, H. H. S. Wong, C. Wang, and J. Shang, "NO2 removal by adsorption on transition-metal-based layered double hydroxides," ACS Environmental Science and Technology Engineering, vol. 1, pp. 375-384, 2021.

187. X. Han, Y. Hong, Y. Ma, W. Lu, J. Li, L. Lin, A. M. Sheveleva, F. Tuna, E. J. L. Mcinnes, C. Dejoie, J. Sun, S. Yang and M. Schroder, "Adsorption of nitrogen dioxide in a redox-active Vanadium metal-oxide framework material," Journal of American Chemical Society, vol. 142, pp. 15235-15239, 2020.

188. X. Han, "Reversible adsorption of nitrogen dioxide within a robust porous metal-organic framework," Nature Materials, vol. 17, pp. 691-696, 2018.

189. Z. Tian, N. Lopez-Salas, C. Liu, T. Liu and M. Antonietti, "C2N: A class of covalent frameworks with unique properties," Advances in Science, vol. 7, pp. 2001-2019, 2020.

190. J. Zhang and W. An, "Single-, double-, and triple-atom catalysts on graphene-like C2N enable electrocatalytic nitrogen reduction: Insight from first principles," Catalysis Science and Technology, vol. 12, pp. 2604-2617, 2022.

191. J. Zeng, L. Xu, Y. Yang, X. Luo, H. J. Li, S. X. Xiong and L. L. Wang, "Boosting the photocatalytic hydrogen evolution performance of monolayer C2N coupled with MoSi2N4: density-functional theory calculations," Physical Chemistry Chemical Physics, vol. 14, pp. 8318-8325, 2021.

192. M. R. A. Kishore, K. Larsson and P. Ravindran, "Two-dimensional CdX/C2N (X = S, Se) heterostructures as potential photocatalysts for water splitting: A DFT study," ACS Omega, vol. 37, pp. 23762-23768, 2020.

193. L. Xu, Z. Ma, Q. Li, T. Chen, B. Peng, J. Zeng, Y. Zhang, K. W. Luo and L. L. Wang, and C. Shuai, "2D layered SiC/C2N van der Waals type-II heterostructure : a visible-light driven photocatalyst for water splitting," New Journal of Chemistry, vol. 44, pp. 15439-15445, 2020.

194. Y. Peng and Q. Li, "A review on kinematic models and corresponding analysis methods for hydrogen storage materials," International Journal of Hydrogen Energy, vol. 41, pp. 18072-18087, 2016.

195. M. Mushtaq, S. Khan and N. Tit, "Magnetization effect of Mn-embedded in C_2N on hydrogen adsorption and gas-sensing properties: Ab-initio analysis," Applied Surface Science, vol. 537, pp. 1470-1479, 2021.

196. S. Khan, M. Mustaq, G. Berdiyorov and N. Tit, "Relevance of metal (Mn versus Ca) embedded C_2N for energy-storage applications: Atomic-scale study," International Journal of Hydrogen Energy, vol. 46, pp. 2445-2463, 2021.

197. M. Mushtaq and N. Tit, "Magnetic single atom catalyst in C_2N to induce adsorption selectivity toward oxidizing gases," Scientific Reports, vol. 11, pp, 1582-1598, 2021.

198. C. Fang and W. An, "Single-metal-atom site with high-spin state embedded in defective BN nanosheet promotes electrocatalytic nitrogen reduction," Nano Research, vol. 14, pp. 4211-4219, 2021.

199. M. He, W. An, Y. Wang, Y. Men and S. Liu, "Hybrid metal-boron diatomic embedded in C_2N monolayer promotes C-C coupling in CO_2 electroreduction," Small, vol. 17, pp. 2104-2145, 2021.

200. W. Thompson XIX, "On the electrodynamic qualities of metals: Effects of magnetization on the electric conductivity of nickel and of iron," Proceedings of the Royal Society of London, pp. 546-550, 1857.

201. M. M. Arafat, B. Dinan, S. A. Akbar and A. S. M. A. Haseeb, "Gas sensors based on one dimensional nano-structured metal-oxides: A review," Sensors, vol. 12, pp. 7207-7258, 2012.

202. M. A. Rashid, A. Koel and T. Rang, "Simulations of graphene nanoribbon field effect transistor for the detection of propane and butane gases: A first principles study," Nanomaterials, vol. 10, pp. 98-113, 2020.

203. E. Artacho, E. Anglada, O. Dieguez and J. D. Gale, "The SIESTA method: Development and applicability," Journal of Physics and Condensed Matter, vol. 20, pp. 1448-1462, 2008.

204. A. Garcia, "Recent developments and applications of 2D materials," Journal of Chemical Physics, vol. 152, pp. 204-216, 2020.

205. M. Cococcioni and S. de Gironcoli, "Linear response approach to the calculation of the effective interaction parameters in the LDA + U method," Physical Review B, vol. 71, pp. 351-368, 2005.

206. I.V. Solovyev and M. Imada, "Screening of Coulomb interactions in transition metals," Physical Review B, vol. 71, pp. 45-71, 2005.

207. M. Springer and F. Aryasetiawan, "Frequency-dependent screened interaction in Ni within the random-phase approximation," Physical Review B, vol. 57, pp. 4364-4368, 1998.

208. M. Yu, S. Yang, C. Wu and N. Marom, "Machine learning the Hubbard U parameter in DFT+U using Bayesian optimization," Computational Materials, vol. 6 pp. 180-186, 2020.

209. N. Tit and M. W. C. Dharma-Wardana, "Superconductivity in carbon nanotubes coupled to transition metal atoms," Europhysical Letters, vol. 62, pp. 405-411, 2003.

210. J. Heyd, G. E. Scuseria and M. Ernzerhof, "Hybrid functionals based on a screened Coulomb potential," Journal of Chemical Physics, vol. 118, pp. 8207-8240, 2003.

211. G. W. Mann, K. Lee, M. Cococcioni, B. Smit and J. B. Neaton, "First-principles Hubbard U approach for small molecule binding in metal-organic frameworks," Journal of Chemical Physics, vol. 144, pp. 1741-1788, 2016.

212. V. Eswaraiah, Q. Zeng, Y. Long and Z. Liu, "Black Phosphorus Nanosheets: Synthesis, Characterization and Applications," Small, vol. 12, pp. 3480-3502, 2016.

213. K. Zhang, Y. Feng, F. Wang, Z. Yang and J. Wang, "Two-dimensional hexagonal boron nitride (2D-hBN): synthesis, properties and applications," Journal of Materials Chemistry C, vol. 5, pp. 11992-12022, 2017.

214. B. Zhao, D. Shen, Z. Zhang, P. Lu, M. Hossain, J. Li, B. Li and X. Duan, "2D Metallic Transition-Metal Dichalcogenides: Structures, Synthesis, Properties, and Applications," Advanced Functional Materials, vol. 31, pp. 2105-2132, 2021.

215. K. Hantanasirisakul and Y. Gogotsi, "Electronic and Optical Properties of 2D Transition Metal Carbides and Nitrides (MXenes)," Advanced Materials, vol. 30, pp. 1804-1877, 2017.

216. M. Alhabeb, K. Maleski, B. Anasori, P. Lelyukh, L. Clark, S. Sin and Y. Gogotsi, "Guidelines for Synthesis and Processing of Two-Dimensional Titanium Carbide (Ti3C2Tx MXene)," Chemical Materials, vol. 29, pp. 7633-7644, 2017.

217. M. M. Dong, G. P. Zhang, Z. L. Li, M. L. Wang, C. K. Wang and X. X. Fu, "Molecular dynamics simulations on fullerene surfactants with different charges at the air–water interface," Physical Chemistry Chemical Physics, vol. 22, pp. 28074-85, 2020.

218. X. Wang, Y. Wang, R. Quhe, Y. Tang, X. Dai and W. Tang, "Designing strained C_2N/GaTe (InTe) heterostructures for photovoltaic and photocatalytic application," Journal of Alloys and Compounds, vol. 816, pp. 1525-1559, 2020.

219. Z. Liang, "Lithium metal batteries: synergetic effects of lithium metal batteries by preferential ionic interactions," Advanced Energy Materials, vol. 11, pp. 2003-2057, 2021.

220. S. Khan, A. Wasfi, M. Mushtaq, F. Awwad and N. Tit, "Transition-metal single atom catalyst embedded in C_2N for toxic-gas reduction reaction and selective gas-sensing application: Atomic-scale study," Applied Surface Science, vol. 599, pp. 1540-1557, 2022.

221. I. Choudhuri and B. Pathak, "Photochemical Water Splitting by Bismuth Chalcogenide Topological Insulators," Chemical Physics Chemistry, vol. 18, pp. 2336-2346, 2017.

222. S. Gong, W. Wan, S. Guan, B. Tai, C. Liu, B. Fu, S. A. Yang and Y. Yao, "Tunable half-metallic magnetism in an atom-thin holey two-dimensional C_2N monolayer," Journal of Material Chemistry C, vol. 5, pp. 8424-8430, 2017.

223. A. M. Yakout, "Future technology for new data storage and communication devices," Journal of Superconductivity and Magnetism, vol. 33, pp. 2557-2580, 2020.

224. Y. P. Feng, L. Shen, M. Yang, A. Wang, M. Zeng, Q. Wu, S. Chintalapati and C. R. Chang, "Prospects of spintronics based on 2D materials," Computational Molecular Science, vol. 7, pp. 131-143, 2017.

225. C. Jia, B. Zhou, Q. Song, X. Zhang and Z. Jiang, "A wide range operating synaptic device based on organic ferroelectricity with low energy consumption," RSC Advances, vol. 8, pp. 1883-1897, 2018.

226. N. K. Jaiswal, N. Tyagi, A. Kumar and P. Srivastava, "Structural and electronic properties of armchair graphene nanoribbons functionalized with fluorine," Applied Surface Science, vol. 396, pp. 471-479, 2017.

227. Y. Ma, Y. Dai, M. Guo, C. Niu, J. Lu and B. Huang, "Electronic and magnetic properties of perfect, vacancy-doped, and nonmetal adsorbed MoSe2, MoTe2 and WS2 monolayers," Physical Chemistry Chemical Physics, vol. 13, pp. 15546-15553 2011.

228. Y. Yang, Y. Liu, B. Man, M. Zhao and W. Li, "Tuning the electronic and magnetic properties of MoS2 nanotubes with vacancy defects," RSC Advances, vol. 9, pp. 1723-1741, 2019.

229. A. Devi, N. Dhiman, N. Kumar, W. Alfalasi, A. Kumar, P. K. Ahluwalia, A. Singh and N. Tit, Scientific Reports, 2023 (submitted)

230. J. Hong, "Exploring atomic defects in molybdenum disulphide monolayers," Nature Communications, vol. 6, pp. 629-711, 2015.

231. P. Cui, J. Zheng, H. Peng, J.H. Choi, Z. Li, C. Zeng, C.K. Shih, J.P. Perdew and Z. Zhang, "Predictive design of intrinsic half-metallicity in zigzag tungsten dichalcogenide nanoribbons," Physical Review B, vol. 100, pp. 1953-1978, 2019.

232. E. C. Ahn, "2D materials-based nanoscale tunnelling field effect transistors: current developments and future prospects," 2D Materials Applied, vol. 114, pp. 219-232, 2020.

233. G. Hu and B. Xiang, "Ferroelectric-like Behaviour Originating from Oxygen Vacancy Dipoles in Amorphous Film for Non-volatile Memory," Nanoscale Resolution Letters, vol. 15, pp. 226-248, 2020.

234. M. Ernzerhof and G.E. Scuseria, "Assessment of the Perdew–Burke–Ernzerhof Exchange-Correlation Functional," Journal of Chemical Physics, vol. 110, pp. 502-539, 1999.

235. B. Wasilewski and M. Werwinski, "Monte Carlo calculations of Curie temperatures of Y1−xGdx(Fe1−yCoy)2 pseudobinary system," Journal of Magnetic Materials, vol. 543, pp. 1686-1698, 2022.

236. B. Wasilewski, W. Marciniak and M. Werwinski, "Curie temperature study of Y(Fe1-xCox)2 and Zr(Fe1-x-Cox)2 systems using mean field theory and Monte Carlo method," Journal of Physics D: Applied Physics, vol. 51, pp. 1750-1768, 2018.

237. H. Yin, C. Liu, G. P. Zheng and Y. Wang, "Ab initio simulation studies on the room-temperature ferroelectricity in two-dimensional β-phase GeS," Applied Physics Letters vol. 114, pp. 1929-1943, 2019.

238. A. P. Durajski, A. E. Auguscik and R. Szczesniak, "Tunable Electronic Properties of Twisted Graphene Layers in High Angles Regime," Physica E, vol. 119, pp.1139-1185, 2020.

239. Y. Liu, Z. Meng, X. Guo, G. Xu, D. Rao, Y. Wang, K. Deng and R. Lu, "Ca-Embedded C2N: an efficient adsorbent for CO2 capture," Physical Chemistry Chemical Physics, vol. 19, pp. 28323-28329, 2017.

240. D. Anbuselvan, S. Nilavazhagan, A. Santhanam, N. Chidhambaram, K. V. Gunavathy, T. Ahmad and S. M. Alshehri, "Room temperature ferromagnetic behavior of nickel-doped zinc oxide dilute magnetic semiconductor for spintronics applications," Physica E, vol. 129, pp. 1146-1165, 2021.

241. M. Li, J. Lu, Z. Chen and K. Amine, "30 years of lithium-ion batteries," Advanced Materials, vol. 30, pp.1800-1861, 2018.

242. A. Fotouhi, D. J. Auger, K. Propp, S. Longo and M. Wild, "A review on electric vehicle battery modelling: From Lithium-ion toward Lithium-Sulphur," Renewable and Sustainable Energy Reviews, vol. 56, pp. 1008-1021, 2016.

243. M. D. Slater, D. Kim, E. Lee and C. S. Johnson, "Review on sodium-ion batteries," Advanced Functional Materials, vol. 23, pp. 947-958, 2013.

244. R. Rajagopalan, Y. Tang, X. Ji, C. Jia and H. Wang, "Advancement and challenges in potassium-ion batteries: A comprehensive review," Advanced Functional Materials, vol. 30, pp.1909-1986, 2020.

204

245. N. Jayaprakash, S. K. Das and L. A. Archer, "The rechargeable aluminum-ion battery," Chemical Communications, vol. 47, pp.12610-12612, 2011.

246. Y. Li and H. Dai, "Recent advances in zinc-air batteries," Chemical Society Reviews, vol. 43, pp. 5257-5275, 2017.

247. Y. X. Wang, B. Zhang, W. Lai, Y. Xu, S. L. Chou, H. K. Liu and S. X. Dou, "Room-temperature Sodium-Sulfur batteries: A comprehensive review on research progress and cell chemistry," Advances in Energy Materials, vol. 7, pp. 1602-1629, 2017.

248. Y. Wang, D. Zhou, V. Palomares, D. Shanmukaraj, B. Sun, X. Tang, C. Wang, M. Armand, T. Rojo and G. Wang, "Revitalising sodium-sulfur batteries for non-high-temperature operation: A crucial review," Energy and Environmental Sciences, vol.13, pp. 3848-3879, 2020.

249. D. Kumar, S.K. Rajouria, S.B. Kuhar and D.K. Kanchan, "Progress and prospects of sodium-sulfur batteries: A review," Solid State Ionics, vol. 312, pp. 8-16, 2017.

250. X. Xu, D. Zhou, X. Qin, K. Lin, F. Kang, B. Li, D. Shanmukaraj, T. Rojo, M. Armand and G. Wang, "A room-temperature sodium-sulfur battery with high capacity and stable cycling performance," Nature Communications, vol. 9, pp. 387-396, 2018.

251. Y. Tian, G. Zeng , A. Rutt , T. Shi , H. Kim , J. Wang , J. Koettgen, Y. Sun , B. Ouyang , T. Chen, Z. Lun , Z. Rong , K. Persson and G. Ceder , "Promises and challenges of next-generation," Chemical Reviews, vol. 121, pp. 1623-1669, 2021.

252. R. Fang, J. Xu and D.W. Wang, "Covalent fixing of sulfur in metal-sulfur batteries," Energy and Environmental Science, vol. 13, pp. 432-471, 2020.

253. P. Hu, F. Xiao, Y. Wu, X. Yang, N. Li, H. Wang and J. Jia, "Covalent encapsulation of sulfur in a graphene/N-doped carbon host for enhanced sodium-sulfur batteries," Chemical Engineering Journal, vol. 443, pp. 136-157, 2022.

254. F. Xiao, X. Yang, H. Wang, J. Xu, Y. Liu, D. Y. W. Yu and A. L. Rogach, "Covalent encapsulation of sulfur in a MOF-derived S, N-doped porous carbon host realized via vapor-infiltration method: Results in enhanced Sodium-Sulfur battery performance," Advanced Energy Materials, vol. 10, pp. 209-231, 2020.

255. T. Hussain, T. Kaewmaraya, Z. Hu, X. S. Zhao, "Efficient control of the shuttle effect in sodium-sulfur batteries with functionalized nanoporous graphenes" ACS Applied Nano Materials, vol. 5, pp. 12637-12645, 2022.

256. F. Xiao, H. Wang, J. Xu, W. Yang, X. Yang, D. Y. W. Yu, A. L. Rogach, "Generating short-chain sulfur suitable for efficient Sodium-Sulfur batteries via atomic copper sites on N, O-codoped carbon composite," Advanced Energy Materials, vol. 11, pp. 210-229, 2021.

257. N. Thatsami, P. Tangpakonsab, P. Moontragoon, R. Umer, T. Hussain, T. Kaewmaraya, "Two-dimensional titanium carbide (Ti3C2Tx) MXenes to inhibit the shuttle effect in sodium-sulfur batteries," Physical Chemistry Chemical Physics, vol. 24, pp. 4187-4195, 2011.

258. M. Naguib, M. Kurtoglu, V. Presser, J. Lu, J. Niu, M. Heon, L. Hultman, Y. Gogotsi, M. W. Barsoum, "Two-dimensional nanocrystals produced by exfoliation of Ti3AlC2," Advanced Materials, vol. 23, pp. 4248-4253, 2011.

259. X. F. Yu, Y. C. Li, J. B. Cheng, Z. B. Liu, Q. Z. Li, W. Z. Li, X. Yang, B. Xiao, "Monolayer Ti2CO2: A promising candidate for NH3 sensor of capture with high sensitivity and selectivity," ACS Applied Material Interfaces, vol. 7, pp. 13707-13713, 2015.

260. P. Khakbaz, M. Moshayedi, S. Hajian, M. Soleimani, B. B. Narakathu, B. J. Bazuin, M. Pourfath, M. Z. Atashbar, "Titanium Carbide MXene as NH3 Sensor: Realistic First-Principles Study," Journal of Physical Chemistry C, vol. 123, pp. 29794-29803, 2019.

261. M. Alhabeb, K. Maleski, B. Anasori, P. Lelyukh, L. Clark, S. Sin and Y. Gogotsi, "Guidelines for synthesis and processing of two-dimensional titanium carbide (Ti3C2Tx MXene)," Chemical Materials, vol. 29, pp. 7633-7644, 2017.

262. K. R. G. Lim, M. Shekhirev, B. C. Wyatt, B. Anasori, Y. Gogotsi, Z. W. She, "Fundamentals of MXene synthesis," Nature Synthesis, vol. 1, pp. 601-614, 2022.

263. P. Nasarre, V. Potiron, H. Drabkin and J. Roche, "Guidance molecules in lung cancer," Cell Adhesion & Migration, vol. 4, 130-145, 2010.

264. D. J. Selkoe, "Defining molecular targets to prevent alzheimer desease," Archives of Neurology, vol. 62, pp. 192-195, 2005.

265. T. Zhang, Z. Chen, J. Zhao and Y. Ding, "Metal-N4/graphene as an efficient anchoring material for lithium-sulfur batteries: A computational study," Diamond and Related Materials, vol. 90, pp. 72-78, 2018.

266. W. Bao, C. E. Shuck, W. Zhang, X. Guo, Y. Gogotsi and G. Wang, "Boosting Performance of Na-S Batteries Using Sulfur-Doped Ti3C2Tx MXene Nanosheets with a Strong Affinity to Sodium Polysulfides," ACS Nano, vol. 13, pp. 11500-11509, 2019.

267. Z. Yan, Y. Liang, W. Hua, X. G. Zhang, W. Lai, Z. Hu, W. Wang, J. Peng, S. Indris, Y. Wang, S. L. Chou, H. Liu and S. X. Dou, "Multiregion Janus-Featured Cobalt Phosphide-Cobalt Composite for Highly Reversible Room-Temperature Sodium-Sulfur Batteries," ACS Nano, vol. 14, pp. 10284-10293, 2020.

268. M. Sajjad, T. Hussain, N. Singh and J. A. Larsson, "Superior Anchoring of Sodium Polysulfides to the Polar C2N 2D Material: A Potential Electrode Enhancer in Sodium-Sulfur Batteries," Langmuir, vol. 36, pp. 13104-13111, 2020.

269. T. Kaewmaraya, T. Hussain, R. Umer, Z. Hu and X. S. Zhao, "Efficient suppression of the shuttle effect in Na-S batteries with an As2S3 anchoring monolayer," Physical Chemistry Chemical Physics, vol. 22, pp. 27300-27307, 2020.

270. P. Ma, D. Fang, Y. Liu, Y. Shang, Y. Shi and H. Y. Yang, "MXene-based materials for electrochemical Sodium-ion storage," Advances in Science, vol. 8, pp. 2003-2018, 2021.

271. Z. Wang, Y. Zhang, H. Jiang, C. Wei, Y. An, L. Tan, S. Xiong and J. Feng, "Free-standing Na2C6O6/MXene composite paper for high-performance organic sodium-ion batteries," Nano Research, vol. 16, pp. 458-465, 2023.

272. M. Tang, J. Li, Y. Wang, W. Han, S. Xu, M. Lu, W. Zhang and H. Li, "Surface terminations of MXene: Synthesis, characterization, and properties," Symmetry, vol. 14 pp. 2232-2242, 2022.

273. Q. Meng, Z. Lo, J. L. Ma and A. Hu, "Theoretical Investigation of Zirconium Carbide MXenes as prospective high-capacity anode materials for Na-ion batteries," Journal of Materials Chemistry A, vol. 6, pp. 13652-13678, 2018.

274. H. H. Haseeb, Y. Li, S. Ayub, Q. Fang, L. Yu, K. Xu and F. Ma, "Defective Phosphorene as a Promising Anchoring Material for Lithium–Sulfur Batteries," Journal of Physical Chemistry C, vol. 124, pp. 2739-2746, 2020.

275. D. Wang, F. Li , R. Lian , J. Xu , D. Kan , Y. Liu , G. Chen, Y. Gogotsi and Y. Wei, "A General Atomic Surface Modification Strategy for Improving Anchoring and Electrocatalysis Behavior of $Ti_3C_2T_2$ MXene in Lithium-Sulfur Batteries" ACS Nano, vol.13, pp. 11078-11086, 2019.

276. Z. Du, X. Chen, W. Hu, C. Chuang , S. Xie, A. Hu, W. Yan, X. Kong , X. Wu, H. Ji and L. J. Wan, "Cobalt in Nitrogen-Doped Graphene as Single-Atom Catalyst for High-Sulfur Content Lithium-Sulfur Batteries," Journal of American Chemical Society, vol. 141, pp. 3977-3985, 2019.

277. G. Henkelman, B. P. Uberuaga and H. Jonsson, "A climbing image nudged elastic band method for finding saddle points and minimum energy paths," Journal of Chemical Physics, vol.113, pp. 9901-9904, 2000.

278. R. Jayan and M. M. Islam, "Single-Atom Catalysts for Improved Cathode Performance in Na–S Batteries: A Density Functional Theory (DFT) Study," Journal of Physical Chemistry C, vol. 125, pp. 4458-4467, 2021.

279. K. Yang, D. Liu, Y. Sun, Z. Qian, S. Zhong and R. Wang, "Metal-N_4@Graphene as Multifunctional Anchoring Materials for Na-S Batteries: First-Principles Study" Nanomaterials, vol. 11, pp. 1197-1206, 2021.

List of Publications

(ORCID ID: 0000-0002-9040-2577)

1) M. Ali, S. Khan, F. Awwad, N. Tit, "High gas-sensing selectivity of bilaterally edge doped graphene nanoribbons towards detecting NO_2, O_2 and SO_3 gas molecules: Ab initio investigation," *Applied Surface Science*, vol. 514, pp. 1-12, 2020.
https://www.sciencedirect.com/science/article/abs/pii/S016943322030622X

2) M. Mushtaq, S. Khan, N. Tit, "Magnetization effect of Mn-embedded in C_2N on hydrogen adsorption and gas-sensing properties: Ab-initio analysis," *Applied Surface Science*, vol. 537, pp. 1-13, 2021.
https://www.sciencedirect.com/science/article/abs/pii/S0169433220327276

3) S. Khan, M. Mushtaq, G. Berdiyorov, N. Tit, "Relevance of metal (Ca versus Mn) embedded C_2N for energy-storage applications: Atomic-scale study," *International Journal of Hydrogen Energy*, vol. 46, pp. 2445-2463, 2021.
https://www.sciencedirect.com/science/article/abs/pii/S0360319920338064

4) S. Khan, A. Wasfi, M. Mushtaq, F. Awwad, N. Tit, "Transition-metal single atom catalyst embedded in C_2N for toxic-gas reduction reaction and selective gas-sensing application: Atomic-scale study," *Applied Surface Science*, vol. 599, pp. 1-14, 2022.
https://www.sciencedirect.com/science/article/abs/pii/S0169433222015768

5) S. Khan, Y. P. Feng, N. Tit, "Synergetic effects of combining TM single- and double- atom catalysts embedded in C_2N on inducing half metallicity: DFT study," *2D Materials*, vol. 10, pp. 1-23, 2023.
https://iopscience.iop.org/issue/2053-1583/10/1

Appendices

Appendix A

Adsorbent-Adsorbate Charge Transfer

To probe the interface interaction between the gas molecule and graphene nanoribbon, the charge density difference may be obtained by subtracting the charge densities of isolated gas molecule and graphene nanoribbon from the total charge density of the hybrid structure, as shown in Fig. A.1. For such aim, we used Bader charge analysis method to illustrate the charge density differences in cases: (a) NO_2@GNR: B, (b) O_2@ GNR: B, and (c) SO_3@ GNR:N.
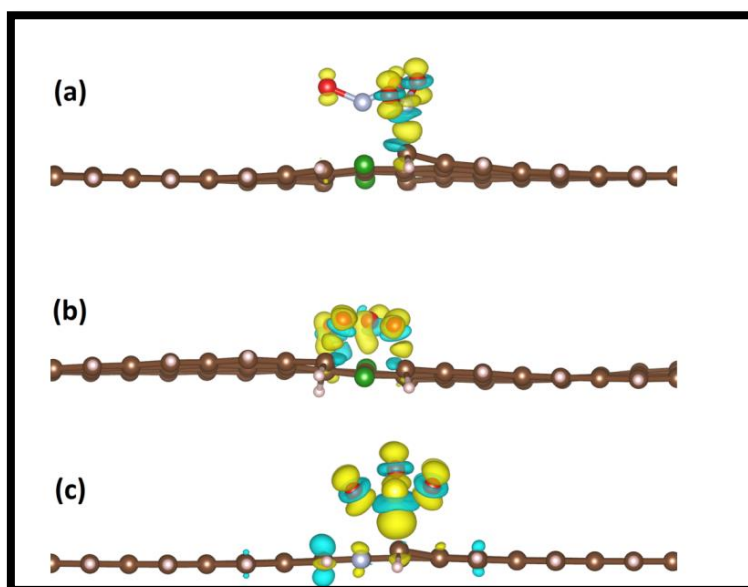
Figure A1: Charge density difference plots of NO_2@GNR:B, O_2@GNR:B and SO_3@GNR:N.

It is clearly shown that the charge depletes from C atoms and accumulates at the interfaces between gas molecules and GNR: B/N. The yellow (cyan) color represents the excess (deficit) of electrons at the interface region. The yellow lobes indicate strong bonding between gas molecules and GNRs. These plots further confirm that the charge transfers from GNR surface to gas molecules. Thus, NO_2, O_2 and SO_3 are oxidizing molecules and forming covalent bonds on the surfaces of GNRs.

Appendix B

Special IV Characteristics (on/off)

The concept of minimum metallic conductivity in a dirty metal was first reported by Mott and experimentally observed by Davis and Compton (i.e., $\sigma_{min} \cong 0.025 e^2/\hbar a$, where e is electronic charge, $\hbar$ is Planck constant, and a is the average distance between impurities). Such minimum metallic conductivity can also be deduced from Drude model of conductivity in metals as the mean-free path must have a lower limit to be the lattice spacing. The minimum metallic conductivity should yield a minimum conductance of about G_{min} =6.08 x 10^{-6} Ω^{-1}, which corresponds to a maximum resistance R_{max}= 0.2M Ω. Until the present, experimental evidence continues to appear and corroborate the existence of minimum metallic conductivity in various systems. To the best of our knowledge, the maximum measurable resistance cannot exceed 3M Ω . For instance, the experimental measurements of resistance in ZnO thin films were reported by Wisz's group to be no more than 1 M Ω and by Al Hardan's group to be less than 3 M Ω. Beyond these values, experimental measurement appears clear as very weak electric currents cannot be detected.

Having said the above, hereafter we discuss the effects of adsorptions of SO_3 molecule on GNR: B and both NO_2 and O_2 molecules on GNR: N. Our ab-initio atomic relaxations showed that SO_3 exhibits a physisorption on GNR: B with adsorption distance of 2.49 Å and weak energy of −0.34 eV. Whereas, both NO_2 and O_2 exhibit chemisorption processes on GNR: N without molecular dissociation. The obtained adsorption energies are: −0.47 eV and −1.89 eV, and the charges gained by the molecules are: 0.36e and 0.97e, respectively. Furthermore, it is remarkable that the molecules NO_2 and O_2, chemisorbed on GNR: N, do make chemical bounds with the carbon atoms neighboring N atoms. The chemical bond lengths are: 2.04 Å and 1.69 Å, respectively. These bonds are elongated as compared to the single sigma bonds: $d_{(C-N)}$ = 1.47 Å and $d_{(C-O)}$ = 1.43 Å, respectively.

From the perspective of transport properties, the physisorption process of SO_3 molecule has no effect on the IV-characteristics of GNR: B. In contrast to this, our results show

that the effects of the chemisorption processes of NO_2 and O_2 on GNR: N on the IV-characteristics to be strong as basically very weak currents are produced (see Fig. A.2). The obtained currents are at maximum of order 10^{-12} and 10^{-17} Amperes, respectively. Obviously, such small currents are experimentally undetectable. Hence, one might think to use GNR:N as alarm sensor, as it can be explored in logical gate. When NO_2 passes through it the current becomes zero. So, while GNR: B can be good gas sensor for NO_2, GNR:N can play the role of alarm sensor.
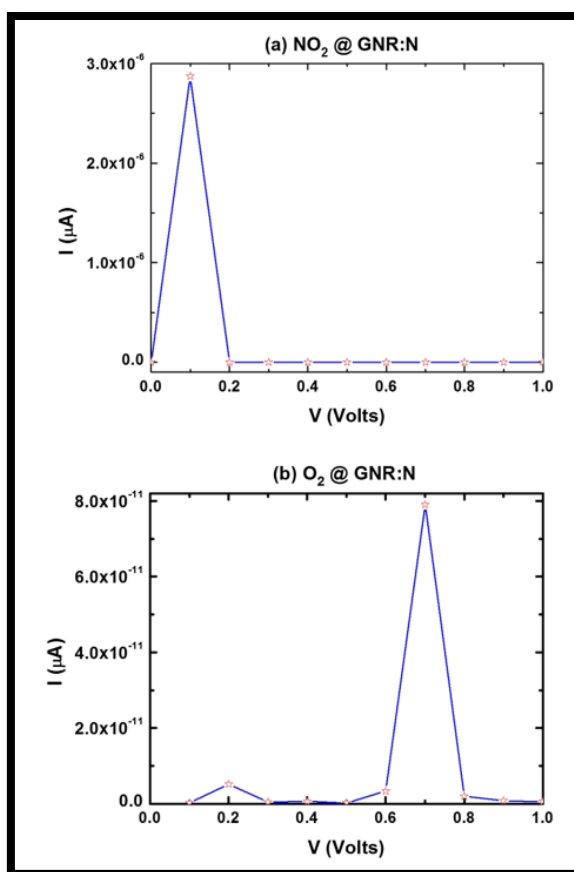

Figure A2: IV characteristics of GNR:N based devices after chemisorption of (a) NO_2 and (b) O_2 molecules.

Appendix C

Computational Details for DFT Calculations

Concerning the computational methods, both ATK and VASP packages were used for tasks to perform atomic relaxation, calculations of adsorption energy, recovery time, and magnetization:

First, the SIESTA's power stems from the use of localized atomic orbitals as a basis set of the Hamiltonian, which empowered the method to deal with large systems. To take translational symmetry into account, Brillouin-zone sampling is explored using special k-point technique, such as Monkhorst Pack (MP) is employed with K-mesh grids of 50x1x1 and 100x5x5 for the respective calculations of atomic relaxation and electronic structures and transport properties, respectively. The convergence criteria for energy and force in case of atomic relaxations are similar as well to the ones used in VASP and described below. In addition, the calculation of spin-polarized Partial Density of States (PDOS) is performed using a smearing of width 0.026 eV. The latest version of SIESTA incorporates the Hubbard parameter (DFT+U) to describe the interaction between TM atoms through onsite parameterization. The adjustment of U parameter is described in the Appendix (A4).

Second, in VASP, the wave-functions are expanded in Linearized Augmented Plane-Waves (LAPW) basis set within an energy cutoff (E_{cut} = 500 eV). Such E_{cut} controls the number of plane waves to be used as basis set in the Hamiltonian. Such a larger cutoff would be computationally more expensive. For the exchange–correlation functional, we employed the General Gradient Approximation (GGA), parameterized by Perdew-Burke-Ernzerhof (PBE), including both the long-range dipole–dipole van der Waals interaction, using the DFT-D3 method of Grimme scheme, and the magnetic interactions due to TM atoms through the Hubbard U parameter. In sampling the Brillouin-zone, MP technique was used with grids of meshes 25x1x1 and 50x1x1 in the calculations of atomic relaxation and spin polarized Partial Density of States (PDOS), respectively. In the structure optimization, all atoms were allowed to relax until the Hellmann Feynman forces on each atom and the total energy become smaller than 0.01 eV/Å and 0.1 meV, respectively. The pressure tolerance was set to be 0.1 GPa.

Appendix D

Choice of Hubbard U parameter

In theoretical studies, the Hubbard U parameter is usually chosen in an empirical way to fit one or several properties of the system under study. For instance, the aimed property could be the band-gap energy, or the magnetic moment of the transition-metal atom, or

even the adsorption energy. The value of U should not be a fitting parameter as it corresponds to a physical property (i.e., related to the strength of a screened electron–electron interaction). Nonetheless, in literature, about two general methods have been followed:

    (a) Constrained DFT (cDFT), and
    (b) Constrained Random-Phase Approximation (cRPA).

In the former method, the parameter U is estimated from the variation of the occupation of the localized orbitals related to the TM dopant. Whereas, in the latter method, the static values from the dynamical polarization should be extracted. Definitely, these two methods should not yield the same results for the screened interaction parameter "U". The main reason for the discrepancy is the fact that the cDFT takes into account only responses coming from only on-site 3d electrons to an external perturbation, while the cRPA includes responses from both on-site and inter-site 3d electrons. In the present investigation, the focus was on SAC of TM embedded in pore of C_2N and meanwhile was not on the calculation of Hubbard U. So, these computational methods were not used, but the U values for different TM-SAC atoms were simply taken from literature. Effective U Hubbard parameter can be calculated by the U-J approach. We recall that U and J should stand for the on-site Coulomb repulsion and the exchange interaction between metal atoms, respectively. As a special case, in our model, we deal with TM-SAC, so that J is vanishingly small. Moreover, using the hybrid functionals (e.g., such as the Heyd-Scuseria-Ernzerhof (HSE)'s exchange–correlation functional in VASP, U can be varied from 0.0 to 8.0 eV in a step of about 0.2 eV in order to benchmark the output results of some specific experimental quantity like bandgap energy, magnetic moment or adsorption energy. For example, Mann and coworkers rigorously studied the binding energy of small molecules to Metal–Organic Frameworks (MOFs). These authors adjusted U Hubbard parameters to yield the best (CO_2 on MOF) adsorption energies to agree with the experimental data for a number of different metal centers (M = Ti, V, Cr, Mn, Fe, Co, Ni, and Cu).

The effect of U parameter on the E_{ads} was reported to be linear and shifting for about 0.041 eV over the range of U = 0-5.4 eV in case of Cobalt-based MOF (Co-MOF-74).

These authors reported the optimized values of U Hubbard, for instance, for the TM-SACs of our current interest to be: U(Mn) = 5.5 eV, U(Fe) = 6.5 eV, U(Co) = 5.3 eV, and U(Ni) = 6.7 eV. While the inclusion of U parameter in case of systems with TM-atoms is necessary, many packages such as VASP and SIESTA use a default on-site value which is about U = 5.0 eV.

In our work in ATK, we have used the default value by switching on the U-Hubbard parameter, whereas in VASP we specified the value (U = 5.0 eV) in the INCAR script. Yet, using the experience of Mann and coworkers, we decided to test the effect of small variation of U Hubbard parameter on the binding energy of our selected TM catalysts (i.e., Mn, Fe, Co, and Ni). We considered the ranges of variation of U between two extreme values as follows:

a) For Mn, U = [4.0,5.5] eV
b) For Fe, U = [4.0,6.5] eV
c) For Co: U = [3.3,5.3] eV
d) For Ni, U = [5.0,6.7] eV

We meant to keep the default value (U = 5.0 eV) therein the interval of variation. Mann and coworkers reported the extreme values [73] using linear response and semi-empirical approximations. Consistent to what was reported by these researchers (who reported a small shifting in binding energy in case of Co-based MOF of about 0.041 eV when U was acted to span the range U = 0 - 5.4 eV). In our cases of M@C_2N-NR, the shifting in binding energy did not exceed 0.010 eV when U was varied over the energy ranges mentioned above.

The results of total and binding energies are reported in Table 5.1. So, we decided to stick to the default value of Hubbard U parameter proposed in the SIESTA packages.

UAE UNIVERSITY DOCTORATE THESIS NO. 2023: 37

The field of Two-Dimensional (2D) materials has been extensively studied since their discovery in 2004, owing to their remarkable combination of properties. In this thesis, Density Functional Theory (DFT) has been employed to explore and study such novel 2D materials for specialized applications such as gas sensing, energy storage and spintronics. This would further pave the way towards developing light weight and cost-effective solutions for the mentioned applications.

Saba Khan received her Doctorate in Physics from the Department of Physics, UAE University and Master of Science/Master of Technology (dual) in Nanoscience and Nanotechnology from Amity University, India. Prior to this she received her Bachelor of Science (Physics) from Hansraj College, University of Delhi, India.

www.uaeu.ac.ae